

# Investigating the structure and function of the plant photosynthetic membrane using atomic force microscopy and Monte Carlo simulations



The  
University  
Of  
Sheffield.

**William Henry John Wood**

A thesis submitted in partial fulfilment of the requirement for the degree of  
Doctor of Philosophy

The University of Sheffield

Faculty of Science

Department of Molecular Biology and Biotechnology

March 2017

## Summary

The relative spatial organisation of protein complexes involved in the light reactions of photosynthesis in plants, (photosystem II (PSII), cytochrome *b<sub>6</sub>f* (*cytb<sub>6</sub>f*), photosystem I (PSI), and ATP synthase) remains unknown, but is crucial as it determines the diffusive path of mobile electron carriers plastoquinone (PQ) and plastocyanin (PC).

Protocols were developed for purifying grana and stromal lamellae membranes for atomic force microscopy (AFM) in model plants spinach (*Spinacia oleracea*) and *Arabidopsis thaliana*. The development of methods to purify stromal lamellae from spinach for AFM allowed for the nanoscale imaging of PSI and ATP synthase for the first time. The 3.2 nm, stroma-protruding subunits of PSI were clearly visible in the AFM images, facilitating its identification. Contrary to the consensus that PSI in plants is monomeric, 25% of PSI were found to exist as dimers, which may facilitate diffusion of protein complexes within the stromal lamellae. ATP synthase was present and intact within the purified stromal lamellae membranes and showed the same height and width as purified *Bos taurus* ATP synthase incorporated into a DOPC lipid bilayer.

The implications of the observed organisation of PSII, *cytb<sub>6</sub>f*, and PSI for the rate of electron transport were investigated using Monte Carlo simulations. AFM data revealed that long-range (>100 nm) diffusion distances are required of the thylakoid luminal protein plastocyanin (PC). The simulations revealed that the diffusion of PC is significantly restricted due the crowded nature of the thylakoid lumen and was affected by the size of the grana/stromal lamellae interface. It was proposed that the size of the interface is, therefore, the result of a compromise between a large interface, which maximises the rate of PC transport, and a small interface which minimises the excitation energy spillover from PSII to PSI.

## Acknowledgements

I would like to thank my supervisors, particularly Matt Johnson, who taught me everything in easy-to-understand, cooking-related analogies: “Membranes are like meat. You *can* freeze them but they’re never as good afterwards”. Jamie Hobbs, not only for supporting me through my PhD but also for his excellent teaching during my master’s degree. A special thanks to Neil Hunter who, while not technically my supervisor, took more than enough interest in my work and offered more than enough guidance than would be expected of one.

Secondly, I will give my thanks to the people directly involved in the work presented in this thesis: Craig MacGregor-Chatwin provided a number of the AFM images of stromal lamellae as well as slightly offensive birthday cards. Xia Huang carried out the work on *Bos Taurus* ATP synthase which was provided by Tobias Spikes of John Walker’s Lab at the MRC Mitochondrial Biology Unit, University of Cambridge. Guy Mayneord who made the graphics of thylakoid membranes over and over again because we were never satisfied. Come to think of it, I think the PSI are just a bit *too* red.

A big thank you to the people who have helped me in the lab: Mo Brindley for organising everything and for re-teaching me how to purify proteins every 2 years or so when I forget, Lizzy Martin for always being there for basically any issue, Cvet Vasilev and John Olsen for all the AFM help, Sam Barnett who is always the first person I go to for code related questions, Cesar Cruz for teaching me how to grow plants, Katie Steel for showing me how to use a bin on my first day and how to keep a well-organised lab book. Of course, I would like to say a massive thank you to everyone else in the Hunter lab even if I haven’t mentioned you by name. Thank you to everyone in the Hobbs lab who have helped me, in particular: Nic Mullin, Jonny Burns, Sandip Kumar and Rik Bailey.

I would also like to thank the people elsewhere in the department and the university: Svet Tzokov and Chris Hill from the EM suite, and Greg Nicholson for help with the plant growth chamber.

Finally, I would like to acknowledge the funding for this PhD project, which was provided by Project Sunshine at the University of Sheffield, and financial support from the Kirkwood Foundation.

# Table of Contents

## Chapter 1. General introduction

1.1.	Photosynthesis in plants	1
1.2.	The light reactions	1
1.3.	Overview of the dark reactions	3
1.4.	The structure of the thylakoid membrane	3
1.5.	Components of the thylakoid membrane.	4
1.5.1.	Lipids of the thylakoid membrane	4
1.5.2.	Chlorophyll	5
1.5.3.	Light-harvesting complex II (LHCII)	7
1.5.4.	Photosystem II (PSII)	7
1.5.5.	Cytochrome <i>b<sub>6</sub>f</i> ( <i>Cytb<sub>6</sub>f</i> )	9
1.5.6.	Plastocyanin (PC)	11
1.5.7.	Photosystem I (PSI)	12
1.5.8.	The ferredoxin-ferredoxin NAPP <sup>+</sup> reductase complex (Fd-FNR)	14
1.5.9.	ATP synthase	14
1.6.	Regulation of the light reactions of photosynthesis	16
1.6.1.	Cyclic electron flow	16
1.6.2.	State transitions	16
1.6.3.	Non-photochemical quenching	17
1.7.	Detergents	17
1.8.	Atomic force microscopy	18
1.9.	PeakForce quantitative nanomechanical mapping <sup>®</sup>	20
1.9.1.	Principals of PeakForce QNM <sup>®</sup> operation	20
1.9.2.	Image Channels	21
1.9.2.1.	Height and PeakForce error	21
1.9.2.2.	DMT modulus	21
1.9.2.3.	Adhesion	21
1.9.2.4.	Deformation	21
1.9.2.5.	Dissipation	22
1.10.	Atomic force microscopy studies on biological and photosynthetic membranes in liquid	22
1.11.	Monte Carlo simulations	23
1.11.1.	Overview of Monte Carlo simulations	23
1.11.2.	Monte Carlo studies for structure/function studies of the thylakoid membrane	24
1.12.	Aims of this work	25

## Chapter 2. Materials and methods

2.1.	Plant Material	26
2.2.	Thylakoid preparation	26
2.3.	Spectroscopy and chlorophyll assay	26

2.4. Digitonin treatment	27
2.5. Differential centrifugation	27
2.6. French Press	27
2.7. Aqueous two-phase system (ATPS) separation	27
2.8. Sucrose gradients	28
2.9. Low-temperature fluorescence	28
2.10. Transmission electron microscopy	28
2.11. SDS-PAGE and BN PAGE gel electrophoresis	28
2.12. Atomic force microscopy	28
2.13. Computational methods	29
2.14. Graphical output	29

### **Chapter 3. Purification of grana and stromal lamellae membranes from *Spinacea oleracea* and *Arabidopsis thaliana* for atomic force microscopy**

3.1 Introduction	30
3.1.1. Overview of thylakoid fractionation	30
3.1.2. Fractionation of thylakoids for AFM imaging	35
3.2. Results	38
3.2.1. Fractionation of Spinach and Arabidopsis thylakoids using digitonin	38
3.2.2. Preparation of grana membranes suitable for AFM from spinach using digitonin solubilisation and differential centrifugation	41
3.2.3. fractionation of spinach thylakoids using French Press	45
3.2.4. Ultrasonication and aqueous two-phase separation	46
3.2.5. Preparation of stromal lamellae membranes from spinach	48
3.2.6. Preparation of grana membranes suitable for AFM from <i>Arabidopsis</i>	51
3.2.7. Preparation of stromal lamellae membranes from <i>Arabidopsis</i>	54
3.3. Discussion	56
3.3.1. Non-detergent methods of spinach thylakoid fractionation	56
3.3.2. Stromal lamellae	57
3.3.3. PSII crystalline regions	57
3.4. Conclusion	58

### **Chapter 4. The nanoscale organisation of stromal lamellae thylakoids from *Spinacia oleracea*.**

4.1. Introduction	59
4.1.1. The macroscale structure of the thylakoid membrane	59
4.1.2. The organisation of protein complexes within the thylakoid membrane	59
4.2. Results	63
4.2.1. Identification of particles in stromal lamellae	63
4.2.2. PSI damage in AFM imaging	66
4.2.3. Automated PSI identification in stromal lamellae	68
4.2.4. The native organisation of PSI in stromal lamellae thylakoids	71
4.2.5. ATP synthase in stromal lamellae thylakoids	77
4.2.6. Imaging grana membranes with attached stromal lamellae	81
4.3. Discussion	84

4.3.1 PSI-LHCI in stromal lamellae	84
4.3.2. ATP synthase in stromal lamellae	85
4.3.3. Implications of contiguous grana and stromal lamellae membranes for the grana margins	88
4.4. Conclusion	90

## **Chapter 5. Monte Carlo simulations of plastocyanin-based electron transport.**

5.1. Introduction	91
5.1.1. Modelling plastoquinone and plastocyanin electron transport	91
5.2. Results	93
5.2.1. A model of the thylakoid membrane	93
5.2.2. Estimating the distance travelled by PC	97
5.2.3. Brownian dynamics simulations of PC-based electron transport	100
5.3. Discussion	110
5.3.1. Implications for P700 <sup>+</sup> reduction kinetics	110
5.3.2. cyclic electron flow	110
5.3.3. limitations of the model and potential improvements.	113
5.4. Conclusion	114

## **Chapter 6. Concluding remarks**

6.1. Concluding remarks	115
References	117
Appendix 1. Source code for the identification of PSI in AFM images	135
Appendix 2. Source code for estimating the diffusive distance of PC	140
Appendix 3. Source code for Brownian dynamics simulations of PC	141

## List of Figures

Figure 1.1. The structure of the thylakoid membrane.

Figure 1.2. The structure and organisation of the thylakoid membrane.

Figure 1.3. The structure and electrodynamics of chlorophyll.

Figure 1.4. The structure of LHCII.

Figure 1.5. The structure of PSII-LHCII.

Figure 1.6. The structure of the cytochrome *b<sub>6</sub>f* complex.

Figure 1.7. The structure of PSI-LHCI.

Figure 1.8. The structure of ATP synthase

Figure 1.9. PeakForce QNM atomic force microscopy.

Figure 3.1. Outline of the thylakoid membrane structure.

Figure 3.2. The Procedure for fractionation of the thylakoid membrane using detergent treatment and differential centrifugation.

Figure 3.3. Fractionation of thylakoids using mechanical breakage and aqueous two-phase system separation.

Figure 3.4. Digitonin solubilisation of Thylakoid membranes from *Spinacia oleracea* and *Arabidopsis thaliana*.

Figure 3.5. Optimisation of AFM imaging of grana from *Spinacia oleracea*.

Figure 3.6. Optimised procedure for the preparation of grana membranes using digitonin for AFM imaging

Figure 3.7. Identification of PSII and *cytb<sub>6</sub>f* from high-resolution AFM images.

Figure 3.8. Comparison of fractionation of *Spinacia oleracea* thylakoids by digitonin and French press treatment using differential centrifugation followed by 10-45% sucrose gradient ultracentrifugation.

Figure 3.9. Purification of subthylakoid vesicles from *Spinacia oleracea* by aqueous two-phase system (ATPS) separation and AFM analysis of grana vesicles.

Figure 3.10. Purification and AFM analysis of stromal lamellae from *Spinacia oleracea*.

Figure 3.11. Optimised procedure for the preparation of Stromal lamellae membranes using digitonin for AFM imaging.

Figure 3.12. Preparation of grana membranes for AFM from *Arabidopsis thaliana*.

Figure 3.13. Crystalline regions of PSII-LHCII in AFM images of *Arabidopsis thaliana* grana.

Figure 3.14. Purification and analysis of stromal lamellae from *Arabidopsis thaliana*.

Figure 3.15. AFM images of grana membranes from *Spinacia oleracea* prepared with 10-45% sucrose gradients containing 0.05% TWEEN-20.

Figure 4.1. Gallery of AFM images of stromal lamellae from *Spinacia oleracea* courtesy of Matthew P. Johnson (\*) and Craig Macgregor-Chatwin (\*\*\*) for the purpose of statistical analysis of the dimensions and organisation of PSI.

Figure 4.2. Analysis of the heights of protrusions from the surface of stromal lamellae membranes reveals two populations of particles, one of which can be identified as PSI.

Figure 4.3. AFM imaging damages PSI over multiple scans.

Figure 4.4. Automated detection of PSI in AFM images of stromal lamellae using a Gaussian cross-correlation model.

Figure 4.5. Nearest neighbour distributions of PSI in the stromal lamellae and of PSII and *cytb<sub>6</sub>f* in the grana.

Figure 4.6 . Identification and proposed structure of PSI-LHCI dimers in stromal lamellae

Figure 4.7. Association of PSI-LHCI results in lipid zones.

Figure 4.8. No change in the nearest neighbour distribution of PSI-LHCI is observed under state transitions.

Figure 4.9. Analysis of the larger stromal lamellae protrusions and comparison to ATP synthase.

Figure 4.10. Evidence that ATP synthase is both present and intact in stromal lamellae membranes.

Figure 4.11. The height of ATP synthase in stromal lamellae is consistent and validated by *Bos taurus* ATP synthase in a DOPC lipid bilayer.

Figure 4.12. Visualising the grana/stromal lamellae interface using AFM.

Fig. 13 Spatial model of membrane in (Fig 12C).

Figure 4.14. The location of ATP synthase in AFM height topographs is associated with signals in the deformation image.

Figure 4.15. Electron micrograph of a grana membrane produced by French Press.

Figure 5.1. Visualising the grana/stromal lamellae interface using AFM.

Figure 5.2. To-scale model of a grana margin in the light and comparison with the structure of PSI-LHCI.

Figure 5.3. Estimating the density of PSII and *cytb<sub>6</sub>f* in the grana and PSI in the stromal lamellae.

Figure 5.4. Vectorial representation used to calculate distances between grana and stromal lamellae particles.

Figure 5.5. Estimating the diffusive distance of *cytb<sub>6</sub>f* to PSI electron transport by PC.

Figure 5.6. Construction of the thylakoid model.

Figure 5.7. Simulating the organisation of PSI-LHCI using particles of realistic geometry

Figure 5.8. Modelling the thylakoid membrane and luminal space.

Figure 5.9. Results of PC diffusion simulations

Figure 5.10. The observed grana/stromal lamellae interface sizes are likely to result from a compromise between maximising the rate of PC diffusion and minimising PSII to PSI energetic spillover.

## List of tables

Table 3.1. The effect of varying concentrations of digitonin on the concentration of chlorophyll (mg/ml) in the 10k, 40k and 140k fractions in *Spinacia oleracea*.

Table 3.2. The effect of varying concentrations of digitonin on the chlorophyll *a*/chlorophyll *b* ratio of material in the 10k, 40k and 140k fractions in *Spinacia oleracea*.

Table 3.3. The effect of varying concentrations of digitonin on the concentration of chlorophyll (mg/ml) I in the 10k, 40k and 140k fractions in *Arabidopsis thaliana*

Table 3.4. The effect of varying concentrations of digitonin on the chlorophyll *a*/chlorophyll *b* ratio of material in the 10k, 40k and 140k fractions in *Arabidopsis thaliana*.

Table 3.5. Fractionation of thylakoids from *Spinacia oleracea* using French press.

Table. 5.1. Exponential fit parameters for the frequency distributions of the diffusion times of plastocyanin as calculated using Monte Carlo simulations.

## List of abbreviations

3-D	3-dimensional
AFM	atomic force microscopy
ATP/ADP	adenosine triphosphate/diphosphate
ATPS	aqueous two-phase system
CEF	cyclic electron flow
Chl	chlorophyll
CURT1	CURVATURE THYLAKOID 1
Cytb <sub>6</sub> f	cytochrome <i>b<sub>6</sub>f</i>
DGDG	digalactosyldiacylglyceride
DOPC	1,2-dioleoyl-sn-glycero-3-phosphocholine
EDTA	ethylenediaminetetraacetic acid
EF	endoplasmic face
EM	electron microscopy
Fd	ferredoxin
FD curve	force-distance curve
FNR	ferredoxin-NADP <sup>+</sup> reductase
FRET	Förster resonance energy transfer
LEF	linear electron flow
LHCI	light harvesting complex I
LHCII	light harvesting complex II
MCMC	Markov chain Monte Carlo
MGDG	monogalactosyldiacylglyceride
NADP	nicotinamide adenine dinucleotide phosphate
NPQ	non-photochemical quenching
OEC	oxygen evolving complex
PC	plastocyanin
PF	protoplasmic face
PF QNM	PeakForce quantitative nanomechanical mapping
PQ	plastoquinone
PSI	photosystem I
PSII	photosystem II
RTP	Room temperature and pressure
SPM	scanning probe microscopy
STM	scanning tunnelling microscopy

# Chapter 1.

## General introduction

“In photosynthesis, where is the chlorophyll; how is it arranged; where are the carotenoids involved in this thing? What is the system of the conversion of light into chemical energy?

It is very easy to answer many of these fundamental biological questions; you just look at the thing!”

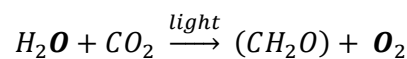
Richard P. Feynman (1959)

From “Plenty of Room at the Bottom”

### 1.1. Photosynthesis in plants.

Photosynthesis is the mechanism whereby light energy is used to carry out molecular synthesis, usually of carbohydrates, to be used as a source of cellular energy. Oxygenic photosynthesis (of which molecular oxygen is a by-product) occurs in cyanobacteria, algae, and plants. The consensus is that oxygenic photosynthesis evolved in early cyanobacteria and was bequeathed to eukaryotic algae by the endosymbiotic engulfment of cyanobacteria, which subsequently lost much of its cellular function to become the chloroplast. Plants descended from the green algal lineage and therefore, inherited the chloroplast. Although chloroplasts possess their own genome, there is evidence of gene translocation from the chloroplast into the plant nuclear genome (Martin *et al.*, 1998). Within the chloroplast lies the plant photosynthetic membrane, called the thylakoid membrane: a highly-folded membrane, packed with protein complexes, that encloses a single luminal space. The thylakoid membrane is the site of the light-dependent reactions of photosynthesis.

Overall, the reactions of both the light and dark reactions can be summarised using a single equation



expressing the conversion of water and carbon dioxide into carbohydrates, molecular oxygen and water using light energy. However, it was demonstrated that  $CO_2$  is not required for the production of  $O_2$  but light is (Hill, 1937). As a result, photosynthesis is often divided into two sub processes: the light-dependent reactions (or more simply the light reactions) involve the capture and transduction of light energy to generate reduced nicotinamide adenine dinucleotide phosphate (NADPH) and adenosine triphosphate (ATP) and occur on or within the thylakoid membrane. Those which synthesise carbohydrates from  $CO_2$  (ie. The Calvin-Benson cycle) are called the dark or light-independent reactions and occur in the stroma of the chloroplast. The dark reactions require ATP and NADPH production in a stoichiometry of 3:2 but the light reactions produce them at a stoichiometry of approximately 2.6:2. Therefore, a mechanism, known as cyclic electron flow (CEF) is used to achieve this balance. This will be discussed in more detail later.

### 1.2. The light reactions.

The Z-scheme of photosynthesis describes the work of two thylakoid membrane-integral photosystems: photosystem II and photosystem I (PSII and PSI respectively), working in series, to drive linear electron flow (LEF) culminating in the reduction NADP (Hill & Bendall, 1960). Fig 1.1A shows

schematically, the components of the Z-scheme and Fig. 1.1B describes the corresponding redox potentials for the reactions. Upon activation by light energy, PSII abstracts an electron from water,

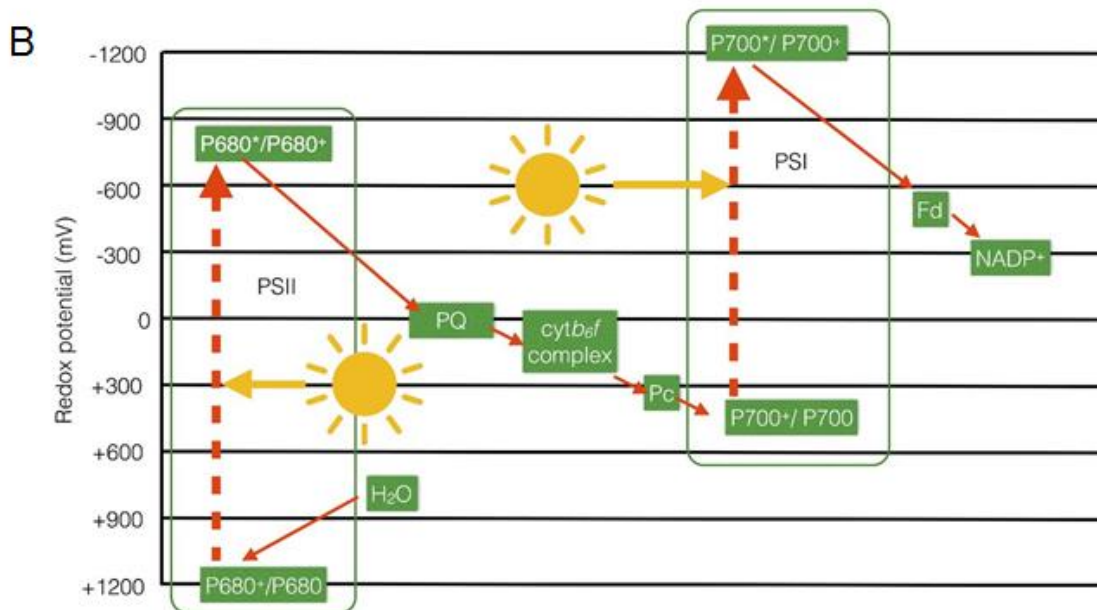
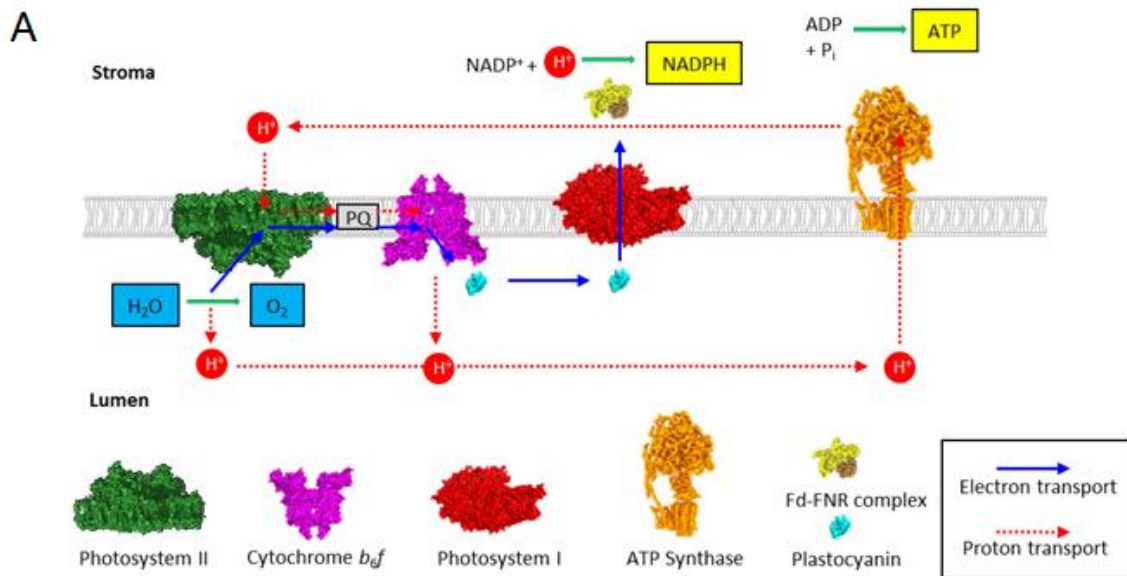
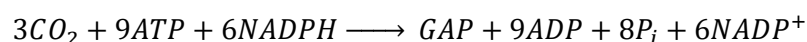


**Figure 1.1. The structure of the thylakoid membrane. A.** The protein complexes involved in and the pathways of electron and proton transport of the thylakoid membrane (PDBs: PSI: 4Y28, Cyt $b_6/f$ : 1Q90, ATP synthase: 5ARA, PSII: 3JCU). **B.** Redox potentials of the steps of linear electron flow in the thylakoid membrane (Johnson, 2016).

forming electrons, protons and molecular oxygen (the latter of which is released into the atmosphere). The acquired electrons are then shuttled through the thylakoid membrane to cytochrome *b<sub>6</sub>f* (*cytb<sub>6</sub>f*) via the lipid soluble electron carrier plastoquinone (PQ). The electron is then transferred from the membrane integral *cytb<sub>6</sub>f* to the small, soluble protein plastocyanin (Pc) in the thylakoid lumen. Pc then acts as an electron donor for PSI which upon light activation, reduces Fd. In the final part of LEF, Ferredoxin (Fd) binds Ferredoxin-NADP<sup>+</sup> reductase (FNR), stimulating the reduction of NADP<sup>+</sup> to produce NADPH. Along with water splitting by PSII, reduction of *cytb<sub>6</sub>f* by PQ is also coupled with proton translocation into the lumen. This results in the generation of a proton gradient across the thylakoid membrane which is utilised by ATP synthase to generate ATP. The balance of the rate of production of NADPH and ATP depends upon cyclic electron flow (CEF) which will be discussed in more detail later.

### 1.3. Overview of the dark reactions.

The primary use for NADPH and ATP produced during the light reactions is for the synthesis of carbohydrates from CO<sub>2</sub>. This process is known as the Calvin-Benson-Bassham (CBB) cycle. In the CBB cycle CO<sub>2</sub> is fixed into ribulose-1,5-bisphosphate (RuBP) by ribulose bisphosphate carboxylase (RuBisCO) to produce two molecules of 3-Phosphoglycerate (3PG) (Voet & Voet, 2011). Through the work of phosphoglycerate kinase, which requires energy from the hydrolysis of ATP, and the work of glyceraldehyde-3-phosphate dehydrogenase, which requires NADPH, 3PG is converted into glyceraldehyde-3-phosphate (GAP). GAP is known as the primary product of photosynthesis and is used in a wide range of biosynthetic pathways, including carbohydrate synthesis. In the final steps of the CBB cycle GAP can also be converted back into RuBP, thereby completing the cycle. Overall, the CBB cycle synthesises GAP from 3CO<sub>2</sub>, 9 ATP and 6NADPH:



The by-products ADP, P<sub>i</sub> and NADP<sup>+</sup> are fed back into the light reactions.

### 1.4. The structure of the thylakoid membrane.

The major components of the light reactions, PSII, *cytb<sub>6</sub>f*, PSI, and ATP synthase are all membrane integral protein complexes embedded in the thylakoid membrane. The thylakoid membrane has two distinct domains, the appressed grana which form a cylindrical stack approximately 500 nm in diameter and greater than 500 nm in height and the non-appressed stromal lamellae, which wrap helically around the grana and make contact with the grana layers at points called junctional slits (Austin and Staehelin, 2010) (Fig. 1.2. A,C). The protein complexes of the thylakoid have been observed not to be homogeneously distributed throughout the thylakoid (Fig 1.2. C), Instead, PSII is

found almost entirely within the grana whereas PSI and ATP synthase are located within the stromal lamellae (Andersson and Anderson, 1980). Segregation between PSII and PSI is driven by differences in the surface charge density of the complexes, with the charges on PSII-LHCII effectively screened at the concentration of cations present in the chloroplast, while those on PSI-LHCI are not (Miller & Staehelin 1976; Barber 1982). PSII-LHCII enriched membrane regions then attract one another leading to the formation of grana stacks that sterically exclude PSI and ATP synthase complexes that have bulky extramembrane subunits protruding on the stromal side. Thus PSI and ATP synthase partition into the stromal lamellae. *Cytb<sub>6</sub>f* is homogeneously distributed throughout the thylakoid (Cox & Anderson, 1981). At the edge of each grana layer lies a highly-curved region that connects one layer to the next. These are known as the grana margins. Using immunogold labelling, Armbruster *et al* (2013) showed CURVATURE THYLAKOID 1 (CURT1) to be enriched at the grana margins. CURT1 protein had a significant effect on the grana morphology of *Arabidopsis* (Armbruster *et al.*, 2013). Plants lacking CURT1 developed grana with extremely large diameter that were fewer in the number of layers in each grana stack whereas plants overexpressing CURT1 developed a larger number of layers but the grana had a much smaller diameter. It was, therefore, proposed that CURT1 controls the thylakoid architecture (more specifically: grana stacking) by inducing curvature at the grana margins.

## **1.5. Components of the thylakoid membrane.**

### **1.5.1. Lipids of the thylakoid membrane.**

Approximately 40% of the dry weight of the plant thylakoid membrane is composed of lipid (Quinn & Williams, 1983) and has a similar lipidome that of cyanobacterial thylakoids (Wada & Murata, 2007). The most abundant lipids of the thylakoid are the galactolipids, mono- and digalactosyldiacylglyceride (MGDG and DGDG respectively) which constitute around 75% of the total lipid composition and occur in a ratio of 2:1 (MGDG:DGDG) (Ruban, 2013). Around 60% MGDG and DGDG are located on the stromal side of the membrane. This spatial heterogeneity may have a role in the control of membrane curvature (Murphy, 1982). Thylakoid membrane lipids contain a glycerol-derived hydrophilic headgroup and, mostly (95%), contain a linolenic fatty acid tail. This nonsaturated fatty acid is thought to create a highly fluid bilayer which may aid the diffusion of lipid bound protein complexes and small molecules such as PQ.

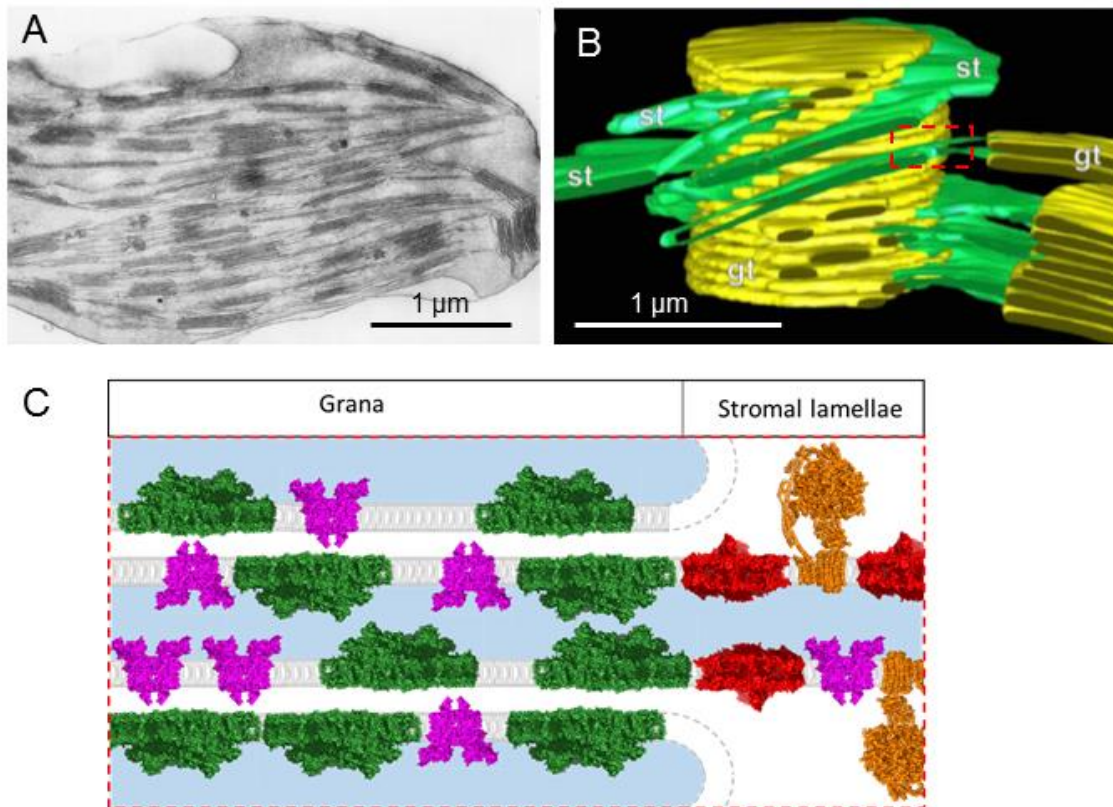


**Figure 1.2. The structure and organisation of the thylakoid membrane.** **A.** An electron micrograph of a chloroplast (adapted from von Wettstein (1961)). **B.** Cryo-electron tomogram of a grana stack (gt) with stromal lamellae (st) emanating helically from it (adapted from Austin & Staehelin (2010)). **C.** PSII resides in the grana and PSI and ATP synthase reside in the stromal lamellae. Cytb<sub>6</sub>f is homogeneously distributed throughout the thylakoid membrane.

### 1.5.2. Chlorophyll.

Chlorophyll is the principal chromophore (light absorber) of photosynthesis (Fig. 1.3A). It contains a chlorin ring, formed of a porphyrin with central magnesium atom, with 24  $\pi$ -orbital delocalised electrons which form a large absorption area and a phytol tail. The phytol tail also provides a hydrophobic surface which promotes protein interactions. Chlorophylls also contain polar ester carbonyl and keto groups which allows for non-covalent binding to protein sidechains in chlorophyll containing proteins. Upon absorption of a red photon (Fig. 1.3B), the  $\pi$ -electrons are excited from the ground state ( $S_0$ ) to the first excited state ( $S_1$ ), a transition visible by the  $Q_y$  peak in the absorption spectrum. Upon absorption of a blue photon, the electrons transition from  $S_0$  to the second excited state  $S_2$ , which is visible in the absorption spectrum as the Soret peak. Excitation energy can migrate from one chlorophyll to another via in a process called excitation energy transfer (Fig. 1.3C). At small separation distances of two chlorophylls (1nm), this manifests as exciton coupling (van Amerongen *et al.*, 2000) which can give rise to quantum coherence effects (Fassioli *et al.*, 2013). When the separation

distance is greater (1-10 nm, Blankenship, 2014) excitation energy occurs via Förster resonance energy transfer (FRET) (Förster, 1948) which requires overlap of the fluorescence emission spectrum of the donor and the absorption spectrum of the acceptor. This ensures that the molecular orbitals share a common energy state. Plants contain two types of chlorophyll, chlorophyll *a* and chlorophyll *b*. Although they have highly similar structures, the C7 of chlorophyll *a* is methylated, chlorophyll *b* has a formyl group. This causes the Soret peak of chlorophyll *b* to be red-shifted in comparison to chlorophyll *a* and the Q<sub>y</sub> peak of chlorophyll *b* to be blue-shifted in comparison to chlorophyll *a*.

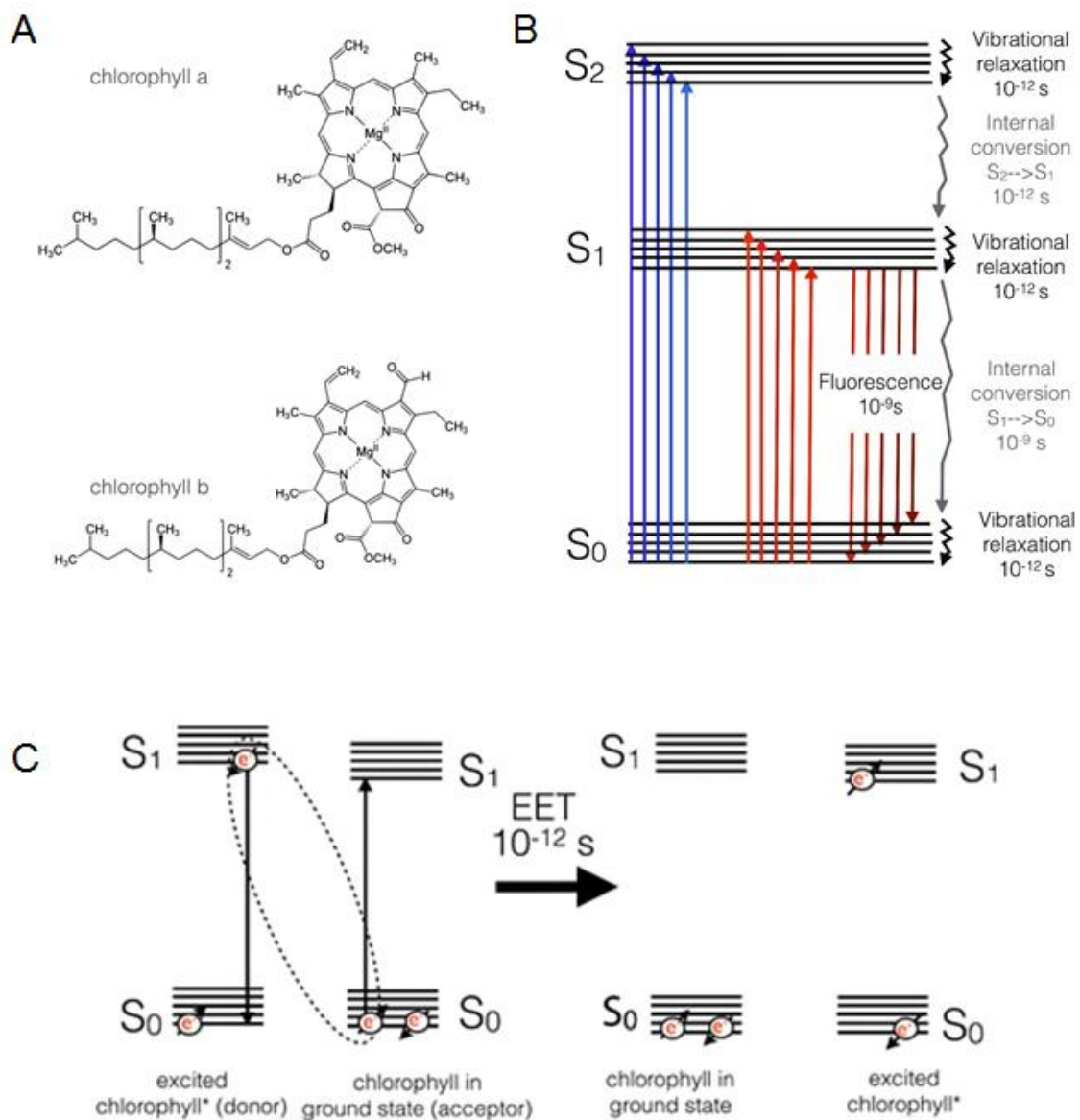


**Figure 1.3. The structure and electrodynamics of chlorophyll.** **A.** The structures of chlorophylls *a* and *b* (Johnson, 2016). **B.** Jablonski diagram of the excitation of and electron by a photon (Johnson, 2016). **C.** Excitation energy transfer from a chlorophyll in a single excited state to another chlorophyll in the ground state (Johnson, 2016).

### 1.5.3. Light-harvesting complex II (LHCII).

PSII is served by a network of chlorophyll containing antennae complexes, light harvesting complex II (LHCII), which absorb sunlight and transport the resultant excitation energy towards the reaction centre. The LHCII antenna system is modular such that the PSII antenna cross-section can be adapted to environmental conditions. For example, in low-light, the number of LHCII in the thylakoid is increased (Kouřil *et al.*, 2012) and, in high-light, LHCII can dissociate from the reaction centre and dissipate energy in a process called non-photochemical quenching (NPQ). LHCII also acts as an antenna complex for PSI, though this becomes most apparent during state transitions, which will be discussed later. The LHCII monomer contains 3 transmembrane  $\alpha$ -helices which bind a total of 14 chlorophyll molecules, 8 chlorophyll *a* and 6 chlorophyll *b* (Liu *et al.*, 2004; Standfuss *et al.*, 2005) (Fig. 1.4A). The chlorophylls are arranged in a circular geometry with centre to centre distances of around 10 Å (Fig. 1.4B). This facilitates excitation transfer both within the same molecule and to neighbouring LHCII (Liu *et al.*, 2004).

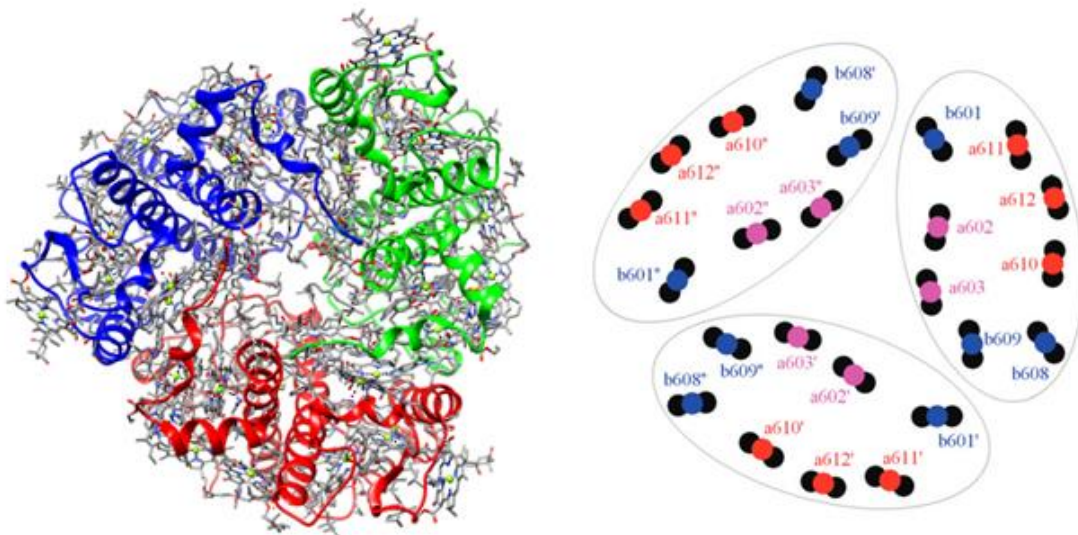
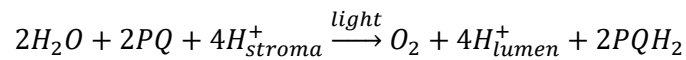


**Figure 1.4. The structure of LHCII.** **A.** The crystal structure of the LHCII trimer from pea (PDB: 2BHW). Individual monomers shown in red green and blue **B.** The organisation of chlorophylls *a* (red & pink) and *b* (blue) (Novodereshkin *et al.*, 2011) in the LHCII trimer.

### 1.5.4. Photosystem II (PSII).

PSII is a photochemical oxidoreductase which has the capacity oxidise water and reduce the lipid soluble electron carrier PQ. The process of H<sub>2</sub>O-PQ oxidoreduction is coupled to proton translocation into the thylakoid lumen, contributing to the proton gradient across the thylakoid membrane (McEvoy & Brudvig, 2006):



The structural unit of PSII contains bound, chlorophyll-containing antenna complexes (Fig. 1.5.). This includes the core antenna complexes CP43 and CP47, the minor antenna complexes CP24, CP26, CP29, along with medium and strongly bound trimeric LHCII (referred to as the M and S trimers respectively) (Ruban, 2013). PSII is dimeric and one may often come across PSII complexes referred to in the literature as C<sub>2</sub>S<sub>2</sub>M<sub>2</sub>. This describes a PSII complex as a dimer containing 2 cores, 2 strongly bound LHCII trimers, and 2 medium bound LHCII trimers. There is also a pool of mobile LHCII which can loosely bind (known as L-trimers), when extra light harvesting capacity is needed (Boekema *et al.*, 1999).

At the heart of PSII lies a special pair of chlorophylls the P680. Upon activation, P680 forms a radical pair P680<sup>+</sup>Q<sub>A</sub><sup>-</sup> with quinone Q<sub>A</sub> facilitated by a nearby pheophytin. The now positively charged P680<sup>+</sup> oxidises nearby tyrosine (Y<sub>z</sub>) which in turn oxidises the nearby four-Mn cluster known as the oxygen evolving complex (OEC) (Vinyard & Brudvig, 2017). The oxidation of water requires four successive oxidations of the OEC by P680, resulting in oxidation states called S<sub>0</sub> to S<sub>4</sub> respectively (Kok *et al.*, 1970). The oxidising potential of the OEC is then sufficient to extract electrons from two water molecules thereby simultaneously reducing P680<sup>+</sup>, forming molecular oxygen and releasing four protons into the grana lumen. The extracted electron is transferred to a bound PQ at the Q<sub>A</sub> binding site and then to a second, this time, mobile, PQ at the Q<sub>B</sub> binding site (Loll *et al.*, 2005). Once Q<sub>B</sub> has received two electrons it is able to take up two protons from the stroma, dissociate from PSII into the lipid bilayer, where it diffuses through the grana membrane to reach *cytb<sub>6</sub>f*.

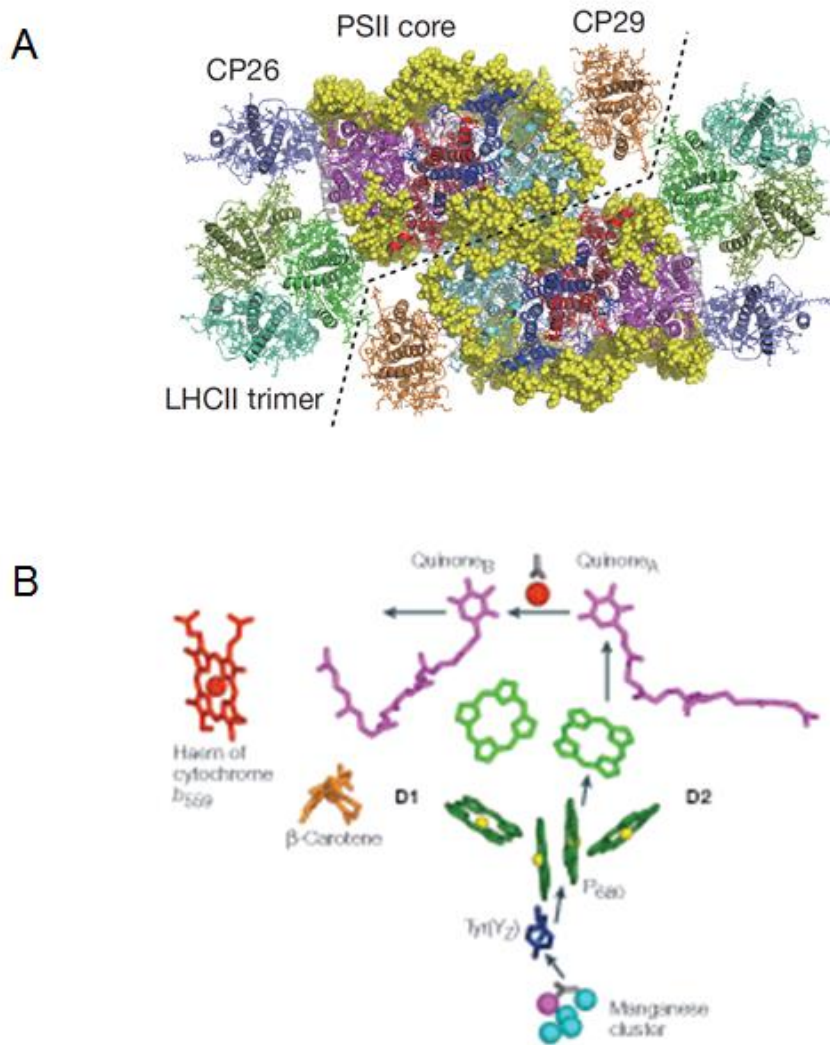


**Figure 1.5. The structure of PSII-LHCII.** **A.** Cryo-EM structure of PSII ( $C_2S_2$ ) from spinach (Wei et al., 2016, PDB: 3JCU) showing two PSII core reaction centres, the core light harvesting complexes CP26 and CP29 and two strongly-bound LHCII trimers. **B.** the electron transfer pathway in the PSII core complex (Nelson & Ben-Shem, 2004). The special pair of chlorophylls donate an electron to the quinones  $Q_A$  and  $Q_B$  and are re-reduced by manganese cluster which obtains electrons via water splitting.

### 1.5.5. Cytochrome $b_6f$ ( $Cytb_6f$ ).

$Cytb_6f$  (Fig 1.6A) is a homodimeric membrane protein complex with two subunits which exist almost entirely within the membrane, cytochrome  $b_6$  ( $cytb_6$ ) and subunit IV; and two subunits of which a significant proportion protrudes into the thylakoid lumen: cytochrome  $f$  ( $cyt f$ ) and the Rieske iron-sulphur protein (ISP) (Stroebel *et al.* 2003). It is homogeneously distributed throughout the thylakoid membrane (Albertsson, 2001) and participates in both linear and cyclic electron flow (Yamori & Shikanai, 2016). It functions as a  $PQH_2$ -PC oxidoreductase and in  $PQH_2$ -PQ oxidoreduction via the so-called Q-cycle (Fig. 1.6.).  $PQH_2$  is twice oxidised at the  $Q_i$  binding site, located on the stromal side of

the lipid bilayer. This triggers the uptake of two protons from the stroma. The oxidation of  $PQH_2$  at the  $Q_i$  site is the rate limiting step of LEF and is pH-sensitive. This pH sensitivity of  $PQH_2$  oxidation is called photosynthetic control. The first electron reduces PC via the high-potential chain, which involves the Rieske iron-sulphur protein and *cyt<sub>f</sub>*. The second electron reduces another plastoquinone at the  $Q_0$  site, on the luminal side of the lipid bilayer. This electron transfer pathway follows the low-potential chain which includes two hemes located within *cyt<sub>b<sub>6</sub></sub>*. This process, not only reduces PC but also causes the translocation of two protons from the stroma to the lumen. Because one of the electrons extracted from  $PQH_2$  is transferred to a second PQ and the  $Q_i$  site, the overall process results in the translocation of two protons for every one electron (Tikhonov, 2014).

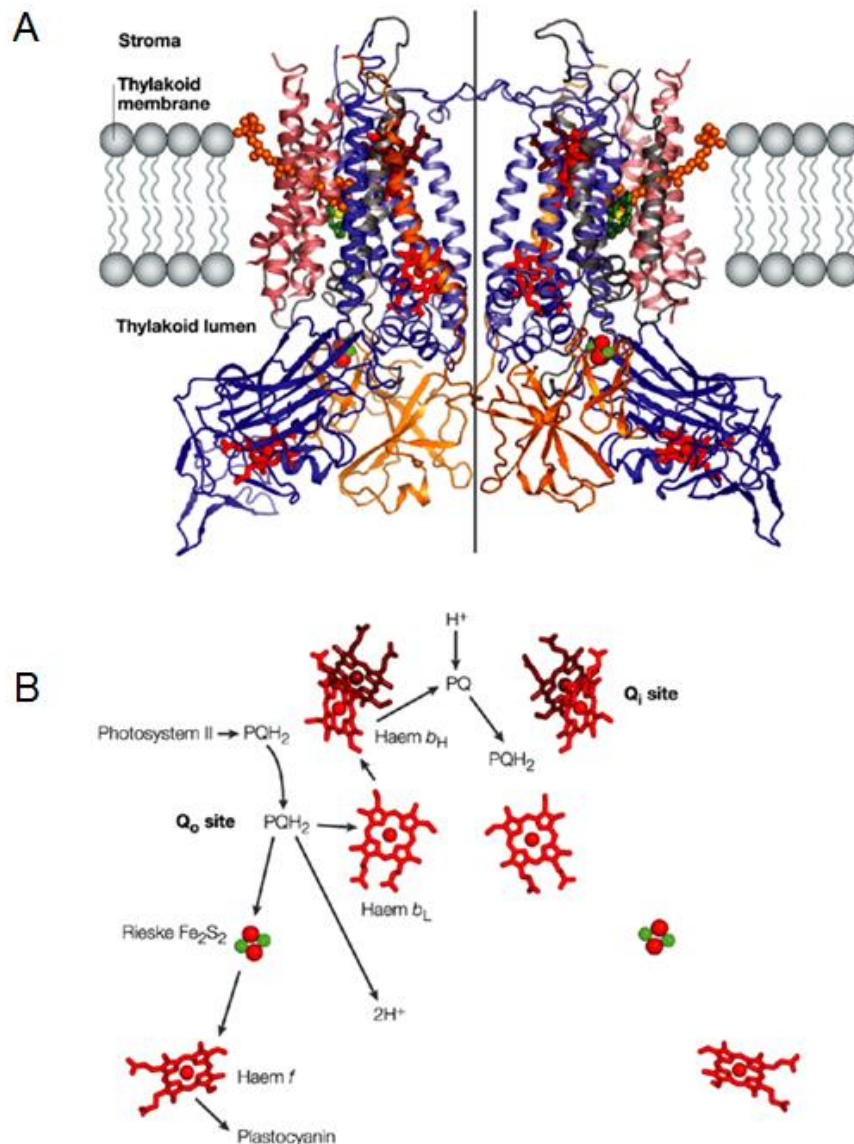


**Figure 1.6. The structure of the cytochrome  $b_6f$  complex.** **A.** The structure of *cytb<sub>6f</sub>* (Nelson & Ben-Shem, 2004) shows that it is a dimeric, membrane integral complex which contains large luminal-protruding regions. **B.** The electron transfer pathways in *cytb<sub>6f</sub>* (Nelson & Ben-Shem, 2004). PQH<sub>2</sub> binds the Q<sub>0</sub> site and reduces the Rieske iron-sulphur cluster. This, in turn, reduces plastocyanin via haem *f*. The reduction of PQ at the Q<sub>i</sub> site increases the proton transfer to electron transfer ratio using the so-called Q-cycle.

### 1.5.6. Plastocyanin (PC).

PC is a soluble 10.5 kDa copper-metalloprotein, mostly composed of  $\beta$ -sheets (Christensen *et al.*, 1991). Though it is a nuclear encoded protein, immunolabelling and proteomics have located PC in the lumen of the thylakoid (Haehnel *et al.*, 1989; Keiselbach *et al.*, 1998). It is thought to be imported into the lumen via the sec pathway (Schubert *et al.*, 2002). Reduced PC binds the PsaF subunit on the luminal side and functions as the primary electron donor of the excited special pair of PSI, P700<sup>+</sup>.

### 1.5.7. Photosystem I (PSI).

PSI (Fig 1.7A) is a light driven PC Fd oxidoreductase. It contains 12 core subunits, PsaA-L, and 4 bound light harvesting complexes (LHCI), Lhca1-4 (Mazor *et al.*, 2015). The LHCI antenna complexes are arranged around the core complex as dimers of Lhca1 and Lhca4 and Lhca2 and Lhca3. The 'special pair' of chlorophylls (P700), the primary photochemical electron donor, lies within the core reaction centre, which is composed of PsaA and PsaB. Two tryptophan residues of PsaA (Trp<sup>651</sup>) and PsaB (Trp<sup>627</sup>) form the hydrophobic recognition site on the luminal side of the membrane (Sommer *et al.*, 2004). Upon light activation, P700<sup>+</sup> rapidly (1.5 ps) reduces the nearby chlorophyll A<sub>0</sub>. This in turn reduces the immobile quinone A<sub>1</sub>. Because the core complex of PsaA and PsaB is a heterodimer, the electron transfer pathway branches from P700<sup>+</sup> and will progress through one of two A<sub>0</sub>/A<sub>1</sub> pathways (Guergova-Kuras *et al.*, 2001). These bifurcating pathways converge on the Fe-S cluster located in PsaC (Oh-oka *et al.*, 1987). This contains 3 Fe-S centres F<sub>x</sub>, F<sub>A</sub>, and F<sub>B</sub> through which electron transport occurs sequentially. The reduction of ferredoxin (Fd), by F<sub>B</sub> is mediated by PsaD, which contains the Fd binding site. Ferredoxin is a soluble Fe-S metalloprotein. It is the final electron acceptor of PSI. PsaD is also important in stabilising the binding of PsaC to PsaA and PsaB (Zhao *et al.*, 1990) Although the consensus is that the PSI-LHCI complex, in plants, is monomeric (Mazor *et al.*, 2015), isolated PSI-LHCI from cyanobacteria have been observed as dimeric, trimeric and tetrameric structures (Karapetyan *et al.*, 1999; Watanabe *et al.*, 2011). It is thought that the subunit PsaH, which is present in plants but not present in cyanobacteria, blocks PsaL-mediated associations which are responsible for trimer formation in cyanobacterial trimers (Kouřil *et al.*, 2005). PsaH is however, essential for complete state transitions (Lunde *et al.*, 2000) suggesting the transition from oligomeric to monomeric PSI may be an adaptation to the different environmental light conditions of plants compared to cyanobacteria. The subunits PsaC, PsaD, and PsaE protrude into the stroma by 3.5 nm (Fotiadis *et al.*, 1998) and it is thought this may physically restrict the entry of PSI into the grana stacks.

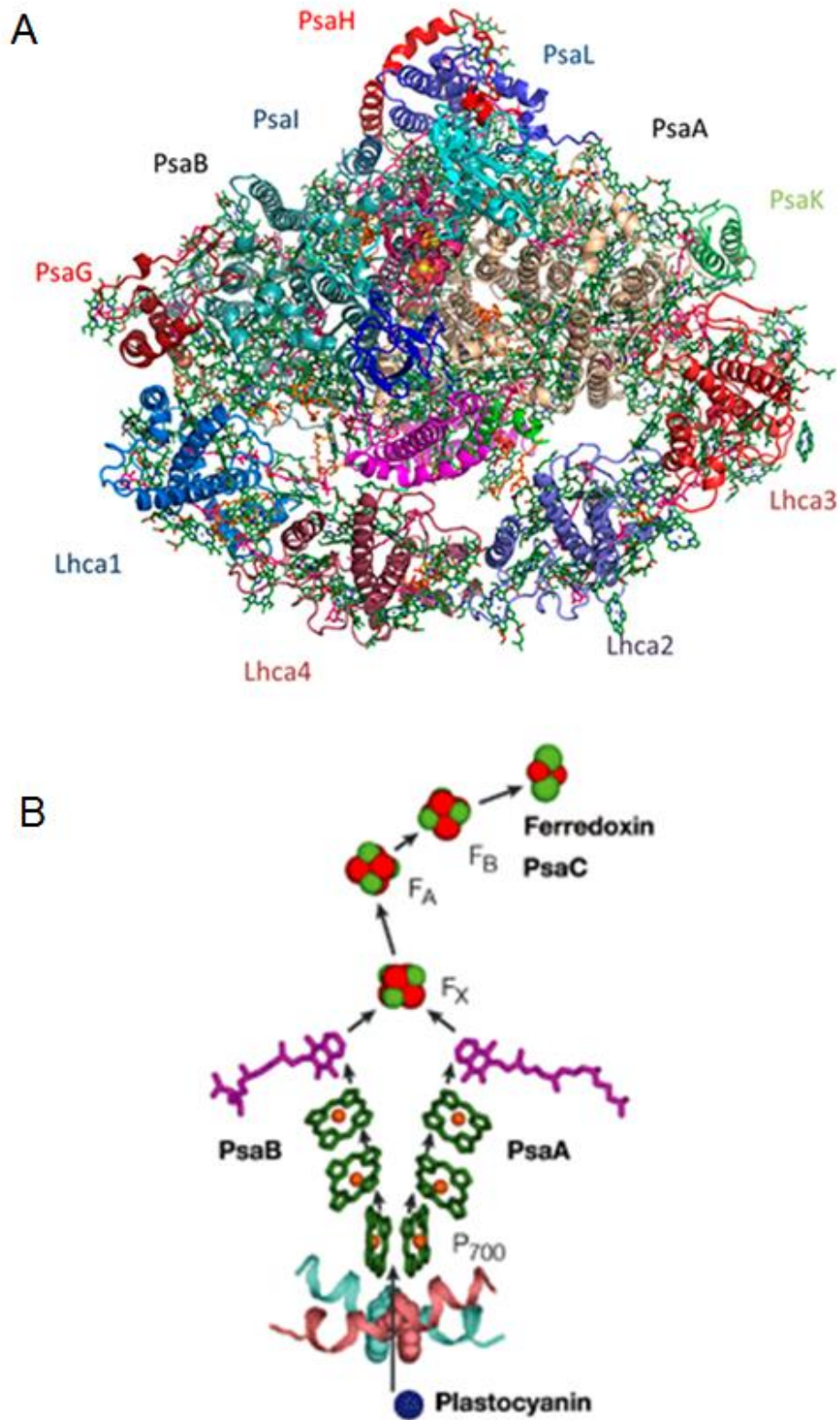


**Figure 1.7. The structure of PSI-LHCI.** **A.** Crystal structure of PSI-LHCI from *Pisum sativum* (pea) (Mazor et al., 2015, PDB: 4Y28). **B.** The electron transfer pathway of PSI. The excited P700 special chlorophyll pair reduces the nearby chlorophylls PsaA or PsaB. Ferredoxin is reduced by electron transport via the iron-sulphur clusters  $F_x$ ,  $F_A$ , and  $F_B$ .

### 1.5.8. Ferredoxin NADP<sup>+</sup> reductase complex (FNR).

The reduction of NADP<sup>+</sup> and oxidation of the donor Fd is the final step in LEF. This results in the production of NADPH, primarily for use in the CBB cycle. Fd-NADP<sup>+</sup> oxidoreduction is mediated by the ferredoxin NADP<sup>+</sup> reductase (FNR) complex (Mulo, 2010). FNR is a 35 kDa hydrophilic flavoprotein, formed of two domains which sandwich a central Flavin adenine dinucleotide (FAD) (Dorowski *et al.*, 2001). Alongside LEF, FNR has been shown to be involved in CEF (Shahak *et al.*, 1981). Indeed, associations of FNR with complexes involved in CEF have been described: including cytochrome *b<sub>6</sub>f* (Clark *et al.*, 1984; Zhang *et al.*, 2001) and the PQ-reducing, membrane-integral complex NADPH dehydrogenase (NDH) complex (Guedeney *et al.*, 1996; Quiles & Cuello, 1998).

### 1.5.9. ATP synthase.

ATP synthase (Fig. 1.8A) utilises the proton gradient across the thylakoid membrane as a source of energy to drive the synthesis of ATP from ADP and P<sub>i</sub> as well as the reverse process of ATP driven proton pumping (Nicholls & Ferguson, 2013). In photosynthesis, the primary function of ATP synthase is the production of ATP using the proton gradient established by electron transport. ATP synthase has two distinct domains, the membrane integral F<sub>o</sub> region which anchors the complex to the membrane, and the F<sub>1</sub> region which contains a catalytic head which is the site of ATP synthesis. The F<sub>o</sub> region is composed of 8 α-helical monomers which form a circular complex with a central pore. This functions to allow the transport of protons from the thylakoid lumen. The F<sub>1</sub> region protrudes into the stroma and precludes its entry into the stacked grana and therefore ATP synthase is located only in the stromal lamellae (Miller & Staehelin, 1976). The F<sub>1</sub> region contains 10 subunits α, α (x3), β(x3), γ, δ and is structurally stabilised by a membrane anchored stator (Zhou *et al.*, 2015). The subunits α, γ, and δ form a central stalk which rotates as protons move through the F<sub>o</sub> ring. The α and β subunits alternate to form a hexagonal head and each pair contains one catalytic site where ATP is generated. ADP and P<sub>i</sub> enters the catalytic site between the α and β subunits (Fig 1.8B). The binding site of ADP itself lies on the β subunits, where it is sandwiched between residues Y<sup>345</sup> and F<sup>424</sup> (Rees *et al.*, 2012). Rotation of the γ subunit by 120°, driven by the flow of protons, closes the cleft between the α and β subunits which brings about the fixture of ADP and P<sub>i</sub> to form ATP. Further rotation of the γ subunit by 120° reopens the α/β cleft, allowing ATP to leave the site. A final 120° rotation orientates the binding to allow for another ADP to bind. In total, 3 ATP molecules are produced per 360° rotation of the γ subunit (Senior *et al.*, 2002).

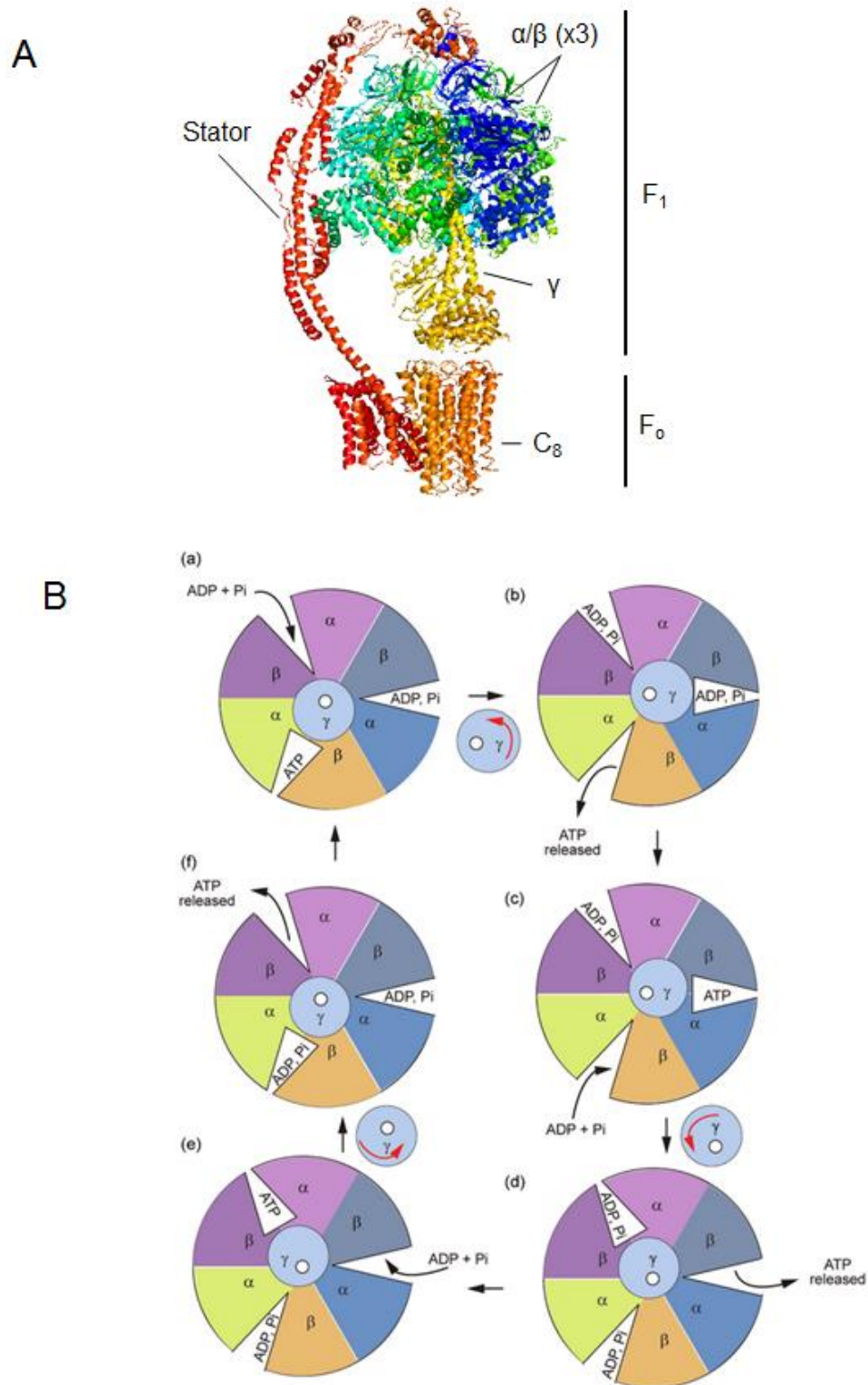


**Figure 1.8. The structure of ATP synthase. A.** Cryo-EM structure of Bovine mitochondrial ATP synthase (PDB 5ARA). Membrane ( $F_0$ ) and stromal ( $F_1$ ) regions as well as individual subunits are labelled. **B.** The mechanism of ATP synthesis (Nicholls & Ferguson, 2013). ADP +  $P_i$  enters the open binding pocket. Rotation of the  $\gamma$  subunit closes the pocket and produces ATP. Further rotation opens the binding pocket, releasing ATP.

## 1.6. Regulation of the light reactions of photosynthesis.

### 1.6.1. Cyclic electron flow.

Carbon assimilation requires an ATP to NADPH ratio of 3:2 but LEF produces only 2.6 ATP for every 2 NADPH (Yamori & Shikanai, 2016). Furthermore, environmental fluctuations cause the demand of ATP to vary with respect to NADPH demand. CEF is a mechanism which optimises the rates of ATP and NADPH production with respect to demand. It was originally discovered by Arnon *et al.* (1954) that plants maintained some capacity for ATP production when PSII mediated H<sub>2</sub>O photolysis was inhibited. It is now understood that there are two pathways involved in CEF: the antimycin A-sensitive pathway via *proton gradient regulation 5* (PGR5)/*PGR5-like photosynthetic phenotype 1* (PGRL1) and the antimycin A-insensitive pathway via the NADH dehydrogenase-like complex (NDH). Both pathways effectively serve as Fd-PQ oxidoreductases, by-passing NADP<sup>+</sup> reduction in order to feed the reduction of the PQ pool. This, in turn, activates the Q-cycle of cytb<sub>6</sub>f leading to proton translocation, and therefore ATP production, without NADP<sup>+</sup> reduction.

### 1.6.2. State transitions.

Plants must be able to respond quickly to changes in environmental light intensity and spectral quality. PSII and PSI must work in series to generate NADPH and ATP in a balanced manner (i.e. at a fixed ratio) but certain wavelengths of light will be preferentially absorbed by either PSII or PSI. This unequal balance of excitation will perturb the balance of NADPH/ATP production because PSI is involved not only in LEF but also in CEF which generates ATP but not NADPH. The primary response to changes in light quality at low light intensities is the state transition (Goldschmidt-Clermont & Bassi, 2015). State transitions balance the excitation energy between the photosystems by the selective association of a mobile pool LHCII to PSII or PSI. The imbalance of excitation is detected by the redox state of the PQ pool (Horton *et al.*, 1980, Horton *et al.*, 1981). When the PQ pool is reduced, LHCII is phosphorylated by STN7 serine-threonine kinase (Bellafiore *et al.*, 2005), dissociates from PSII and binds to PSI (Kouřil *et al.*, 2005). The binding of phosphorylated LHCII to PSI-LHCI requires the subunit PsaH (Lunde *et al.*, 2000) and there is now evidence that a second pathway may also be involved in energy transfer from LHCII to PSI, via an interaction with LHCI (Benson *et al.*, 2015; Yadav *et al.*, 2017). When the PQ pool is oxidised, LHCII is dephosphorylated by PPH1/TAP38 (Pribil *et al.*, 2010; Shapiguzov *et al.*, 2010) and binds to PSII at the peripheral loose or L binding site (Galka *et al.*, 2012).

### 1.6.3. Non-photochemical quenching.

In high light environments, excess energy can damage photosynthetic reaction centres, causing a fall in photosynthetic efficiency. This is known as photoinhibition. PSII is particularly sensitive as P680 acts in a highly oxidising regime (+1.17V) (Ruban, 2013). Non-photochemical quenching (NPQ), or more specifically, energy dependent quenching (qE), is a photoprotective mechanism whereby the excitation state lifetime of chlorophyll is decreased (Gilmore *et al.*, 1995) causing excess energy to be lost via photon emission. The onset of qE is triggered when an increase in the proton gradient ( $\Delta pH$ ) (Wraight & Crofts, 1970) triggers the protonation of Psbs (Li *et al.*, 2004) and the activation of violaxanthin deepoxidase (Demmig-Adams, 1990). Together, protonation of PsbS and synthesis of zeaxanthin triggers a conformational change within the LHC antenna system leading to the aggregation of LHCII (Johnson *et al.* 2011) and quenching sites that dissipate excitation energy as heat.

### 1.7. Detergents.

Detergents are frequently used in the purification of membranes and membrane proteins. They are amphiphilic molecules which, in a similar way to lipids, contain a hydrophilic 'head' and a hydrophobic 'tail'. At the critical micellar concentration (CMC) they spontaneously form spherical micelles in liquid solution (Sneddon *et al.*, 2004). There are three main groups of detergents: ionic (anionic and cationic), which contain positively charged head groups, non-ionic and zwitterionic detergents. Due to the amphiphilic nature of detergents, they interact with and disrupt lipid bilayers and, in the process, membrane proteins can be solubilised. Detergents disrupt and enter the lipid bilayer and form a 'shield' around the lipophilic regions of the protein (lipids may be retained within the detergent shield). This allows the protein/lipid/detergent complex to become soluble in an aqueous medium and the protein is therefore removed from the lipid bilayer (le Maire *et al.*, 2000). Generally speaking, the non-ionic detergents are the mildest and have the least capacity to denature proteins. They are therefore the most widely used in membrane and protein purification methods. Non-ionic detergents such as digitonin (Boardman & Anderson, 1964), *n*-dodecyl- $\alpha$ -D-maltoside ( $\alpha$ -DDM) (van Roon *et al.*, 2000) and TRITON-X100 (Berthold *et al.*, 1981) have been used to disrupt the thylakoid membrane, allowing the PSII-enriched grana or the PSI-enriched stromal lamellae to be separated and will be discussed in more detail in chapter 3. The major complexes of the thylakoid membranes have also been purified using detergents to solubilise them. For example the use of  $\alpha$ -DDM for the purification of PSII (Wei *et al.*, 2016) and PSI (Mazor *et al.*, 2015) or HECAMEG for the purification of *cytb<sub>6</sub>f* (Pierre *et al.*, 1995)

## 1.8. Atomic force microscopy.

Conventional microscopy techniques generally rely on lenses. These are used to magnify and focus the image of a sample. For example, in light microscopes, glass lenses are used to focus light reflected by the sample thereby producing a magnified image. Atomic force microscopy (AFM) is based on an entirely different premise. Instead, a microscopically sharp tip is traced over the surface one wishes to image and the height of the tip is recorded to produce a 3-D topography of the surface. It is one of a number of similar techniques belonging to a group collectively known as scanning probe microscopy (SPM).

The predecessor of AFM and the first SPM technique was the scanning tunnelling microscope (STM) (Binnig & Rohrer, 1982). STM works by exploiting the theory of electron tunnelling. If a voltage is applied between two conductive materials in a vacuum, then the tunnelling current between them will be proportional to the voltage applied and decay exponentially as a function of the distance between them. Binnig and Rohrer (1982) were able to produce topographic images of surfaces such as gold and silicon. As the tip was traced over the surface, higher regions and lower regions were measured as higher and lower tunnelling currents respectively. A piezo (a ceramic material that can expand and contract in response to an applied voltage) was used to move the tip up and down in response to the undulations of the surface, maintaining a constant distance between the tip and the surface. Gerd Binnig and Heinrich Rohrer were credited with the Nobel Prize in Physics for the development of STM in 1986.

Although the invention of STM had a profound impact on surface science, it was limited by a need to operate in vacuum and on conductive samples. In order to attain the imaging capabilities of STM whilst avoiding these limitations, a new technique was required. AFM was first developed in 1986 and was shown to produce nanoscale lateral resolution and angstrom scale vertical resolution on a non-conducting ceramic surface whilst operating in air (Binnig & Quate, 1986). As with STM, a microscopically sharp tip is used. However, in the case of AFM, inter-atomic forces (which are ubiquitous in all materials) are used as a measure of contact between the tip and the sample. Because these forces are extremely small, the authors required a method highly sensitive to small forces. In the first AFM configuration the tip is located on the end of a cantilever with a sufficiently low spring constant to be able to bend in response to the undulations in the surface (as measured by inter-atomic forces) without damaging the surface. The deflection was originally measured using an STM mounted above the cantilever. Appropriate contact between the tip and the sample was then maintained using a piezo which moved the tip in the vertical direction by keeping the tunnelling current constant.

Nowadays cantilever deflection is generally measured by coating the back of the cantilever in a reflective material and reflecting a laser beam on the top of the cantilever onto a photodetecting diode. Deflection of the cantilever can thereby be measured by changes to the path of the laser beam. This early form of AFM in which the force between the tip and the sample is kept constant is known as contact mode as the tip maintains inter-atomic contact with the sample while imaging.

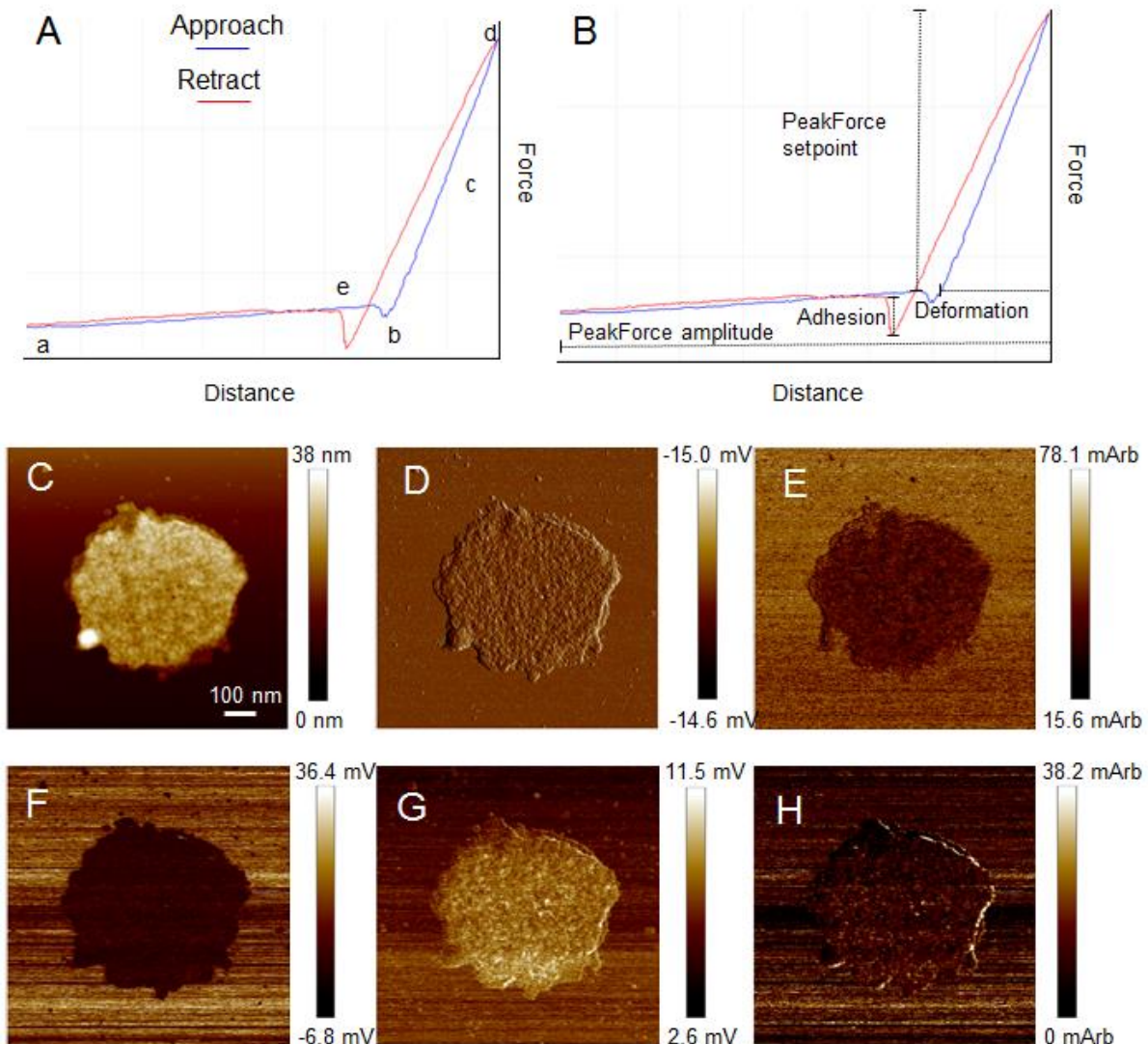


**Figure 1.9. PeakForce QNM atomic force microscopy.** **A.** A force-distance curve of the approach (blue) and retract (red) of an AFM tip. At (a) the tip is at maximum height. the tip is brought closer to the surface making contact at (b). (c) shows the linear force increase with further movement towards the surface. The peak force is reached at (d). This is followed by an immediate retraction. At (e) contact with the surface is broken. **B.** An annotated force-distance curve showing how images of the various channels are calculated. **C-H.** Example images of a membrane in different channels: height (C), PeakForce error (D), DMT modulus (E), adhesion (F), deformation (G) and dissipation (H).

## **1.9. PeakForce quantitative nanomechanical mapping®.**

PeakForce quantitative nanomechanical mapping® (PeakForce QNM®) is an AFM imaging mode developed by Bruker. It is capable of generating high-resolution topological images while simultaneously measuring mechanical properties of the sample. Development of Scanasyst® software which optimises the control parameters during imaging also makes PeakForce QNM® a very simple AFM mode to operate.

### **1.9.1. Principals of PeakForce QNM® operation.**

PeakForce QNM® is a force-distance (FD) curve based imaging mode (Fig 1.9.). An FD curve is a plot of the distance of the AFM tip from the surface (as measured by the z-piezo) on the abscissa and the force exerted upon the tip on the ordinate axis. In order to engage (make contact with) the surface, the tip is moved towards the surface until the force between the tip and the surface reaches a set level known as the peak force engage setpoint. The software then commences scanning. Care must be taken when setting the peak force engage setpoint: too low and the vibrations in cantilever as the tip approached the surface may trigger a false engage, too high and one risks causing damage to the tip and/or the sample.

Scanning the surface is performed by oscillating the sample (in this mode it is the sample mounted on the z-piezo not the tip) at a rate known as the peakforce frequency. This is usually around 1-2 kHz and maintains intermittent contact between the tip and the surface. For each oscillation, an FD curve is produced. The tip begins at a specified height from the surface known as the peakforce amplitude (a in Fig 1.9A) and approaches the surface. When the tip comes close to the surface, there may be a small attractive force which appears as a negative force in the FD-curve (b in Fig 1.9A). This is usually referred to as “snap to contact”. The tip is now in contact with the sample and further approach of the tip towards the sample causes the cantilever to bend. This causes the force to increase linearly with the distance travelled by the tip (c in Fig 1.9A) as the cantilever behaves effectively as a Hookian spring. The approach to the surface continues until a specified force known as the peakforce setpoint is measured (d in Fig 1.9A), and then the tip is retracted. As the tip breaks contact with the sample there may be an attractive force that has to be overcome (e in Fig 1.9A). The cycle of approach and retract is repeated while the tip is simultaneously moved in x and y directions using the FD curve to measure the undulations in the sample. The height of the surface is monitored by controlling the piezo and forms an image called the height image (Fig. 1.9C). For example, if the peakforce amplitude is 10 nm but the peakforce setpoint is reached at 9 nm, then the software assumes the surface has risen by 1 nm since previous contact and resets the baseline of the z-piezo accordingly. The rate by which the

z-piezo baseline is changed in response to changes in the height of the surface is known as the gain. That is, a higher gain will cause a more rapid response. Setting the gain too high however will cause the piezo to respond to random fluctuations of the cantilever, causing artefacts in the image. The difference between the peakforce amplitude and the actual distance the tip travels before reaching the peakforce setpoint is called the peakforce error (Fig 1.9D). The error is often recorded as an image itself and although it offers little useful information, often shows smaller particles with a greater contrast than the height image. This is due to the fact that producing a height image requires a response from the z-piezo while peakforce error is measured instantaneously.

## **1.9.2. Image Channels.**

### **1.9.2.1. Height and PeakForce error.**

The height and the peakforce error, as described previously, form two of the image channels contained in a single image file. Other examples of image channels include DMT modulus, adhesion, deformation and dissipation (Fig 1.9B-H). In the case of each of these 4 channels, each pixel of the image is represented by a value taken from the FD curve taken at that particular x-y coordinate (Fig 1.9B). All channels in PeakForce QNM<sup>®</sup> are based on the Derjaguin-Muller-Toporov (DMT) (Derjaguin *et al.*, 1975) model which describe tip-surface interactions by approximating the tip as a sphere and the sample surface as a plane.

### **1.9.2.2. DMT modulus.**

This is a measure of the Young's modulus of sample based on the DMT model (Fig. 1.9E). A higher DMT modulus corresponds to a higher stiffness of the sample. From the FD curve this corresponds to the gradient of the linear portion of the approach curve between contact and the peak force.

### **1.9.2.3. Adhesion.**

The adhesion is the force required to remove the tip from the surface as the result of tip-surface interactions. It manifests as a negative trough on the retract curve as the tip returns to contact distance. On the image, lower or more negative values correspond to a higher adhesion (Fig. 1.9B,F).

### **1.9.2.4. Deformation.**

Deformation is defined as the distance travelled by the tip between the point of contact with the sample and the peak force (Fig. 1.9B,G). During this period, further travelling of the tip requires the

movement or compression of the sample. This is what is referred to as deformation. To eliminate noise, the point of contact is not set to the distance at which the force becomes positive, but at an arbitrary force threshold called the deformation force level. This is often set to 15% of the peak force setpoint.

#### **1.9.2.5. Dissipation.**

Dissipation is defined as the work done to the sample by the tip (Fig. 1.9H). Alternatively, this can be viewed as the energy of the moving tip lost as it is dampened by the sample. From the FD curve the dissipation can be calculated by integrating the difference between the approach and retract curves.

### **1.10. Atomic force microscopy studies on biological and photosynthetic membranes in liquid.**

The capability of AFM to operate in liquid (Drake *et al.*, 1989) allows for molecular resolution imaging of biological samples (Ratneshwar & John, 1994), particularly of membranes (Muller *et al.*, 1995). Rather than tip-sample interactions resulting entirely from inter-atomic forces as in AFM in vacuum or in air, AFM in liquid require the balance of repulsive electrostatic interactions with a layer of electrolytes close to the surface of the sample (Muller *et al.*, 1999). The most common method of stabilising samples is by adsorption to freshly cleaved mica in buffer containing electrolytes (Muller *et al.*, 1997). The first AFM images of multicomponent photosynthetic membranes revealed the organisation (Bahatyrova *et al.*, 2004; Olsen *et al.*, 2008), assembly (Adams *et al.*, 2011) and dynamics (Scheuring & Sturgis, 2005) of reaction centres (RC-LH1-PufX) and light harvesting complexes (LH2) in chromatophores of *Rhodobacter sphaeroides*. More recently liquid AFM has been used to image grana membranes from plant thylakoids (Sznee *et al.*, 2011; Johnson *et al.*, 2014; Phuthong *et al.*, 2015). A detailed review of AFM studies of plant thylakoids will be given in chapter 3.

## 1.11. Monte Carlo simulations.

### 1.11.1. Overview of Monte Carlo simulations.

Computer simulation of physical systems bridge the gap between theory and experiment. Often, real-life scientific problems are too complicated to be amenable to analytical approaches and the measurement of certain quantities may be impossible in an experimental setting (the momenta of individual particles for example). Using computers, one can numerically calculate many parameters of the system so long as the underlying physics and the assumptions of the system are handled correctly. Here the word system refers to a thermodynamic system: An isolated quantity of matter and energy in a volume of space.

The Monte Carlo method is a name given to a range of algorithms for sampling from probability distributions that are not amenable to analytic analysis, such as those which are high in dimensionality or result from a complicated system. There are two main approaches in the Monte Carlo method. If every outcome is equally likely, then *direct sampling* can be employed. This is when states of the system are sampled at random. Otherwise Markov-chain sampling is used. In this case the algorithm samples as it moves from one state to another within the system only if it is accessible from the previous state. The change of state occurs at a probability dictated by the system being studied.

The algorithm used to sample from the Boltzmann distribution, which describes a probability distribution of states of a physical system based on thermodynamics is the Metropolis-Hastings algorithm (Metropolis *et al.*, 1953), a Markov-chain Monte Carlo method. In the Metropolis-Hastings approach, the transition probability from one state to another is determined by the difference in the Hamiltonian (the total energy) of the system between the two states. Markov chain Monte Carlo methods must satisfy two requirements in order to be able to sample the probability distribution correctly (Newman & Barkema, 2001). One these criteria is *detailed balance*, the principal that the transition probability from A to B multiplied by the probability of being in state A is equal to the transition probability from B to A multiplied by the probability of being in state B

$$\Pi_a P(A \rightarrow B) = \Pi_b P(B \rightarrow A)$$

The second criterion is the principal of *ergodicity*: every state of the system must be accessible in a finite time frame from any other state.

The Hamiltonian is central to the Metropolis-Hastings algorithm which can be described as follows.

1. Calculate the Hamiltonian of the system ( $H_0$ ) (i.e. sum of the energy components).
2. Make a small change to the system (for example, incrementally move a particle) and calculate the new Hamiltonian ( $H_1$ ).
3. Calculate the probability of the change occurring ( $P$ ):

If  $H_1 \leq H_0$ :

$$P = 1$$

If  $H_1 > H_0$ :

$$P = e^{-\frac{H_1 - H_0}{K_B T}}$$

4. Accept change with probability  $P$ .

From this algorithm one can see that if the new state is of lower energy, then the change will always be accepted. This represents the drive to a lower potential energy. If the new state is higher energy, then the probability of accepting the change declines exponentially with the magnitude of the change in energy. This represents the entropic drive of the system. Upon many repetitions of this algorithm, the system will reach equilibrium and then it is possible to sample its equilibrium properties, such as pressure, inter-particle distance, reaction kinetics and many other parameters (depending on the system).

#### **1.11.2. Monte Carlo studies for structure/function studies of the thylakoid membrane.**

MCMC simulations of LHCII and PSII in the grana have revealed that interlayer (stacking) interactions between LHCII lead to a coexistence of fluid and crystalline domains of PSII-LHCII (Schneider & Geissler, 2013). The authors note that environmental changes may cause a phase transition which results in the whole grana double layer becoming crystalline. PSII-LHCII crystalline domains have also been observed in models containing only intralayer interactions (Lee *et al.*, 2015) and are highly sensitive to the packing fraction (density) of PSII and LHCII as well as the ratio of PSII to LHCII. Using the model as described in (Schneider & Geissler, 2013), Kapil *et al.* (2016) revealed that this response to environmental change also affects the capacity for light harvesting with higher crystallinity resulting in larger LHCII pools which dissipate energy.

The organisation of the grana will affect the rate of plastoquinone diffusion between PSII and cytb<sub>6</sub>f and previous studies have used Monte Carlo simulations to investigate this issue (Mitchell *et al.*, 1990; Tremmel *et al.*, 2003). These simulations are often referred to as Brownian dynamics simulations because they simulate the Brownian motion of mobile particles in a model of their environment.

Typically, these are carried out on a lattice (usually square or triangular) with a defined spacing ( $\Delta x$ ). The particle has the ability to move forward, backwards, left, right, up or down (if the space is 3-D) with equal probability at each time step  $t$ . Then, the time between each step is given by the diffusion equation

$$\Delta t = \frac{\Delta x^2}{6D}$$

Where  $D$  is the diffusion constant. Note that this is equivalent to the change in the Hamiltonian being zero in the Metropolis-Hastings algorithm. If the mobile particle should encounter an obstacle such as another particle or a boundary in the next step, this is represented by an infinite energy, a change of state that has the probability zero in the Metropolis-Hastings algorithm and will therefore not occur. This is usually known as a hard wall potential.

### 1.12 Aims of this work

Recent studies have shown AFM is capable of high-resolution imaging of plant thylakoid membranes in liquid (Sznee *et al.*, 2011; Johnson *et al.*, 2014; Phuthong *et al.*, 2015). Efforts to date have focussed on the organisation of PSII and cytochrome *b<sub>6</sub>f* in the grana, often using pre-existing protocols for grana purification. As successful AFM imaging is highly dependent on highly pure and preferably, very flat samples, I will continue to develop protocols using digitonin to purify grana membranes from spinach for AFM imaging. The optimised protocol may also be adapted to purify grana from *Arabidopsis thaliana* an important model plant.

A major part of this project will be the development of a protocol for the purification of stromal lamellae from spinach for AFM imaging. To-date, no AFM imaging of the stromal lamellae has been described in the published literature with the exception of Phuthong *et al.* (2015) who describe a single image of a region of stromal lamellae contiguous with a grana membrane. We expect to see PSI at relatively high density in the stromal lamellae as a protrusion of approximately 3.5 nm in height and 11 nm in diameter (Fotiadis *et al.*, 1998; Phuthong *et al.*, 2015).

AFM data on the organisation of PSII, *cyt b<sub>6</sub>f*, and PSI within the thylakoid membrane are likely to yield important insights into the rates of electron transport. Previous studies have suggested that PC may have to diffuse over long distances (>100 nm) (Johnson *et al.*, 2014) in a crowded luminal space (Kirchhoff *et al.*, 2011). I intend to use Monte Carlo simulations to investigate how the organisational and structural aspects of the thylakoid membrane affect PC-based electron transport.

## **Chapter 2.**

### **Materials and methods**

### 2.1. Plant Material.

Mature market bought *Spinecea oleracea* leaves were used throughout. Wild-type *Arabidopsis thaliana* (Col-0) was grown in  $120 \mu\text{mol m}^{-2} \text{s}^{-2}$  light intensity at  $21^\circ\text{C}$  for 6 weeks.

### 2.2. Thylakoid preparation.

Leaves were depetioled and placed in a pre-cooled kitchen blender. Ice-cold homogenisation buffer (50 mM sodium phosphate buffer (pH 7.4), 5 mM  $\text{MgCl}_2$ , 300 mM sucrose) was added at a ratio of 100 ml to 100 g leaf material. The material was homogenised for around 30 seconds and filtered twice: firstly, through two layers of muslin cloth and, secondly through a layer of cotton wool sandwiched between two sheets of muslin cloth. The filtered homogenate was then decanted in equal volumes in 50 ml Falcon tubes, and centrifuged for 15 minutes at 3800 rpm on a ThermoScientific Sorvall ST 16R centrifuge at  $4^\circ\text{C}$ . The pellet was resuspended in 50 ml osmotic break buffer (10 mM tricine (pH 7.4), 5 mM  $\text{MgCl}_2$ ) and left for 1 minute on ice before 50 ml of osmotic halting buffer (10 mM tricine (pH 7.4), 5 mM  $\text{MgCl}_2$ , 400 mM sucrose) was added. The sample was then centrifuged for 10 minutes at 3800 rpm, the resulting pellet yielding thylakoids.

### 2.3. Spectroscopy and chlorophyll assay.

Absorption spectra were taken on an Agilent Technologies Cary 60 UV-VIS spectrophotometer. Chlorophyll concentrations and a/b ratios were calculated according to Porra *et al.*, (1989):

4  $\mu\text{l}$  of thylakoid suspension was added to 2 ml of 80% acetone in a 2 ml eppendorf tube and vortexed. The solution was centrifuged at 14000 rpm in benchtop centrifuge for 3 minutes. The absorption of the acetone suspension was taken at 750, 663 and 646 nm. The following equations were solved for the concentrations of chlorophylls a and b

$$[\text{Chl a}] = (12.25A_{646}^* - 2.55 A_{646}^*)/2$$

$$[\text{Chl b}] = (20.31A_{646}^* - 4.91 A_{663}^*)/2$$

Where

$$A_{646}^* = A_{646} - A_{750}$$

$$A_{663}^* = A_{663} - A_{750}$$

The total chlorophyll concentration is defined as:

$$[\text{Chl a}] + [\text{Chl b}]$$

and the a/b ratio is defined as:

$$[\text{Chl a}] / [\text{Chl b}]$$

#### **2.4. Digitonin treatment.**

Thylakoids were treated with varying concentrations (%w/V) of digitonin (CAT: 300410-5GM) purchased from Calbiochem. 10 %w/V digitonin stock was added to 10 mM HEPES (pH 7.4), 5 mM MgCl<sub>2</sub> and 0.5 mg ml<sup>-1</sup> Chl thylakoid concentration (unless stated otherwise) until desired digitonin concentration was acquired. The solution was mixed by 5 seconds of vortexing and incubated for 1 hour on ice (mixed every 15 minutes). Unbroken thylakoids were removed by centrifugation for 5 minutes at 1000 g.

#### **2.5. Differential centrifugation.**

Fractionation of subthylakoid particles was carried out on a Beckman L7-65 Ultracentrifuge using a Beckman Ti-50.2 rotor at 4°C. Centrifugation steps were as follows:

- 30 minutes at 10 000 g (the pellet is referred to as the 10 k fraction in the text)
- 30 minutes at 40 000 g (40 k fraction)
- 1 hour at 140 000 g (140 k fraction)

At each step the pellet was resuspended in 10 mM HEPES (pH 7.4), 100 mM sucrose, 5 mM NaCl and the supernatant was used as material for the next centrifugation step.

#### **2.6. French Press.**

Thylakoids were diluted to 4 mg/ml chlorophyll in 10 mM sodium phosphate buffer pH 7.4, 5 mM MgCl<sub>2</sub>, 5 mM NaCl, 100 mM sucrose. Thylakoids were broken using French press at 1500 psi and EDTA was added to a final concentration of 5 mM. The thylakoids were then treated a second time using French press at 1500 psi.

#### **2.7. Aqueous two-phase system (ATPS) separation.**

Solutions were kept on ice at all times. ATPS separation was carried out essentially as in Danielsson & Albertsson (2009, 2013). 1 ml of thylakoids (at 4 mg/ml) were added to 24 ml of aqueous two-phase system (0.2% (w/v) Dextran, 0.4% (w/v) PEG 3350). The system was then shaken and centrifuged at 3000 g for 5 minutes to stimulate phase separation. The resulting top phase was then removed and

added to 12 ml fresh bottom phase. Like-wise, 12 ml fresh top phase was added to the resultant bottom phase. The process was then repeated twice more.

### **2.8. Sucrose gradients.**

10-45 % (w/w) continuous 11 ml sucrose gradients were poured using a Hoefer SG 100 Gradient Maker and a Gilson Minipuls 3 peristaltic pump. 0.5 ml sample was added carefully to the top of the gradients and the gradients were centrifuged using SW41 rotor on a Beckman L7-65 ultracentrifuge at 4°C (rotor speeds and centrifugation times specified in text).

### **2.9. Low-temperature fluorescence.**

Low-temperature (77K) fluorescence was performed using an Oxford Scientific optistat DM liquid nitrogen-cooled cryostat (Oxford Instruments). Fluorescence emission spectra were obtained using a SPEX FluoroLog FL3-22 spectrometer using a Xenon light source using an excitation wavelength of 435 nm.

### **2.10. Transmission electron microscopy.**

Samples were diluted to 1  $\mu\text{g ml}^{-1}$  and adsorbed to carbon coated EM grids. The grids were stained using Uranyl formate, rinsed with deionised water, and dried under a steady stream of nitrogen. EM was carried out on a TM-100 microscopy with a direct electron detector camera.

### **2.11. SDS-PAGE and BN PAGE gel electrophoresis.**

SDS-PAGE and BN PAGE were run on Invitrogen NuPAGE 12 % Bis-Tris 1 mm x 10 well gel. Each well contained 10  $\mu\text{g}$  of chlorophyll in 20  $\mu\text{l}$  NuPAGE LDS sample buffer. Gel electrophoresis was carried out at 150 V for 75 minutes

### **2.12. Atomic force microscopy.**

Membrane samples were adsorbed to a freshly-cleaved mica surfaces in adsorption buffers and for time periods as specified in the text. In all cases, mica surfaces were rinsed by removing half of the liquid and replacing with fresh buffer: three times with adsorption buffer and three times with imaging buffer. PeakForce QNM AFM was performed on a Bruker Multimode 8 AFM using Nanoscope software. All AFM used Bruker SNL-10 (Type C) cantilevers in imaging buffer (as specified in the text) at room temperature. AFM operation parameters were as follows:

PeakForce setpoint: 0.04-0.08 V

PeakForce amplitude: 10-25 nm

PeakForce frequency: 2 kHz

Samples per line: 512 or above

Scan rate: 0.5-1 Hz

AFM images were analysed using Nanoscope analysis 1.50 software. Cross sections were displayed using Graphpad Prism 6.

### **2.13. Computational methods.**

Monte Carlo simulations and automatic PSI identification programs were written in the Python (2.7.11) programming language in a 64 bit Python environment (Enthought Canopy) using Numpy, Matplotlib and Random modules. Python scripts were executed on a 64 bit Windows 7 operating system on a single Intel Core i7 3.2 GHz processor. Source code is provided in chapter appendices.

### **2.14. Graphical output.**

All graphs were produced using Graphpad Prism 6 unless otherwise specified. This includes the calculation of frequency distributions and Gaussian curve fitting (least-squares).

## Chapter 3.

# Purification of grana and stromal lamellae membranes from *Spinecea oleracea* and *Arabidopsis thaliana* for atomic force microscopy

### Summary

The thylakoid membrane of the plant chloroplast has a complex architecture. Its two distinct regions, the PSII-enriched grana and the PSI-enriched stromal lamellae each contain their own protein composition. Historically, detergent treatments and mechanical breakage methods have been used to break the thylakoid membrane and separate the constituent grana and stromal lamellae. Techniques such as fluorescence spectroscopy, electron microscopy, gel-electrophoresis among others have revealed that the PSII and PSI partition into the grana and stromal lamellae respectively, ATP synthase is only present in the stromal lamellae, while *cytb<sub>6</sub>f* is distributed throughout the thylakoid membrane.

In this chapter, we develop methods for preparing grana and stromal lamellae membranes for AFM imaging: a technique which is capable of producing nanometre-scale 3-D images of biological membranes in liquid and at RTP. A number of methods of thylakoid breakage, which are well characterised in the literature were reviewed and tested for their suitability for producing membranes for AFM imaging. These include treatments with detergents such as digitonin and mechanical methods such as French Press. Grana and stromal lamellae were separated using differential centrifugation, sucrose gradient ultracentrifugation and aqueous two-phase system (ATPS) separation.

The results described in this chapter indicate that fractionation of the thylakoids with the mild detergent digitonin most reliably produces grana and stromal lamellae membranes suitable for AFM analysis. The digitonin protocol originally developed using spinach was then adapted for the model plant *Arabidopsis thaliana*.

### 3.1 Introduction.

#### 3.1.1. Overview of thylakoid fractionation.

The chloroplast houses the complete photosynthetic machinery of plants (Arnon, 1955). Early evidence revealed that the light reactions of photosynthesis contained two photochemical reactions (Emerson *et al.*, 1957): the reduction of  $\text{NADP}^+$ , and the photolysis of water (Hill, 1937). Each photochemical reaction was found to contain its own system of chlorophyll pigments: system I (photosystem I), associated with  $\text{NADP}^+$  reduction, preferentially absorbs longer wavelengths of light, while system II (Photosystem II), associated with the Hill reaction, absorbs more light at shorter wavelengths. These two photochemical reactions were later proposed to be sequentially connected by a sequence of electron transfer reactions in the famous Z-scheme proposed by Hill and Bendall (1960). Early EM images revealed the dense grana of the thylakoid membrane within the chloroplast to be composed of many layers of membranes (von Wettstein, 1961) (Fig. 3.1, Fig. 1.2). Emanating from the grana were a series of non-stacked lamellae. However, it was not obvious at the time if or how the photochemical reactions were associated with the different thylakoid membrane regions. Anderson & Boardman (1964) developed a method for isolating particles with different ratios of Chlorophyll *a* and chlorophyll *b* (Chl *a/b*) (Fig. 3.2). Chloroplasts were treated with the mild detergent digitonin and centrifuged repeatedly at 1000 g, 10 000 g, 50 000 g, and 144 000 g. the so-called “heavy fraction”, pelleting at 1000 – 10 000 g, contained particles with Chl *a/b* ratios lower than those of the intact chloroplast whereas the “light fraction”, pelleting at 50 000 – 144 000 g, contained particles with higher Chl *a/b* than that of intact chloroplasts. Furthermore, the heavy fraction was active in the Hill reaction in the presence of oxidants: ferricyanide or trichlorophenolindophenol, but showed low activity in  $\text{NADP}^+$  reduction, even in the presence of reductants (Anderson & Boardman, 1966). Conversely, the light fractions were found to be inactive in the Hill reaction but were active in  $\text{NADP}^+$  reduction in the presence of reductants sodium ascorbate or dichlorophenolindophenol. 77 K fluorescence emission spectra of the heavy fraction was found to closely resemble that of the intact chloroplast as it showed two peaks of approximately equal amplitude at 680 nm and 735 nm (Boardman *et al.*, 1966). In the light fraction, however, the longer-wavelength 735 nm peak was greatly enhanced. This indicated that the light fraction was enriched in photosystem I.

Michel and Michel-Wolwerz (1967) developed a non-detergent method of chloroplast fractionation using French press. The treatment yielded a heavy fraction of low Chl *a/b* and active in the Hill reaction and a light fraction of high Chl *a/b* and active in  $\text{NADP}^+$  reduction upon separation by differential centrifugation (Sane *et al.*, 1970) or sucrose gradient ultracentrifugation (Murata & Brown, 1970). These fractions are of course similar to the heavy and light fractions obtained by digitonin in the

method of Anderson and Boardman (1964), although the heavy fraction of Michel and Michel-Wolwerz (1967) contained comparatively more PSI. EM imaging of freeze-fracture and freeze-etched faces of the heavy fraction revealed that it was derived from the grana stacks of the thylakoid (Sane & Park, 1970). The stromal lamellae were removed in the process of mechanical breakage and constituted the light fraction (Sane *et al.*, 1970). Further purification of thylakoid particles obtained following French press treatment was achieved using an aqueous two-phase system (ATPS) (Albertsson, 1971). An ATPS is a polymer mix which separates into two phases: a denser bottom phase and a lighter top phase. A mixture of particles added to the ATPS will then partition into one of the two phases depending on its surface properties and interactions with the phase system. Using an ATPS of 6.1 % (w/w) Dextran-500 and 6.1% (w/w) polyethylene glycol (PEG) 4000 Åkerlund *et al.* (1976) demonstrated the heavy and light particles produced using French press and differential centrifugation could be purified further (Fig. 3.3). The heavy grana fraction partitioned into the bottom (Dextran) phase increasing the PSII/PSI ratio whereas the light stromal lamellae fraction partitioned into the top (PEG) phase. Using this approach in combination with SDS-PAGE electrophoresis, which retained up to 90 % of total chlorophyll of the sample, Andersson and Anderson (1980) established that the PSI/PSII ratio of the grana and stromal lamellae is 0.72 and 15 respectively, revealing the extent to which they are spatially separated in the thylakoid membrane. Further mechanical breakage and ATPS separation of the bottom phase (grana) fraction resulted in the appearance a new top phase with Chl *a/b* ratio similar to that of intact thylakoids and PSI-enriched in comparison to the grana fraction (Wollenberger *et al.*, 1994, Wollenberger *et al.*, 1995). Crucially, the PSI in this fraction was found to differ from PSI in the stromal lamellae in that its antenna size was 30 % larger, suggesting a greater degree of contact with LHCII. The authors propose that this fraction results from the grana margins, which are separated from the grana in the second fractionation procedure.

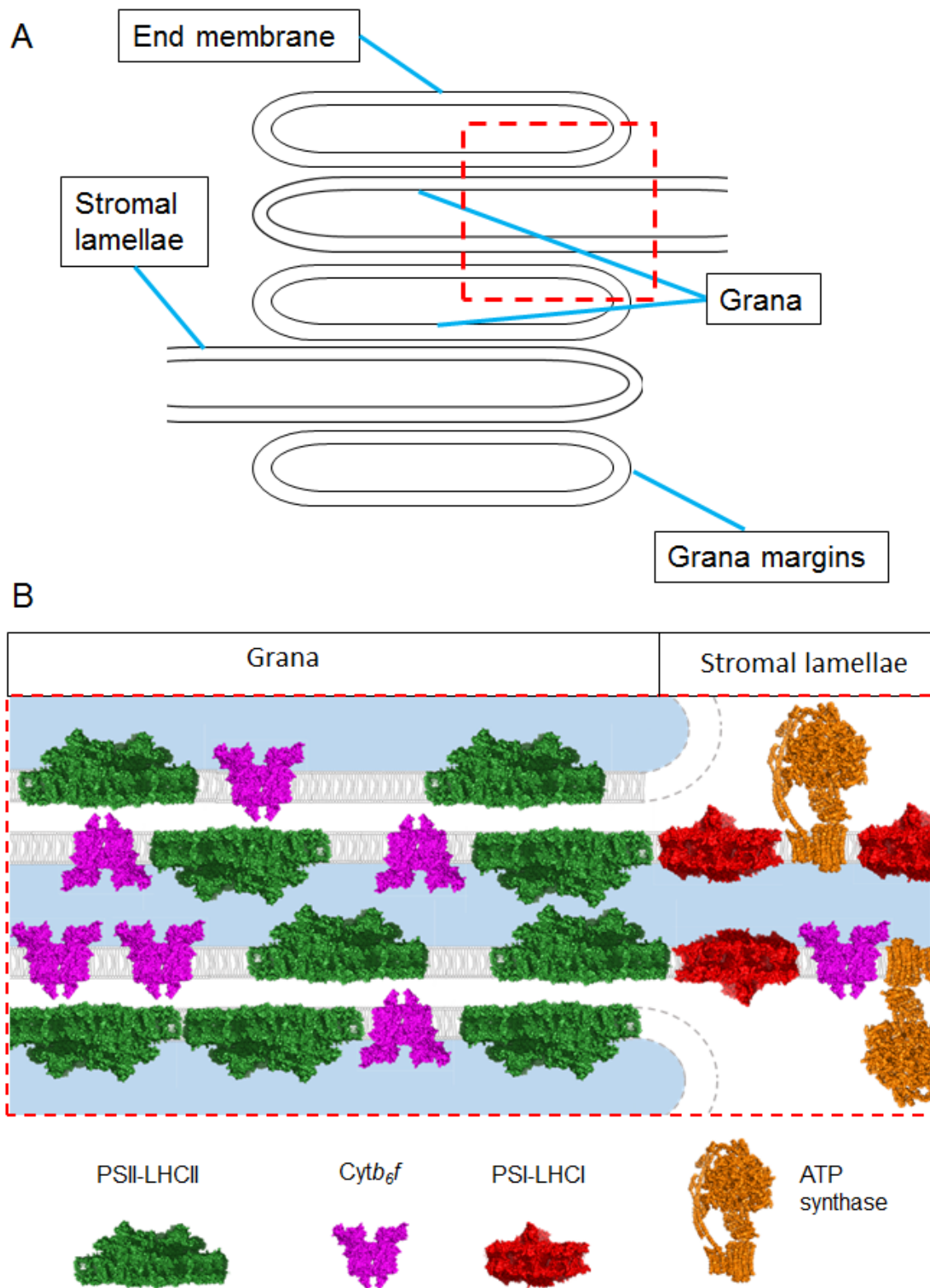


**Figure 3.1. Outline of the thylakoid membrane structure.** **A.** Schematic representation of the thylakoid and nomenclature of the different regions. **B.** A region of the thylakoid labelled in (A) with red box showing lateral heterogeneity of PSII (PDB: 3JCU), PSI (PDB: 4Y28), *Cytb<sub>6</sub>f* (PDB: 1Q90) and ATP synthase (PDB: 5ARA)

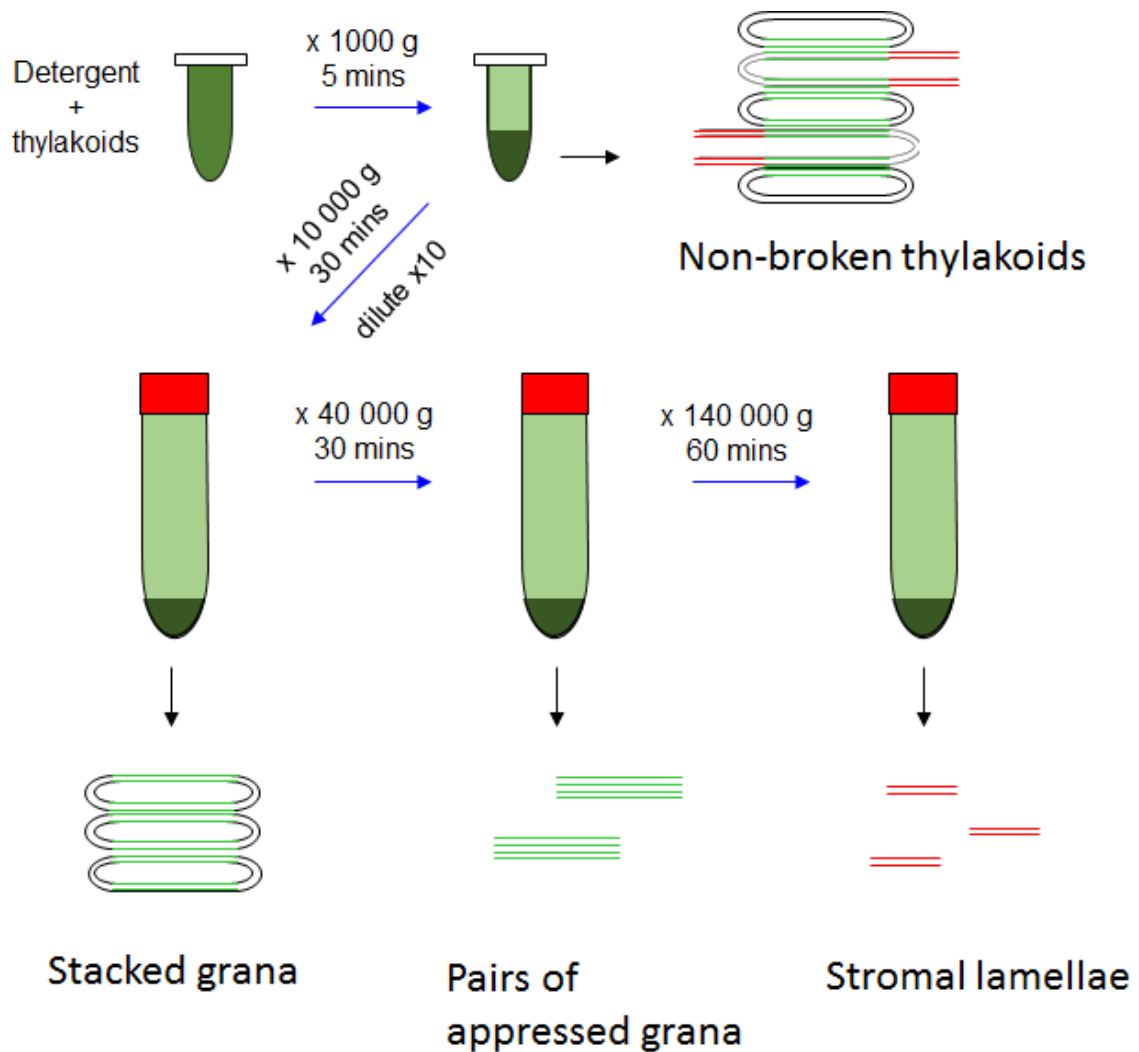


**Figure 3.2. The procedure for fractionation of the thylakoid membrane using detergent treatment and differential centrifugation.** Thylakoids were treated with detergent and centrifuged at 1000 g to remove a pellet of intact (non-broken) thylakoids. The broken thylakoids were then subjected to three centrifugations in series. The centrifugation pellets at 10 000 g, 40 000 g and 140 000 g were enriched in stacked grana (green, margins shown in black), pairs of appressed grana (green) and stromal lamellae (red) respectively.

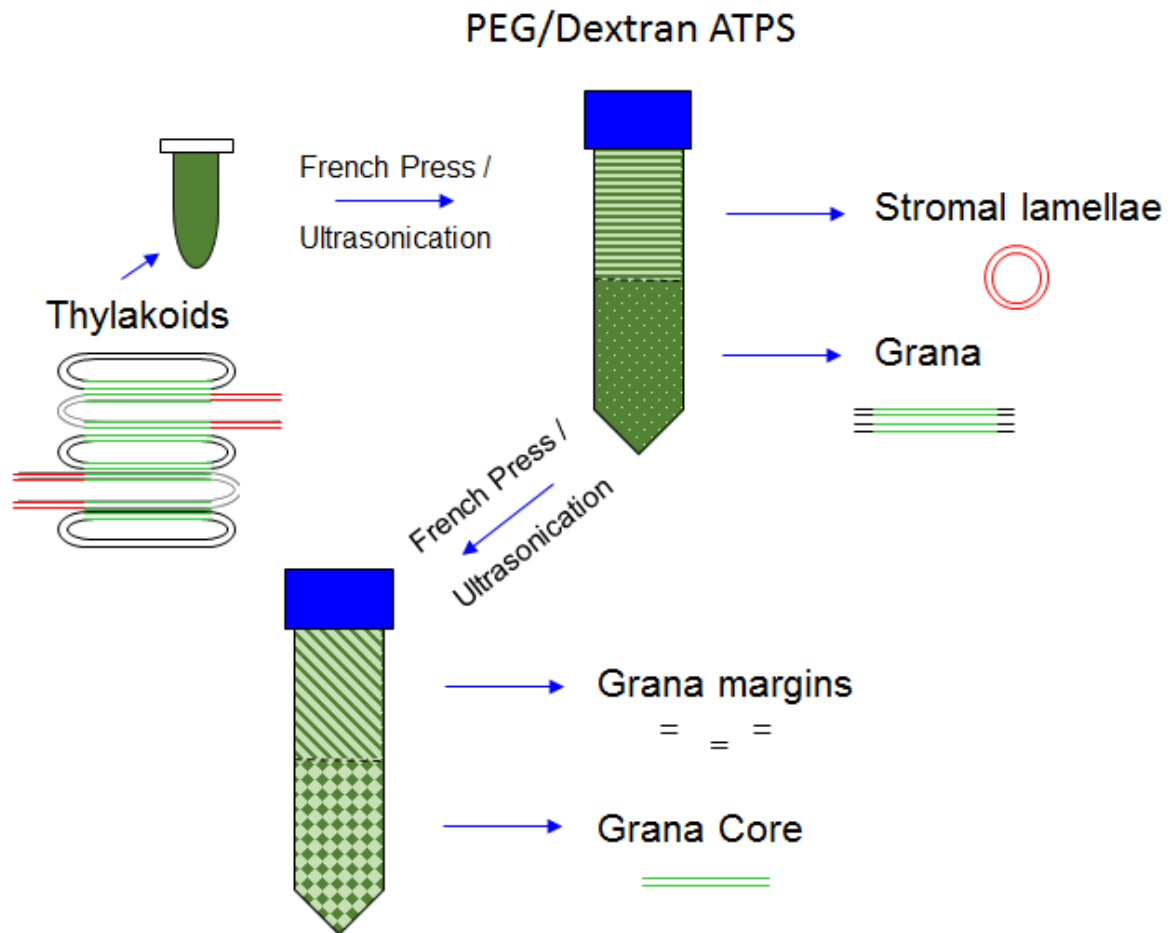


**Figure 3.3. Fractionation of thylakoids using mechanical breakage and aqueous two-phase system (ATPS) separation.** Thylakoids were broken using French press or ultrasonication and added to a mixture of dextran and polyethylene glycol (PEG). The mixture phase separated to form an ATPS. The higher affinity of PSII-enriched membranes to the (bottom) dextran phase and the PSI-enriched membranes to the (top) PEG phase allows for separation of the grana and the stromal lamellae. Further breakage and ATPS separation of the grana membranes separates the grana core from the grana margins.

### 3.1.2. Fractionation of thylakoids for AFM imaging.

The first AFM studies of grana membranes used the approach of Berthold, Babcock and Yocum (1981) in which thylakoid membranes were fractionated using the detergent TRITON-X100 and differential centrifugation. The highly PSII-enriched grana fractions produced in this way are often referred to as BBY membranes after the authors who first described them. The approach, described in Kirchhoff *et al.*, (2004), treated the thylakoid membranes at 5 mg/ml chlorophyll with 5 % (w/w) TRITON-X100 for 15 minutes. The grana fraction was obtained by centrifugation at 28 000 g for 30 minutes. Samples were prepared for AFM by adding a 50  $\mu$ l drop to a freshly-cleaved mica surface and incubating for 2 minutes before rinsing 10 times with Millipore water and drying under a stream of nitrogen (Kirchhoff *et al.*, 2008). AFM imaging of the membranes revealed three layers of membranes 11.9 nm, 22.4 nm, and 33.5 nm, stacked on top of one-another and became progressively smaller from bottom to top. This allowed the AFM to image the top face of each of the layers. The second layer, at 22.4 nm in height was found to contain dimeric protrusions with a separation of  $\approx$ 10 nm and heights of 4-6 nm, consistent with the dimensions of the luminal extramembrane subunits of PSII. Using the comparatively mild detergent n-dodecyl- $\alpha$ , D-maltoside, van Roon *et al.* (2000) fractionated thylakoids and used gel filtration to purify grana membranes and dilute the detergent content in the sample. This protocol yielded pairs of appressed grana membranes, which were circular in shape, with an average diameter of 360 nm, and possessed a similar protein content to those obtained using TRITON-X100. They were also “inside-out”, resulting in the luminal extramembrane subunits of PSII being visible on the top face. AFM imaging of grana membranes prepared in this manner revealed dimeric PSII to be occasionally arranged in semi-crystalline rows of dimers (Sznee *et al.*, 2011). Occasionally, membrane regions emanating from the bottom layer of the pair of appressed membranes revealed particles with diameters of  $10.8 \pm 1.1$  nm and heights ranging from 3 nm to 3.6 nm (Phuthong *et al.*, 2015). This is consistent with the extramembrane PSI-LHCI subunits on the stromal face of the stromal lamellae (Fotiadis *et al.*, 1998). Using the digitonin approach of Anderson and Boardman (1966), Johnson *et al.* (2014) were able to purify pairs of appressed grana membranes, which retained *cytb<sub>6</sub>f* in addition to PSII for AFM imaging. The *cytb<sub>6</sub>f* complexes protruded by  $3.0 \pm 0.1$  nm, consistent with the atomic structure (Stroebele *et al.*, 2003) and were found to be randomly dispersed amongst the PSII complexes, which rise 4 nm above the membrane surface. These results were confirmed using affinity-mapping atomic force microscopy in which the AFM tip is functionalised with a redox partner one is trying to locate. In this example, the AFM tip was functionalised with oxidised PC, the cognate electron acceptor of *cytb<sub>6</sub>f*. When the AFM tip comes into contact with *cytb<sub>6</sub>f*, specific interactions mediated by the tethered PC trigger measurable adhesion forces, hence allowing *cytb<sub>6</sub>f* to be identified and localised

simultaneously. Crucially, the location of these specific interactions correlated with the 3 nm protrusions.

AFM is a powerful and unique method of investigating the nanoscale structure of biological membranes, such as thylakoids, under liquid. However, it remains limited by current methods of thylakoid fractionation. In this chapter, methods of fractionation and purification of the grana and stromal lamellae were developed and optimised for both spinach and *Arabidopsis*. The purpose of these methods, namely providing samples for AFM, was kept in mind throughout and therefore each experiment was followed up by AFM analysis. Much of the previous work on the structure of the thylakoid membrane has used spinach as a model organism. However, over the previous few decades, *Arabidopsis thaliana* (thale cress), a small, flowering plant with a short life-cycle of around 7-8 weeks, has emerged over the preceding decades as a genetically amenable model organism (Koornneef and Meinke, 2010). This is largely due to the establishment of an *Agrobacterium*-based transformation protocol and the acquisition of its complete genome sequence (The Arabopsis Genome Initiative, 2000). Recent advances from biochemical analyses have shed new light on the structure and dynamics of the *Arabidopsis* thylakoid membrane (Pribil *et al.*, 2014). In part, this is due to the production of knock-out and over-expression mutants of curvature thylakoid (CURT) proteins (Armbruster *et al.*, 2013), Kinase and phosphatase (Bellafiore *et al.*, 2005; Bonardi *et al.*, 2005; Pribil *et al.*, 2010) among others. Therefore, a more detailed investigation of the structure of the *Arabidopsis* thylakoid membrane would be both valuable and timely. To date, very little research has been published involving structural study of the *Arabidopsis* thylakoid membrane by AFM. The few publications that exist focused entirely on the grana, were often low resolution AFM and dried membranes were used (as opposed to AFM in liquid) (Kirchhoff *et al.*, 2008; Onoa *et al.*, 2014.; Puthiyaveetil *et al.*, 2014). It is therefore of scientific interest to develop reliable purification protocols of grana and stromal lamellae membranes from *Arabidopsis thaliana*, for AFM imaging under liquid conditions, alongside spinach. Although AFM generally requires a greater amount of preparation and optimisation to produce highly purified and flat samples for imaging compared to EM, it offers a number of advantages. Whereas EM techniques require frozen, dehydrated, heavy-metal stained samples, and operate in vacuum, AFM operates in liquid and therefore biological samples can be imaged in near-native conditions. When imaging biomembranes or proteins in liquid, they remain functionally active, which offers opportunity to measure native interactions between sample proteins and those attached to an AFM tip (Vasilev *et al.*, 2014; Johnson *et al.*, 2014). The nanoscale lateral resolution and sub-nanometer height resolution also allow protein complexes to be identified by direct comparison with published atomic structures allowing detailed atomic models of entire biomolecular systems to be produced (Scheuring *et al.*, 2007; Şener *et al.*, 2007).



## 3.2. Results.

### 3.2.1. Fractionation of Spinach and *Arabidopsis* thylakoids using digitonin.

The solubilisation of thylakoids from spinach and *Arabidopsis* by digitonin was investigated (Fig. 3.4). Thylakoids were diluted to 0.5 mg/ml chlorophyll in 10 mM HEPES (pH 7.4), 5 mM MgCl<sub>2</sub>. 10 % (w/v) digitonin was added until the desired concentration was reached and the solution was left on ice for one hour. As indicated by the percentage of material pelleted at 1000 g, both spinach and *Arabidopsis* show a high amount ( $\approx 95\%$ ) of fractionation even at 0.5 % (w/v) digitonin (Fig. 3.4A). This does not increase significantly as the digitonin concentration is increased to 2 % (w/v). However, differential centrifugation analysis reveals subtle differences in the fractionation of spinach (Tables 1&2) and *Arabidopsis* (tables 3&4) as a result of varying digitonin concentration. Spinach thylakoids solubilised over a range of digitonin concentrations (0.5 – 2.0 % (w/v)) were centrifuged for 30 minutes at 10 000 g, 30 minutes at 40 000 g and for one hour at 140 000 g. The 40 000 g pellet is equivalent to the 'heavy fraction' described in the introduction, which contains grana membranes enriched in PSII (Boardman & Anderson, 1964). The 10 000 g centrifugation step removes larger grana membranes, which may be stacks of membranes with more than two layers. Removal of the 10 000 g pellet before carrying out the 40 000 g centrifugation step yields a 40 000 g fraction amenable to AFM imaging (Johnson *et al.*, 2014). The 140 000 g pellet is equivalent to the light fraction of Boardman & Anderson, (1964), which is enriched in PSI and represents the stromal lamellae. Herein, the 10 000 g, 40 000 g, and the 140 000 g pellets will be referred to (respectively) as the 10 k, 40 k, and 140 k fractions to be concise. The assumption will also be made that the 10 k, 40 k, and 140 k are synonymous with grana stacks, grana double layers and stromal lamellae as shown in Figure 3.2. It was observed that increasing the concentration of digitonin used for thylakoid solubilisation affected the fractionation process. More specifically, an increased digitonin concentration was found to reduce the proportional size of the 10 k fraction in comparison with that of the 40 k and 140 k fractions in spinach (Table 3.1). This suggests that an increase of digitonin concentration encouraged the separation of grana stacks into pairs of appressed membranes, as well as a monotonic increase of solubilisation with increased digitonin concentration. Moreover, the chlorophyll *a* to chlorophyll *b* ratio (Chl *a/b*) was also found to be reduced in the 10 k and 40 k fractions with increased digitonin concentrations (Table 3.2). One may speculate that this may result from the further solubilisation at higher digitonin concentrations of stromal lamellae fragments that remain attached to the grana at low digitonin concentrations. The same results as described above for spinach were also found to hold true in *Arabidopsis* (Tables 3.3&3.4). However, a comparison of the proportion of 1 % digitonin fractionated material in the 10 k, 40 k, and 140 k fractions in spinach and *Arabidopsis* reveal a possible difference in thylakoid structure

(Fig. 3.4B). It is clear that the 10 k fraction of spinach contains a much larger proportion of the fractionated thylakoid material in comparison with *Arabidopsis*. This may be indicative of a higher degree of stacking or a greater stacking interaction between grana layers in spinach which would result in less disruption by digitonin of the grana and, therefore, a higher proportion of fractionated material remaining stacked and pelleting in the 10 k fraction.

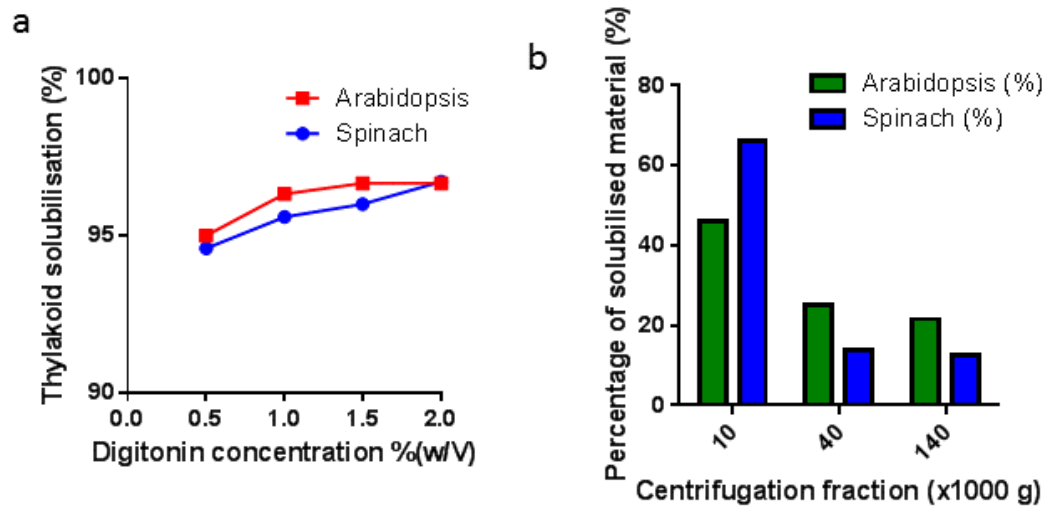


**Figure 3.4. Digitonin solubilisation of Thylakoid membranes from *Spinacia oleracea* and *Arabidopsis thaliana*.** **A.** Percent of thylakoid material fractionated upon incubation in digitonin solution of varying concentrations. **B.** The percentage of fractionated thylakoid using 1% digitonin by chlorophyll concentration present in 10k, 40k, and 140k fractions.

We have shown that the so-called 10k fraction, decreases in both the amount of material and the Chl *a/b* ratio as a result of increasing digitonin concentration. The observation of the decrease in Chl *a/b* indicates a loss of PSI and this may be an indication of the action of digitonin at the grana margins. If this is the point of action of digitonin this goes some way to explaining why fractionation yields such excellent separation of the grana and stromal lamellae in the first place. It is reasonable to conclude that the effects of detergent are hampered in the stacked grana, possibly due to its restricted entry into the grana stacks or because the grana, being so densely packed with PSII, *cytb<sub>6</sub>f* and LHCII is more resistant to detergent action.

A comparison of fractionation experiments conducted on spinach and *Arabidopsis* provides evidence for subtle differences in thylakoid structure in the different plants. Consider Fig. 3.4B, for example. It is clear that the proportion of the 140k fraction in *Arabidopsis* makes up a greater fraction of the whole in comparison with spinach. One may suggest two scenarios. 1. Stromal lamellae constitutes more of

the thylakoid membrane of *Arabidopsis* than it does in spinach. 2. Digitonin fractionation is less effective for fractionation of *Arabidopsis* thylakoids than in spinach and may produce fractions more heterogeneous in size and composition.

Digitonin concentration (%w/v)	0.5 %	1 %	1.5 %	2 %
10 (x1000 g) pellet	1.125	1	0.84	0.68
40 (x1000 g) pellet	0.213	0.21	0.361	0.34
140 (x1000 g) pellet	0.16	0.19	0.21	0.18

**Table 3.1. The effect of varying concentrations of digitonin on the concentration of chlorophyll (mg/ml) in the 10k, 40k and 140k fractions in *Spinacia oleracea*.**

Digitonin concentration (%w/v)	0.5 %	1 %	1.5 %	2 %
10 (x1000 g) pellet	2.81	2.74	2.58	2.47
40 (x1000 g) pellet	3.07	2.86	2.61	2.38
140 (x1000 g) pellet	4.98	5.31	4.96	4.74

**Table 3.2. The effect of varying concentrations of digitonin on the chlorophyll *a*/ chlorophyll *b* ratio of material in the 10k, 40k and 140k fractions in *Spinacia oleracea*.**

Digitonin concentration (%w/v)	0.5 %	1 %	1.5 %	2 %
10 (x1000 g) pellet	1.68	1.32	1.16	1.1
40 (x1000 g) pellet	0.9	0.72	0.62	0.54
140 (x1000 g) pellet	0.6	0.62	No pellet	0.42

**Table 3.3. The effect of varying concentrations of digitonin on the concentration of chlorophyll (mg/ml) I in the 10k, 40k and 140k fractions in *Arabidopsis thaliana***

Digitonin concentration (%w/v)	0.5 %	1 %	1.5 %	2 %
10 (x1000 g) pellet	2.45	2.37	2.32	2.24
40 (x1000 g) pellet	2.9	2.69	2.53	2.51
140 (x1000 g) pellet	4.59	3.91	No pellet	3.46

**Table 3.4. The effect of varying concentrations of digitonin on the chlorophyll *a*/ chlorophyll *b* ratio of material in the 10k, 40k and 140k fractions in *Arabidopsis thaliana*.**

### 3.2.2. Preparation of grana membranes suitable for AFM from spinach using digitonin solubilisation and differential centrifugation.

The 40 k pellet, containing grana vesicles, was found to yield flat, double-layer membranes suitable for AFM imaging, but only when solubilised at concentration of digitonin reaching 2 % (w/v) (Fig. 3.5A-E). Large, spherical particles at lower digitonin concentrations (Fig. 3.5A, for example) suggest that grana membranes formed in the fractionation process may form vesicles until a sufficiently high digitonin concentration is used. This may be the result of resealing around the edges, leading to osmotic swelling. Cross sections of grana membranes (Fig. 3.5E) formed using 2 % digitonin show circular membranes of approximately 500 nm in diameter and 16-18 nm in height. This is consistent with previous AFM images of grana membranes prepared using  $\alpha$ -DM (Frese *et al.*, 2011, Phuthong *et al.*, 2015) and digitonin (Johnson *et al.*, 2014). The procedure for adsorption to the mica surface was shown to be optimal when a sample concentration of 4  $\mu$ g/ml chlorophyll in 10 mM HEPES, 5 mM KCl is adsorbed at room temperature for 1 hour (Fig 5F-H). Figure 6 outlines the optimised protocol for the purification of grana membranes for AFM.

The lateral resolution of AFM varies with the sharpness of the cantilever tip, but occasionally resolution on the order of a few nanometres can be achieved. Fig. 3.7A) shows a gallery of grana membranes at high resolution. In these images, one can clearly see individual protruding particles. The heights of such particles from the membrane surface were found to contain two interspersed populations (Fig. 3.7B) of  $3.1 \pm 0.3$  nm and  $4.1 \pm 0.3$  nm which agree with the heights of *cytb<sub>6</sub>f* and PSII respectively (Fig. 3.3C) and are consistent with the work of Johnson *et al* (2014). The membranes were  $463 \pm 51$  nm (N=15) in diameter and  $19.5 \pm 0.8$  nm in height (Fig. 3.7D). Subtracting the width of the membrane bilayers ( $2 \times 4$  nm) and the protruding extramembrane portions of PSI-LHCII ( $2 \times 4.1 \pm 0.3$  nm) from the total height, we estimate the height of the stromal gap of the grana to be  $3.5 \pm 0.7$  nm.

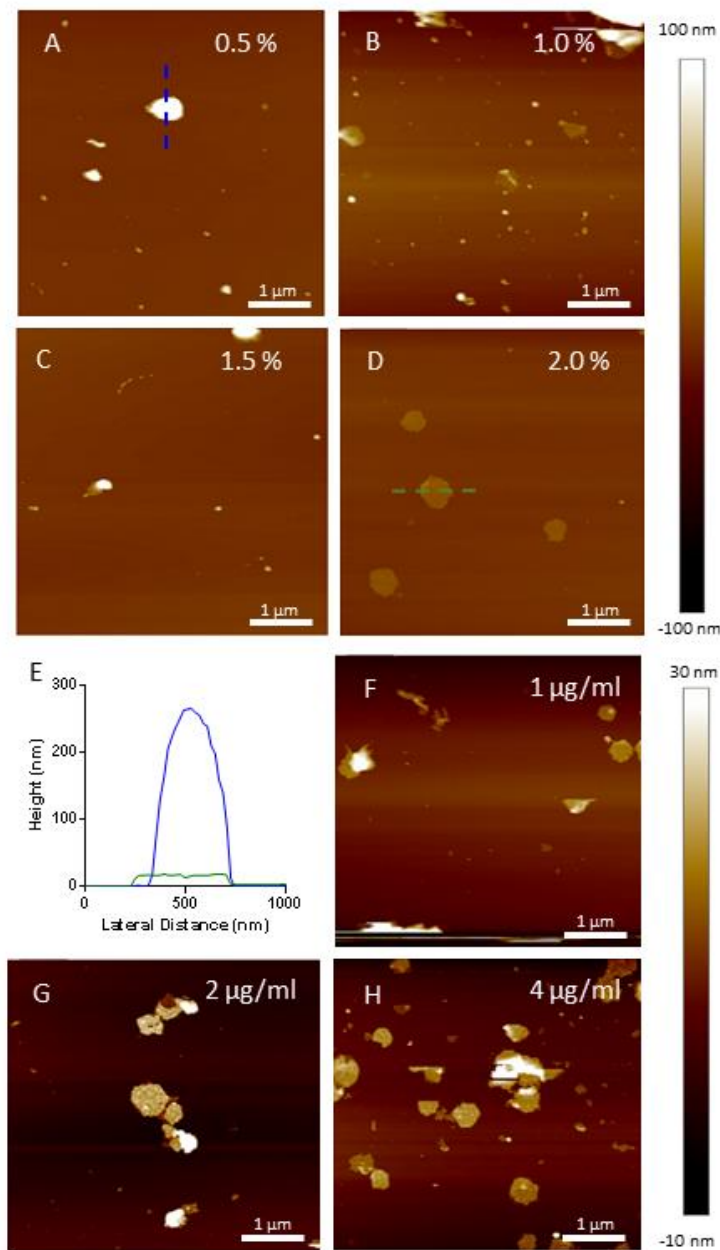


**Figure 3.5. Optimisation of AFM imaging of grana from *Spinacia oleracea*.** **A-D.** AFM images of the 40k fraction from *Spinacia oleracea* treated with 0.5% (A), 1.0% (B), 1.5% (C) or 2.0% (D) digitonin. **E.** Cross-section through grana membrane in (D, white-dashed line) showing that the double-layer grana membranes are 500 nm in diameter and 16-18 nm in height. **F-H.** Optimisation of the concentration of sample (µg/ml chlorophyll). Samples were incubated on the mica surface in adsorption buffer for one hour at 1 µg/ml (F), 2 µg/ml (G) and 4 µg/ml (H) and showed that 4 µg/ml is optimal in order to quickly find a region of interest during AFM imaging.

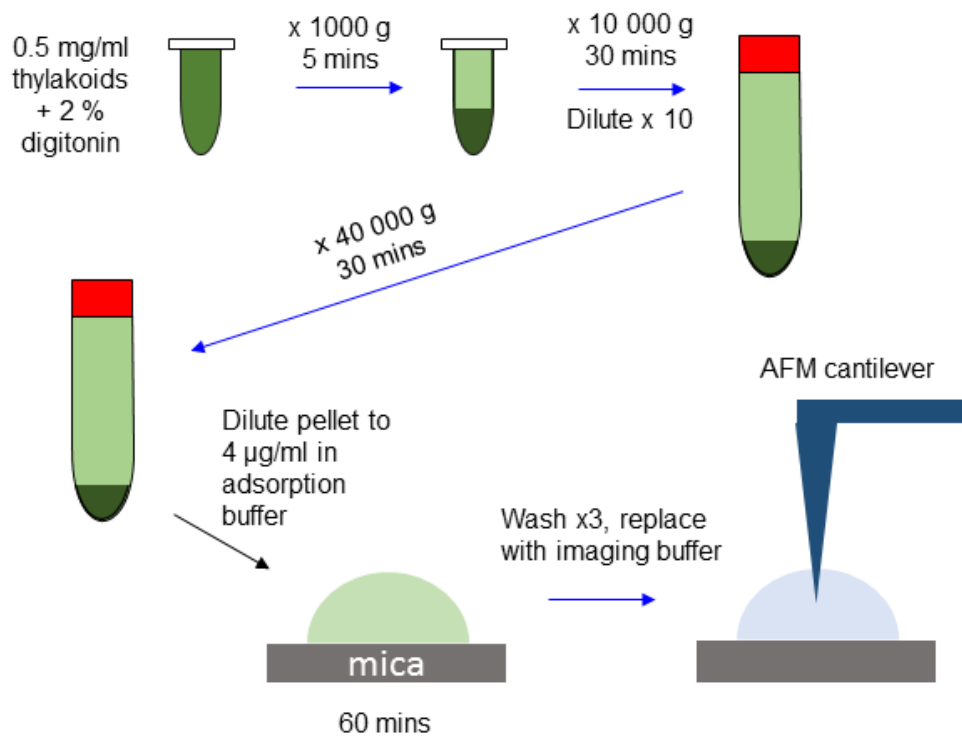


**Figure 3.6. Optimised procedure for the preparation of grana membranes using digitonin for AFM imaging.** Upon treatment with 2% digitonin, centrifugation at 40 000 g yields a pellet enriched in double-layer grana membranes. The membranes were adsorbed to a freshly-cleaved mica substrate in adsorption buffer (10 mM HEPES (pH 7.4), 5 mM KCl), washed, and imaged by AFM in imaging buffer (5 mM MgCl<sub>2</sub>, 10 mM HEPES (pH 7.4), 5 mM KCl).

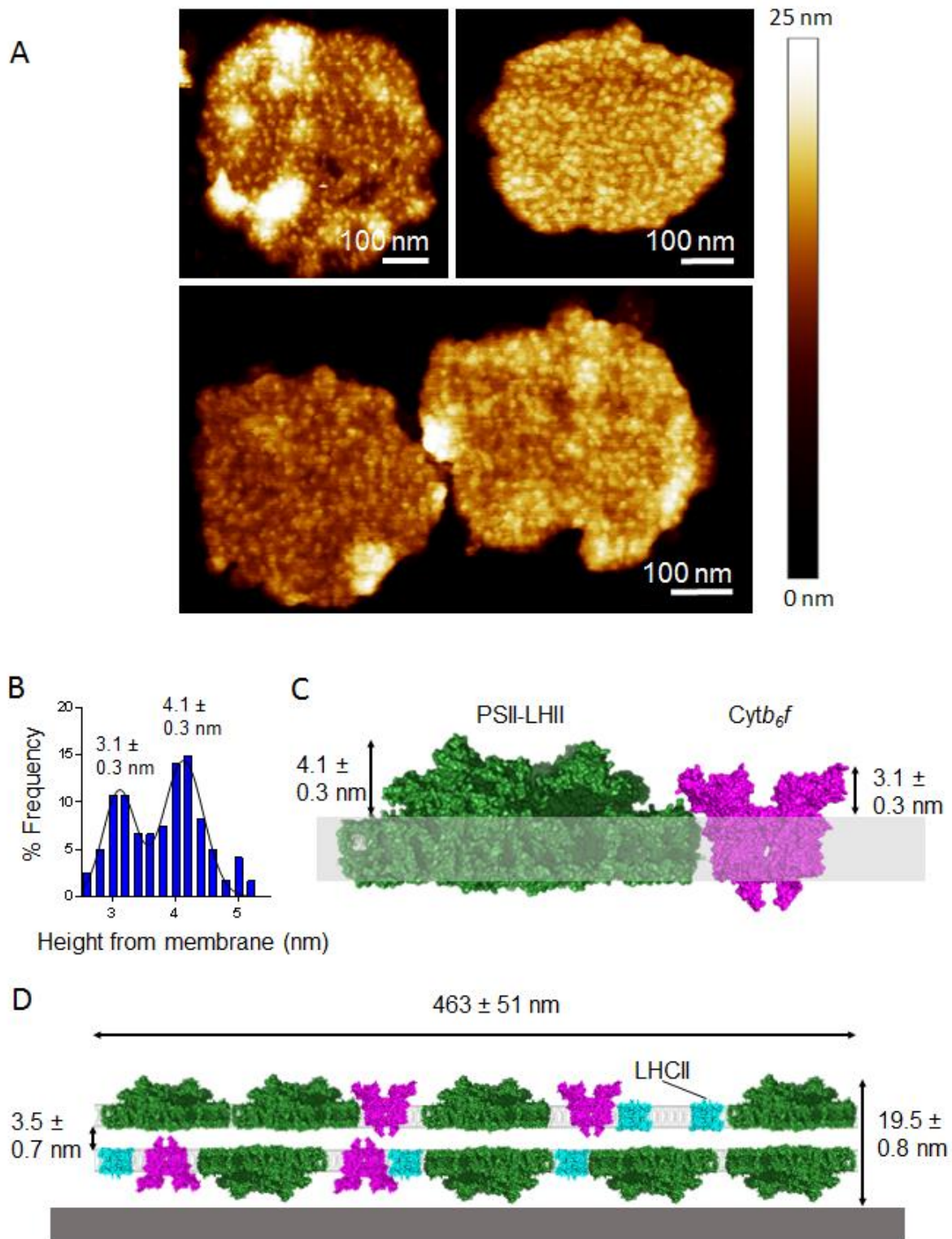


**Figure 3.7. Identification of PSII and *cytb<sub>6</sub>f* from high-resolution AFM images.** **A.** Gallery of high-resolution AFM images of grana from *Spinacia oleracea*. **B.** Histogram of the heights of protrusions from the membrane surface showing means and standard deviations from a double Gaussian fit. **C.** The mean heights from (B) are in close agreement with those of the structures of PSII (PDB: 3JCU) and *cytb<sub>6</sub>f* (PDB: 1Q90). **D.** Average dimensions of observed grana membranes (LHCII PDB: 2BHW).

### 3.2.3. fractionation of spinach thylakoids using French Press.

Thylakoids were diluted to 0.5 mg/ml and broken using a French Press at a pressure of 1500 psi. EDTA was added to 5 mM and the process was repeated. Unbroken thylakoids were then removed by centrifugation at 1000 g for 5 minutes. Differential centrifugation analysis revealed some heterogeneity in the chlorophyll content but in a dramatically different way to digitonin fractionation. Firstly, the 10 k fraction of the French Press treated thylakoids made up a greater proportion of fractionated material (Table 3.5) with approximately 82 % of fractionated material pelleting in the 10 k fraction. Secondly, the chlorophyll *a* to chlorophyll *b* ratios of the fractions were not as expected. A Chl *a/b* value of 3.0 for the 10 k fraction is close to the value of 3.22 for the intact thylakoids: indicating that the fraction contained a significant amount of PSI. This is possibly the result of only partial breakage of thylakoids, a proposition which would also explain why the 10 k fraction, containing larger membrane fragments is enriched in French Press fractionation. The 40 k and 140 k fractions, with *a/b* ratios of 4.0 and 5.73 respectively, were found to be enriched in PSI. This may be due to two factors. The failure of French Press to fully break the thylakoids into constituent grana and stromal lamellae domains has caused much of the PSII containing membranes to pellet in the 10 k pellet leaving mostly PSI containing fractions at higher centrifugation forces. The higher *a/b* of 5.7 for the 140 k fraction produced using French Press compared to that observed upon treatment with digitonin (4.74-5.31: see Table 3.2) may be due to the partial solubilisation of PSI from the stromal lamellae when using digitonin. That is, mechanical fractionation may result in a 140 k fraction that retains a higher concentration of PSI which is closer to the native situation. Sucrose gradient centrifugation revealed that the 10 k and 40 k French Press fractions produced particularly strong bands at 38 and 37% (w/w) sucrose (Fig. 3.8): therefore, indicating that the fractions did indeed contain true membrane fractions. The 140 k pellet however, produced only a “smear” (herein a smear in the context of sucrose gradient ultracentrifugation will be used in reference to a lack of any specific banding but an expansive, homogenous green colouring of the gradient indicative of a continuous range of particle sizes).

	Chlorophyll (mg/ml)	Chl <i>a/b</i>
10 (x1000 g) pellet	2.44	3.04
40 (x1000 g) pellet	0.6	4
140 (x1000 g) pellet	0.21	5.73

**Table 3.5. Fractionation of thylakoids from *Spinacia oleracea* using French press.** Table shows concentration of chlorophyll (mg/ml) and the chlorophyll *a* / *b* ratio in each fraction.

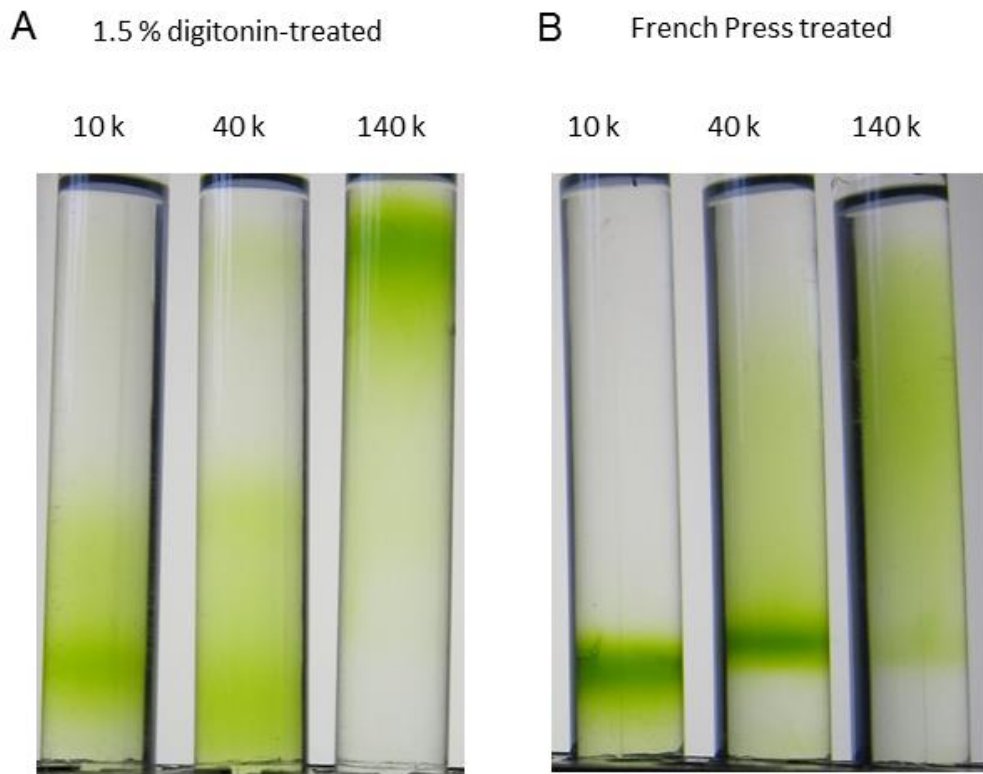


**Figure 3.8. Comparison of fractionation of *Spinacia oleracea* thylakoids by digitonin and French press treatment using differential centrifugation followed by 10-45% sucrose gradient ultracentrifugation.** Thylakoids were incubated with 1.5% digitonin on ice for one hour (A) or were treated with French press (B) and centrifuged at 10 000, 40 000 and 14000 g for 30 minutes, 30 minutes and 60 minutes respectively. The pellets were resuspended in 0.5 ml resuspension buffer and loaded onto 10-45% sucrose gradients before centrifugation at 90 000 g for 60 minutes. Sucrose gradients contain 0.05% digitonin.

#### 3.2.4. Ultrasonication and aqueous two-phase separation.

Thylakoids were fractionated using French Press and ATPS separation. The room temperature absorption spectra revealed a large difference between the grana and stromal lamellae vesicles (Fig. 3.9A). The grana core seemed slightly enriched in PSII compared to grana vesicles and the grana margins seemed slightly enriched in PSII compared to the stromal lamellae vesicles. AFM analysis revealed that the grana vesicles produce slightly flattened membrane vesicles with diameters of 300-500 nm and heights varying widely from 15 nm to > 100 nm when absorbed to a mica surface (Fig. 3.9B,C). However, grana produced using this method were mostly vesicular and, owing to the curvature of these membranes, molecular resolution AFM imaging was unattainable. AFM analysis of the grana margins (Fig 9D) and grana core (Fig 9E) membranes revealed small fragments of membrane on the order of tens of nanometres in diameter.

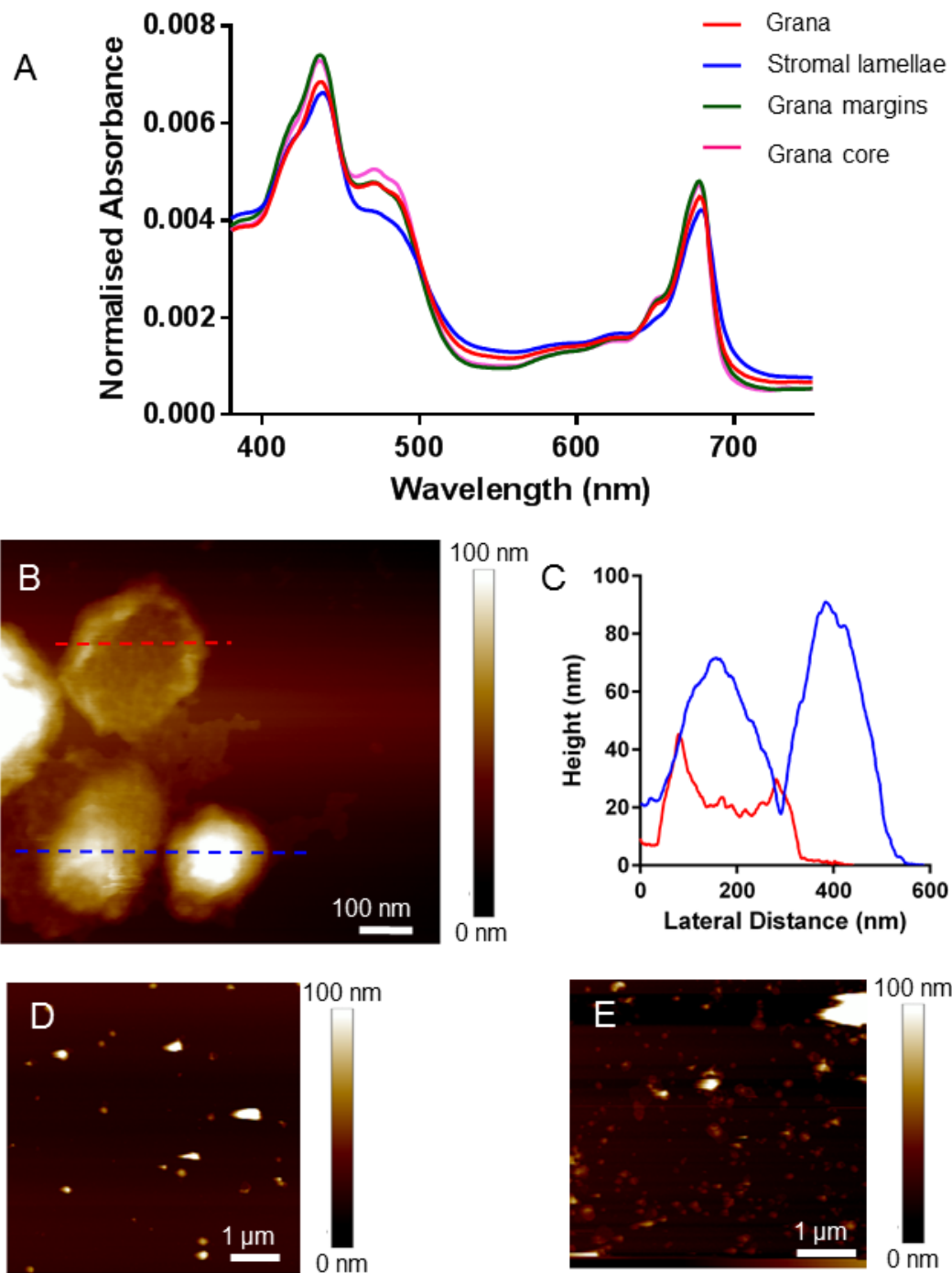


**Figure 3.9. Purification of subthylakoid vesicles from *Spinacia oleracea* by aqueous two-phase system (ATPS) separation and AFM analysis of grana vesicles.** **A.** Room temperature absorption spectra from ATPS fractions. **B.** Example AFM image of semi-appressed vesicles. **C.** Cross section height profiles of appressed (red) and non-appressed (blue) vesicles as indicated by dashed lines in (B). **D.** Grana core **E.** Grana margins

### 3.2.5. Preparation of stromal lamellae membranes from spinach.

Previous AFM studies have revealed much about the organisation of PSII and *cytb<sub>6</sub>f* in the grana (see section 3.1.2). However, comparatively little is known about the organisation of the stromal lamellae (Ruban & Johnson, 2015). Beginning with the protocols outlined in section 3.1.1. and in figures 3.2 and 3.3, I set out to develop a reliable protocol for purifying stromal lamellae membranes for AFM imaging. It was observed that although both the 140 k pellet from the digitonin preparation and the top phase from the ATPS preparation both show chlorophyll fluorescence and denaturing gel characteristics of PSI enriched membranes (i.e. stromal lamellae), neither preparation yielded a sample suitable for AFM. This was due to the membranes being vesicular as opposed to flat, which is a requirement for high-resolution AFM imaging. A method was developed for the purification of stromal lamellae from spinach thylakoids using sucrose gradient ultracentrifugation. Thylakoids were solubilised using a range of digitonin concentrations (0.4 – 2.0 %) in 10 mM HEPES and 5 mM MgCl<sub>2</sub> at 0.5 mg/ml chlorophyll. Unsolubilised material and large grana particles were removed by centrifugation at 16000 g for 30 minutes. The supernatant was then loaded onto a 10 – 45 % sucrose gradient, which was subsequently centrifuged at 270000 g for 2 hours (Fig. 3.10A). The gradients were found to be lacking any specific banding pattern but instead showed a smear from the top to 2.5 cm from the bottom (36 % sucrose). Aliquots were taken from 2.5 cm, 3.5 cm and 4.5 cm from the bottom (36 %, 27 % and 20 % sucrose respectively) and subjected to AFM analysis. The main observations of AFM analysis were that: firstly, the 3.5 cm 27 % aliquot showed the most potential for large flat patches over the range of digitonin concentration in the solubilisation step (Fig. 3.10B-D). Secondly and possibly most dramatically, was the difference in the digitonin concentration of the sucrose gradient: at 0.05 % the AFM images showed vesicular membranes (Fig. 3.10E,F), whereas the membranes were mostly flat when the gradients contained 0.1 % digitonin (Fig 10G). The optimal concentration of digitonin for the solubilisation of the thylakoids was found to be 0.7 %. One issue with this procedure was the fairly low yield of material. Further experiments showed that this procedure could be scaled up to use a higher concentration of thylakoids at 1 mg/ml if solubilisation was carried out using 2 % digitonin. High-resolution imaging of flat stromal lamellae membranes revealed hitherto unidentified particles. An enlarged image (Fig 10H) and cross section height profile (Fig. 3.10I) of a membrane in Fig. 3.10B (indicated by a green box) shows particles  $3.2 \pm 1.8$  nm in height and thought to be the protruding PsaC, PsaD, and PsaE subunits of PSI. Further analysis of the fine structure of these membranes revealed by AFM imaging will be presented in subsequent chapters. Figure 3.11 outlines the recommended protocol for purification of stromal lamellae membranes for AFM imaging. The buffer used (referred to as stromal lamellae buffer) for adsorption to the mica substrate and AFM imaging contained 10 mM HEPES (pH 7.4), 5 mM MgCl<sub>2</sub> and 125 mM KCl. The increased salt concentration

allowed for adsorption using less sample material and for a shorter time period (10 minutes) compared to grana membranes. This was possible because stromal lamellae were found to be less prone to aggregation in salt-containing (particularly  $MgCl_2$ ) buffers.

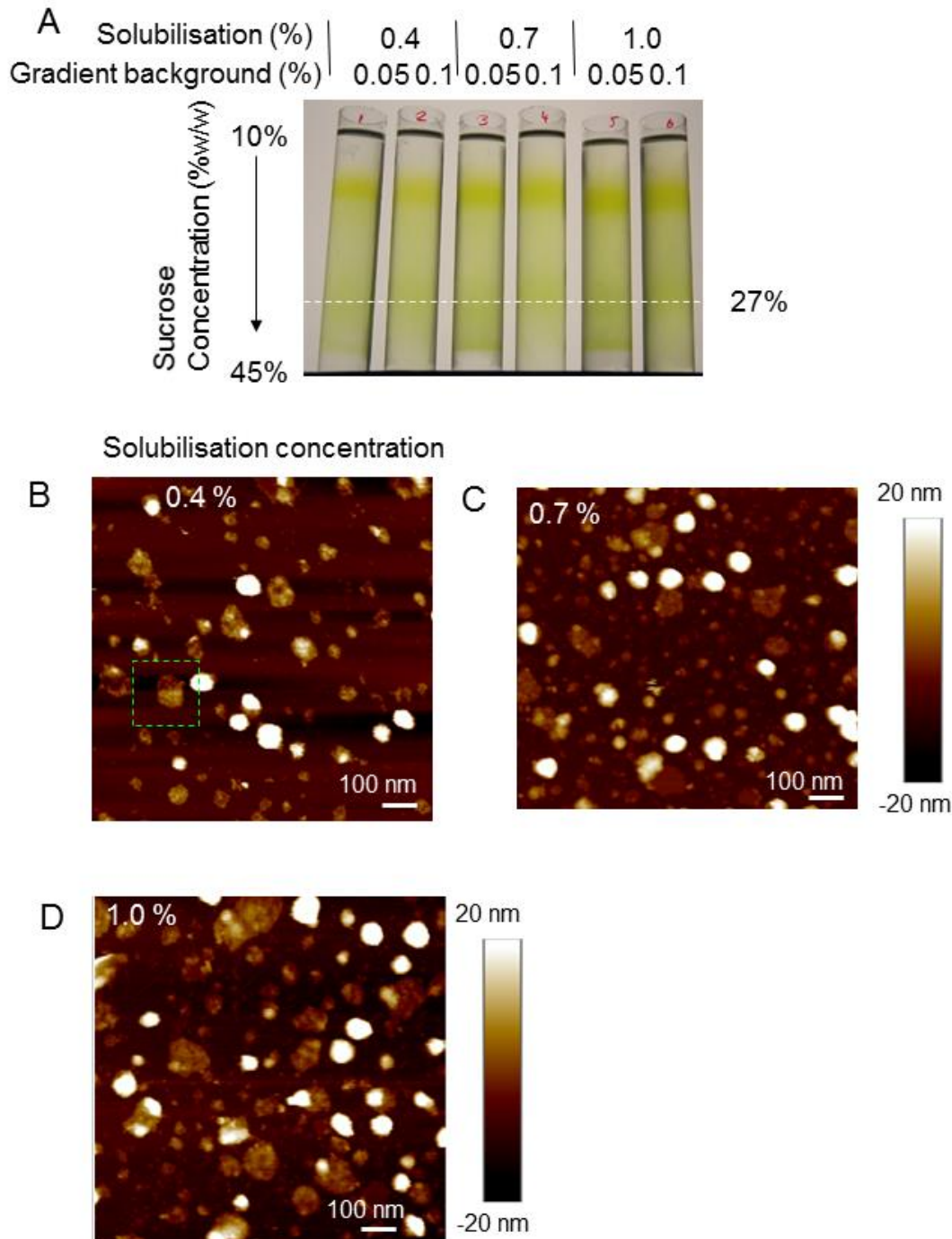


**Figure 3.10. Purification and AFM analysis of stromal lamellae from *Spinacia oleracea*.** **A.** Sucrose gradients showing concentrations of digitonin used in thylakoid solubilisation step and in the gradient itself. Stromal lamellae fraction was taken from 27% sucrose. **B-D,** AFM images of stromal lamellae from thylakoids solubilised at 0.4% (B), 0.7% (C), and 1.0% (D) (background concentration is 0.1% in all).

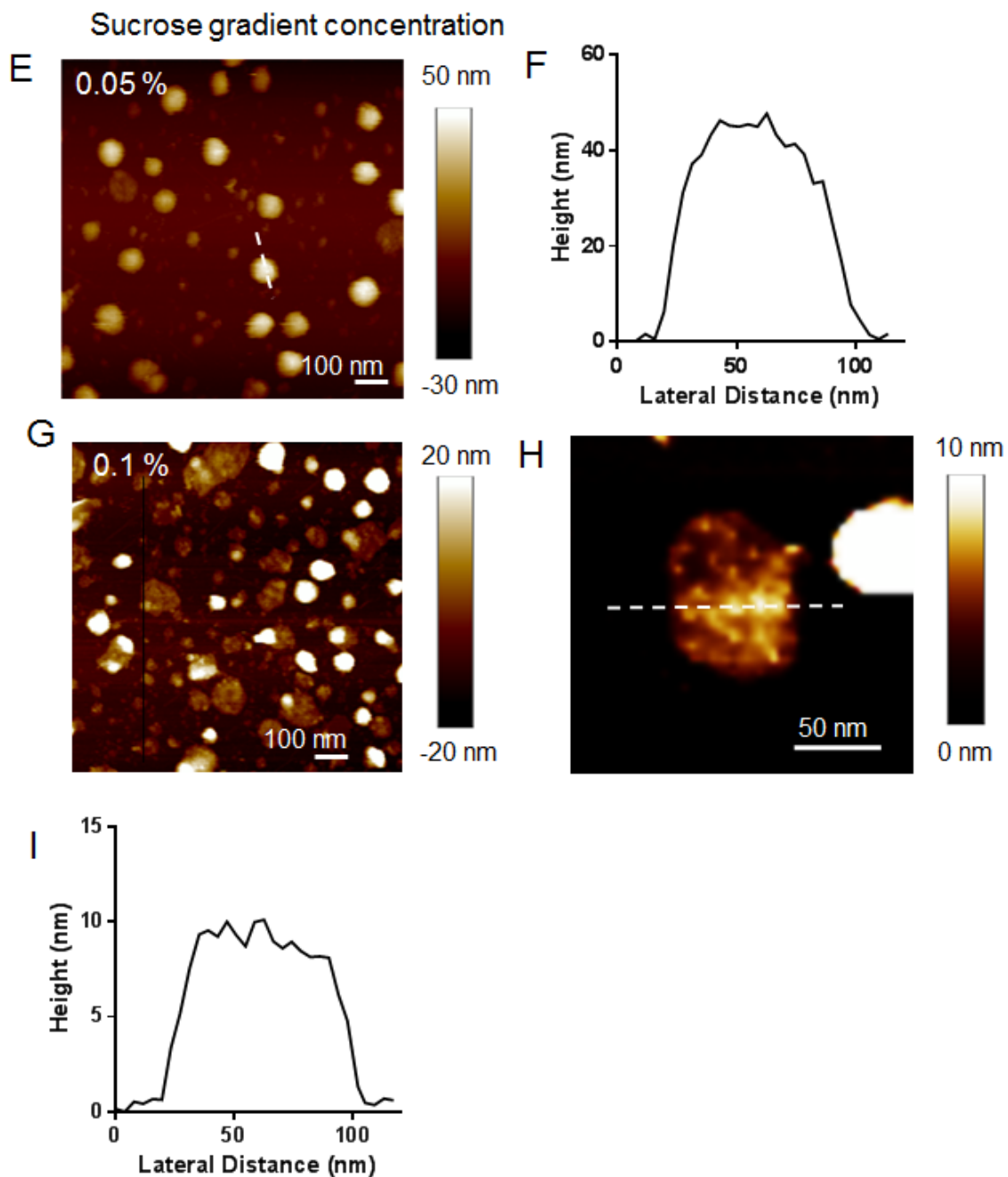


**Figure 3.10 continued. Purification and AFM analysis of stromal lamellae from *Spinacia oleracea*.** E,F. AFM images of stromal lamellae solubilised with 1.0 % digitonin and purified using sucrose gradients containing 0.05% (E) and 0.1% (F) digitonin. G. Enlarged image of highlighted region in B (green square). H. Cross section height profile across white dashed line in (G).

### 3.2.6. Preparation of grana membranes suitable for AFM from *Arabidopsis*.

*Arabidopsis* thylakoids were solubilised over a range of digitonin concentrations and separated by differential centrifugation (Fig. 3.4). In contrast with spinach, the 40 k fraction did not contain double layer grana membranes as revealed by AFM analysis. It was assumed that the 10 k fractions, due to its size and *a/b* ratio of around 2.5, consisted of stacked or partially stacked grana. It was therefore considered that double layer grana membranes suitable for AFM may be obtainable by further mechanical breakage of the 10 k pellet. The 10 k sample was diluted to 5 µg/ml chlorophyll in 10 ml 10 mM HEPES (pH 7.4) and subjected to either 40 % ultrasonication for 2 minutes (high) or 20 % ultrasonication for 1 minute (low) (Fig. 3.12A). A control was included without ultrasonication. To estimate the amount of breakage, the treated sample was passed through 450 µm and 200 µm filters and the concentration allowed to pass through was estimated using absorption at 678 nm. Both low and high ultrasonication resulted in a significant amount of breakage, high resulting in much more than low. For AFM analysis, the 450 µm filtrate was used. This was an effort to reduce the number of very large particles yet retain the double layer grana membranes which have been previously found to pass through 450 µm filters. In the low ultrasonication regime, two species of grana particles were found to exist: single and double layers. This can readily be seen in the cross section height profiles (Fig. 3.12B). Fig. 3.12(C,D) Shows example images of double layer grana membranes. With diameters of approximately 500 nm and heights of 16-20 nm, these are highly similar to those seen previously for grana membranes from spinach (Fig. 3.7). Single-layer grana membranes (Fig. 3.12E,F) were found to be much smaller than the double layer membranes with diameters usually of 200-300 nm. They were also much more irregular in shape. As the high ultrasonication regime contained exclusively single layer membranes it can be assumed that, in the process of the treatment, membranes are progressively broken from stacked grana, to yield double layer grana membranes and single layer membranes. However, even with extremely low sonication conditions (10 % for 15 seconds) the frequency of double layer membranes was found to be very low. An unexpected advantage to imaging single layer grana membranes of their double layer counterparts is that the single layers lie flat on the mica and thus offer an increased contrast of the PSII and *cytb<sub>6</sub>f* protrusions from the membrane surface (Fig. 3.12F). Crystalline regions of PSII-LHCII were observed in single-layer (Fig. 3.13A,B) and double-layer (Fig. 3.13C,D) grana membranes from *Arabidopsis*. The observed unit cell was 20x25 nm with rows intercepting at 65°, forming a parallelogram unit. The dimensions of the unit cell were found to be too large for the C<sub>2</sub>S<sub>2</sub> PSII-LHCII complex (Fig. 3.13E). Instead, the dimensions of the unit cell were more closely in agreement with a C<sub>2</sub>S<sub>2</sub>M<sub>2</sub> PSII-LHCII crystalline domain (Fig. 3.13F) as described by Yakushevskaya *et al.*, (2001).

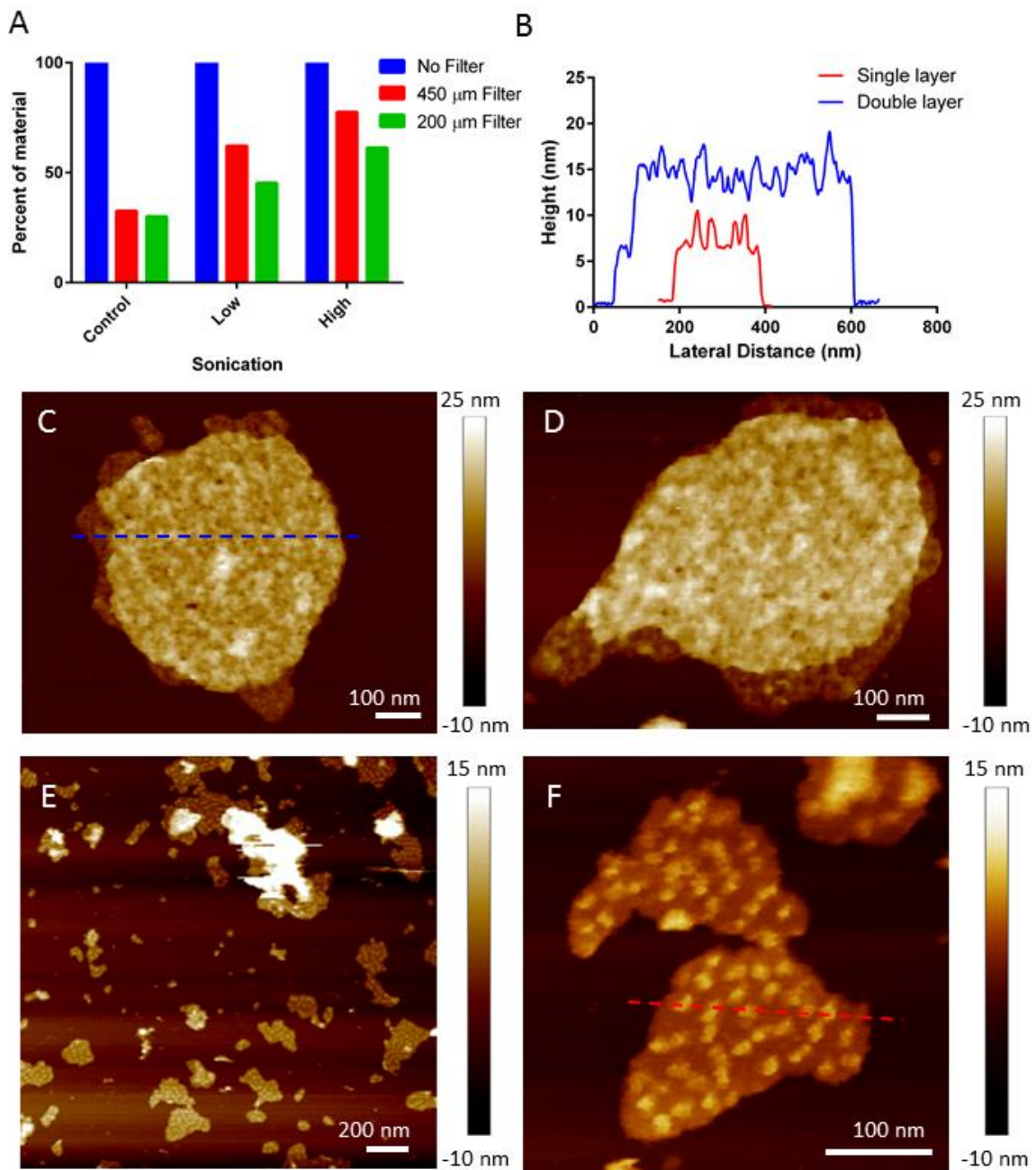


**Figure 3.12. Preparation of grana membranes for AFM from *Arabidopsis thaliana*.** **A.** Treatment of the 10k fraction with sonication results in a greater proportion of material able to pass through 450  $\mu$ m and 200  $\mu$ m filters. **B.** Cross section height profiles of double- (blue) and single-layer (red) grana membranes resulting from the sonication of the 10k fraction (taken from dashed lines in (C) and (F) respectively). **C,D.** Example AFM images of double-layer grana membranes. **E,F.** Example AFM images of single-layer grana membranes.

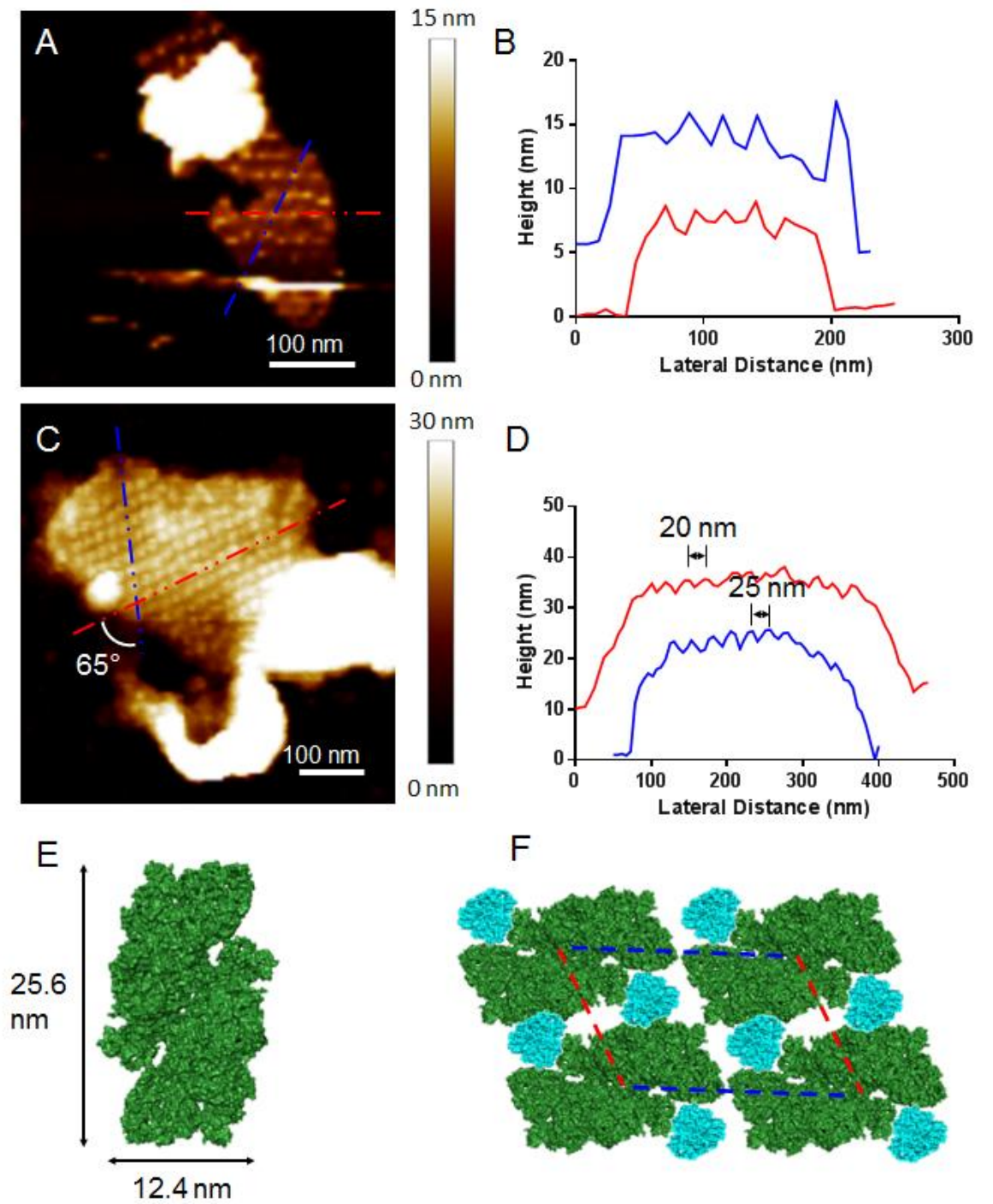


**Figure 3.13. Crystalline regions of PSII-LHCII in AFM images of *Arabidopsis thaliana* grana.** **A.** PSII-LHCII crystalline region in single-layer grana membrane. **B.** Cross section height profile of red and blue dashed lines in **(A)**. **C.** PSII-LHCII crystalline region in double-layer grana membrane. **D.** Cross section height profile of red and blue dashed lines in **(C)**. **E.** Dimension of  $C_2S_2$  PSII-LHCII (PDB: 3JCU). **F.** Model of PSII-LHCII ( $C_2S_2M_2$ ) crystal (20x25 nm). Moderately bound LHCII shown in cyan.

### 3.2.7. Preparation of stromal lamellae membranes from *Arabidopsis thaliana*.

In comparison with the purification of grana from *Arabidopsis*, the purification of stromal lamellae was found to be much less troublesome. Essentially, the same protocol developed for the purification of stromal lamellae from spinach was used (Fig. 3.11) though the yield was higher for *Arabidopsis* than spinach and so had to be diluted more before adsorption to a mica surface for AFM. This is consistent with the observation that *Arabidopsis* produces a higher yield in the 40 k and 140 k fractions (Fig. 3.4B). As with spinach, stromal lamellae membranes from *Arabidopsis* suitable for AFM imaging could be prepared via separation of digitonin-solubilised thylakoids by sucrose gradient ultracentrifugation on a 10-45% sucrose gradient for 2 hours at 90 000 g (Fig. 3.14A). AFM images (Fig. 3.14B,C) and cross section height profiles (Fig. 3.14D) reveal single layer membranes which contain protrusions of approximately 3 nm in height (Fig. 3.14E), as with stromal lamellae from spinach. These protrusions are proposed to be the PsaC, PsaD and PsaE subunits of PSI. In *Arabidopsis*, it was found that the optimum digitonin concentration for obtaining flat stromal lamellae membranes on the sucrose gradient was 0.05%, as opposed to 0.1% in spinach (Fig. 3.10E,F).

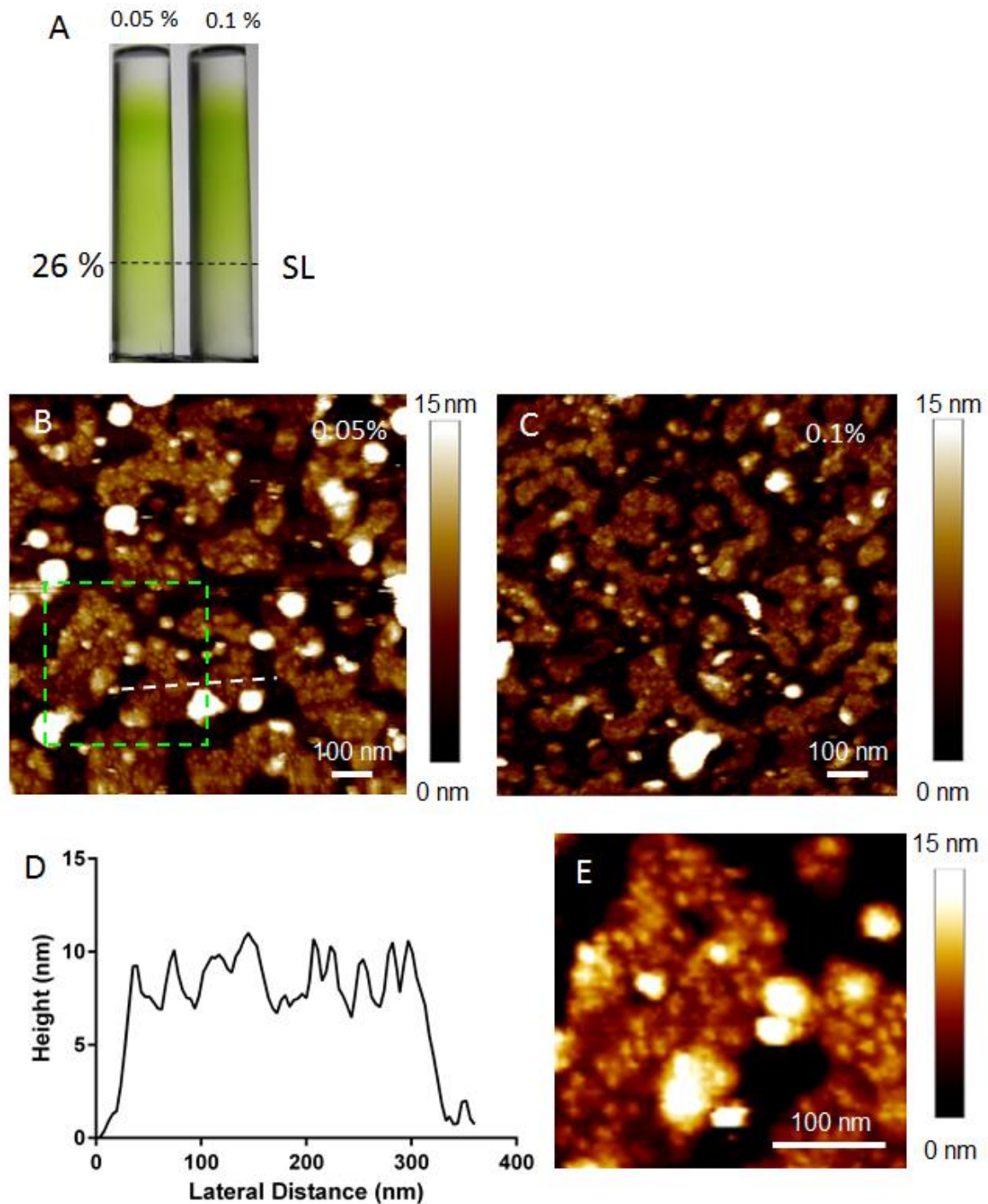


**Figure 3.14. Purification and analysis of stromal lamellae from *Arabidopsis thaliana*.** **A.** *Arabidopsis* thylakoids were pre-treated with 0.7% digitonin and centrifuged at 18000g for 30 minutes. The supernatant was loaded onto 10-45% sucrose gradients containing 0.05 or 0.1 % digitonin ((A) as indicated) and centrifuged at 40 000 g for 2 hours. Fractions taken at 26 % sucrose (3.5 cm from the base of the tube) yielded single-layer membranes. **B.** Example cross section height profile of a single layer stromal lamellae membrane from *Arabidopsis thaliana* (through dashed white line in (C)). **C,D.** Example AFM images of stromal lamellae membranes taken from sucrose gradients in (A) containing 0.05% (C) or 0.1% digitonin. **E.** Magnified image of region highlighted with green box in (B).

### 3.3. Discussion.

#### 3.3.1. Detergent methods of spinach thylakoid fractionation.

It has been shown that grana and stromal lamellae membranes can be obtained using the mild detergent digitonin. There are disadvantages to the use of detergents in the fractionation of thylakoid membranes. Although digitonin has been established as a mild detergent in the context of thylakoid fractionation compared to others such as TRITON X100 or  $\alpha$ -DDM, it has been shown that 1-1.5% digitonin will solubilise around 20-25% of chlorophyll-binding thylakoid protein complexes (Greico *et al.*, 2015). Therefore, care should be taken in AFM analysis especially when inferring the stoichiometry of protein complexes. Johnson *et al.* (2014) demonstrated that using  $\alpha$ -DDM to fractionate spinach thylakoids resulted in the loss of *cytb<sub>6</sub>f*. Indeed, it was found that replacing the 0.05% or 0.1% digitonin in sucrose gradients with TWEEN-20 caused small holes to appear in grana membranes (Fig. 3.15). It has been observed that TWEEN-20 will solubilise *cytb<sub>6</sub>f* (Webber *et al.*, 1988) and it may be the case therefore, that the holes are created by the removal of *cytb<sub>6</sub>f* by TWEEN-20 from the grana membranes, as is the case with  $\alpha$ -DDM treatment. Note that the holes in the membranes of Fig. 3.15 seem to be homogeneously distributed throughout the grana membrane. This is in agreement with *cytb<sub>6</sub>f* being homogeneously distributed among PSII in the grana (Johnson *et al.* 2014).

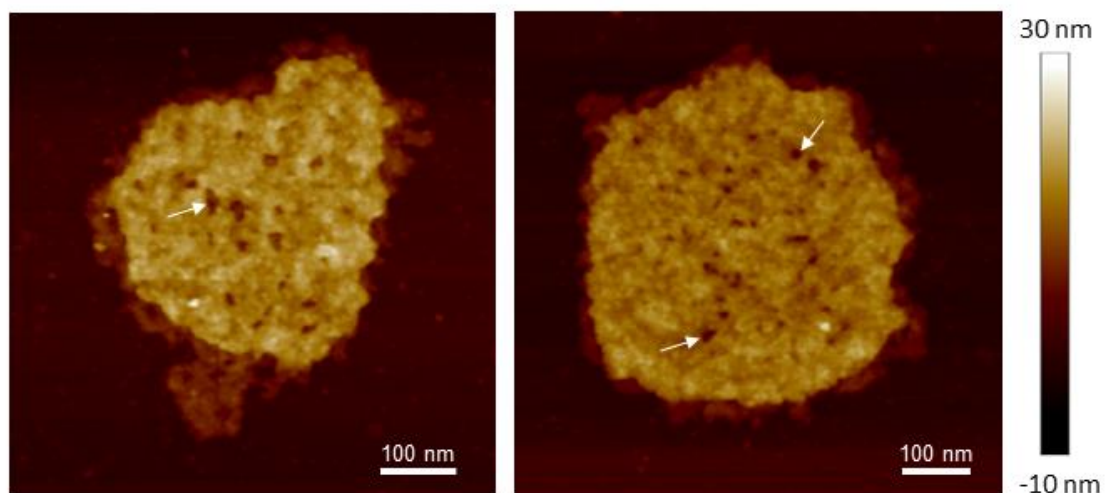


**Figure 3.15. AFM images of grana membranes from *Spinacia oleracea* prepared with 10-45% sucrose gradients containing 0.05% TWEEN-20.** Examples of holes in the grana membrane as a result of TWEEN-20 solubilisation are indicated by white arrows.

### 3.3.2. Stromal lamellae.

Recall from (Fig. 3.4C,E) that the 10 k fraction decreases in both quantity and Chl *a/b* with increased concentrations of digitonin. This supports the proposition that digitonin acts to remove the stromal lamellae from the grana and that the stacking and high protein density of the grana resists the action of digitonin.

In *Arabidopsis*, stromal lamellae produced by sucrose gradient ultracentrifugation in the presence of 0.05% digitonin (Fig. 3.9C) were found to be larger or more intact than those produced in the presence of 0.1% digitonin. In contrast, stromal lamellae from spinach were purified in a sucrose gradient containing 0.1% digitonin. This suggests that *Arabidopsis* thylakoids, or the stromal lamellae therein are more sensitive to the effects of digitonin and are therefore further solubilised by 0.1% digitonin in the sucrose gradient. Given that a question often asked is: “How is it that having solubilised thylakoids using 1% digitonin, a change in the concentration of digitonin in the sucrose gradient from 0.05% to 0.1% makes any difference at all” I will propose an explanation. The supernatant of the solubilised thylakoids after the initial centrifugation at 18 000 g, (i.e. that which is loaded onto the sucrose gradient) was subject to AFM analysis. It was found that this fraction consisted of lipid, maybe from plastoglobules, lipid vesicles that are associated with the stromal surface of the thylakoid (Austin *et al.*, 2006). One may argue that lipids, may be separated from the thylakoid membranes within the sucrose gradient. This would increase the local ratio of digitonin to thylakoid lipid and therefore amplify the effect of digitonin in the sucrose gradient. Another, factor that may play an important role is the shear force imposed on the thylakoid membranes as they move through the gradient.

### 3.3.3. PSII crystalline regions.

PSII crystalline regions have been observed in EM and AFM images of grana membranes. The extent to which they are present depends on growth conditions and purification conditions. Although PSII crystalline, regions have been seen in AFM images of grana membranes, it has often been in situations in which the integrity of the membrane has been compromised. For example, by drying (Onoa *et al.*, 2014) or the use of detergents such as  $\alpha$ -DDM (Sznee *et al.*, 2011) which is known to solubilise *cytb<sub>f</sub>* (Johnson *et al.*, 2014). Computational modelling of the thylakoid membrane suggested that interlayer interactions between the stromal faces of LHClI may mediate PSII crystallisation (Schneider & Geissler, 2013). Here, however, PSII crystallisation has been observed in single layer membranes where

intermembrane interactions are non-existent. No PSII-LHCII crystalline regions were observed in AFM images of spinach grana.

### **3.4. Conclusion.**

Using AFM, one can image biological material in liquid at room temperature and pressure at a resolution which allows the identification of individual protein complexes. However, a highly pure and often a very flat sample is required. For this reason, the development of purification protocols is generally of high importance for AFM studies and make up the majority of the work in such endeavours. In this chapter, protocols have been developed and optimised for the purification of grana and stromal lamellae membranes from both spinach and *Arabidopsis*, which will serve as a gateway for further AFM research of photosynthesis. The main criteria for evaluating the effectiveness of the protocols described in this chapter was their ability to yield flat membranes amenable to AFM. The concentration of digitonin seemed to be the most important variable in this respect, treatment of thylakoids (at 0.5 mg/ml) required 2% and 1% digitonin to produce flat membrane patches of grana and stromal lamellae respectively. The minimum concentrations of digitonin required to produce flat membranes were used in order to reduce the risk of over-solubilisation and loss of proteins from the membranes. Of greatest importance in this chapter is the development of a protocol for the purification of single-layer stromal lamellae membranes which allowed the native membrane organisation of PSI-LHCI to be imaged for the first time.

## Chapter 4.

# The nanoscale organisation of stromal lamellae thylakoids from *Spinacia oleracea*

### Summary

AFM images of grana membranes from spinach have revealed the organisation of PSII and *cytb<sub>6</sub>f* in the grana, however, comparatively little is known about the organisation of PSI in the stromal lamellae. This is, in part, due to the difficulty of purifying flat stromal lamellae membranes suitable for AFM imaging. In the previous chapter, a method was developed for the purification of stromal lamellae membranes. Putative PSI complexes were visible as approximately 3 nm protrusions from the membrane surface.

Further investigations revealed that the putative PSI particles closely resemble those predicted by the crystal structure (PDB: 4Y28). Furthermore, the 3 nm gap between the bottom side of the stromal lamellae membranes and the mica substrate they are adhered to suggests the presence of *cytb<sub>6</sub>f*, consistent with the consensus that *cytb<sub>6</sub>f* is homogeneously distributed throughout the thylakoid membrane. Unexpectedly, PSI was observed to form a dimeric arrangement, mediated by core to core contacts, 25.5% of the time. The prevailing consensus has historically been that PSI is monomeric in plants. However, recently, a structure of the PSI dimer has been observed in cryo-EM single-particle analysis (Yadav *et al.*, 2017) with a PsaC to PsaC distance which is consistent the PSI dimer described in this chapter. It was also observed that the proportion of stromal lamellae membranes devoid of protein is much greater than that of grana membranes and it is possible that this allows for more space for protein complexes to diffuse within the stromal lamellae.

The presence of intact ATP synthase was confirmed in stromal lamellae, however, the height of putative ATP synthase particles was much shorter than those predicted from the cryo-EM structure (PDB: 5ARA). Crucially, *Bos taurus* ATP synthase incorporated into DOPC liposomes showed the same height and width as ATP synthase in stromal lamellae. This was interpreted as strong evidence for the positive identification of ATP synthase. It was proposed that the reason for the discrepancy between the predicted and observed heights may be due to a reversible deformation of ATP synthase under the stress of the AFM tip.

Finally, we discuss the significance of the grana/stromal lamellae interface, the point of contact between the grana and the stromal lamellae. AFM images of grana occasionally showed that regions of stromal lamellae remain attached to the grana. Using information gleaned from previous AFM studies of grana and stromal lamellae individually, these contiguous membranes allow for the construction of a model of the thylakoid membrane system. This model incorporates strict separation of PSII and PSI and will be used to simulate LEF in a later chapter.

## **4.1. Introduction.**

### **4.1.1. The macroscale structure of the thylakoid membrane.**

Early EM images of freeze-fractured chloroplasts revealed the thylakoid membrane to consist of cylindrical stacks of appressed membranes called grana and stromal lamellae membranes which emanate from the grana (Wettstein, 1961, Wehrmeyer, 1964). The principle of lateral heterogeneity, the partitioning of PSII and PSI into the grana and stromal lamellae respectively, was established by the fractionation of thylakoids using detergents (Anderson & Boardman, 1964) and French Press (Andersson & Anderson, 1980). It was observed that depleting thylakoids in solution of divalent cations (most notably  $Mg^{2+}$ ) simultaneously decreased the yield of PSII Chl *a* fluorescence and increased the yield of PSI Chl *a* fluorescence at 77k (Murata *et al.*, 1970). This is due to excitation energy spillover: because PSI is a faster energy trap than PSII, excitations will more likely terminate with PSI if PSII and PSI are in close proximity. The observation of spillover in cation depleted thylakoids was found to result from grana unstacking (Gross & Prasher, 1974) which allows for mixing of PSII and PSI (Staehelin, 1976). This, of course, suggests that the thylakoid structure is responsible for maintaining lateral heterogeneity. Indeed, the surface charges of PSII-LHCII are effectively screened by the concentration of  $Mg^{2+}$  present in the chloroplast but those of PSI-LHCI are not (Barber, 1982). Cryo-EM tomography reveals the structure of the thylakoid membrane in three dimensions (Austin & Staehelin, 2011). The thylakoid is comprised of a cylindrical stack of grana with the stromal lamellae wrapped helically around them. At each grana layer, the stromal lamellae contact the grana at openings called 'junctional slits', which allow the passage of soluble molecules in a shared luminal space. It has been observed that the luminal space of the grana will expand in the light and contract in the dark (Kirchhoff *et al.*, 2011), which may control the restricted diffusion of PC within the crowded grana lumen.

### **4.1.2. The organisation of protein complexes within the thylakoid membrane.**

The biochemical evidence for lateral heterogeneity was supported by the observations made using EM techniques. Arntzen, Dilley and Crane (1969) revealed two populations of particles, a population of large particles and one of small particles, within EM images of freeze-etched thylakoid membranes which were spatially separate but came into contact at clearly defined boundaries. Crucially, only the larger particles were present in the so called heavy fraction known to be enriched in PSII activity and this was taken as evidence that the large particles were indeed PSII. Using French Press, which breaks the thylakoids in much the same way as digitonin but instead uses mechanical force to cause the breakage, Sane, Goodchild and Park (1970) showed that the method retains the stacked structure of

the grana after breakage to a much greater extent than digitonin. This allowed them to associate the heavy fraction, enriched with PSII, with the stacked grana and the PSI enriched lighter fraction with the non-stacked stromal lamellae regions (Goodchild & Park, 1971). A developing picture of the thylakoid membrane was at this point materialising with the stacked grana containing mostly PSII and some PSI and the stromal lamellae which contained PSI and ATP synthase with a small amount of PSII (Andersson and Anderson, 1980).

Freeze-fracture EM (FFEM) on thylakoids continued to be the predominant method of study of the thylakoid structure throughout the 1970's and 1980's. In the literature of the time PSII particles were often referred to as EF particles. This is because they were mainly found on the exoplasmic face (EF) of the stacked thylakoid regions, where biochemical studies showed most PSII was found. Similarly, PSI particles were referred to as PF particles as they were mainly found on the protoplasmic face (PF) of the unstacked thylakoid membrane regions (Staehelin *et al.*, 1976). FFEM studies on thylakoids fractionated by French Press and aqueous two-phase separation (ATPS) (Anderson *et al.*, 1978) and studies on barley mutants devoid of PSI and PSII confirmed these assignments (Simpson, 1982). Higher resolution freeze-etch EM images showed structural details of the EF/PSII particles. The particles were 17.5 nm by 10.2 nm (Simpson, 1978) and were dimeric: the particles were split down the middle, perpendicular to the long axis (Simpson 1986). Simpson 1986, established that the luminal protrusion of the EF PSII particles contained the oxygen evolving machinery. This was because removal of the extrinsic luminal polypeptides of PSII in both thylakoids and bottom phase ATPS vesicles resulted in loss of oxygen evolving capability. These observations were confirmed with the emergence of the first structure of the PSII supercomplex using EM and single-particle averaging (Boekema *et al.*, 1995). The PSII supercomplex was found to be formed of two monomers, each of which contain one core in which the oxygen evolving complex and electron transfer machinery is housed, light harvesting complexes CP24, CP26, and CP29 as well as an LHCII trimer. The number of LHCII trimers associated with the PSII supercomplex varies from 2 as described above (The  $C_2S_2$  supercomplex with two cores and two strongly bound reaction centres) to 6 (The  $C_2S_2M_2L_2$  supercomplex containing 2 cores, two strongly bound LHCII, two moderately bound LHCII and two loosely bound LHCII) (Boekema *et al.* 1999).

The organisation of  $Cytb_6f$  has been contested using various methods of thylakoid fractionation. Thylakoid membranes fractionated using digitonin (Boardman & Anderson, 1967) and French Press (separated using ATPS) (Cox & Andersson, 1981; Anderson, 1982) suggest that  $cytb_6f$  is homogeneously distributed throughout both the grana and the stromal lamellae. On the other hand, grana membranes produced using TRITON-X100 (Berthold *et al.*, 1981) or  $\alpha$ -DDM (van Roon *et al.*, 2000) were found to be devoid of  $cytb_6f$ . Immunolabelling EM studies (Allred & Staehelin, 1985, Hinshaw & Miller, 1993)

support the former scenario, wherein *cytb<sub>6</sub>f* is homogeneously distributed throughout the thylakoid. The presence of *cytb<sub>6</sub>f* within grana membranes produced using digitonin has been confirmed using affinity-mapping AFM (Johnson *et al.*, 2014).

At the edge of the grana lies a highly-curved region known as the grana margin (Anderson, 1989). The high curvature of the grana margins either facilitates or is the result of the thylakoid folding which leads to grana stacking. The composition and functionality of this region is still highly contested. Due to the high curvature of the grana margins Murphy (1982) suggested that they may lack proteins entirely. The first attempt to elucidate the protein components of the grana margin saw the use of the detergent TWEEN-20 (Webber *et al.*, 1988) which was found to preferentially solubilise the grana margins. Upon removal of the grana and stromal lamellae by centrifugation, the authors assumed the material left in the supernatant, which contained *cytb<sub>6</sub>f*, PSI and ATP synthase, were derived of the grana margins. Wollenberger *et al.* (1994) asserted that grana margins could be obtained from grana vesicles prepared by French Press and ATPS. Further sonication of the grana vesicles and ATPS results in a PSII enriched grana core with a chl *a/b* of 2.3 and a grana margins fraction with a chl *a/b* of 2.6. This fraction made up 12% of the total thylakoid membrane and was enriched in PSI. Importantly PSI in the grana margins was found to have 10-15% larger antenna size than PSI in the stromal lamellae (though PSI in the grana was found to have an antenna size 40% higher than that of the grana margins). The PSI of the grana margins was proposed to be primarily involved with LEF (Wollenberger *et al.*, 1995 Albertsson). Nevertheless, recent structural studies on thylakoid membranes using cryo EM support the view that the highly-curved margins are devoid of protein (Daum *et al.*, 2010) and moreover no transitional region containing both PSI and PSII was ever observed in the plethora of FFEM data either (e.g. Staehelin, 1976).

In comparison with the grana, the organisation of the stromal lamellae is less well-known. Biochemical evidence has shown it is enriched in PSI (Boardman *et al.*, 1966, Andersson & Anderson, 1980). Likewise, ATP synthase is found solely in the non-appressed regions (Miller & Staehelin 1976, Allred & Staehelin 1985). Both are likely to be excluded from the appressed grana regions as they have extramembrane subunits which protrude on the stromal side and therefore physical restrict access. AFM images of 2-D crystals of PSI reveal that the subunits PsaC, PsaD and PsaE protrude into the stroma approximately 3.5 nm (Fotiadis *et al.*, 1998). These extrinsic subunits were easily removable by the force incurred on them by the AFM tip during imaging. Furthermore, increasing the force with which the tip interacted with the sample increased the rate of removal of these subunits. Historically, AFM imaging of chloroplast ATP synthase has been restricted to either the F<sub>0</sub> C-ring (Seelert *et al.*, 2000, Seelert *et al.*, 2003) or intact (F<sub>0</sub>F<sub>1</sub>) ATP synthase reconstituted intact lipid bilayers (Neff *et al.*,

1997) which were observed to protrude  $10 \pm 3$  nm from the lipid surface. To date, chloroplast ATP synthase has not been imaged in its native stromal lamellae environment. Due to the lack of contrast observed of stromal lamellae in EM and having previously no protocols for purification of stromal lamellae for AFM, little is still known of the nanoscale organisation of these complexes. In this chapter, using methods developed in chapter 3, the nanoscale structure of stromal lamellae from *Spinacia oleracea* was investigated.

## 4.2. Results.

### 4.2.1. Identification of particles in stromal lamellae.

AFM images of stromal lamellae membranes were analysed. Alongside images acquired by the author, several images were provided courtesy of Matthew Johnson and Craig MacGregor-Chatwin (Fig 4.1). These were included in the analyses described in this chapter. Several types of extrinsic membrane protrusions are visible in the AFM images of stromal lamellae thylakoids. The major class was  $\sim 3$  nm nanometres in height (Fig 4.2A), while less numerous larger  $\sim 7$  nm (Fig 4.2B, Fig 4.1 green arrows) and smaller  $\sim 1$  nm features are also observed (Fig 4.2C, Fig 4.1 magenta arrows). Using Gwyddion software, the heights of these protrusions were measured from the membrane surface: the height peak of the protrusion minus the height at the nearest point the membrane is flat (Fig 4.2A arrow\*). Producing a histogram of the heights of protrusions of stromal lamellae revealed two distinct peaks (Fig 4.2D):  $3.2 \pm 0.8$  nm and  $7.4 \pm 1.6$  nm ( $n=277$ ). The two populations correspond to protrusions shown in the cross sections of Fig 4.2A and 2B respectively. The 1 nm protrusions shown in Fig 4.2C occur too infrequently to form a separate peak in Fig 4.2D. Further analysis of the protrusions corresponding to the 3.2 nm peak in Fig 4.1D reveal that these protrusions reach a height from the mica substrate of  $10.2 \pm 0.6$  nm (Fig 4.2E) and have a width of  $8.9 \pm 1.5$  nm (Fig 2F). It was proposed, due to the size of the particles and the density in the membrane, that the 3.2 nm protrusions correspond to the PsaC, PsaD and PsaE subunits of PSI. The observed height of  $3.2 \pm 0.8$  nm ( $h_1$  in Fig 4.2G) was found to match that of the PsaC, PsaD and PsaE subunits of PSI, as measured in PyMol, which protrude 3.2 nm into the stroma ( $h_2$  in Fig 4.2G). However, the height from the mica surface ( $10.2 \pm 0.6$  nm,  $h_3$  in Fig 4.2G) did not correspond with the height of PSI measured in PyMol at 8.2 nm ( $h_4$  in Fig 4.2G). This may be due to the protrusions on the luminal side of the stromal lamellae. Indeed, the stromal lamellae is known to contain *cytb<sub>6</sub>f* and PSII (Anderson and Andersson, 1980), each of which are known to protrude by 3.1 nm and 4.1 nm (Chapter 3 figure) respectively. Analysis of the PSI structure in pymol reveals that it may protrude up to 1 nm into the lumen ( $h_5$  in Fig 4.2G). Previous studies have shown that the stromal lamellae membrane itself is 4 nm across ( $h_6$  in Fig 4.2G) (Daum *et al.*, 2010). Subtracting the heights of the PSI stromal protrusions and the height of the stromal-protruding subunits and the membrane width from the observed height from the mica, it was calculated that the membrane is, on average, elevated approximately 3 nm from the mica surface. This is in agreement with the height of the luminal protrusions of *cytb<sub>6</sub>f* ( $h_7$  in Fig 4.2G). It was proposed therefore the observed height of stromal lamellae membranes was due elevation by *cytb<sub>6</sub>f*. However, due to lack of topology on the stromal face of *cytb<sub>6</sub>f* it was not possible to explicitly determine their location within the membrane by AFM. The ratio of *cytb<sub>6</sub>f* to PSI was calculated using

absorption spectroscopy to be  $0.31 \pm 0.05$  and thus may be present in significant frequencies to elevate the membrane as described.

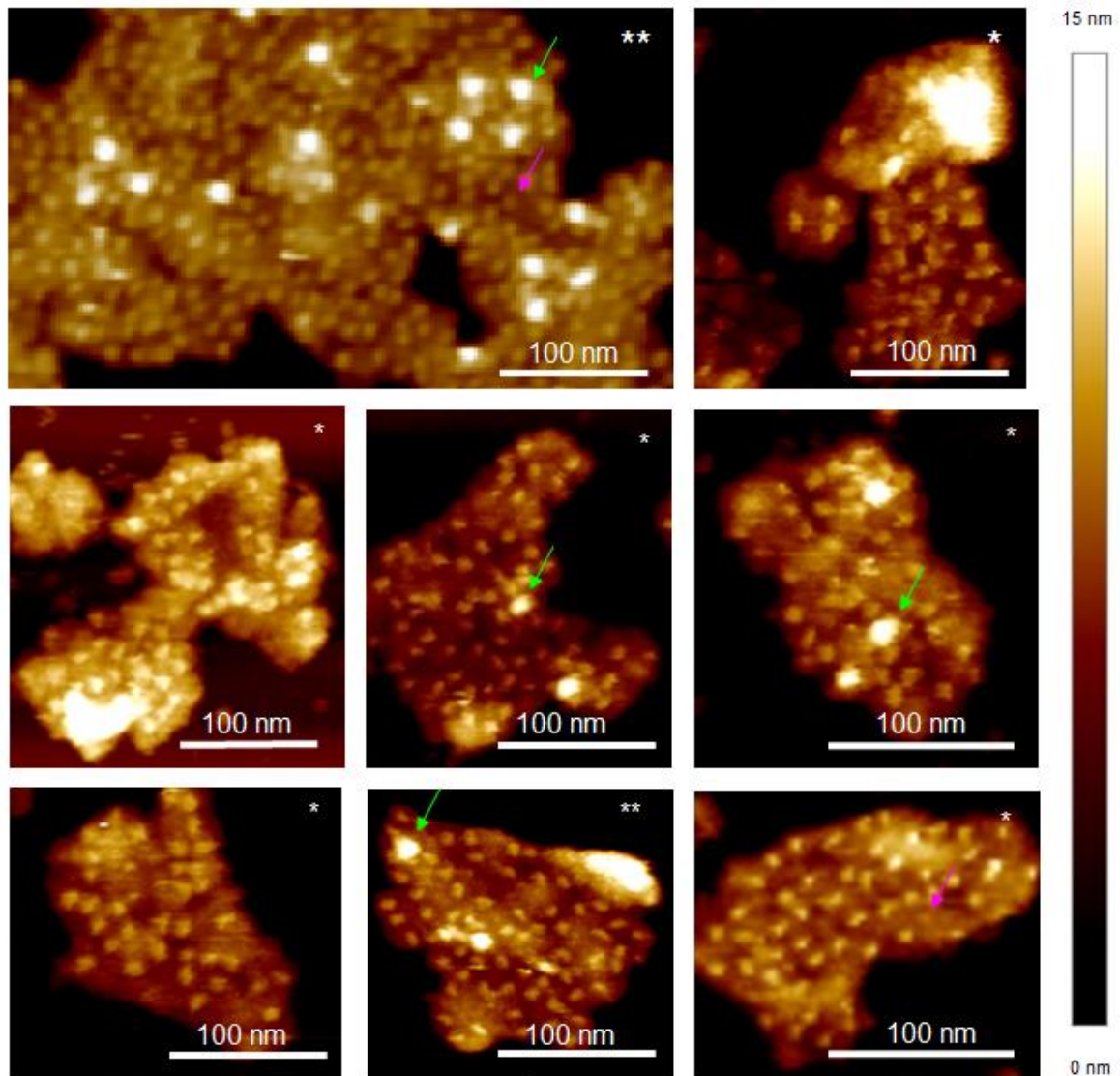


**Figure 4.1.** Gallery of AFM images of stromal lamellae from *Spinecea oleracea* courtesy of Matthew P. Johnson (\*) and Craig Macgregor-Chatwin (\*\*) for the purpose of statistical analysis of the dimensions and organisation of PSI. Larger protrusions highlighted with green arrows. Putative *cyt b<sub>6</sub>/f* particles highlighted with pink arrows.

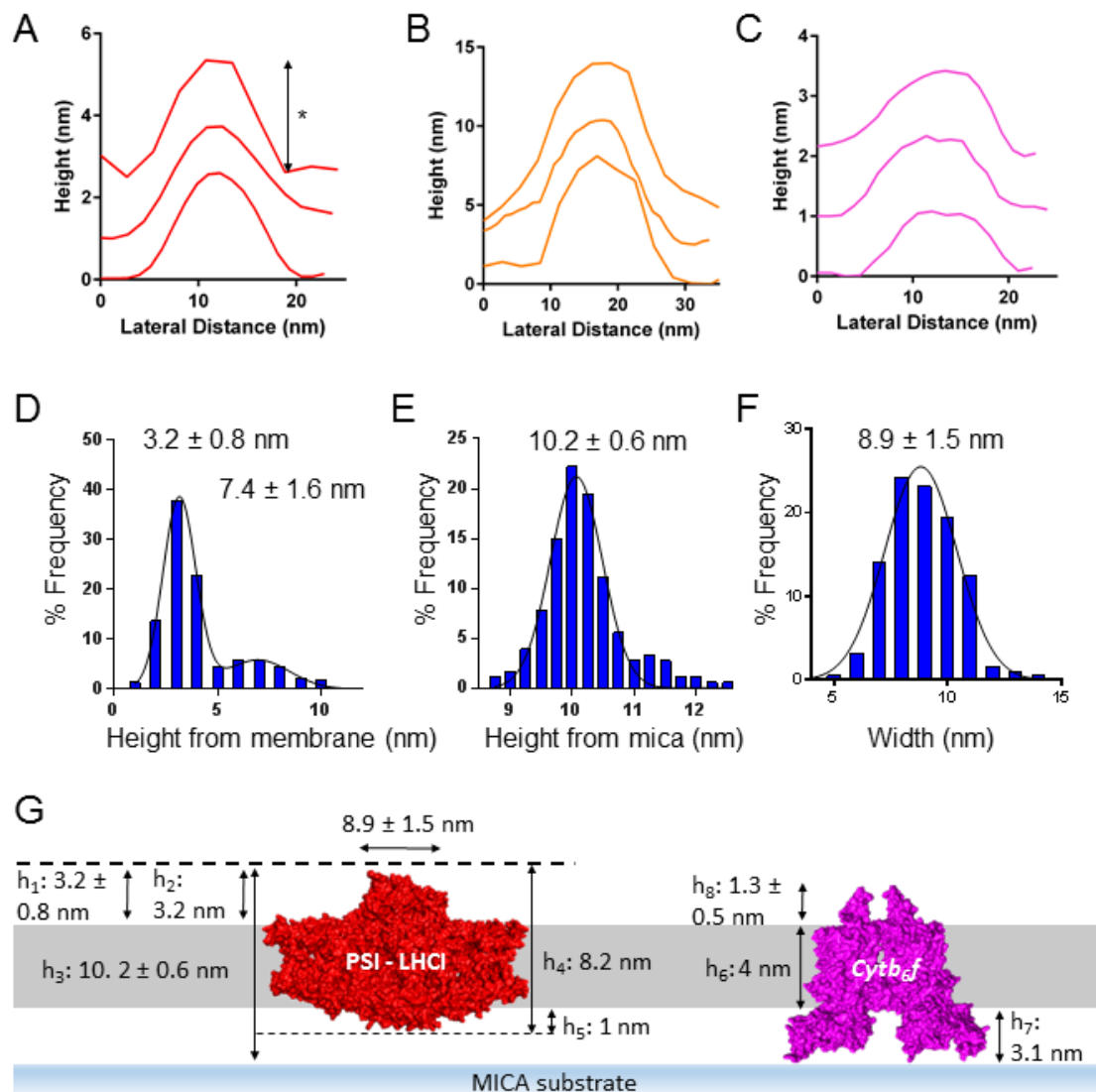


**Figure 4.2. Analysis of the heights of protrusions from the surface of stromal lamellae membranes reveals two populations of particles, one of which can be identified as PSI.** A-C. Cross section height profiles of the most frequently observed protrusions at approximately 3 nm (A), 7 nm (B) and the less frequent protrusions observed at 1 nm (C). D. histogram of the heights of protrusions from stromal lamellae membrane with double-Gaussian fit. Each Gaussian shows mean and standard deviation (n=277). E. Heights from the mica substrate of the smaller particles (mean 3.2 nm in (A)) showing mean and standard deviation of a Gaussian fit. F. Width (lateral size) of the 3.2 nm protrusions. G. The 3.2 nm protrusion resembles the dimension of PSI (PDB: 4Y28) although the 10.2 nm height from the mica suggests that there is a gap between the membrane and the mica substrate. This gap, calculated to be around 3.1 nm, is proposed to be due to the luminal protrusions of *cytb<sub>6</sub>f*.

#### 4.2.2. PSI damage in AFM imaging.

During PSI imaging, PSI complexes were becoming irreversibly damaged upon contact with the AFM tip. Fig (4.3A) shows four consecutive AFM images wherein stromal lamellae membranes can be seen. Three membranes were chosen and are highlighted with boxes, each with a unique colour so the membranes can be identified in subsequent images. Enlarged versions of the highlighted membranes show that, in the first image of each membrane (image 1 for blue and green, image 2 for red), protrusions previously evidenced to be the stromal subunits of PSI are clearly visible. However, over 2 or 3 scans the protrusions seem to vanish from the membrane. Crucially, the membrane highlighted in red appears only in image 2 and is seen to be of high resolution. At this point the membranes highlighted in blue and green have already decreased significantly in resolution. From this, one can infer that the vanishing of the protrusions over multiple scan is not due to changes in the properties of the AFM (tip contamination or blunting for example) and is likely to be due to damage to the PSI complex. For this reason, AFM imaging of stromal lamellae membranes should be carried out at low peakforce setpoint (the force at which the AFM tip is brought into contact with the sample). It may be the case that, because the PsaC, PsaD and PsaE subunits of PSI do not contain integral membrane domains, these subunits are simply knocked off the rest of the complex by the AFM tip. Treatment with glutaraldehyde, a cross-linking agent, was added to the stromal lamellae membrane solution before or after the membranes had been adsorbed to the mica surface to cross link the extrinsic PSI subunits to the PSI core. It was hoped that this would make them more resistant to the force of the AFM but was found to be counterproductive for two reasons. Firstly, it was found that the treatment resulted in the appearance of large particles on the stromal lamellae, most likely particles previously in solution that had been cross linked to the membranes. Secondly, the mica surface was found to become coated with glutaraldehyde, making the AFM tip more prone to contamination.

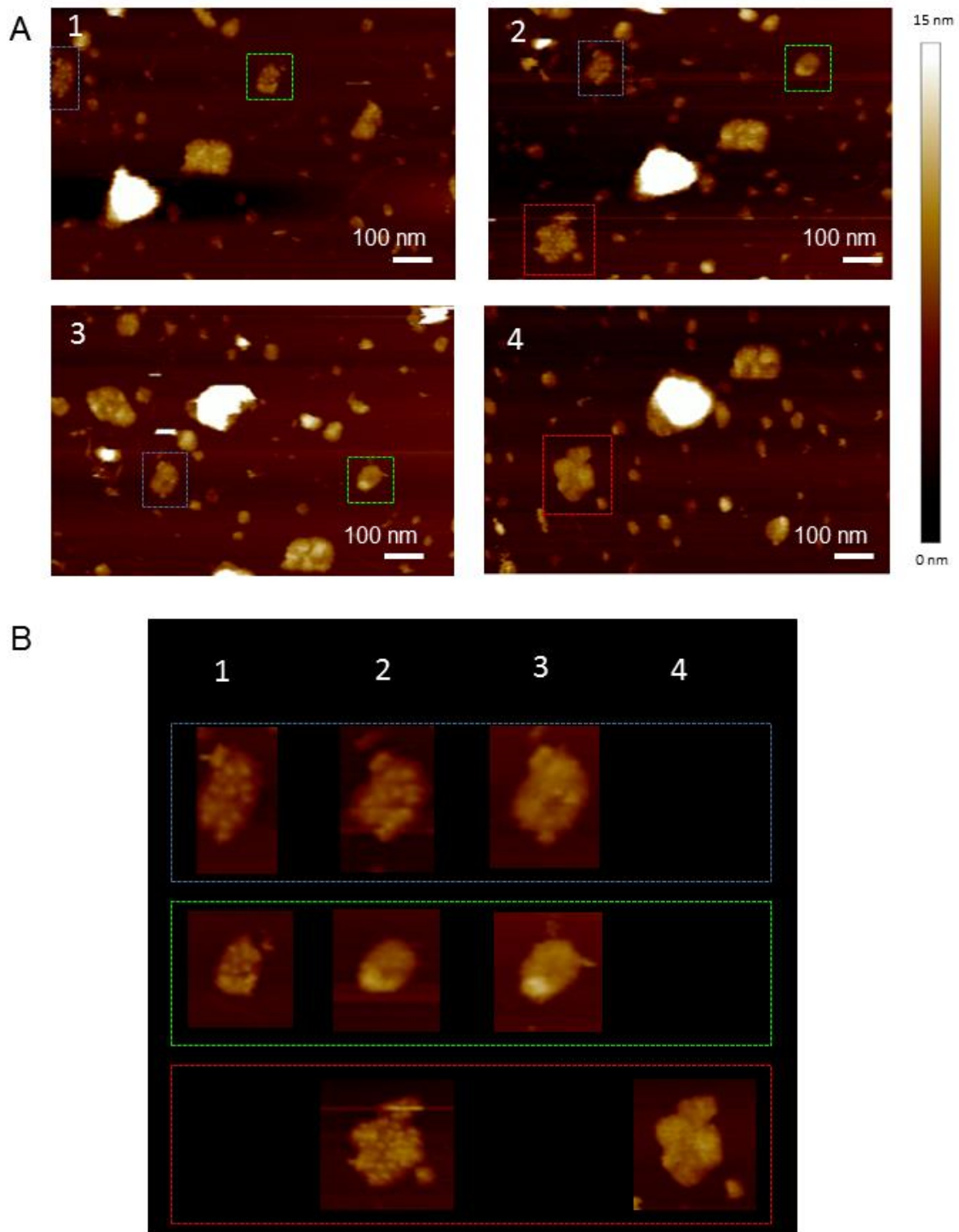


**Figure 4.3. AFM imaging damages PSI over multiple scans.** **A.** Four consecutive scans of an area containing stromal lamellae membranes. Membranes wherein PSI complexes are clearly visible in the first instance are highlighted in blue green and orange boxes and tracked over the subsequent scans. **B.** Highlighted membranes appear to lose their protruding subunits over 2-3 scans, thus indicating damage to PSI complexes.

### 4.2.3. Automated PSI identification in stromal lamellae.

The organisation of PSI in the stromal lamellae was investigated. Due to the large number of particles, manual extraction of the coordinates of each PSI particle was found to be time consuming. Instead, the aim was to automate the process of extracting the x-y coordinates of PSI within AFM images of stromal lamellae membranes (Fig 5). Fig 4.4A shows a cross-section height profile of a stromal lamellae membrane with PSI particles identified using blue circles. Due in part to convolution with the AFM tip the protruding “bumps” of PSI resembled a 3-D Gaussian function (Fig 4.4B). The protruding PSI subunits within stromal lamellae were found to have a height of 3.2 nm and a width of 8.9 nm (Fig 4.2). These measurements were used to construct a Gaussian model of the geometry of PSI as observed in AFM images. For a given pixel ( $X_c, Y_c$ ), a Gaussian was constructed over an area 100 nm<sup>2</sup> using the height and width of PSI previously determined to calculate the amplitude and standard deviation of the Gaussian

$$z(x_c, y_c) = 3.2e^{-\frac{(x_c - x_n)^2 + (y_c - y_n)^2}{22.03}}$$

Where ( $X_n, Y_n$ ) is the location of the pixel within the 100 nm<sup>2</sup> area. The Gaussian model is subtracted from the height at the central pixel  $z(X_c, Y_c)$  in order to fit it to the topography of the image (Fig 4.4C). The chi-square value over the 100 nm<sup>2</sup> region was used as a measure of good fit and was calculated for every pixel in an image. Using a suitable threshold for the chi-square value (<1 for example) whereby pixels with higher values were excluded, the model was found to be able to reliably identify PSI particles (Fig 4.4E). By further fine tuning of the chi-square threshold and by consolidating neighbouring clusters of positive identifications, it was possible to eliminate most of the false positives (Fig 4.4F). False positives remaining were removed manually. false negatives were found to be very uncommon. The PSI detection algorithm was used to derive the nearest neighbour distribution of PSI in the stromal lamellae (Fig 4.5A) and calculated an average nearest neighbour distance of  $15.0 \pm 2.8$  nm. The distribution was fit with a Gaussian function which would infer a degree of randomness to the organisation of PSI but the data seems to have a positive skew. This may be indicative of PSI-PSI associations causing a subset of the complexes to be closer to one another than the average. Indeed, the left tail of the distribution drops off rapidly, approaching zero at 10 nm, suggesting this as the approximate closest peak to peak distance of neighbouring PSI complexes. Compare the nearest neighbour distribution of PSI to that of PSII/*cytb<sub>6f</sub>* in the grana (Fig 4.5B) which shows a larger mean nearest neighbour distance ( $19.0 \pm 2.8$  nm) and appears much more symmetrically distributed. This agrees with the observation that PSII and *cytb<sub>6f</sub>* are most often randomly and homogeneously distributed in the grana.

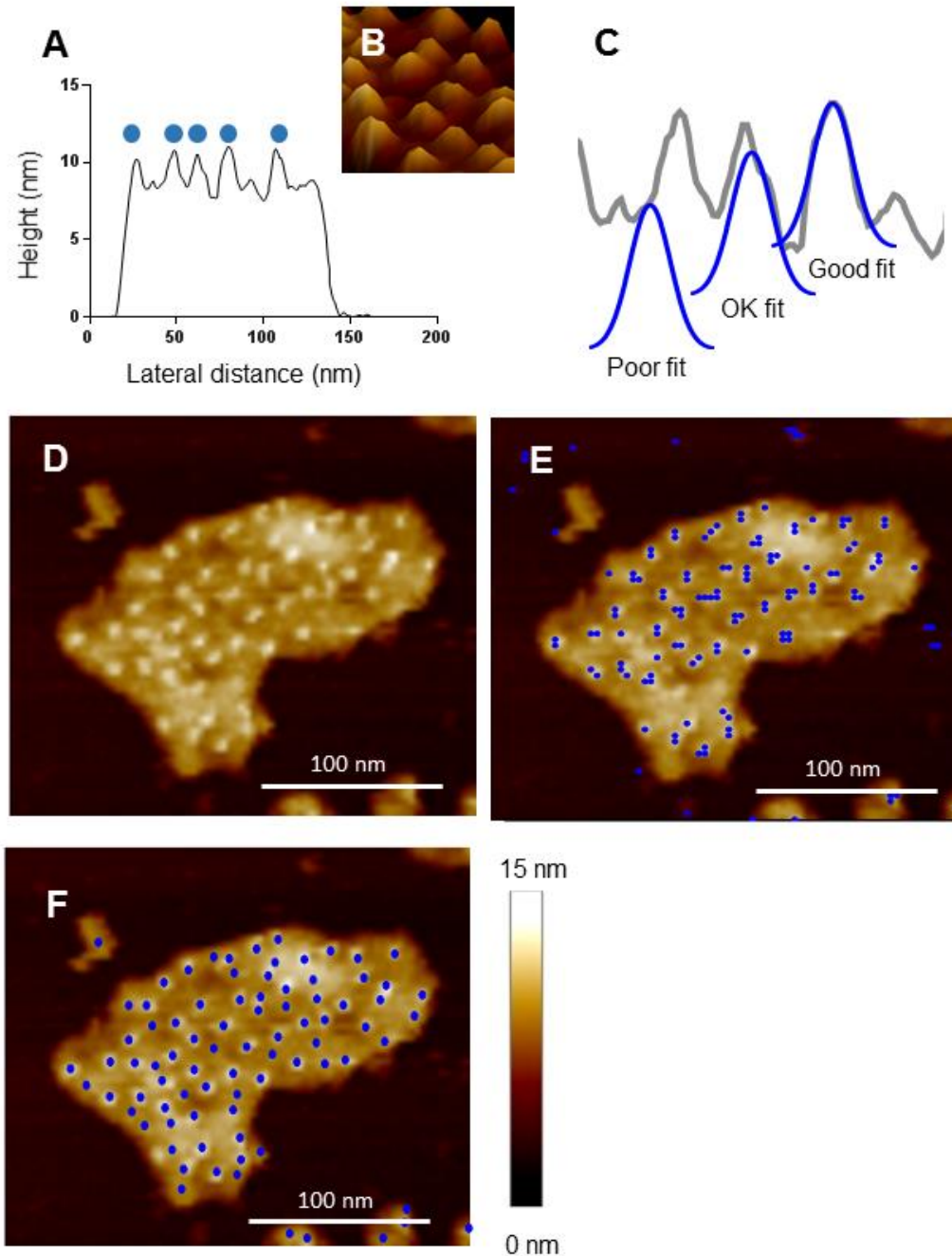


**Figure 4.4. Automated detection of PSI in AFM images of stromal lamellae using a Gaussian cross-correlation model.** **A.** A cross section of a stromal lamellae membrane (PSI indicated by blue circles). **B.** 3-D AFM image of PSI protrusions. **C.** Comparison of cross section in (A) with a Gaussian function showing best fit when the function lies directly over a PSI protrusion. **D-F.** A Gaussian  $z(x,y)$  centred on the pixel and spread over  $10 \text{ nm}^2$  is scanned over the AFM image line by line. **E.** Blue dots indicate pixels with cross correlation values below a given threshold. **F.** Further adjustment of the threshold and consolidation of clusters further increases the accuracy of PSI identification.

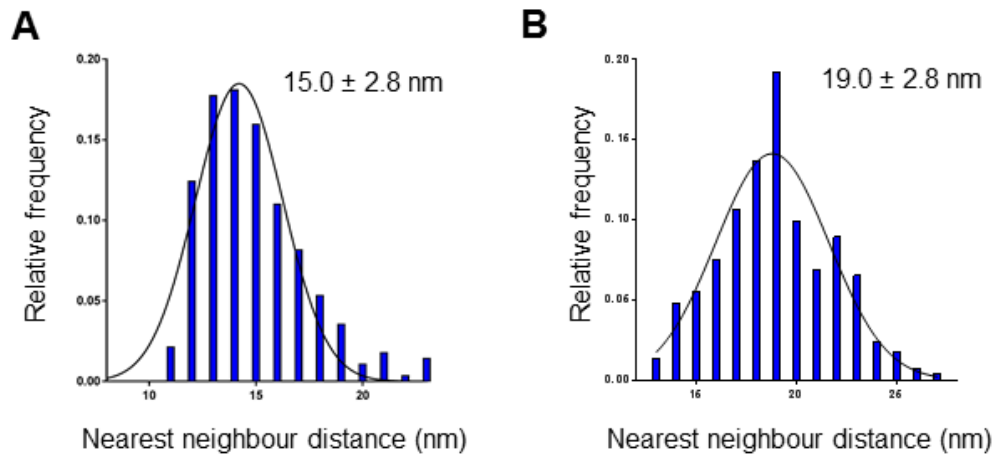


**Figure 4.5. Nearest neighbour distributions of PSI in the stromal lamellae (A) and of PSII and *cytb<sub>6</sub>f* in the grana (B) . Each display mean and standard deviation of a Gaussian fit.**

#### 4.2.4. The native organisation of PSI in stromal lamellae thylakoids.

To further investigate the organisation of PSI in stromal lamellae, a framework was developed to identify PSI-PSI associations (Fig 4.6). Several possible interactions may occur between two PSI complexes. Whereas cyanobacterial PSI is known to form dimeric, trimeric and tetrameric structures (Karapetyan *et al.*, 1999; Watanabe *et al.*, 2011), plant and algal PSI has, until recently, thought to have been monomeric. It is thought that the subunit PsaH, which is present in plants and important for LHCI binding during state transitions (Lunde *et al.*, 2000) but is not present in cyanobacteria, prevents oligomer formation. This is because PsaH surrounds and modifies PsaL (Kouřil *et al.*, 2005) which mediates trimerisation in cyanobacteria (Chitnis & Chitnis, 1993). A recent EM study showing a PSI dimer structure from plants has been published (Yadav *et al.*, 2017). This dimer results from core to core interactions and resembles the structure shown in Fig 4.6A. As a measure of separation distance between the protruding subunits of PSI, isoleucine 29 of PsaC was used as a reference point. This was chosen because isoleucine 29 lies at the top (height) and centre (laterally) of the protruding region of PSI. The distance between the isoleucine 29 of a PSI and the isoleucine 29 of the neighbouring PSI (within a dimeric structure) was referred to as the separation distance. The separation distances of PSI in three different dimeric orientations were measured in UCSF Chimera 1.10.2 (Fig 4.6A-C). The dimeric structure proposed by Yadav *et al.* (2017) has a separation distance of 11.2 nm (Fig 4.6A). The other contact orientations measured were core to LHCI (Fig 4.6B) and LHCI to LHCI (Fig 4.6B), which have separation distances of 14.5 nm and 16.3 nm respectively. The separation distances of PSI particles in AFM images of stromal lamellae revealed that a significant proportion are likely to adopt the orientation of Fig 4.6A (Fig 4.6C white ellipses). By including only separation distances less than 14 nm, it was possible to exclude core to LHCI and LHCI to LHCI contacts and therefore include only core to core contacts. The proportion of PSI complexes within each membrane with separation distances of less than 14 nm was  $25.5 \pm 20.6\%$  ( $n=381$  PSI particles,  $n=9$  membranes). Within this subset of PSI complexes, the mean separation distance was found to be  $12.4 \pm 1.0$  nm (Fig 4.6E,F) which is largely consistent with the arrangement shown in Fig 4.6F. Interestingly, a large variation was observed in the percentage of dimerisation between membranes. Some membranes (Fig 4.6D, bottom left) consisted almost entirely of dimeric PSI whereas in others (Fig 4.6D, top middle) PSI was largely monomeric. Two possible reasons for this are: initial PSI dimerisation may trigger further PSI dimerisation in a positive feedback process or, alternatively, PSI dimerisation may be an active process controlled by external factors.

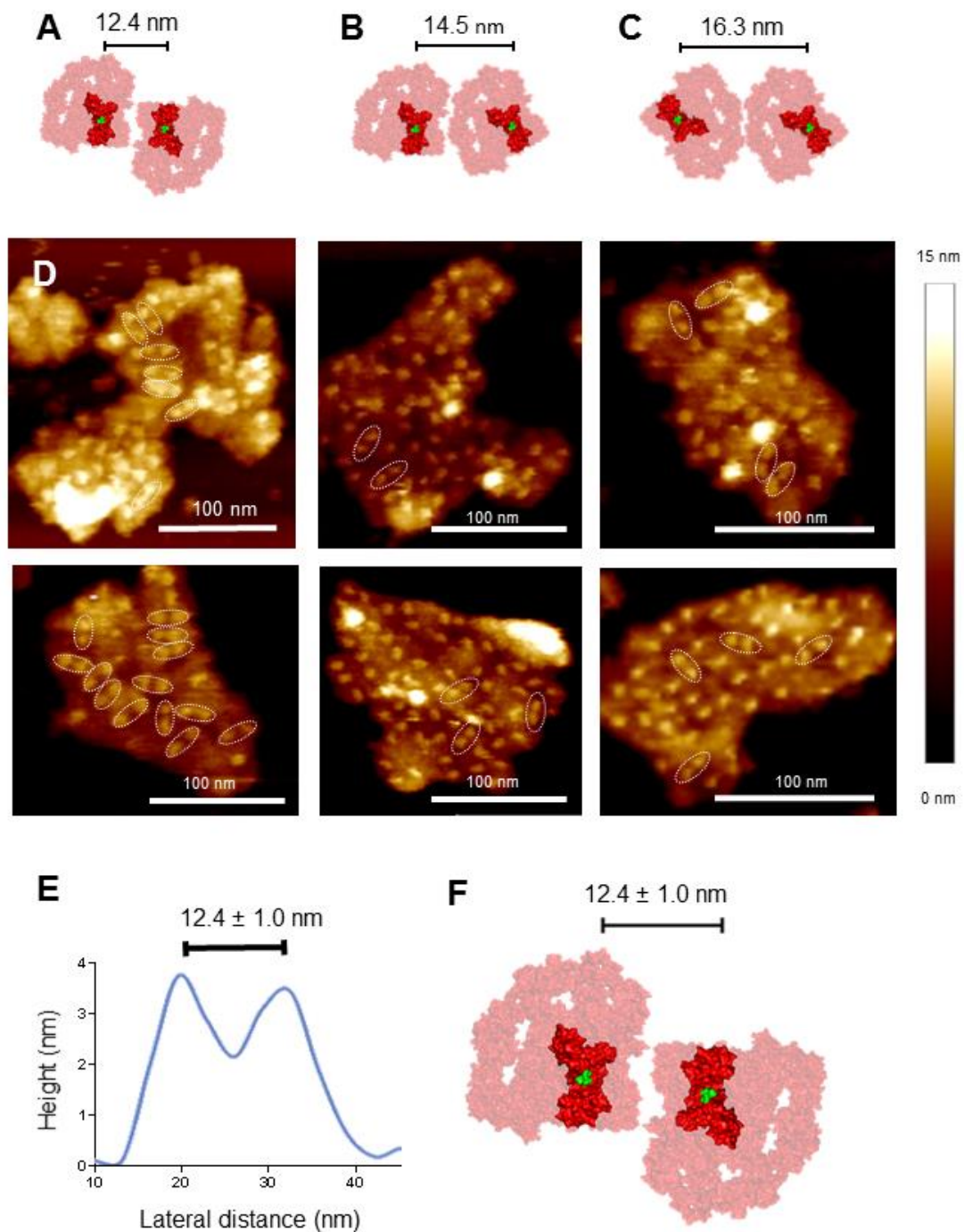


**Figure 4.6 . Identification and proposed structure of PSI-LHCI dimers in stromal lamellae.** **A-C.** Distances between PSI-LHCI complexes in three different arrangements as measured between Isoleucine 29 of PSaC in Pymol. Possible dimeric structures may arise from contact between PSI cores (A), core and Lhca (B) or between Lhca and Lhca (C). **D.** A gallery of AFM images of stromal lamellae (from Fig. 1) with dimers (distance < 14 nm in order to include only core-core contacts) highlighted with white ellipses. **E,F.** Cross section height profile (E) and molecular model (F) (PDB: 4Y28) of observed PSI-LHCI dimers

The association of PSI in the stromal lamellae resulted in regions of lipid devoid of protein (Fig 4.7). Fig 4.7A,B show AFM images of stromal lamellae (Fig 4.7A) and grana (Fig 4.7B) coloured to show lipid regions devoid of protein in red (regions <0.5 nm above the membrane surface), proteins of low topographic relief (regions >0.5 nm and <2.5 nm above the membrane surface) and large extrinsic membrane protrusions (regions >2.5 nm above the membrane) in blue/white. To the eye the stromal lamellae contains a significant amount of lipid-only regions, whereas only a very small amount is present in the grana. A custom python script was used to count the area fraction of each membrane of lipid, low topographic relief protein and protrusions (Fig 4.7C). The categories were defined as heights given in accordance with the colour scheme described above ( <0.5 nm, 0.5-2.5 nm, and >2.5 nm from the membrane surface). In stromal lamellae, the area of the membrane occupied by lipid only regions was  $15.0 \pm 3.4 \%$  (n=5) whereas, for the grana, a value of  $5.0 \pm 1.1 \%$  (n=5) was calculated. This difference was highly statistically significant (P=0.0003, t-test). No significant difference between the grana and the stromal lamellae was observed for the area fractions of low relief protein or protrusions.

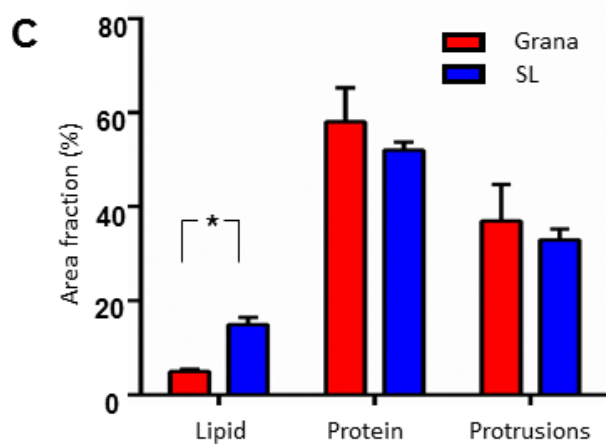
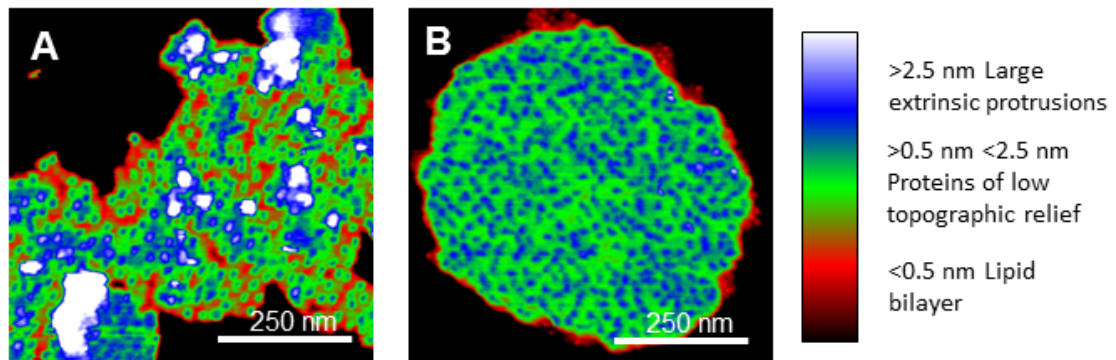


**Figure 4.7. Association of PSI-LHCI results in lipid zones. A,B.** AFM images of stromal lamellae (A) grana (B) with colour threshold to show lipid zones in red (regions <0.5 nm above the membrane surface), proteins of low topographic relief (regions >0.5 nm and <2.5 nm above the membrane surface) and large extrinsic membrane protrusions (regions >2.5 nm above the membrane) in blue/white. **C.** A comparison of lipid, protein and protruding regions in grana (red) and stromal lamellae (blue) thylakoids (displaying mean and standard error, N = 5, \* indicates  $p \leq 0.001$  by t-test).

The association of PSI may facilitate diffusion of other proteins within the stromal lamellae. One such process which requires diffusion is state transitions (For review, see Goldschmidt-Clermont & Bassi, 2015): The kinase driven dissociation of LHCII from PSII in the grana and association of LHCII to PSI in the stromal lamellae in order to balance the turnover rate of the two photosystems in varying light conditions. The nearest neighbour distribution of PSI in AFM images of stromal lamellae from *Spinacia oleracea* in state I (Fig 4.8A) and state II (Fig 4.8B) was attained. Spinach leaves were treated with 15  $\mu$ E far-red (720 nm) or red (650 nm) light for one hour prior to homogenisation to produce thylakoids in state I and state II respectively. Buffers used for thylakoid purification contained 10 mM NaF to inhibit kinase/phosphatase activity. The distributions (Fig 4.8C) yielded no significant difference between state I (mean =  $12.5 \pm 2.4$  nm, n = 54 PSI particles) and state II (mean  $12.8 \pm 3.1$  nm, n = 64 particles) nor between state I or II and the dark-adapted ( $12.4 \pm 1.0$  nm, Fig 4.5A). BN-PAGE electrophoresis confirmed that stromal lamellae in state II contained PSII-LHCI-LHCII complexes (Fig 4.8D).

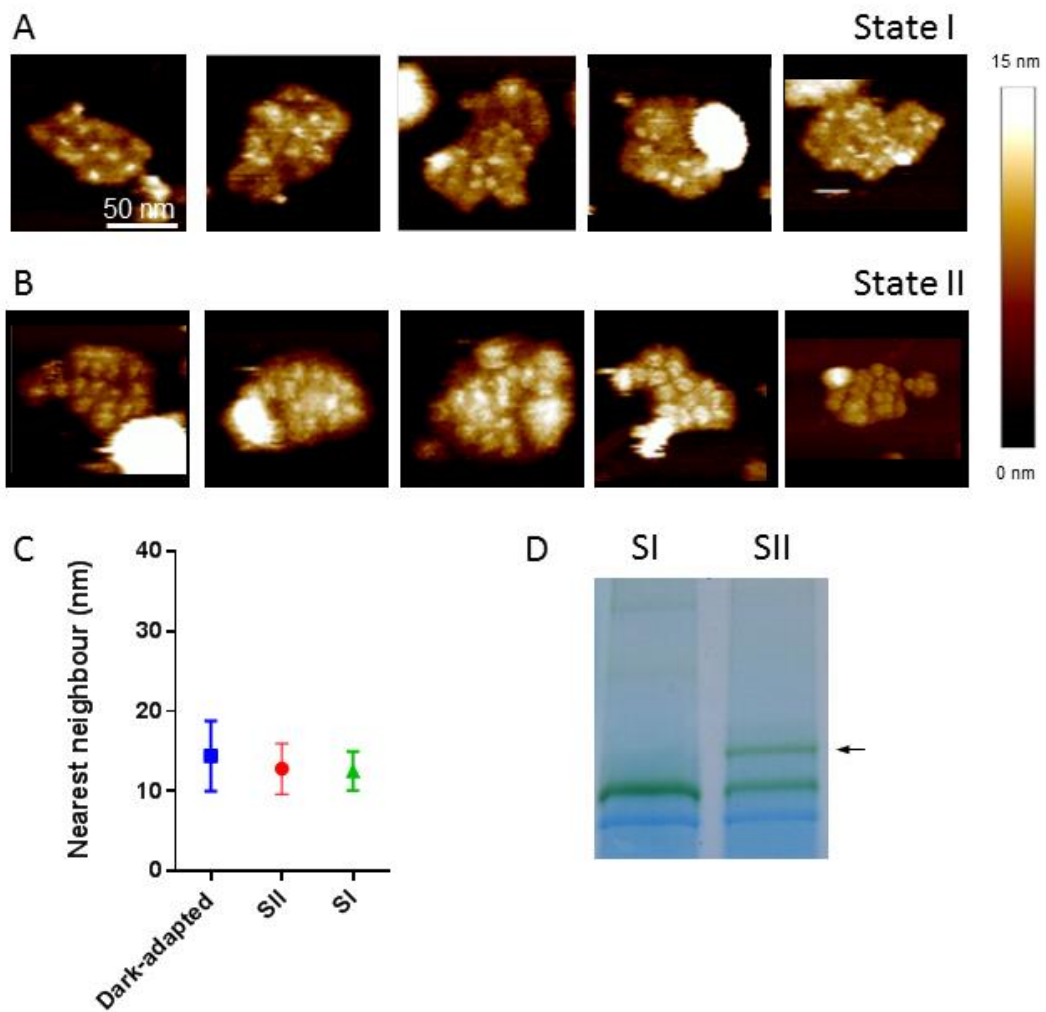


**Figure 4.8. No change in the nearest neighbour distribution of PSI-LHCI is observed under state transitions.** **A,B.** Images of stromal lamellae in SI (A) and SII (B). **C.** Mean and standard deviation of nearest neighbour distribution of PSI-LHCI of wild-type (WT), SI and SII stromal lamellae. **D.** BN-PAGE of SI and SII stromal lamellae membranes with PSI-LHCI-LHCII complex, indicative of SII, is labelled with an arrow.

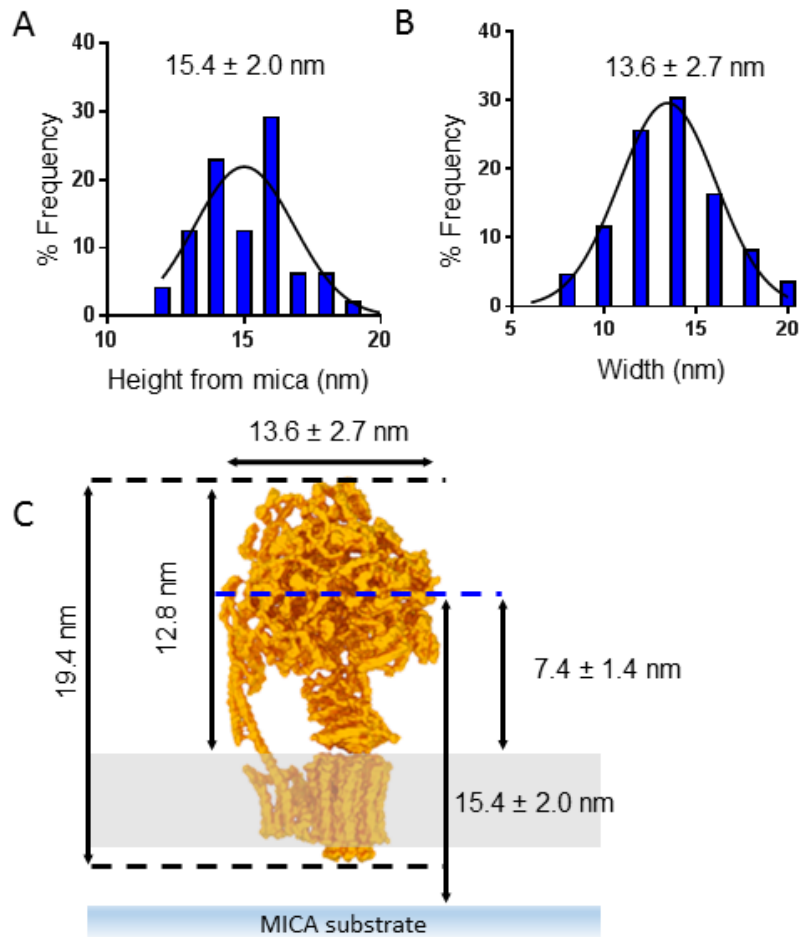
#### 4.2.5. ATP synthase in stromal lamellae thylakoids.

Alongside PSI in the stromal lamellae, several other protein complexes reside. Due to the large number and size of ATP synthase, this complex should be clearly visible in the AFM images. Recall, in Fig 4.2A, that two species of protruding particle were observed, one with a height from the membrane surface of  $3.2 \pm 0.8$  nm and now identified as PSI, and another with a height of  $7.4 \pm 1.6$  nm. The next challenge was to identify the 7.4 nm protruding particle (Fig 4.9). Further analysis revealed that this particle had a height from the mica substrate of  $15.4 \pm 2.0$  nm (Fig 4.9A) and a width of  $13.6 \pm 2.7$  nm ( $n = 86$ ) (Fig 4.9B). The heights of putative ATP synthase particles measured were found to be inconsistent with those predicted from the known cryo-EM structure (PDB: 5ARA) (Fig 4.9C). The black dashed lines show the height of ATP synthase predicted from the cryo-EM structure is 19.4 nm, protruding 12.8 nm from the membrane surface. The blue dashed line shows the observed height of the putative particles in AFM images. Due to the gap between the stromal lamellae membrane and the mica substrate (Fig 4.2D) it was deemed more appropriate to use the height of the particles from the membrane surface as a reference.

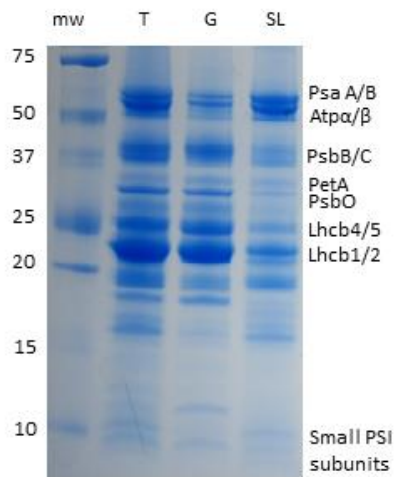
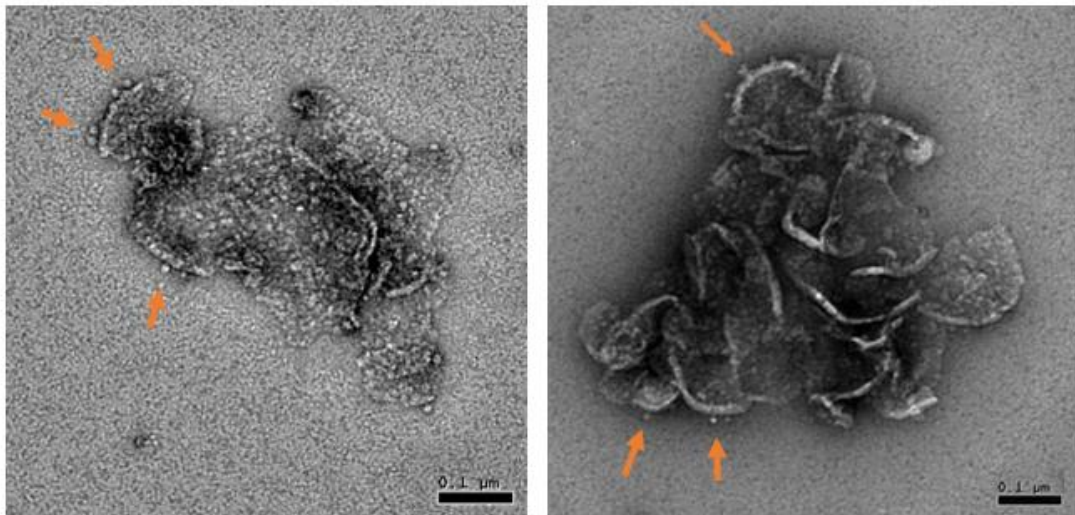
The presence of intact ATP synthase was evidenced in stromal lamellae membranes using SDS-PAGE and electron microscopy (EM) (Fig 4.10). SDS-PAGE confirmed the presence of ATP $\alpha/\beta$  subunits (Fig 4.10A) which were found to be enriched in stromal lamellae compared to grana membranes. Furthermore, ATP synthase was visible in EM images of stromal lamellae (Fig 4.10B). The characteristic shape of the F<sub>1</sub> region of ATP synthase can be seen most clearly when the complex is located on the edge of the membrane (orange arrows), offering increased contrast against the background. Measurement of the height of such ATP synthase particles in ImageJ showed values up to 13 nm, consistent with intact ATP synthase.

It was proposed that the discrepancy between the expected and observed heights of putative ATP synthase protrusions in AFM images may be due to damage of the F<sub>1</sub> ATP synthase region incurred by the AFM tip. Multiple scans of the same ATP synthase complexes however suggest that this is not the case (Fig 4.11). Upon three consecutive scans of the same stromal lamellae membrane with five ATP synthase complexes clearly visible (Fig 4.11A-C) no change in height was observed (Fig 4.11D). Of course, one may argue that the complex may have been damaged in the first scan and the damaged complex is therefore imaged multiple times but the observed height is reproducible between particles and over multiple scans. In a collaborative effort, further evidence that the particles were indeed of ATP synthase was provided by reconstituting *Bos taurus* mitochondrial ATP synthase into DOPC liposomes and subjecting the liposomes to AFM analysis (Fig 11E). Here, Tobias Spikes and Sir John Walker provided the purified ATP synthase, Xia Huang and Craig MacGregor-Chatwin reconstituted

the ATP synthase into DOPC liposomes and carried out the AFM, and William Wood analysed the data. Individual ATP synthase complexes can be clearly identified in the AFM height images (Fig 4.11E). The height ( $7.3 \pm 0.9$  nm) and width ( $14.6 \pm 1.8$  nm,  $n = 25$ ) of *Bos taurus* ATP synthase were all consistent with those observed in stromal lamellae (Fig 4.11F).



**Figure 4.9. Analysis of the larger stromal lamellae protrusions and comparison to ATP synthase.** **A.** Histogram of the heights of the  $7.4 \pm 1.6$  nm protrusions (Fig. 2A) in stromal lamellae from the mica substrate. **B.** Histogram of the width (lateral size) of the same particles. **C.** Comparison of the measured dimensions of the large protrusions in the stromal lamellae (blue line) with those measured of ATP synthase (PDB: 5ARA) in Pymol (black lines).

**A****B**

**Figure 4.10. Evidence that ATP synthase is both present and intact in stromal lamellae membranes.** **A.** SDS-PAGE showing PSI, ATP synthase and Cytochrome  $b_6f$  distribution in thylakoids (T), grana membranes (G) and stromal lamellae membranes (SL). **B.** EM images of stromal lamellae membranes. stromal protrusions of ATP synthase highlighted by orange arrows.

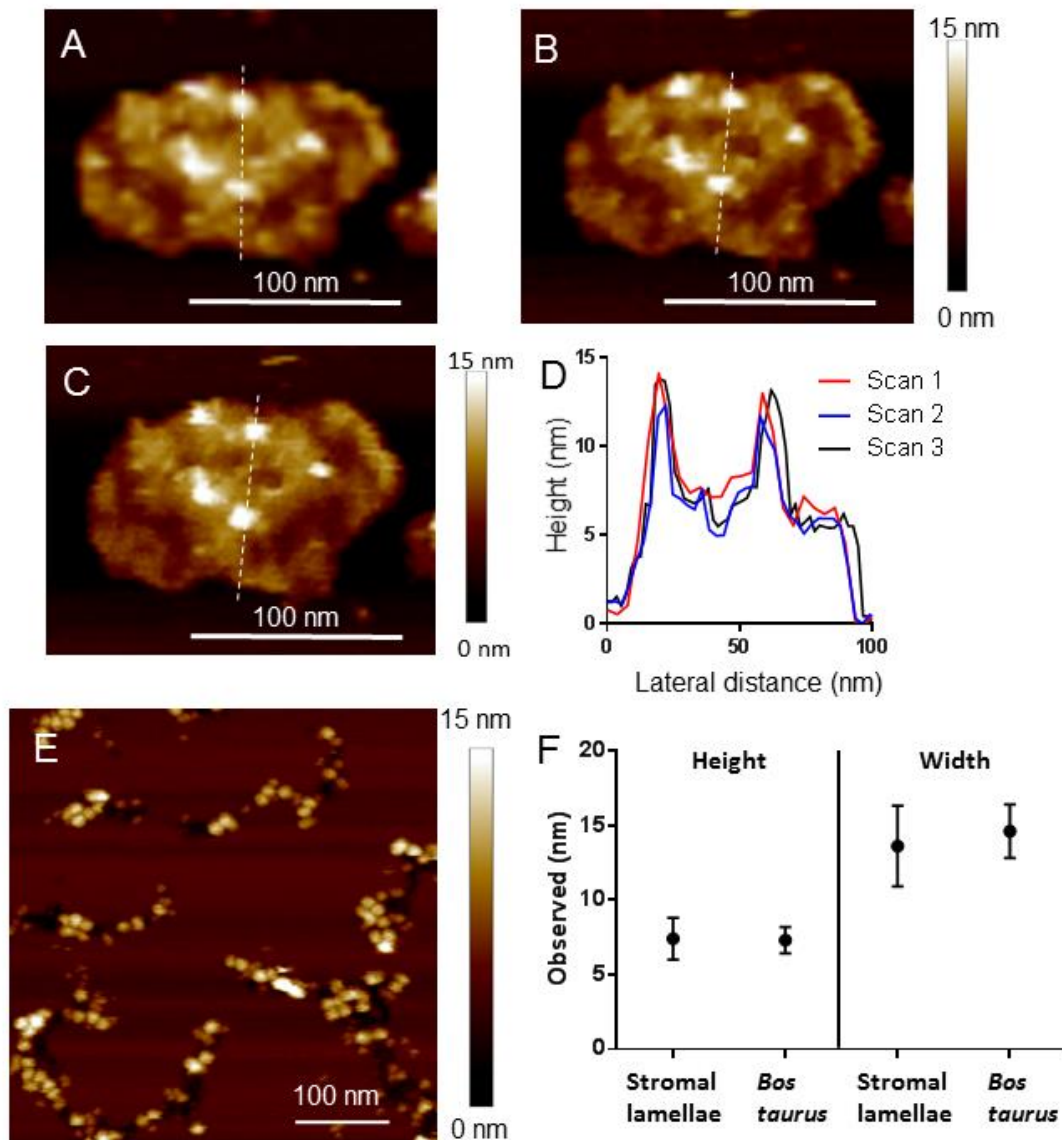


**Figure 4.11. The height of ATP synthase in stromal lamellae is consistent and validated by *Bos taurus* ATP synthase in a DOPC lipid bilayer.** A-C, Three consecutive scans of AFM stromal lamellae membrane ATP synthase clearly visible. D, cross-sections through the dashed white lines in (A-C) demonstrate no change in the height or lateral dimensions of the particles. E, AFM topographs of *Bos taurus* ATP synthase (courtesy of Sir John Walker, Tobias Spikes) reconstituted into a DOPC lipid bilayer (courtesy of Xia Huang, Craig MacGregor-Chatwin). F, The average height and width of *Bos taurus* ATP synthase is almost indistinguishable from that of ATP synthase observed in stromal lamellae.

#### 4.2.6. Imaging grana membranes with attached stromal lamellae.

Occasionally, grana particles prepared using digitonin (Fig 4.12) were found to contain contiguous regions of stromal lamellae (Fig 4.12A-C). In these membranes, the stromal lamellae emanate from the bottom of the two appressed grana layers revealing the stromal face in which PSI (red arrows) and ATP synthase (orange arrows) can clearly be seen (Fig 4.12D). Any grana membranes which appeared to contain stromal lamellae regions but no particles were visible were excluded to avoid the possibility that they resulted from damaged grana and that the putative stromal lamellae region was the stromal face of the lower grana layer. PSI and ATP synthase were observed up to the boundary of the grana and the average nearest neighbour distance for PSI was  $16.3 \pm 5.7$  nm, indistinguishable from that of PSI in purified stromal lamellae membranes. Because junctional slits are known to be the point of contact between the grana and the stromal lamellae, it must be the case that the images presented in Fig 4.12 were membranes derived of a grana/stromal lamellae interface at the junctional slit, which had remained partially intact upon fractionation. This supports a model of lateral heterogeneity of PSII and PSI with a distinct boundary (Andersson and Anderson, 1980). The functional implications of this will be further investigated in chapter 5. In Fig 4.13, a model was presented of the grana/stromal lamellae interface by utilising AFM data and incorporating known structures of PSII-LHCII (PDB: 3JCU), PSI-LHCI (PDB: 4Y28), *Cytb<sub>6</sub>f* (PDB: 1Q90), and ATP synthase (PDB: 5ARA) into the membrane shown in Fig 4.12C.

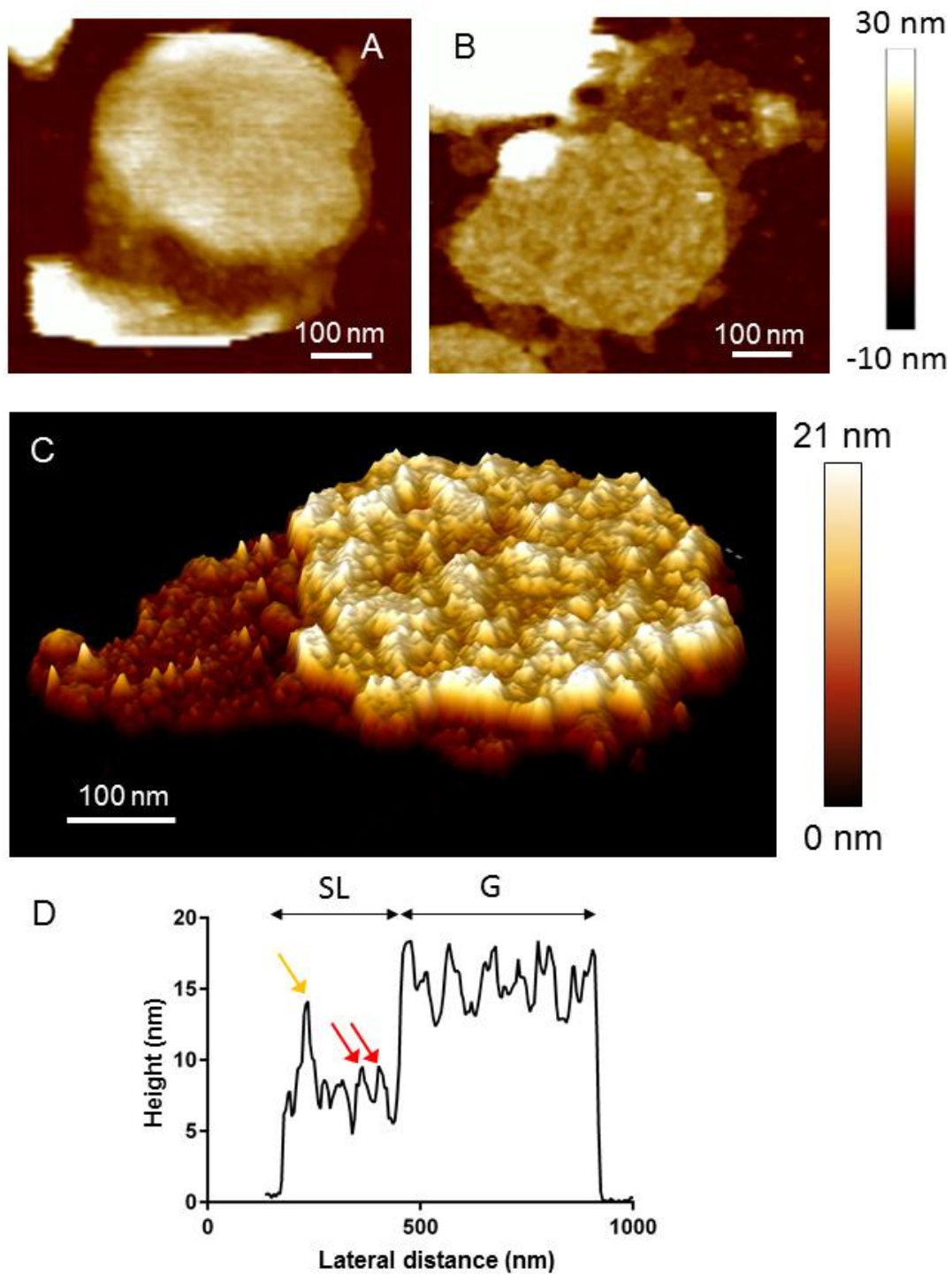


**Figure 4.12. Visualising the grana/stromal lamellae interface using AFM.** A,B. AFM images of contiguous grana and stromal lamellae membranes. C. 3-D rendered AFM image of a contiguous grana and stromal lamellae membrane. D. Cross section through membrane in (C) with annotations showing grana region (G), stromal lamellae region (SL), PSI (red arrows) and ATP synthase (orange arrow).

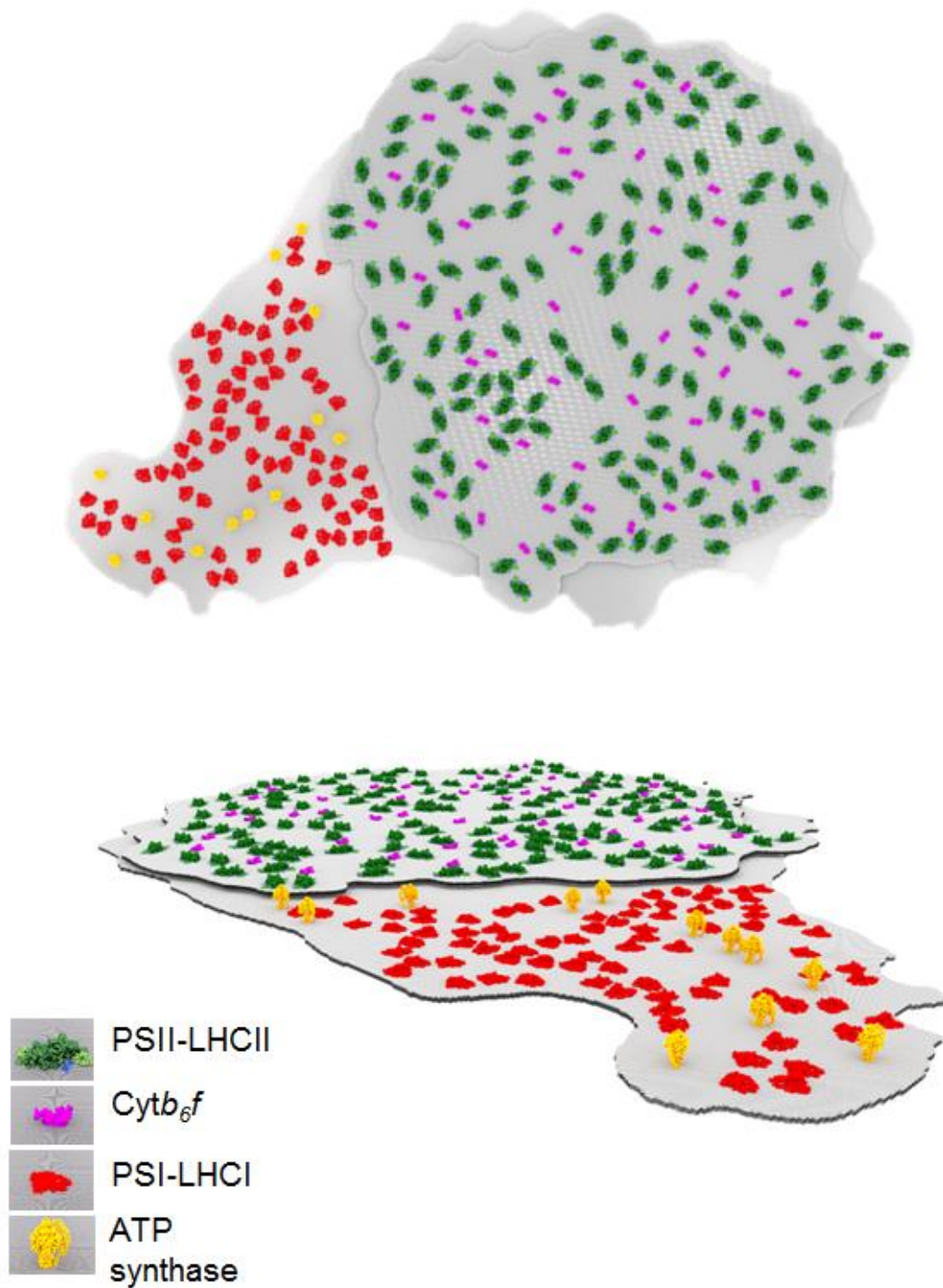


**Fig. 13 Spatial model of membrane in (Fig 12C)** (Courtesy of Guy E. Mayneord) incorporating known structures of PSII-LHCII supercomplex (PDB: 3JCU, shown in green), PSI-LHCI supercomplex (PDB: 4Y28, red), Cyt<sub>b</sub><sub>6</sub>f (PDB: 1Q90, magenta), ATP synthase (PDB: 5ARA, orange)

### 4.3. Discussion.

#### 4.3.1 PSI-LHCI in stromal lamellae.

The results described above, are presented as evidence for the identification of PSI and ATP synthase in stromal lamellae thylakoids. SDS-PAGE (Fig. 4.10A) and BN-PAGE (Fig 4.8D) gel electrophoresis along with 77K fluorescence revealed stromal lamellae contained significant amounts of PSI. The dimensions of the protrusions of putative PSI in AFM images closely resemble those of the PsaC, PsaD, and PsaE subunits of PSI and the protrusions of putative stromal lamellae described in Phuthong *et al.* (2015). The irreversible damage of PSI by AFM imaging was best compensated by reducing the force with which the AFM tip is brought into contact with the sample and by scanning each membrane only once (alternatively, one may confine analyses to the first image of a membrane). It was proposed that the reason PSI is prone to damage is because the PsaC, PsaD, and PsaE subunits, the subunits visible as 3.2 nm protrusions contain no transmembrane regions or even regions that project into the inner part of the complex or membrane. They may therefore, be less able to withstand forces incurred by the AFM tip than if they did possess membrane integral domains.

It was observed that PSI is present as part of a dimer in 25.5 % of cases, with a peak to peak distance which is consistent with the structure recently discovered by (Yadav *et al.*, 2017). This new evidence overturns the prevailing view that PSI in plant is entirely monomeric. This was because although previous studies have observed solubilised PSI in dimer form, it was often present in a non-native configuration i.e. the stromal protruding subunits of one monomer faced the opposite way to the other. Despite the presence of PSI dimers in plants, it seems that most of the PSI is present in monomeric form, at least under the conditions used in this study, suggesting that the selective pressure for PSI oligomerisation that exists in cyanobacteria is less important in plants. Modelling of excitation energy transfer dynamics in trimeric PSI from cyanobacteria suggests that some limited sharing of energy can occur between the component monomers (Şener *et al.*, 2004), which may be an advantage in low light environments typical of many cyanobacterial niches. In contrast, land plants evolved in an environment where light was less often limiting but fluctuated frequently in intensity and spectral quality. This may mean that processes involved in regulation of photosynthesis may be of a higher importance in plants. It is widely believed that the PsaH subunit, which is present in plants but not in cyanobacteria, is responsible for the blocking of PsaL-mediated trimer formation (Kouřil *et al.*, 2005). Lunde *et al* (2000) showed that the ability of PSI to form a complex within LHCII in state II, whereby excitation energy transfer from LHCII to PSII is possible, is severely impaired in strains of *Arabidopsis thaliana* lacking PsaH. It is therefore likely that plant PSI has adapted in support of state transitions. The PSI dimer observed in plants is mediated by different contacts to those of

cyanobacterial dimers (as well as trimers and tetramers) suggesting that, rather than a continuation from cyanobacterial oligomerisation, where the contact was lost by the introduction of new subunits, a remaining drive for dimerisation led to contacts forming elsewhere. If the evolutionary driving force behind dimer formation does not come from excitation transport but from assembly, repair and regulatory processes it may be the case that this is a space saving solution. This is consistent with the observed abundance of lipid only zones in stromal lamellae compared to the grana (Fig 4.7). The stromal lamella is a highly dynamic region of the thylakoid membrane, involved in state transitions and PSII repair. This diffusion space may aid the transport of large protein complexes involved in such processes. The organisation of PSI was investigated within stromal lamellae in states I and II (Fig 4.8). No change in the nearest neighbour distribution was found even after two biological repeats. Admittedly, the membranes used in this experiment were somewhat smaller than usual (in both states), which more likely resulted from over-solubilisation of the membranes rather than any *in vivo* change in the size of the stromal lamellae.

#### **4.3.2. ATP synthase in stromal lamellae.**

SDS-PAGE revealed that stromal lamellae contained significant amounts of ATP synthase and EM images revealed that the ATP synthase complexes were intact. Although the height of ATP synthase in stromal lamellae was much smaller than predicted from its structure, its height and width were found to be consistent with ATP synthase of *Bos taurus*.

In comparison with PSI, with ATP synthase, the mechanical interaction with the AFM tip was subtler. Although intact ATP synthase was present in stromal lamellae, its height was observed to be much less than predicted from its structure. It may be the case that rather than being irreversibly damaged instead, ATP synthase may undergo a reversible conformational change under the stress of the AFM tip (Fig 4.14). Indeed, it was observed that the location of the ATP synthase complexes in the AFM height images of stromal lamellae (Fig 4.14A) coincided with strong signals in the AFM deformation images (Fig 4.14B). This was also observed for *Bos taurus* ATP synthase in DOPC (Fig 4.14C,D). While not equal to, the deformation is closely correlated to the indentation of the AFM tip into the sample. The average deformation of the ATP synthase complexes was found to be  $3.9 \pm 0.9$  nm in stromal lamellae and  $3.5 \pm 0.3$  nm for *Bos taurus* ATP synthase in DOPC. Therefore, the true height would likely be a value much closer to that predicted from its structure (Fig 4.14E-G). Furthermore, the observed deformation is reproducible over multiple scans (Fig 4.14H-K). This suggests that a reversible conformational change is brought about by the force of the AFM tip. Although the deformation signal in PF-QNM has been used to quantify to indentation of the tip into the sample (Picas *et al.*, 2012, Walczyk *et al.*, 2013), there are issues associated with the signal which lead to inaccuracies in the

numbers given (particularly at the nanometre scale as is the case in this study). Firstly, the point of contact may be misrepresented if there are positive interactions between the tip and the sample (Walczyk *et al.*, 2013) leading to an overestimation of the deformation. Secondly, the operating software of the AFM requires a force threshold (typically 15% of the peak force setpoint) with which to identify surface contact, which could lead to an underestimation of the deformation. Thirdly, the deformation may be inaccurate if the sample deforms in an inconsistent way. For example, if the  $F_1$  region of ATP synthase is highly flexible it may have no bias in any direction when stressed by the AFM tip and therefore may be pushed in any direction depending on the angle of contact with the tip and the direction in which the tip is moving. To date, only a small amount of research is dedicated to measuring the mechanical properties of individual molecules, but the recent development of PF-QNM AFM promises to offer new insights within this field (Dufrêne *et al.*, 2013).

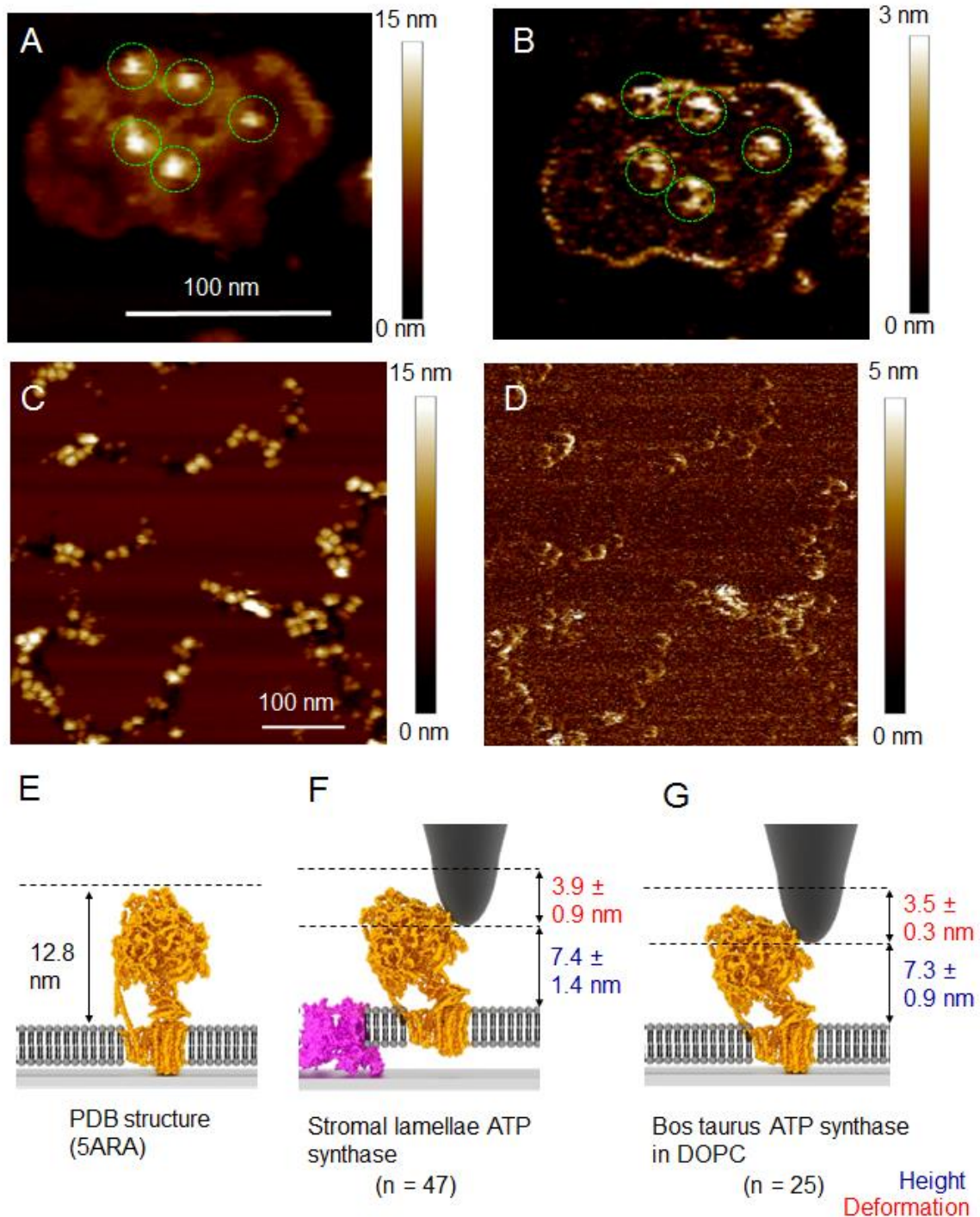


**Figure 4.14. The location of ATP synthase in AFM height topographs is associated with signals in the deformation image.** **A,B.** The location of stromal lamellae ATP synthase highlighted in AFM height topographs (A) correlates with strong localised signals in the deformation image (B). **C,D.** The height (C) and deformation (D) AFM topographs of *Bos taurus* ATP synthase reconstituted into a DOPC lipid bilayer. **E-F.** The predicted height of ATP synthase (E) from its structure (PDB: 5ARA) was observed to be inconsistent with observed values in stromal lamellae (F) and *Bos taurus* (G) ATP synthase. However, the deformation, which is closely correlated with tip indentation is observed to be a consistent factor in both cases.

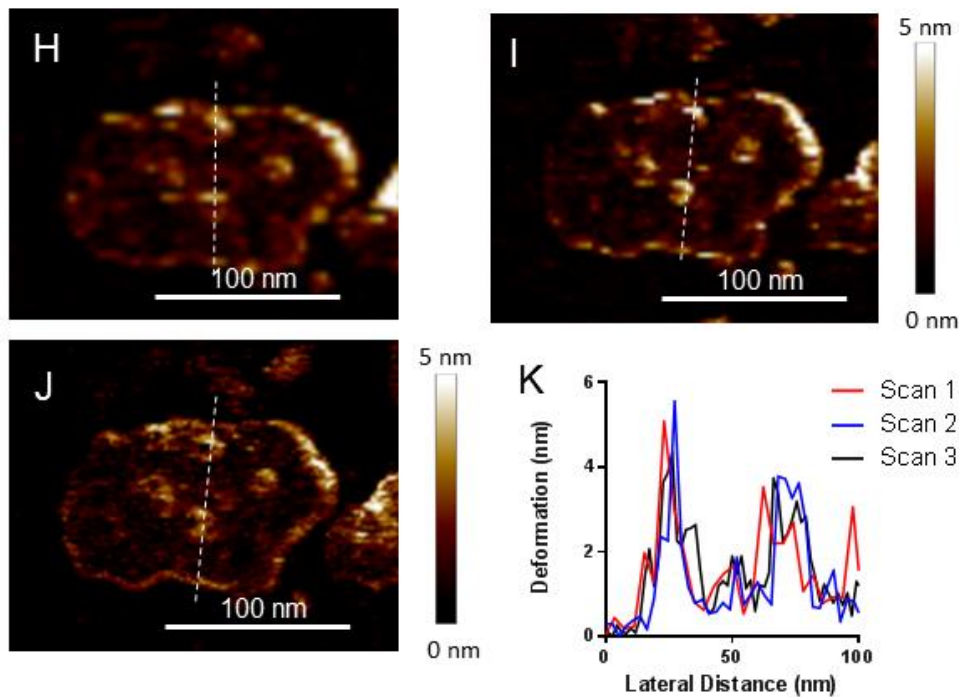


**Figure 4.14 continued.** H-J. Three consecutive AFM deformation images of stromal lamellae membrane in (A-C). K. cross-sections through the dashed white lines in (H-J) (scans 1-3 taken from cross sections in H-J respectively) show that deformation is consistent over multiple scans.

#### 4.3.3. Implications of contiguous grana and stromal lamellae membranes for the grana margins.

Recall that grana vesicles prepared by French Press and ATPS separation can be fractionated further to yield a fraction enriched in PSII and another enriched in PSI (relative to the first grana fraction) (Andersson *et al.*, 1976) (Fig 3.3). The latter became synonymous with the grana margins (Wollenberger *et al.*, 1994, 1995) as this fraction was proposed to be derived of the curve regions of the thylakoid which adjoin the appressed grana. In chapter 3, this fraction was found to contain small fragments of membrane. Consider now that the so-called grana margins fraction was derived of the same grana fraction as imaged in this study of which occasionally contain contiguous regions of stromal lamellae. This includes grana vesicles produced by French Press (Fig 4.15). One may argue the PSI enriched fraction derived of the grana could indeed have resulted from removal of fragments from membranes such as those seen in Fig 4.12. Of course, if one has a membranous fraction containing both PSII and PSI, by nature of the method of ATPS separation, further processing will always result in PSI enrichment in the top phase and PSII enrichment in the bottom phase. This is because the two photosystems have different affinities to each phase and so even if thylakoids were broken in a

spatially random manner, there would still be partial separation of PSI and PSII into the top and bottom phases respectively. In summary, in light of the evidence presented in this chapter, it is proposed that the so-called grana margins prepared using ATPS actually result from PSI-enriched stromal lamellae contiguous of the grana.

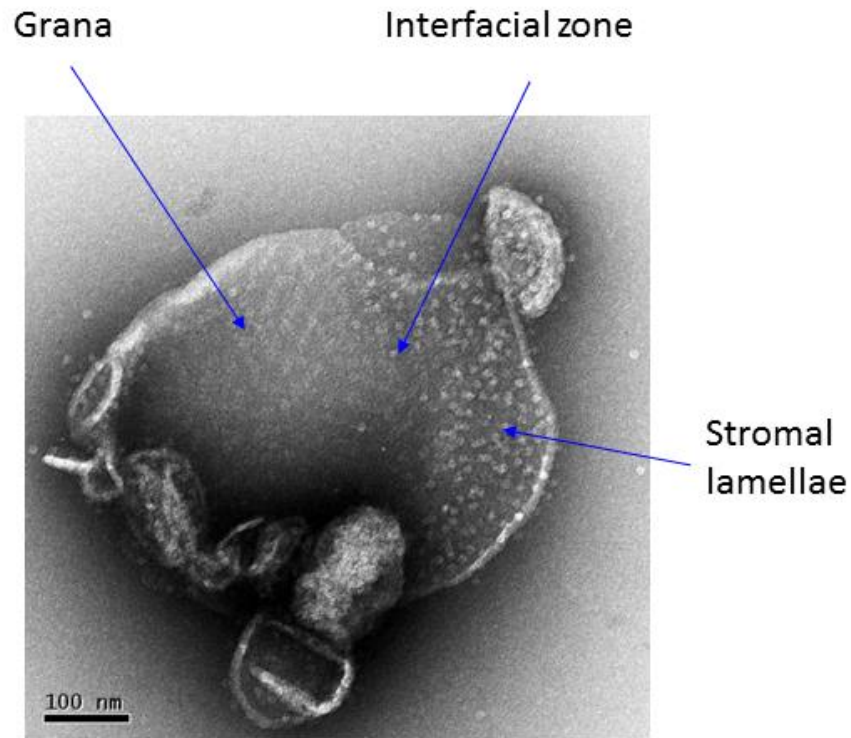


**Figure 4.15. Electron micrograph of a grana membrane produced by French Press.** The grana and contiguous stromal lamellae regions are clearly visible and indicated by blue arrows.

#### 4.4. Conclusion.

The identification of particular classes of protein complexes within AFM images still represents a significant challenge. Nevertheless, by combining biochemistry, topological height data and mechanical information derived from the AFM force-distance curves we were still able to make reasoned assignments. For the first time, the nanoscale organisation of PSI and ATP synthase in the stromal lamellae thylakoids in plants were determined, showing that they are randomly arranged in a membrane with much lower protein density than that seen in the grana, and this likely facilitates the protein diffusion dynamics required for PSII repair and state transitions.

## Chapter 5.

# Monte Carlo simulations of plastocyanin-based electron transport

### Summary

The spatial separation of PSII and PSI within the thylakoid membrane necessitate the long-range diffusion of PQ or PC. A recent AFM study (Johnson et al., 2014) has revealed that PSII and *cytb<sub>6</sub>f* are in close proximity in the grana necessitating only short-range diffusion of PQ in the protein-crowded membrane. The burden of long-range electron transport therefore falls on the luminal soluble copper-protein PC, which itself must negotiate a protein-crowded thylakoid luminal space that is likely to restrict the rate of its diffusion.

In this chapter, a model of the thylakoid membrane is constructed using AFM data acquired in previous chapters and Monte Carlo simulations were used to calculate the spatial and temporal scales involved in PC-based electron transport. The Monte Carlo sampling showed that the average diffusion distance of PC from granal *cytb<sub>6</sub>f* to PSI in the stromal lamellae is much larger than previous estimates. Moreover, the size of the grana/stromal lamellae interface, while seldom studied, is shown to have a profound impact on the distance travelled by PC. Brownian dynamics simulations were used to calculate the half-times of PC-based electron transport. Previous experimental data (Haehnel *et al.*, 1980) have shown the reduction of PSI to be a biphasic phenomenon consisting of a short (20  $\mu$ s) phase, thought to result from the electron transfer time of PSI bound reduced PC, and a long (200  $\mu$ s) phase thought to be due to diffusion of PC from *cytb<sub>6</sub>f* to PSI. The results of this chapter are consistent with this theory.

The size of the grana/stromal lamellae interface used in simulations that result in PC diffusion times most closely reflected in the observed PSI reduction kinetics were approximately one half to two thirds of the grana perimeter. It is suggested therefore that the native interface size may result from a compromise between rapid PC diffusion (large interface) and the need to minimise the deleterious spillover of excitation energy from PSII to PSI (small interface).

## 5.1. Introduction.

### 5.1.1. Modelling plastoquinone and plastocyanin electron transport.

PSII and PSI lie in separate domains of the thylakoid (the grana and stromal lamellae respectively) whereas *cytb<sub>6</sub>f* is distributed homogeneously throughout the thylakoid. This spatial separation places the burden of long-range diffusion on one or both of the mobile electron carriers plastoquinone(PQ) and plastocyanin (PC). PQ is the lipid-soluble electron carrier between PSII and *cytb<sub>6</sub>f* and PC is the soluble luminal protein, which acts as an electron carrier between *cytb<sub>6</sub>f* and PSI. Therefore, whether *cytb<sub>6</sub>f* lies in closer proximity to PSII or PSI will determine which of the two mobile electron carriers diffuses over long-distances (greater than 100 nm).

PQ is reduced at the Q<sub>b</sub> binding site of PSII, diffuses within the lipid bilayer, and is oxidised by *cytb<sub>6</sub>f*. The oxidation of PQH<sub>2</sub> at the Q<sub>o</sub> site of *cytb<sub>6</sub>f*, with half-time of 20 ms, is thought to be the rate-limiting step of LEF (Stiehl & Witt, 1969). The thylakoid membrane is a very crowded place with around 70% of the grana area being composed of protein. These integral membrane proteins, namely: PSII-LHCII, LHCII and *cytb<sub>6</sub>f*, effectively form immobile obstacles at a concentration close to that of the percolation threshold (Tremmel *et al.*, 2003; Tikhonov & Vershubskii, 2014), the point at which a mobile particle becomes trapped within a finite area or volume. Whereas, in normal diffusion, the mean-square displacement is linearly proportion to elapsed time, when diffusion is restricted by obstacles however, diffusion is anomalous and the mean-square displacement is proportional to a power of time less than one (Saxton, 1994). Due to the high packing fraction of proteins in the grana, PQ was proposed to be restricted into microdomains (Lavergne *et al.*, 1992, Joliot *et al.*, 1992). This hypothesis followed from spectroscopic analysis of PQ reduction by PSII which exhibited biphasic kinetics. The so-called 'fast' pool, which had a half-time of 25-60 ms and comprised 50-70% of the total PQ, and the 'slow' pool which had a half-time of 0.8-1 s. it was proposed that the fast pool resulted from diffusion within microdomains, which contain 3-4 PSII reaction centres, and the slow phase was the result of transport between microdomains. This concept was investigated using Monte Carlo simulation (Mitchell *et al.*, 1990; Drepper *et al.*, 1993; Tremmel *et al.*, 2003). The Brownian dynamics approach was used by Mitchell *et al.* (1990) to estimate the diffusion constant of PQ in the grana membrane. This model was based on an alternating array of PSII and *cytb<sub>6</sub>f* at a packing fraction of 0.3 and suggested that long-range PQ diffusion is possible. However, in a follow up study, results of simulations using a more realistic model (random organisation of particles at a packing fraction of 0.5-0.7) suggested that PQ is likely to be confined to small domains due to PSII and *cytb<sub>6</sub>f* percolation (Drepper *et al.*, 1993). Tremmel *et al.* (2003) modelled PQ diffusion as a point particle restricted by immobile obstacles (PSII-LHCII, LHCII, and *cytb<sub>6</sub>f*, using realistic geometries), randomly placing them on a 200x200 nm square

grid with a step size of 1 nm and periodic (torus topology) boundary conditions. In each simulation, 1000 mobile tracers representing PQ were generated from a single  $Q_b$  site of a random PSII and allowed to diffuse from that point. The results revealed a percolation threshold of 0.7, which is approximately the packing fraction of the grana. At this point, PQ was found to be restricted to finite domains with a pathlength of 15 – 20 nm (N.b. this is similar to the average nearest neighbour value of  $19.0 \pm 2.8$  nm (Fig. 4.5b) for PSII and *cytb<sub>6</sub>f* in the grana). However, estimates of the percent of binding sites  $Q_b$  of PSII, and  $Q_o$  and  $Q_r$  of *cytb<sub>6</sub>f* which were obstructed by other protein complexes (i.e. the entry of PQ into these sites was blocked) were found to be low at 13.2, 4.2 and 13.2 respectively (Tremmel *et al.*, 2003). Therefore, it seems likely that long-range PQ diffusion is extremely restricted by the density of proteins within the grana and is instead confined to small micro or nanodomains containing PSII and *cytb<sub>6</sub>f*.

Having established that PQ-based electron transport between PSII and *cytb<sub>6</sub>f* is short-range, the partitioning of PSI into the stromal lamellae indicates that PC must be a long-range diffusive electron carrier. It was first established that PC was the electron donor of PSI by measuring the reduction kinetics of  $P700^+$  (Haehnel *et al.*, 1980).  $P700^+$  shows biphasic kinetics with half-times of 20 and 200  $\mu$ s. Specific inhibition of plastocyanin reduces both phases but interestingly, addition of 200 mM sorbitol reduced both the relative amplitude and the half-time of the 200  $\mu$ s phase. Because sorbitol is known to decrease the volume of the lumen, it was proposed that this phase resulted from a ‘mobile’ plastocyanin pool. The 20  $\mu$ s phase was proposed to result from PC that was bound to PSI at the time of measurement. This agrees with the reduction half-time of PSI-bound PC of 10-14  $\mu$ s (Bottin & Matthis, 1985). Comparing the redox kinetics of PC and *cytb<sub>6</sub>f* it was observed that 70% of the plastocyanin pool is in disequilibrium with  $P700^+$  reduction (Kirchhoff *et al.*, 2004). The authors proposed that this is due to the restricted long-range diffusion of PC within the grana lumen. The 30% of the PC pool in equilibrium with *cytb<sub>6</sub>f* was proposed to be due to short-range diffusion to PSI in the grana end membranes. This static picture of PC diffusion in the lumen however, may be simplistic. Indeed, the width of the grana lumen was observed to be variable and affected by light intensity (Kirchhoff *et al.*, 2011). The thickness of the grana lumen was found to increase from  $4.7 \pm 0.8$  nm for dark-adapted thylakoids to  $9.2 \pm 0.6$  nm upon treatment with  $500 \mu$ M photons  $m^{-2}s^{-1}$  for one hour. Only in dark-adapted thylakoids were the subunits of PSII and *cytb<sub>6</sub>f* that protrude into the lumen shown to be a hindrance to long-range PC diffusion. Immunogold labelling of PC revealed that, in the dark, PC is predominantly localised in the stromal lamellae but in the light it is preferentially localised in the grana (Haehnel *et al.*, 1989). The ratio of the density of anti-PC antibody in the grana to the density in the stromal lamellae was found to increase two-fold from 0.68 in the dark to 1.25 in the light, which supports the notion that light-mediated swelling of the grana lumen facilitates PC diffusion

(Kirchhoff *et al.*, 2011). Here, using Monte Carlo simulations, we investigate PC-based electron transport in the light, paying attention to the role of the grana/stromal lamellae interface size.

## 5.2. Results.

### 5.2.1. A model of the thylakoid membrane.

Occasionally, fragments of stromal lamellae membranes remained attached to digitonin-purified grana membranes, and these could be imaged by AFM (Fig 5.1). Fig. 5.1A-C show a selection of contiguous grana/stromal lamellae membranes wherein PSI and/or ATP synthase are clearly visible. Any grana membranes which appeared to contain stromal lamellae regions but no particles were visible were excluded to avoid the possibility that they resulted from damaged grana and that the putative stromal lamellae region was the stromal face of the lower grana layer. The percentage of the grana perimeter occupied by interfacial stromal lamellae was estimated at 33%, 24% and 28% for (Fig. 5.1) A, B and C respectively. PSI and ATP synthase were observed up to the boundary of the grana and the average nearest neighbour distance for PSI was  $16.3 \pm 5.7$  nm, indistinguishable from that of PSI in purified stromal lamellae membranes. The AFM data therefore supports the idea of a strict boundary between the grana and stromal lamellae, which occurs at the interface. This is supported by the EM image of a French Press prepared grana membrane with attached stromal lamellae in chapter 4 (Fig. 4.15) that shows a strict separation of grana and stromal lamellae particles with no transitional mixed region between them. The sharp lateral heterogeneity observed in the AFM and EM images contrasts with various biochemical studies that inferred a mixed region of PSI and PSII exists at the highly-curved grana margins (e.g. Wollenberger *et al.*, 1994, Wollenberger *et al.*, 1995, Puthiyaveetil *et al.*, 2014). Comparison of the size of the PSI-LHCI complex compared with the degree of curvature of the grana margins (Fig. 5.2) shows that these regions are unable to accommodate protein, consistent with the cryo EM study of Daum *et al.*, 2010. Note also the width of the grana lumen chosen for the model, namely 10 nm, is an approximation of  $9.2 \pm 0.6$  nm for light treated thylakoids (Kirchhoff *et al.*, 2011) and that the curvature of the grana margins in dark adapted thylakoids is even more severe, with a grana lumen width of  $4.7 \pm 0.8$  nm. Therefore, the thylakoid model presented in this chapter doesn't include such a transitional region. The density of PSII and *cytb<sub>6</sub>f* in the grana and PSI in the stromal lamellae included in the model was calculated from AFM images (Fig. 5.3). The particle density of a single membrane was defined as the number of particles (Fig 5.3A,C) within a membrane, divided by the area of that membrane (Fig 5.3B,D). The average of 10 stromal lamellae membranes and 5 grana membranes were used to calculate average densities of PSI ( $0.0025 \pm 0.0002$  PSI/nm<sup>2</sup>) and PSII/*cytb<sub>6</sub>f* ( $0.0014 \pm 0.0003$  (PSII+*cytb<sub>6</sub>f*)/nm<sup>2</sup>) (Fig 5.3E).

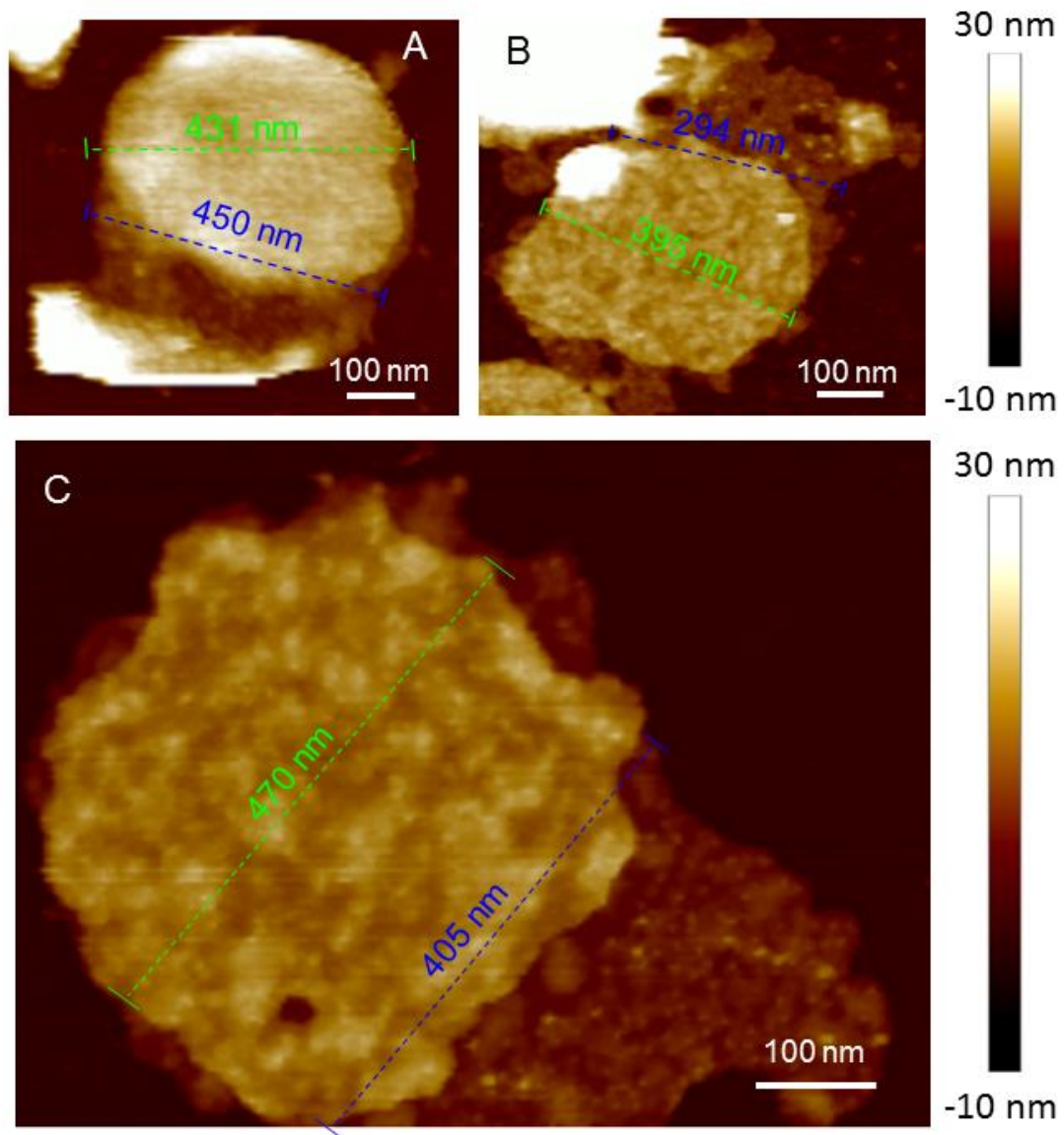


**Figure 5.1. Visualising the grana/stromal lamellae interface using AFM. A-C.** AFM images of contiguous grana and stromal lamellae membranes showing diameter of grana (green) and width of grana/stromal lamellae interface (blue).

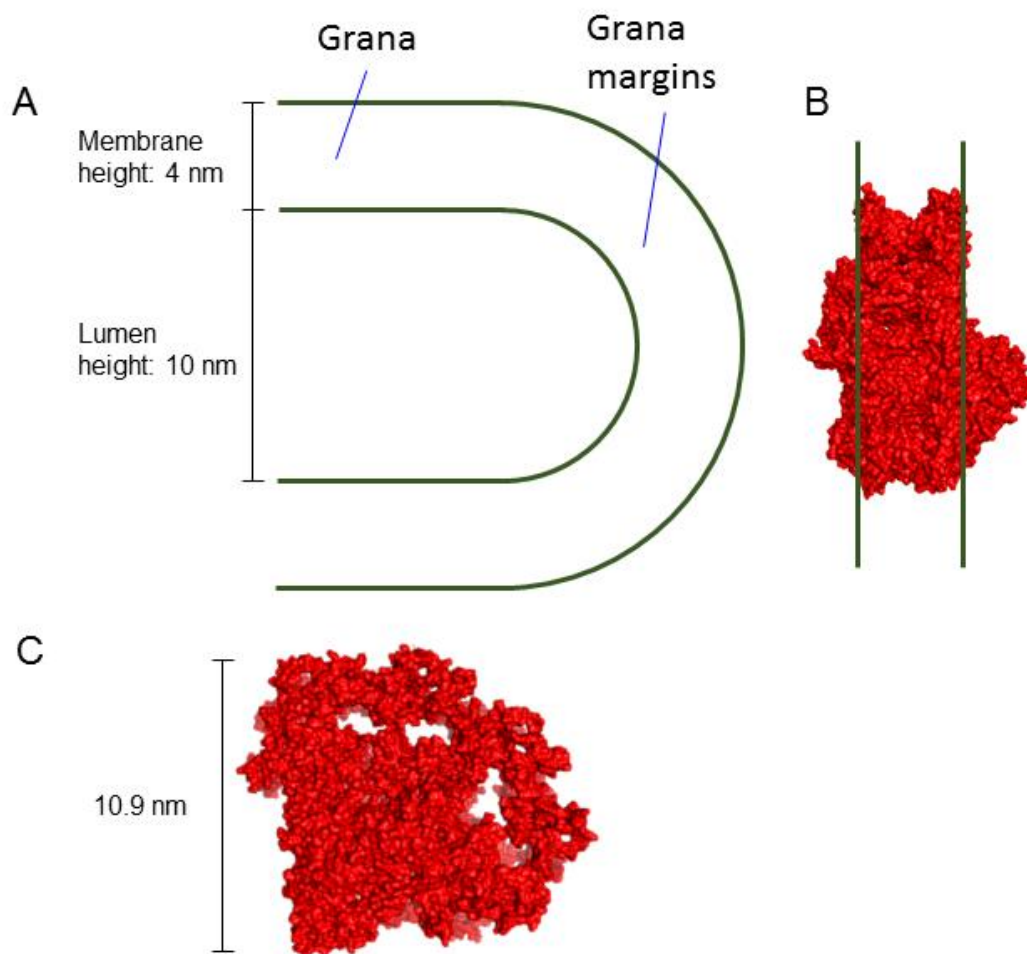


**Figure 5.2. To-scale model of a grana margin in the light and comparison with the structure of PSI-LHCI.** **A.** The grana margin is modelled with semi-circular curvature. Radii of inner and outer membrane surfaces are 5 nm and 9 nm to adhere to a model thylakoid with a 10 nm lumen. **B.** Side view of PSI-LHCI (PDB: 4Y28) to scale with (A). Green lines indicate the outer surfaces of the membrane and are separated by 4 nm. **C.** top view of PSI-LHCI with scale bar.

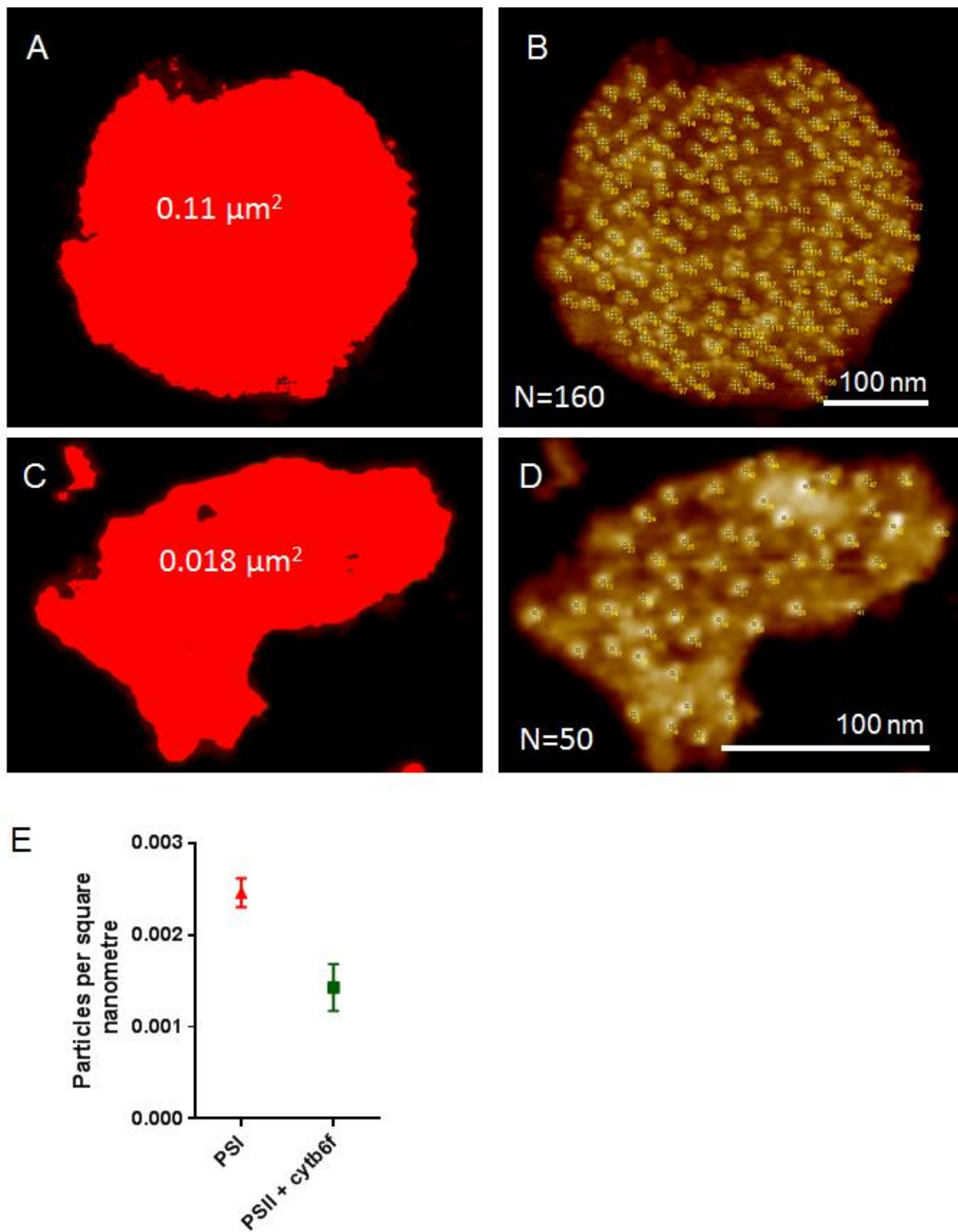


**Figure 5.3. Estimating the density of PSII and *cytb<sub>6</sub>f* in the grana and PSI in the stromal lamellae.** **A,B.** Density of PSII and *cytb<sub>6</sub>f* in the grana calculated from the area (A, red indicates pixel included in area calculation) and the number of particles (B). **C,D.** The area (C) and Number of particles (D) of a stromal lamellae membrane. **E.** Average density (No. particles  $\times$   $\text{nm}^{-2}$ ) of PSI in the stromal lamellae (red, N=10) and PSII and *cytb<sub>6</sub>f* in the grana (N=5).

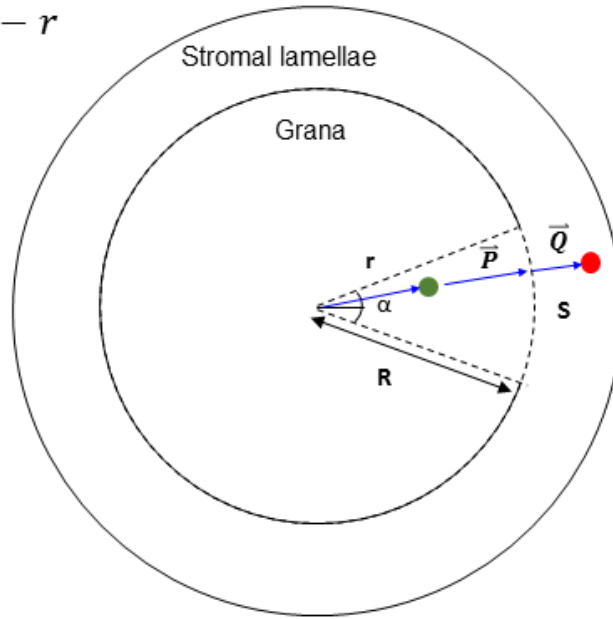
### 5.2.2. Estimating the distance travelled by PC.

The grana/stromal lamellae interface forms the gateway for the entry of reduced PC from *cytb<sub>6</sub>f* in the grana to the stromal lamellae, where it is the electron donor to PSI. A mathematical framework was developed to estimate the diffusion distance of PC involved in linear electron transport and how this distance varies with the size of the grana/stromal lamellae interface. The dependence of the PC diffusion distance on the grana/stromal lamellae interface size was estimated using Monte Carlo sampling. The shortest path from a grana particle to a stromal lamellae particle (namely *cytb<sub>6</sub>f* and PSI respectively) was defined as the sum of the lengths of two vectors (Fig. 5.4). Namely, from the grana particle to the interface ( $\vec{P}$ ) and from the interface to the nearest stromal lamellae particle ( $\vec{Q}$ ). The shortest path was defined therefore as  $|\vec{P}| + |\vec{Q}|$ . For  $\vec{P}$ , two regimes exist. Either the shortest distance to the interface is in a radial direction toward the interface (Fig. 5.4A) or further diffusion is required before reaching the edge of the interface (Fig. 5.4B). Let R and S be the radius of the grana (minus the radius of a grana particle) and the length of the interface (the point of contact between the grana and stromal lamellae) respectively. Then

$$|\vec{P}| = \begin{cases} R - r & \text{if } \theta_r \leq \alpha/2 \\ \sqrt{r^2 + R^2 - 2rR \cos(\theta_r - \alpha/2)} & \text{if } \theta_r > \alpha/2 \end{cases} \quad (1.)$$

Where  $r$  and  $\theta_r$  are the polar coordinates of the grana particle such that  $0 \leq r \leq R$  and was sampled with a square root weighting (to preserve a homogeneous particle density) and  $0 \leq \theta_r \leq \pi$  was sampled uniformly. Here  $\alpha = S/R$  is the angular width of the interface. The stromal lamellae component of the diffusive path  $\vec{Q}$  was sampled from the nearest neighbour distribution of PSI taken from AFM data.  $10^4$  distances were sampled for each interface size, ranging from 10 to 1500 nm in steps of 10 nm (Fig. 5.5A). As noted previously, the interface was often observed to occupy approximately one third to one half of the periphery of the grana (Fig. 5.1). This gives a range of average distances for PC diffusion of 207 – 228 nm, and range much higher than previous estimates 60-70 nm which assumed an annulus of PSI at the periphery of the grana (Kirchhoff *et al.*, 2004). This is equivalent to the limit as the interface size approaches the grana perimeter size in our simulations and the value of 80 nm for PC diffusion distance at an interface size of 1500 nm reflects this. The graph in Fig. 5.5A shows the mean and standard deviation of the PC diffusion distances over a range of interface sizes. This however is a simplification of a much more complex distribution when visualised in 3-D (Fig. 5.5B). This is largely due to the cycloidal component of  $|\vec{P}|$ .

A  $\vec{P} = R - r$



B  $\vec{P} = \sqrt{r^2 + R^2 - 2rR \cos(\theta_r - \alpha/2)}$

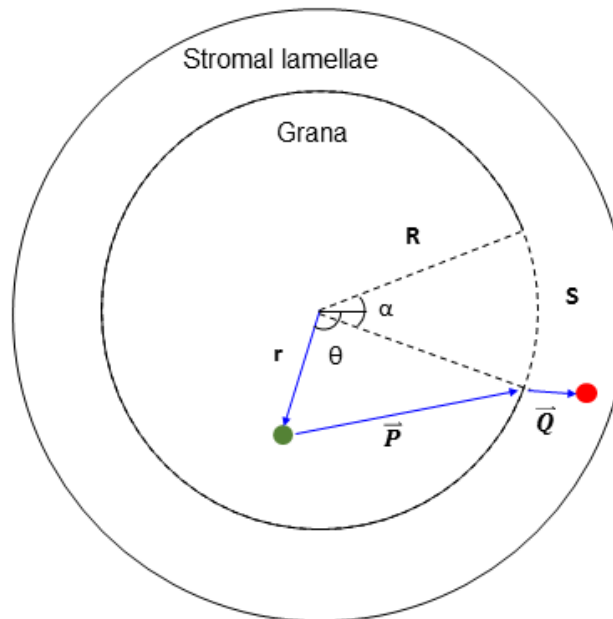


**Figure 5.4. Vectorial representation used to calculate distances between grana (green circle) and stromal lamellae (red circle) particles.** The distance from the grana particle to the nearest point on the interface is calculated ( $\vec{P}$ ). **A.** When the grana particle lies within the region enclosed by dashed lines. **B.** When the grana particles lies outside the region enclosed by dashed lines.

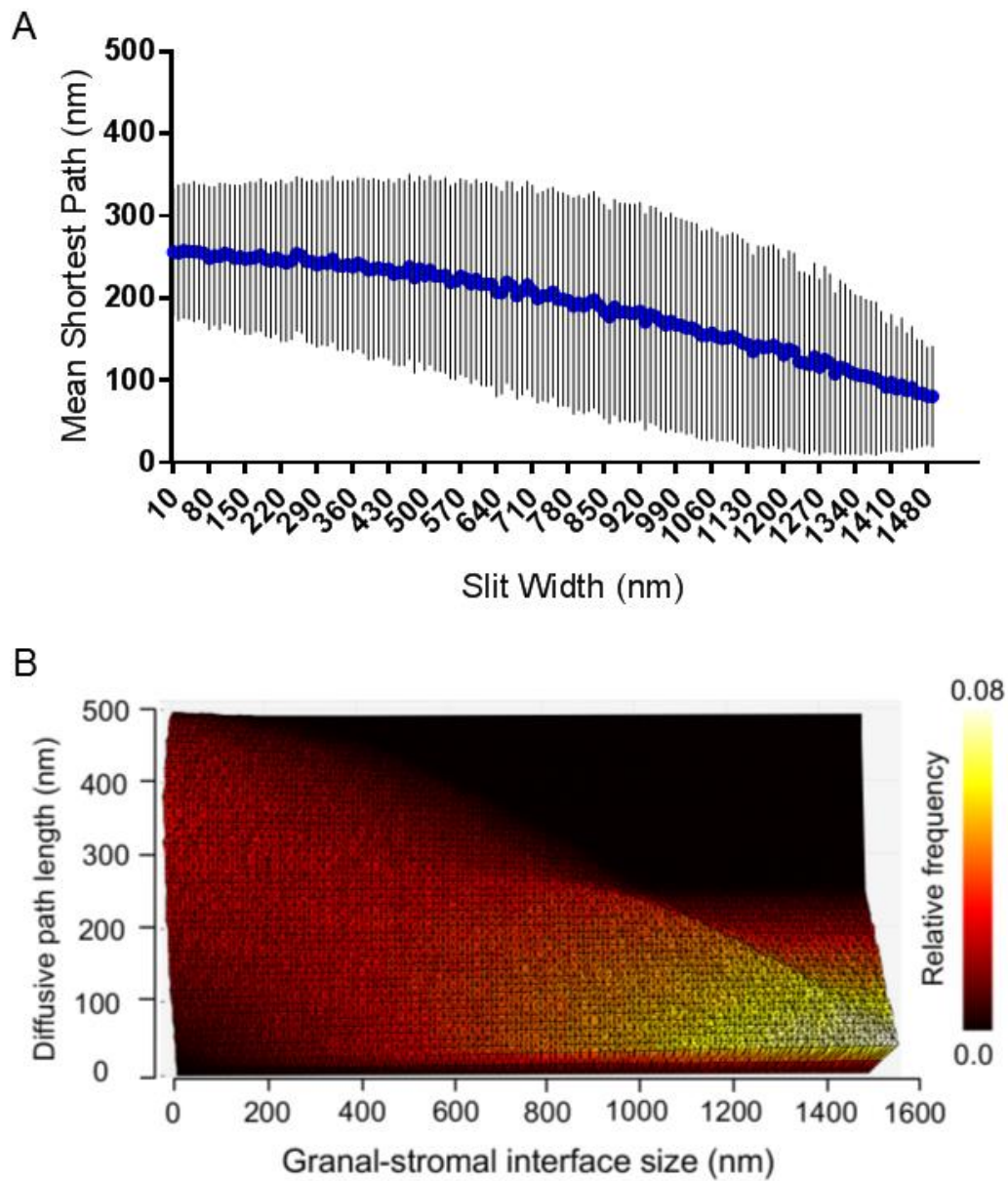


**Figure 5.5. Estimating the diffusive distance of cytb<sub>6</sub>f to PSI electron transport by PC. A.** The mean diffusive distance of PC (blue) and standard deviation. Each value is based on 10000 data points. **B.** A 3-D histogram of data presented in (A).

### 5.2.3. Brownian dynamics simulations of PC-based electron transport.

For time-resolved simulations, a model of a thylakoid membrane system was constructed containing a grana region a stromal lamellae region and an interfacial zone to allow for the passage of PC (Fig. 5.6; Fig. 5.7). The grana were composed of two layers separated by 10 nm (An approximation of  $9.2 \pm 0.6$  nm from Kirchhoff *et al.* (2011)) and of radius 250 nm, each containing 277 particles (density:  $1.4 \times 10^{-3} \text{ nm}^{-2}$ ). The stromal lamellae consisted of two layers also separated by 10 nm, each a 100 nm circle concentric of the grana, containing 462 particles (density:  $2.45 \times 10^{-3} \text{ nm}^{-2}$ ). For simplicity grana and stromal lamellae particles were modelled as hard disks of radius 6.7 nm and 5 nm respectively and were stationary over the course of the simulations. These dimensions were determined from the smallest observed nearest neighbour values in the AFM data. The grana particles (considering the approximation of 1 nm for the radius of PC) protrude into the luminal space effectively by 5 nm as cylinders of radius 6.7 nm. The membranes were populated by particles in the following way (Fig. 5.6A): a particle was placed at a random point within the allowed space. If the space was already occupied by another particle, the new particle was moved around in small, random increments until an unoccupied area was found. This was repeated until the correct particle density was acquired (Fig 5.6B). To test the role of PSI-PSI interactions in the organisation of PSI in stromal lamellae membranes, 153 PSI particles were placed on a 250x250 nm grid with periodic (torus-topology) boundary conditions (i.e. when a particle passes the right-hand boundary it appears on the left-hand side). The particles were allowed to interact with one-another via a linear potential essentially as described in (Duneau & Sturgis, 2013)(Fig. 5.6C). The maximum range of the potential was at a PSI centre to centre distance of 10 nm and increased from a minimum interaction energy at contact, ranging from 0 to 2  $K_B T$ , to zero at this point. The average nearest neighbour distance was observed to closely resemble experimental (AFM) data when no potential (0.0  $K_B T$ ) was incurred (Fig. 5.6D). The average nearest neighbour distances of the zero-potential model and the AFM data were  $13.9 \pm 3.1$  nm and  $15 \pm 2.8$  nm respectively, suggesting a random organisation of PSI is appropriate to model the thylakoid membrane.

In the previous chapter (Fig. 4.6) we described the identification of dimers with the criterion of centre-to-centre distances less than 14 nm. This was to include only core-to-core contacts. The AFM suggested 25.5 % of 381 particles were dimeric. However, the nearest neighbour distribution of the zero-potential model of Fig. 5.6D predicted 52.9% of PSI were dimeric by this criterion. This extremely high result was likely due to the use of hard discs to model PSI geometry. To obtain a more accurate distribution we used the PDB structure 4Y28 to produce a model of PSI of realistic geometry. The structure was projected onto the plain of the thylakoid membrane (z was set to zero) and onto a

square grid of 1 nm spacing. A novel algorithm was developed for the detection of overlap between particles. Particle geometries were represented by a matrix P of dimension mxn in m dimensions. In 2 dimensions, the columns of P contain the coordinates of cells occupied by the particle. Average (x,y) values were subtracted to centre the particle at the origin. Spatial ( $X_i$ ) and rotational ( $\theta_i$ ) coordinates of a set of particles were used to transform the original P to a given point in space  $P'$

$$P'_i = T(R(\theta_i), X_i) \quad (2.)$$

Where T and R are translation and rotation operations.

We define the matrix M as the concatenation of all  $P'_i$  along the column axis:

$$M(2 \times N) = [P'_1 P'_2 \dots P'_N] \quad (3.)$$

For each time step

$$P'_i(X_i, \theta_i) \rightarrow P'_i(X_i + \Delta X_i, \theta_i + \Delta \theta_i) \quad (4.)$$

The new M is created. We define the function  $\eta_{\text{unique}}(M)$  as the number of unique columns of M.

Theorem 1.  $P'_i(X_i + \Delta X_i, \theta_i + \Delta \theta_i)$  spatially overlaps at least one other particle in M if and only if

$$\eta_{\text{unique}}(M) < \eta_{\text{unique}}(P'_i(X_i + \Delta X_i, \theta_i + \Delta \theta_i)) + \eta_{\text{unique}}(M | P'_i(X_i + \Delta X_i, \theta_i + \Delta \theta_i)) \quad (5.)$$

Where  $A|B$  (A but not B) refers to the set difference of the columns of A and B.

Proof: as  $\eta_{\text{unique}}(M)$  is equivalent to the number of elements in the set of columns of M and because M contains the columns of  $P'_i$  then

$$\{Col(P'_i)\} \subset \{Col(M)\} \quad (6.)$$

Which is equivalent to

$$\forall x \in \{Col(M)\}, x \in \{Col(P'_i)\} \text{ or } x \in \{Col(M|P'_i)\} \text{ or } x \in \{Col(P'_i) \cap \{Col(M|P'_i)\} \} \quad (7.)$$

And so

$$\eta_{\text{unique}}(M) = \eta_{\text{unique}}(P'_i) + \eta_{\text{unique}}(M | P'_i) - |\{Col(P'_i)\} \cap \{Col(M|P'_i)\}| \quad (8.)$$

Where  $||$  refers to the cardinality of the set. This is equivalent to (5.) if

$$|\{Col(P'_i)\} \cap \{Col(M|P'_i)\}| > 0 \quad (9.)$$

Implying, if true, that there exists at least one column common to both  $P'_i$  and  $M|P'_i$   $\square$

We use existing libraries for the function  $\eta_{\text{unique}}$ , namely the Python Pandas module, but significantly reduce computation time by defining a suitable function  $f$  which maps the rows of  $M$  onto a 1D space

$$f: M(m \times N) \rightarrow M(1 \times N) \quad (10.)$$

such that the uniqueness of the columns of  $M$  is preserved. For  $n$  dimensions, we find a suitable  $f$  in the form

$$f(M) = CM \quad (11.)$$

where

$$C = [1 \ c_1 \ c_2 \ \dots \ c_n] : c_1 > \text{range}(M_{1j}), c_2 > \text{range}(M_{2j}) \times c_1, \dots, \text{range}(M_{nj}) \times c_1 \times c_2 \times \dots \times c_n \quad (12.)$$

In 2 dimensions

$$f(M) = f(x, y) = x + c_1 y \quad (13.)$$

Here range refers to the maximum number of accessible cells along a given dimension, not the range in the chosen unit of distance.

Theorem 2. Column  $i$  of  $f(M) = CM$  is unique in  $CM$  if and only if column  $i$  of  $M$  is unique in  $M$ .

Proof: let  $x_n$  be the index of the  $n^{\text{th}}$  cell along the  $x$  axis then

$$f(x_n, y_m) = c_1 m + n \quad (14.)$$

Allowing  $y_n$  to be equal to zero we find

$$f(x_n, 0) = n \quad (15.)$$

Which is uniquely defined for all  $m$ . Along the  $y$  axis we also find.

$$f(x_n, y_{m+1}) = f(x_n, y_m) + c_1 \quad (16.)$$

Which, by induction, defines  $f$  uniquely along the  $y$  axis. The same proof by induction extends to higher dimensions if (12.) is true  $\square$

522 PSI-LHCI particles (density:  $2.45 \times 10^{-3} \text{ nm}^{-2}$ ) were placed on a square grid and allowed to evolve in time as in Fig. 5.6 (Fig. 5.7A). The average nearest neighbour distance was  $15.6 \pm 2.9$  (Fig. 5.7B) which more closely resemble that observed in AFM images ( $15 \pm 2.8 \text{ nm}$ ). A large difference in the

fraction of PSI that exist as dimers was observed in the realistic geometry model compared to the hard-disc model. For the realistic geometry model, 23% of PSI particles were dimeric. This was much closer to the value of 25.5% observed in AFM data (see Chapter 4.2.4) than 52.9% as observed in the hard-disc model. However, one should note that as the simulations in Fig. 5.7 describe a random organisation of PSI-LHCI, the fact that the number of dimers in the model and in the AFM data so closely resemble one another may be at odds with the claims made in chapters 4.2.4 and 4.3.1 that PSI retain a degree of capacity to form dimers *in vivo*. In light of the structure of dimeric PSI described by Yadav *et al.* 2017, it seems that the degree to which PSI forms dimers in plants is not yet clear.

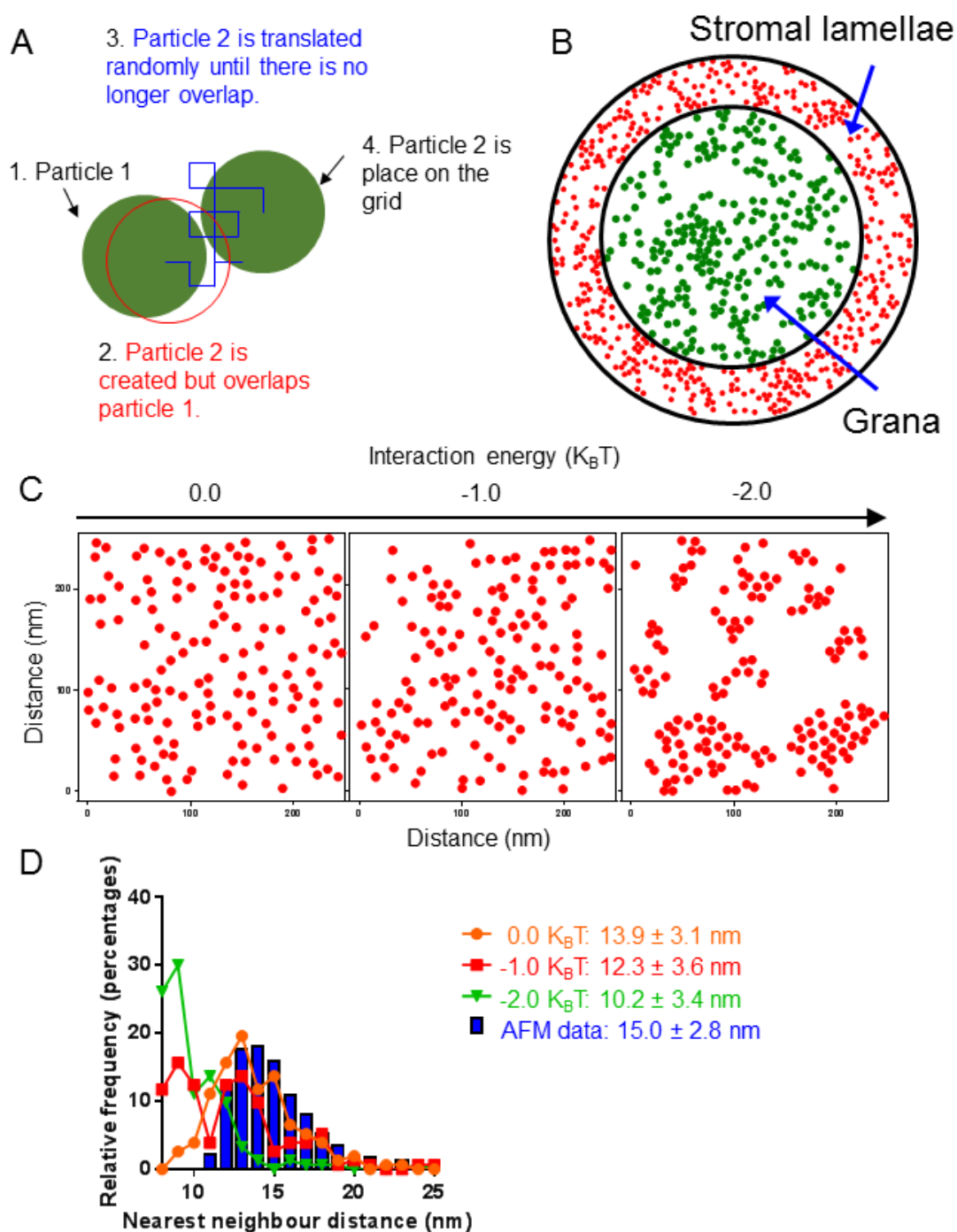


**Figure 5.6. Construction of the thylakoid model.** **A.** Particles were placed on a grid at random and moved in random increments if overlaps occurred. **B.** The populated system of particles as a result of algorithm described in (A). **C.** Equilibrium organisation of 153 PSI particles in the thylakoid model interacting via a linear potential of **D.** Equilibrium nearest neighbour distributions of PSI particles in the thylakoid model with interaction energies of 0 (orange), 1 (red) and 2 (green)  $K_B T$  alongside AFM data (blue columns) for comparison.

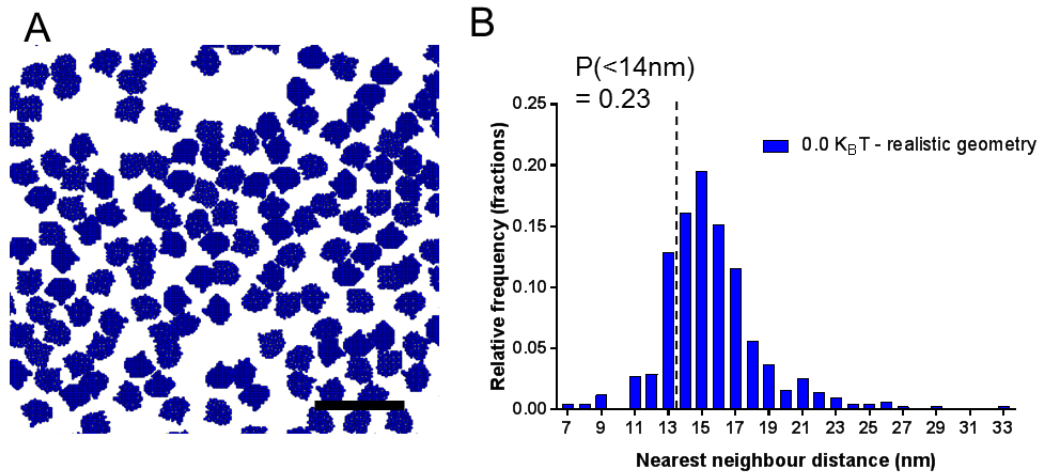


**Figure 5.7. Simulating the organisation of PSI-LHCI using particles of realistic geometry.** **A.** 250 nm x 250 nm image of PSI-LHCI particles. Scale bar = 50 nm. **B.** Nearest neighbour distribution based on 522 particles. The mean nearest neighbour distance was  $15.6 \pm 2.9$  nm and 23% PSI particles existed as dimers according to the criterion of centre to centre distance less than 14 nm.

Once the membranes were populated as described in Fig. 5.6A,B, a random organisation of the particles was ensured by allowing the particles to diffuse randomly for  $10^6$  time steps (Fig. 5.8A). The resulting nearest neighbour distribution of the grana (Fig. 5.8C) and stromal lamellae particles (Fig. 5.8D) had mean values of  $15.6 \pm 4.6$  and  $11.5 \pm 3.2$  nm. These were found to closely experimentally derived nearest neighbour distributions, which had mean values of  $19.0 \pm 2.8$  nm and  $15.4 \pm 2.8$  nm for PSII and *cytb<sub>6</sub>f* in the grana and PSI in stromal lamellae respectively (see Fig. 4.5). The computationally derived distributions did however seem to be more positively skewed, probably due to the lack of other particles within the model which would serve to increase the separation distance on the average.

To calculate the time taken for PC to diffuse between *cytb<sub>6</sub>f* and PSI, 150 random walk simulations were carried out on a 3-dimensional square lattice with 1 nm spacing, for each interface size, ranging from 50 – 1500 nm (the approximate range for a grana of 500 nm diameter). The random walk was terminated when PC was within 5 nm of the centre of PSI (Kovalenko *et al.*, 2016). A diffusion coefficient for PC (*D*) of  $0.9 \times 10^{-8}$  cm<sup>2</sup>s<sup>-1</sup> was used (Sanderson *et al.*, 1986). The grana particles (taking into account the approximation of 1 nm for the radius of PC) protrude into the luminal space effectively by 5 nm as cylinders of radius 6.7 nm (note that because of the random organisation of PSII and *cytb<sub>6</sub>f*, they are effectively indistinguishable from one another. This is why the general term *grana particle* is used). For each random walk simulation, a PC was spawned at a random grana particle and a random walk was generated until the PC particle came within the radius (5 nm) of a PSI particle in the stromal lamellae. The time step was calculated according to

$$\langle X^2 \rangle = 6D\Delta t \quad (17.)$$

where X is the grid spacing of 1 nm as previously described.

The calculated mean time of PC diffusion over a range of interface sizes is shown in Fig. 5.9A and covers a large range of values from 2.4 ms (interface = 50 nm) to 0.1 ms (interface = 1450 nm). To compare simulated diffusion times to experimentally derived values it was more appropriate to work with the half-time of the diffusive paths. That is the time taken for half of the PC to diffuse between *cytb<sub>6f</sub>* and PSI for a given interface size. In order to calculate the half-times of PC diffusion, a histogram of times taken was constructed for each interface size (Fig. 5.9B) and was fit with an exponential decay function (Fig. 5.9C)

$$F(t) = Y_0 e^{-Kt} \quad (18.)$$

Where t is the time in milliseconds, Y<sub>0</sub> is the y intercept and K is rate of decay. The curves were fitted using generalised least-squares (Parameters and goodness-of-fit values given in Table 1). The half-time (t<sub>1/2</sub>) of the process can then be calculated using

$$t_{1/2} = \frac{\ln 2}{K} \quad (19.)$$

The calculated half-times for PC diffusion as a function of interface size are given in Fig 9D.

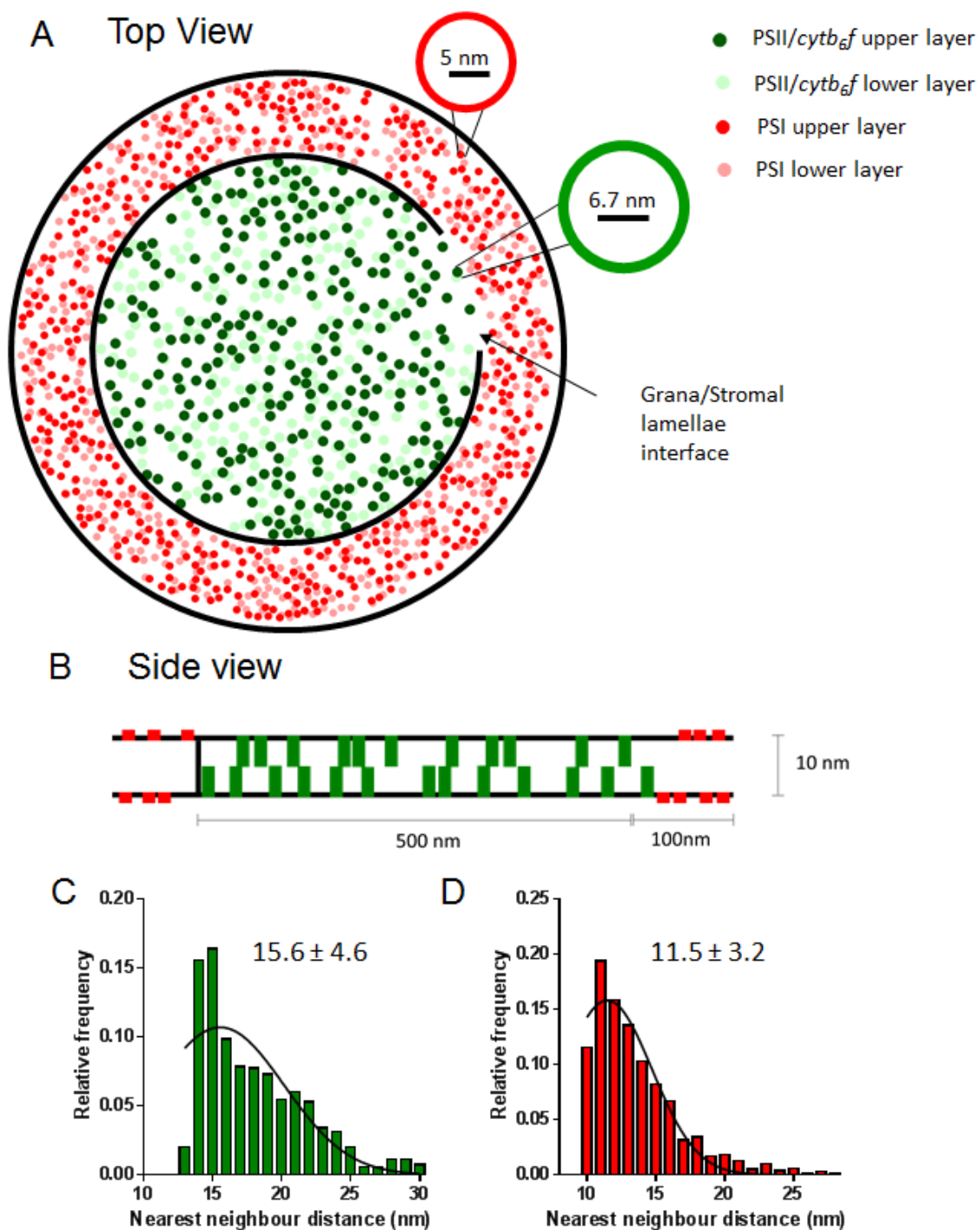


**Figure 5.8. Modelling the thylakoid membrane and luminal space.** A,B. Thylakoid model and grana/stromal lamellae particle arrangement used for time-resolved PC diffusion simulations after  $10^6$  Monte Carlo time steps to ensure random mixing. (A) shows the view from above (perpendicular to the grana membrane) and (B) shows the view from the side showing grana particles protruding into the lumen. C. Nearest neighbour distribution of grana particles in (A, top layer.  $N=277$ ). D. Nearest neighbour distribution of stromal lamellae particles in (A, top layer.  $N=462$ )

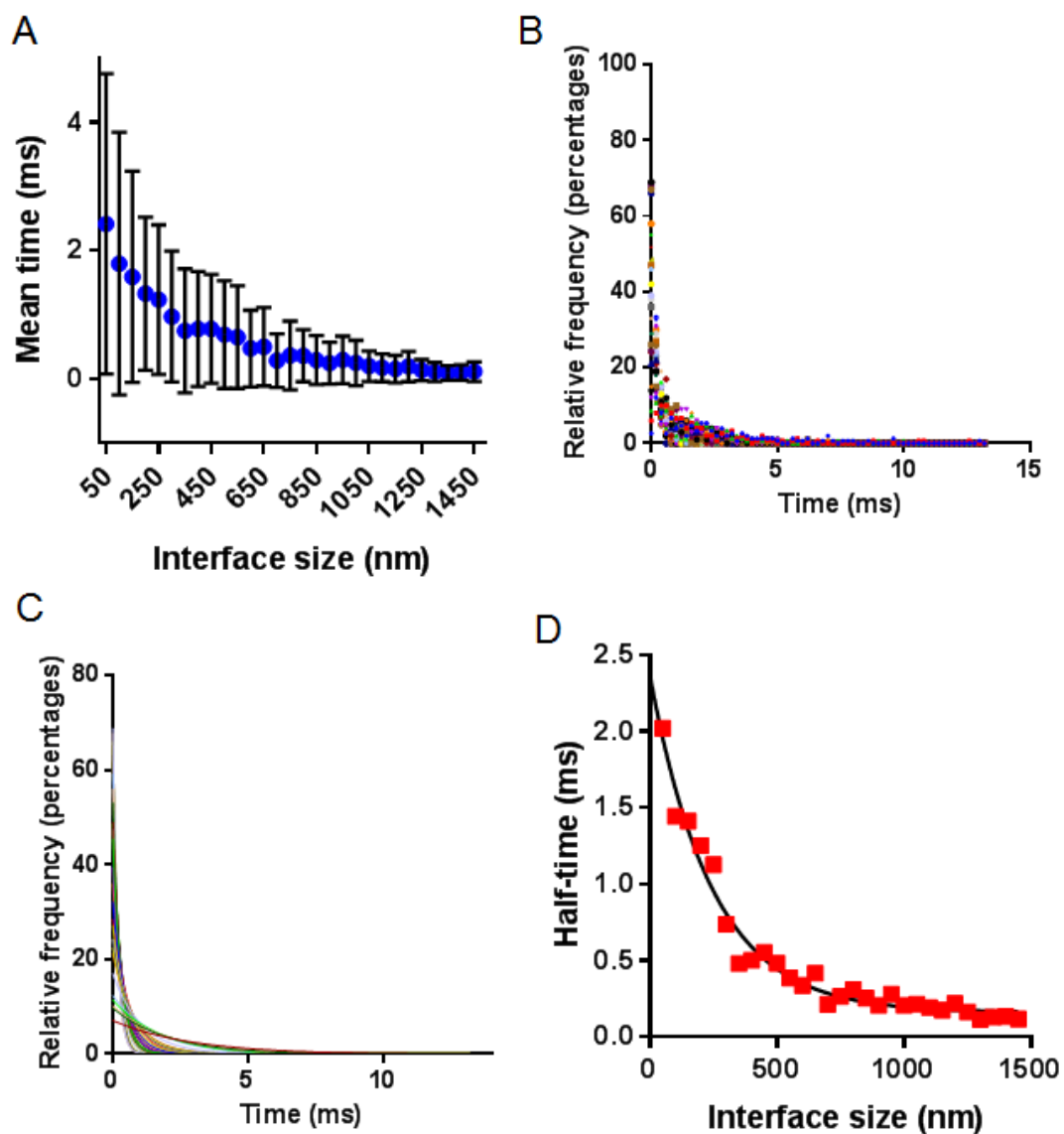


**Figure 5.9. Results of PC diffusion simulations.** **A.** mean time (ms) taken for PC to diffuse between cytb<sub>6</sub> in the grana to PSI in the stromal lamellae as a function of interface size (nm). **B,C.** Frequency distributions (B) and exponential fits of frequency distributions (C) for diffusive times for each interface size. **D.** Half-times of PC diffusion as a function of interface size.

Parameter	50	100	150	200	250	300	350	400	450	500	550	600	650	700	750	800	850	900	950	1000	1050	1100	1150	1200	1250	1300	1350	1400	1450	
meanFit Size	50	100	150	200	250	300	350	400	450	500	550	600	650	700	750	800	850	900	950	1000	1050	1100	1150	1200	1250	1300	1350	1400	1450	
Best-fit values	7.098	8.703	10.13	11.42	12.33	14.94	23.72	22.43	21.23	24.21	27.14	32.12	28.43	48.41	39.12	35.59	41.44	37.36	36.59	47.49	48.92	52.97	55.92	58.09	68.74	67.48	64.99	67.69		
Parameter	-0.165	-0.105	-0.1514	-0.1566	-0.1147	0.01333	0.08861	0.1081	0.06651	0.05162	0.1581	0.07764	0.09986	0.07533	0.03348	0.004715	0.01292	0.04599	-0.03481	0.03499	-0.06036	-0.04999	-0.00054	-0.00987	-0.0735	0.01312	-0.05155	-0.03997	0.03697	
K	0.3428	0.4797	0.4802	0.5328	0.6139	0.9379	1.448	1.378	1.282	1.44	1.796	2.062	1.661	3.248	2.615	2.219	2.708	3.349	2.476	3.137	3.21	3.598	3.593	3.148	4.214	6.005	5.189	5.182	5.917	
Half life	2.022	1.445	1.434	1.324	1.139	0.7394	0.4798	0.5026	0.5338	0.4814	0.3888	0.3361	0.4172	0.2156	0.2661	0.3123	0.2862	0.207	0.28	0.2083	0.216	0.2827	0.1791	0.2203	0.1645	0.1155	0.131	0.1345	0.1171	
Tau	2.918	2.085	2.04	1.809	1.639	1.087	0.6922	0.7365	0.7989	0.6945	0.5697	0.4889	0.6019	0.3082	0.3824	0.4505	0.3696	0.2985	0.4039	0.3006	0.3116	0.278	0.2541	0.3178	0.2373	0.1666	0.1891	0.1941	0.169	
Std Error	7.114	8.808	10.1	11.57	12.45	16.94	23.64	22.12	21.16	24.16	28.98	32.04	28.44	43.31	35.26	33.96	41.43	37.32	36.96	47.46	48.97	53.02	55.96	48.57	58.15	68.71	67.54	66.03	67.66	
Parameter	0.632	0.51	0.5128	0.7033	0.6339	0.8067	0.8061	0.8335	0.7303	1.109	0.7338	0.9905	0.9865	0.6407	0.5379	0.478	0.3978	0.4677	0.3178	0.5658	1.114	0.8309	0.9843	1.021	0.7923	0.4092	0.5304	0.5149	0.4893	
K	0.1142	0.17	0.1702	0.2051	0.1707	0.1627	0.1331	0.1389	0.1314	0.1153	0.1485	0.09205	0.08549	0.07737	0.06885	0.05478	0.1152	0.1007	0.07521	0.1796	0.06983	0.07735	0.137	0.1024	0.05166	0.09737	0.06551	0.0618	0.0645	
Std Error	0.9968	0.4892	0.5003	0.6859	0.6162	0.7996	0.8047	0.8235	0.7478	1.1307	0.7338	0.9919	0.9385	0.6453	0.3295	0.4789	0.399	0.8713	0.7396	0.5961	1.319	0.5334	0.6012	1.028	0.7965	0.4119	0.3358	0.318	0.4873	
Confidence Interval	5.835	8.684	9.107	10.01	11.05	13.33	22.11	20.78	18.75	21.59	25.64	30.14	27.26	44.13	38.20	35.00	40.63	45.63	38.48	46.36	46.39	46.39	51.91	54.73	46.47	57.51	67.92	66.42	64.96	66.72
Parameter	8.390	10.72	11.39	12.82	13.61	18.37	25.33	24.07	22.72	26.82	28.69	34.10	29.60	46.69	40.43	36.91	42.24	49.09	41.36	48.62	51.54	54.03	57.12	50.35	60.67	59.56	68.34	67.02	68.67	
K	0.7427	0.4447	0.4915	0.5664	0.4358	0.3116	0.1793	0.1692	0.1890	0.3808	0.0712	0.2129	0.1929	0.09544	0.1011	0.1423	0.1842	0.2360	0.1153	0.4012	0.1895	0.1951	0.3335	0.2611	0.07808	0.07808	0.07808	0.07808	0.07808	0.07808
Std Error	2.516	2.247	2.1887	2.292	2.265	2.192	2.352	2.389	2.129	0.4840	0.3884	0.3682	2.1749	0.2461	0.2080	0.1528	0.1214	0.2762	0.1664	2.1852	0.3003	0.08951	0.1150	0.2137	0.1470	0.1283	0.08304	0.09091	0.11604	
Parameter	0.2098	0.3842	0.3968	0.4208	0.5018	0.7837	1.275	1.202	1.100	1.172	1.621	1.883	1.542	1.066	2.477	2.113	2.609	3.108	2.313	1.172	2.875	3.454	3.763	2.891	3.977	5.827	5.099	4.899	5.710	
K	0.4737	0.5743	0.5837	0.6791	0.7260	1.089	1.614	1.551	1.403	1.708	1.972	2.280	1.780	3.423	2.753	2.326	2.803	3.990	2.619	3.483	3.544	3.742	4.108	3.402	4.851	6.176	5.480	5.314	6.124	
Std Error	1.487	1.207	1.188	1.037	0.9548	0.6364	0.4239	0.4470	0.4841	0.4039	0.3027	0.3893	0.3027	0.2023	0.2800	0.2473	0.2673	0.191	0.2627	0.1990	0.1956	0.1687	0.2038	0.1397	0.1132	0.1132	0.1132	0.1132	0.1132	
Half life	1.304	1.800	1.747	1.610	1.381	0.8812	0.5434	0.5796	0.6299	0.5914	0.4277	0.3777	0.2484	0.2261	0.2798	0.2380	0.2687	0.2186	0.2397	0.2185	0.2412	0.2007	0.1842	0.2398	0.1743	0.1190	0.1199	0.1195	0.1214	
Tau	1.787	2.596	2.520	2.322	1.995	1.275	0.7840	0.8318	0.9087	0.8312	0.6170	0.5449	0.3361	0.4027	0.4733	0.3983	0.5217	0.4124	0.3153	0.3479	0.2996	0.2658	0.3459	0.2514	0.1716	0.1961	0.2012	0.2175		
Std Error	5.022	8.822	8.281	10.20	11.19	13.35	22.03	20.67	18.67	21.85	25.48	30.06	27.27	44.05	38.15	35.00	40.63	45.63	38.48	46.36	46.39	46.39	51.91	54.73	46.47	57.51	67.92	66.42	64.96	66.72
Parameter	8.409	10.79	11.31	12.84	13.70	18.94	25.23	23.99	22.69	24.77	28.49	34.02	29.61	46.62	40.38	36.92	42.23	49.06	41.40	48.59	51.61	54.09	57.16	50.62	60.74	59.34	68.60	67.07	68.64	
Confidence Interval	5.835	8.684	9.107	10.01	11.05	13.33	22.11	20.78	18.75	21.59	25.64	30.14	27.26	44.13	38.20	35.00	40.63	45.63	38.48	46.36	46.39	46.39	51.91	54.73	46.47	57.51	67.92	66.42	64.96	66.72
Parameter	8.390	10.72	11.39	12.82	13.61	18.37	25.33	24.07	22.72	26.82	28.69	34.10	29.60	46.69	40.43	36.91	42.24	49.09	41.36	48.62	51.54	54.03	57.12	50.35	60.67	59.56	68.34	67.02	68.67	
Confidence Interval	5.835	8.684	9.107	10.01	11.05	13.33	22.11	20.78	18.75	21.59	25.64	30.14	27.26	44.13	38.20	35.00	40.63	45.63	38.48	46.36	46.39	46.39	51.91	54.73	46.47	57.51	67.92	66.42	64.96	66.72
Parameter	0.7427	0.4447	0.4915	0.5664	0.4358	0.3116	0.1793	0.1692	0.1890	0.3808	0.0712	0.2129	0.1929	0.09544	0.1011	0.1423	0.1842	0.2360	0.1153	0.4012	0.1895	0.1951	0.3335	0.2611	0.07808	0.07808	0.07808	0.07808	0.07808	0.07808
Std Error	2.516	2.247	2.1887	2.292	2.265	2.192	2.352	2.389	2.129	0.4840	0.3884	0.3682	2.1749	0.2461	0.2080	0.1528	0.1214	0.2762	0.1664	2.1852	0.3003	0.08951	0.1150	0.2137	0.1470	0.1283	0.08304	0.09091	0.11604	
Confidence Interval	5.835	8.684	9.107	10.01	11.05	13.33	22.11	20.78	18.75	21.59	25.64	30.14	27.26	44.13	38.20	35.00	40.63	45.63	38.48	46.36	46.39	46.39	51.91	54.73	46.47	57.51	67.92	66.42	64.96	66.72
Parameter	8.390	10.72	11.39	12.82	13.61	18.37	25.33	24.07	22.72	26.82	28.69	34.10	29.60	46.69	40.43	36.91	42.24	49.09	41.36	48.62	51.54	54.03	57.12	50.35	60.67	59.56	68.34	67.02	68.67	
Confidence Interval	5.835	8.684	9.107	10.01	11.05	13.33	22.11	20.78	18.75	21.59	25.64	30.14	27.26	44.13	38.20	35.00	40.63	45.63	38.48	46.36	46.39	46.39	51.91	54.73	46.47	57.51	67.92	66.42	64.96	66.72
Parameter	0.7427	0.4447	0.4915	0.5664	0.4358	0.3116	0.1793	0.1692	0.1890	0.3808	0.0712	0.2129	0.1929	0.09544	0.1011	0.1423	0.1842	0.2360	0.1153	0.4012	0.1895	0.1951	0.3335	0.2611	0.07808	0.07808	0.07808	0.07808	0.07808	0.07808
Std Error	2.516	2.247	2.1887	2.292	2.265	2.192	2.352	2.389	2.129	0.4840	0.3884	0.3682	2.1749	0.2461	0.2080	0.1528	0.1214	0.2762	0.1664	2.1852	0.3003	0.08951	0.1150	0.2137	0.1470	0.1283	0.08304	0.09091	0.11604	
Confidence Interval	5.835	8.684	9.107	10.01	11.05	13.33	22.11	20.78	18.75	21.59	25.64	30.14	27.26	44.13	38.20	35.00	40.63	45.63	38.48	46.36	46.39	46.39	51.91	54.73	46.47	57.51	67.92	66.42	64.96	66.72
Parameter	8.390	10.72	11.39	12.82	13.61	18.37	25.33	24.07	22.72	26.82	28.69	34.10	29.60	46.69	40.43	36.91	42.24	49.09	41.36	48.62	51.54	54.03	57.12	50.35	60.67	59.56	68.34	67.02	68.67	
Confidence Interval	5.835	8.684	9.107	10.01	11.05	13.33	22.11	20.78	18.75	21.59	25.64	30.14	27.26	44.13	38.20	35.00	40.63	45.63	38.48	46.36	46.39	46.39	51.91	54.73	46.47	57.51	67.92	66.42	64.96	66.72
Parameter	0.7427	0.4447	0.4915	0.5664	0.4358	0.3116	0.1793	0.1692	0.1890	0.3808	0.0712	0.2129	0.1929	0.09544	0.1011	0.1423	0.1842													

### 5.3. Discussion.

#### 5.3.1. Implications for P700<sup>+</sup> reduction kinetics.

Previous studies of P700<sup>+</sup> reduction by PC have found the kinetics to be biphasic, with half-times of 20  $\mu\text{s}$  and 200-300  $\mu\text{s}$  (Haehnel *et al.*, 1980). As the half-time of electron transfer between PC and PSI is 12-18  $\mu\text{s}$  (Antal, 2013), the 20  $\mu\text{s}$  phase is most likely the result of PC bound to PSI at the time of measurement. It has been proposed that the 200-300  $\mu\text{s}$  phase is due to the long-range diffusion from the grana to the stromal lamellae (Kirchhoff *et al.*, 2004). The results of the simulations of PC diffusion show that the half-times for this process vary between 2 ms and 117  $\mu\text{s}$ . This supports the notion that the 200-300  $\mu\text{s}$  phase results from the long-range diffusion of PC (Kirchhoff *et al.*, 2011). Half-time values between 200 and 300  $\mu\text{s}$  (Fig. 5.10A, Magenta) were observed from interface sizes of 700-1050 (Fig. 5.10A, Yellow), approximately one half to two thirds of the grana perimeter. This is somewhat consistent with the size of the grana/stromal lamellae interfaces observed in AFM images (Fig. 5.1), though it is difficult to estimate the amount of the stromal lamellae that would occupy the grana perimeter *in vivo* that may have been removed by the digitonin treatment. From the half-time curve in Fig. 5.10A it is apparent that decreasing the size of the interface would massively decrease the rate of PSI reduction by restricting the diffusion of PC (Fig. 5.10B(1)). By way of contrast, it seems that increasing the size of the interface above that which is observed ( $\approx 1000$  nm) has increased the rate of PSI reduction only slightly when compared to the exponentially changing rate at small interface sizes. Therefore, there is little incentive to increase the size of the interface beyond that of two thirds of the grana perimeter. Indeed, doing so would increase the amount of contact between the grana and stromal lamellae and therefore might be predicted to increase the amount of excitation energy spillover from PSII to PSI (Fig. 5.10B(3)). It is proposed therefore that the observed interface sizes and PC kinetics thereof are the result of a compromise: one which seeks to maximise the rate of PC diffusion between *cytb<sub>6</sub>f* in the grana and the PSI in the stromal lamellae whilst at the same time minimising the amount of contact between PSII and PSI and the grana/stromal lamellae interface (Fig. 5.10B(2)).

#### 5.3.2. Cyclic electron flow.

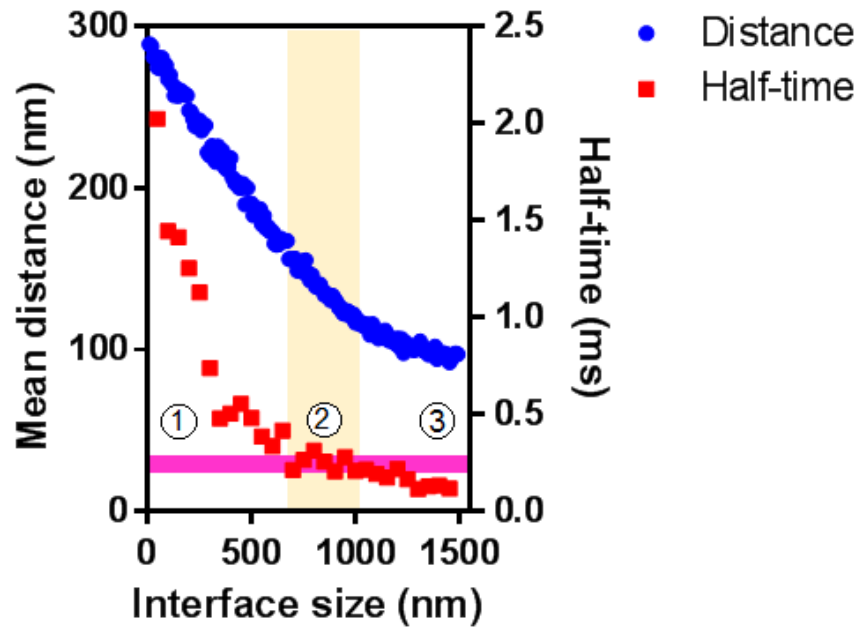
It must be noted that that the model used to calculate has a few simplifications and limitations that may be address in future work. Firstly, the simulations take into account only linear electron flow from *cytb<sub>6</sub>f* in the grana to PSI in the stromal lamellae. Cyclic electron flow occurs between *cytb<sub>6</sub>f* and PSI in the stromal lamellae. If one assumes that *cytb<sub>6</sub>f* is homogeneously distributed within the stromal lamellae then a reasonable approximation for the diffusive distance of PC involved in cyclic electron

flow can be the average nearest neighbour distance of PSI (15 nm). Then the average time can be approximated in the 2-D plane

$$t = \frac{(15 \text{ nm})^2}{4 \times 0.9 \times 10^6 \text{ nm}^2 \text{ s}^{-1}} = 60 \mu\text{s}$$

Which is much shorter than that of 200-300  $\mu\text{s}$  for linear electron flow. This component is neglected in the simulations as the experimentally derived P700<sup>+</sup> kinetics experiments do not measure cyclic electron flow. This is due to the presence of PSI electron acceptors such as anthraquinone-2-sulfonate (Haehnel *et al*, 1980).

A



B

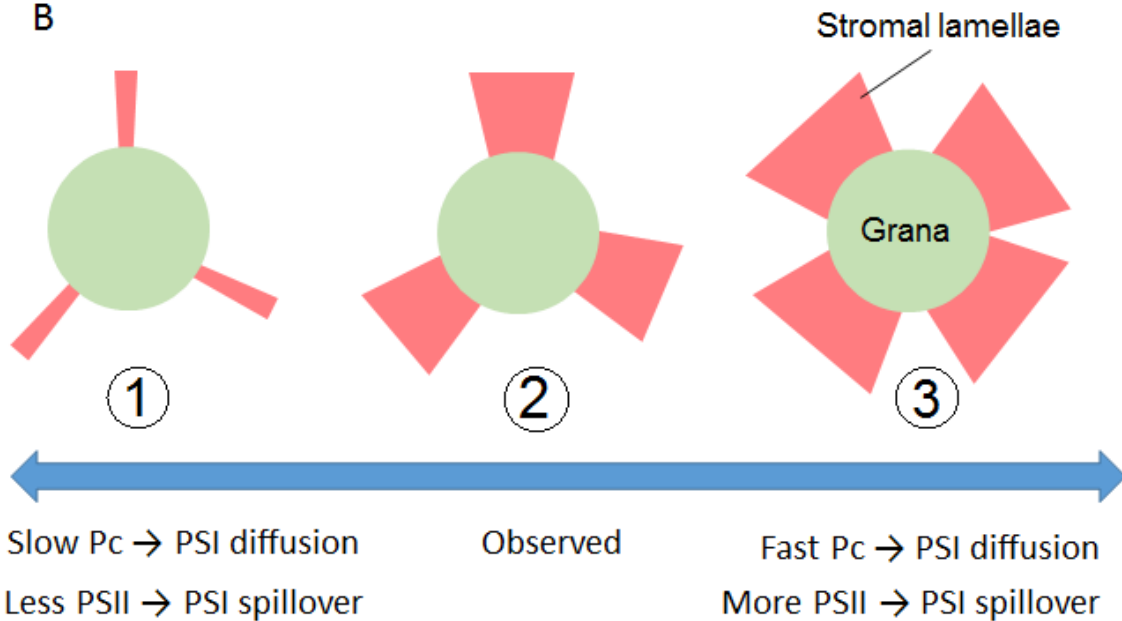


**Figure 5.10. The observed grana/stromal lamellae interface sizes are likely to result from a compromise between maximising the rate of PC diffusion and minimising PSII to PSI energetic spillover.** **A.** Mean distance (Fig. 4A) and half-time (Fig. 4D) as a function of interface size with 200-300  $\mu$ s half-time range highlighted in magenta and the range of interface sizes laying within the magenta range highlighted in yellow. **B.** Diagram depicting three configurations of stromal-granal interface that correspond to the time/distance zones in panel (E). The overlap point (2) lies in the zone of compromise that minimises spillover from PSII to PSI, while allowing acceptable rates of PSI reduction. Smaller interfaces e.g. point (1) lead to slower rates of PSI reduction, while larger interfaces may increase PSII to PSI spillover (3).

### 5.3.3. Limitations of the model and potential improvements.

A difficulty encountered in simulating the diffusion of PC was accounting for the soluble content of the thylakoid lumen. The thylakoid lumen is known to contain over 100 different kinds of protein (Keiselbach *et al.*, 1998) but the concentrations of these proteins in the lumen remains mostly unknown. The volume of the thylakoid lumen itself is unknown and the proportion of luminal proteins which are excluded from the grana due to size is unknown. Indeed, what is known is that the thickness of the grana lumen changes due to environmental light conditions (Kirchhoff *et al.*, 2011) and therefore these parameters themselves are a function of environmental variables. Each of the unknown parameters described would of course change the diffusion coefficient of PC. This highlights the need for quantitative proteomics studies of the chloroplast which would allow for more detailed and realistic simulations to be carried out in future. One solution may be to approximate the protein composition of the thylakoid lumen with that of a cell cytoplasm. The ratio between the diffusion constants of proteins measured in aqueous buffer and measured in the cell cytoplasm ( $D/D_0$ ) vary massively within the range 0.007-0.49 (Luby-Phelps, 2000). That said, due to the exponential nature of the half-times as a function of interface size (Fig. 5.4D), large changes in the diffusion coefficient amount only to small changes in the interface size range observed at 200-300  $\mu\text{s}$ . Any changes to the diffusion constant by macromolecular crowding of soluble proteins would have a linear effect when the concentration is below the percolation threshold (Saxton, 1987) which would move the half-times curve to the left or right. Therefore, the qualitative nature of Fig. 5.4D would be conserved and the conclusions drawn, namely that the grana/stromal lamellae interface maximises the rate of PC diffusion while simultaneously minimising PSII/PSI contact (spillover), are valid.

Further improvements to the model may include the introduction of the association and dissociation kinetics of PC. The rate of association of reduced PC is  $3.5\text{-}5 \times 10^8 \text{ M}^{-1} \text{ s}^{-1}$  which can be considered by choosing a suitable probability of binding when PC is near PSI. What is striking is the low rate of dissociation of oxidised PC from PSI (half-time of 100  $\mu\text{s}$ ) (Antal, 2013). In order to account for this, one would have to estimate the proportion of PSI particles with PC bound and block the binding of PC to these particles. Effectively this would be equivalent to decreasing the density of PSI in the stromal lamellae and therefore PC would have further to travel on average. The average distance PC travelled within the stromal lamellae before encountering PSI was 8.6 nm. This was consistent across all interface sizes and is due to the high density of PSI in the stromal lamellae. Therefore, unless a large proportion of PSI are blocked by PC at any given time this added complexity is unlikely to affect the outcome of the simulations.

The work described here shows the importance of the grana/stromal lamellae interface in linear electron transport. In this study, the rate of PC diffusion was calculated for interface sizes ranging from a small opening (50 nm) to almost the entire perimeter of the grana (1500 nm). However, the actual proportion of the grana perimeter which is interfacial with the stromal lamellae is unknown. Austin & Staehelin (2010) describe the distribution of the size of interfaces (junctional slits) which range from 30 – 435 nm. The number of interfaces per grana layer however is unknown. It may also be the case that the interface size is actively regulated and therefore may be highly variable. Further investigation is needed, to understand the role of the grana stromal lamellae interface photosynthesis. Using AFM on purified grana membranes is limited in what it can do to improve the understanding of the function of the interface. It provides evidence that the stromal lamellae and grana come into contact at the interface and form a strict boundary. However, one must be wary of using this data in a quantitative way. The interface sizes are certainly on the larger side of the distribution in Austin and Staehelin (2010), and this may arise as an artefact of digitonin treatment. It may be the case that only larger interfaces can withstand digitonin treatment and that smaller interfaces are removed. This also may explain why only one interface is usually observed in each grana membrane. Of course, in most cases, no stromal lamellae region is observed at all. Most grana prepared with digitonin appear as in figure 3.7, which suggests that digitonin mostly separates the stromal lamellae from the grana and what we see in images such as Fig. 5.1 are rare events.

#### **5.4. Conclusion.**

Using AFM data acquired from the present and previous chapters, it was possible to construct a 3-D model of the organisation of PSII, *cytb<sub>6</sub>f* and PSI in the thylakoid membrane. The simple model of the thylakoid machinery described in this chapter is a framework that could easily be improved by future insights into the structure of the thylakoid membrane. Simulations of the diffusion of PC were carried out over a range of interface sizes: the point of contact of the grana and stromal lamellae. It was established, that the interface size profoundly affects the rate of PC diffusion and that the experimentally derived kinetics published by Haehnel *et al.* (1980) arise from a compromise between the need to maximise the rate of PC diffusion while simultaneously minimise the contact and therefore excitation energy spillover between PSII and PSI.

## **Chapter 6.**

### **Concluding remarks**

### 6.1. Concluding remarks.

In chapter 3, methods for the isolation of grana and stromal lamellae membranes suitable for AFM, from both spinach and *Arabidopsis*, were developed. This allowed a detailed investigation into the organisation of PSI and ATP synthase in the stromal lamellae which was the subject of chapter 4. In chapter 5, the information obtained from AFM imaging of grana and stromal lamellae membranes is used to produce a model of the thylakoid membrane. We were interested in how the obligatory long-range diffusion of PC in LEF was affected by the degree of contact between the grana and the stromal lamellae. Our model indicates that PC diffusion between *cytb<sub>6</sub>f* and PSI could become rate limiting if the interface size between the grana and the stromal lamellae becomes too small, a factor which may play a role in shaping the complex 3-D architecture of the thylakoid membrane.

Though I will not repeat the limitations and potential criticisms of the experiments and the model described in this thesis (each of which have been discussed in detail previously). Instead, I will say that the main redeeming factor for any limitations is that the model presented is likely the closest approximation of the *in vivo* spatial organisation of PSII, *cytb<sub>6</sub>f*, and PSI produced to date. While the Brownian dynamics simulations used to investigate the diffusive dynamics of PC within the model are by no means cutting-edge, the scale of the model incorporating two layers of grana membranes and associated stromal lamellae, containing a total of 1478 particles, is cutting-edge with respect to incorporating the structure of the thylakoid membrane from the nanoscale to the microscale. Future work might encompass further details and complications, such as incorporating more realistic geometries of the proteins in the grana lumen, thus creating a more realistic space of PC to diffuse in. Electrostatic interactions at the PC binding sites of *cytb<sub>6</sub>f* and PSI, such as those described by Kovalenko *et al.* (2016) may aid the understanding of the role of binding and unbinding in electron transport. Adopting an agent-based approach to modelling PC diffusion, simulating each PC particle simultaneously rather than one at a time, would allow one to simulate the equilibrium properties of this process *in silico* as an alternative to simulating so-called flash-kinetics which were used in this study. Modelling of natural systems benefits nowadays from the wide availability of large processing clusters and the development of parallelisation algorithms that allow bigger and more computationally intensive software to be run more inexpensively and in less time. Therefore, great improvements in the modelling and simulation experiments described here can be envisaged in the coming years.

The technical developments in AFM and cryo-EM will be of increasing importance in the future, if we are to ascertain the relationship between the structure and function of the thylakoid membrane. In this thesis, the nanoscale structure of the grana and the stromal lamellae have been obtained by the

imaging fractionated rather than intact thylakoids. Further advances in our understanding requires the nanoscale organisation of PSII, *cytb<sub>6</sub>f*, PSI and ATP synthase to be understood in the context of the 3-D architecture of the thylakoid membrane. Although cryo-EM is yet to match the resolution of AFM at the single molecule level, recent advances in technology and methodology now allow individual proteins to be imaged in the context of their 3-D environment (Engel *et al.*, 2015). Furthermore, a current limitation of AFM is the need for highly pure and very flat samples. But this also may be subject to change as Kumar *et al.*, 2017 showed that highly curved membrane surface can be imaged at high resolution using smaller, higher-sensitivity cantilevers. This is possible due in part to the recent advent of FastScan AFM.

Understanding the native architecture of the thylakoid membrane is only the beginning. What may be an even bigger challenge is to determine how this architecture changes with environmental pressures. We discussed previously the light driven swelling of the grana lumen (Kirchhoff *et al.*, 2011; Herbstova *et al.*, 2012). State transitions play a role in both macroscale (Chuartzman *et al.*, 2008) and nanoscale (Bassi *et al.*, 1988; Minagawa, 2011) architecture of the thylakoid membrane. A comprehensive and holistic understanding of plant photosynthesis in all its complexity is a serious challenge, but is crucial to improving the photosynthetic efficiency of food and biofuel crops to meet the challenge of a growing world population.

## References.

Adams, P.G., Mothersole, D.J., Ng, I.W., Olsen, J.D. and Hunter, C.N., 2011. Monomeric RC–LH1 core complexes retard LH2 assembly and intracytoplasmic membrane formation in PufX-minus mutants of *Rhodobacter sphaeroides*. *Biochimica et Biophysica Acta (BBA)-Bioenergetics*, 1807(9), pp.1044-1055.

Åkerlund, H.E., Andersson, B. and Albertsson, P.Å., 1976. Isolation of photosystem II enriched membrane vesicles from spinach chloroplasts by phase partition. *Biochimica et Biophysica Acta (BBA)-Bioenergetics*, 449(3), pp.525-535.

Albertsson, P. (1971). *Partition of Cell Particles and Macromolecules* (2<sup>nd</sup> Edition). (John Wiley & Sons).

Albertsson, P.Å., 2001. A quantitative model of the domain structure of the photosynthetic membrane. *Trends in plant science*, 6(8), pp.349-354.

Allred, D.R. and Staehelin, L.A., 1986. Spatial organization of the cytochrome b6-f complex within chloroplast thylakoid membranes. *Biochimica et Biophysica Acta (BBA)-Bioenergetics*, 849(1), pp.94-103.

Andersson, B. and Anderson, J.M., 1980. Lateral heterogeneity in the distribution of chlorophyll-protein complexes of the thylakoid membranes of spinach chloroplasts. *Biochimica et Biophysica Acta (BBA)-Bioenergetics*, 593(2), pp.427-440.

Anderson 1989

Anderson, J.M., 1989. The grana margins of plant thylakoid membranes. *Physiologia Plantarum*, 76(2), pp.243-248.

Anderson, J.M., 2012. Lateral heterogeneity of plant thylakoid protein complexes: early reminiscences. *Philosophical Transactions of the Royal Society B: Biological Sciences*, 367(1608), pp.3384-3388.

Anderson, J.M. and Boardman, N., 1966. Fractionation of the photochemical systems of photosynthesis I. Chlorophyll contents and photochemical activities of particles isolated from

spinach chloroplasts. *Biochimica et Biophysica Acta (BBA)-Biophysics including Photosynthesis*, 112(3), pp.403-421. Andersson and Anderson, 1980

Andersson, B., Simpson, D.J. and Høyer-Hansen, G., 1978. Freeze-fracture evidence for the isolation of inside-out spinach thylakoid vesicles. *Carlsberg Research Communications*, 43(2), p.77.

Arabidopsis Genome Initiative, 2000. Analysis of the genome sequence of the flowering plant *Arabidopsis thaliana*. *nature*, 408(6814), p.796.

Amarnath, K., Bennett, D.I., Schneider, A.R. and Fleming, G.R., 2016. Multiscale model of light harvesting by photosystem II in plants. *Proceedings of the National Academy of Sciences*, 113(5), pp.1156-1161.

Armbruster, U., Pribil, M., Viola, S., Xu, W., Scharfenberg, M., Hertle, A.P., Rojahn, U., Jensen, P.E., Rappaport, F., Joliot, P. and Dörmann, P., 2013. Arabidopsis CURVATURE THYLAKOID1 proteins modify thylakoid architecture by inducing membrane curvature. *The Plant Cell*, 25(7), pp.2661-2678.

Arnon, D.I., Allen, M.B. and Whatley, F.R., 1954. Photosynthesis by isolated chloroplasts. *Nature*, 174(4426), pp.394-396.

Arnon, D.I., 1955. The chloroplast as a complete photosynthetic unit. *Science*, 122(3157), pp.9-16.

Arntzen, C.J., Dilley, R.A. and Crane, F.L., 1969. A comparison of chloroplast membrane surfaces visualized by freeze-etch and negative staining techniques; and ultrastructural characterization of membrane fractions obtained from digitonin-treated spinach chloroplasts. *The Journal of cell biology*, 43(1), p.16.

Austin, J.R., Frost, E., Vidi, P.A., Kessler, F. and Staehelin, L.A., 2006. Plastoglobules are lipoprotein subcompartments of the chloroplast that are permanently coupled to thylakoid membranes and contain biosynthetic enzymes. *The Plant Cell*, 18(7), pp.1693-1703.

Austin, J.R. and Staehelin, L.A., 2011. Three-dimensional architecture of grana and stroma thylakoids of higher plants as determined by electron tomography. *Plant physiology*, 155(4), pp.1601-1611.

Bahatyrova, S., Frese, R.N., Siebert, C.A., Olsen, J.D., van der Werf, K.O., van Grondelle, R., Niederman, R.A., Bullough, P.A., Otto, C. and Hunter, C.N., 2004. The native architecture of a photosynthetic membrane. *Nature*, 430(7003), pp.1058-1062.

Barber, J., 1982. Influence of surface charges on thylakoid structure and function. *Annual Review of Plant Physiology*, 33(1), pp.261-295.

Bellafiore, S., Barneche, F., Peltier, G. and Rochaix, J.D., 2005. State transitions and light adaptation require chloroplast thylakoid protein kinase STN7. *Nature*, 433(7028), pp.892-895.

Berthold, D.A., Babcock, G.T. and Yocum, C.F., 1981. A highly resolved, oxygen-evolving photosystem II preparation from spinach thylakoid membranes: EPR and electron-transport properties. *Febs Letters*, 134(2), pp.231-234.

Binnig, G. and Rohrer, H. (1982). Scanning Tunneling Microscopy. *Surface Science*. 126. 236-244

Binnig, G. and Quate, C. F. (1986). Atomic Force Microscope. *Physical Review Letters*. 56. (9). 930-933.

Blankenship, R.E., 2013. *Molecular mechanisms of photosynthesis*. John Wiley & Sons.

Boardman, N.K. and Anderson, J.M., 1964. Isolation from spinach chloroplasts of particles containing different proportions of chlorophyll a and chlorophyll b and their possible role in the light reactions of photosynthesis. *Nature*, 203, pp.166-167.

Boardman, N.K., Thorne, S.W. and Anderson, J.M., 1966. Fluorescence properties of particles obtained by digitonin fragmentation of spinach chloroplasts. *Proceedings of the National Academy of Sciences*, 56(2), pp.586-593..

Boardman, N.K. and Anderson, J.M., 1967. Fractionation of the photochemical systems of photosynthesis. II. Cytochrome and carotenoid contents of particles isolated from spinach chloroplasts. *Biochimica et Biophysica Acta (BBA)-Bioenergetics*, 143(1), pp.187-203.

Boekema, E., Hankamer, B., Bald, D., Kruij, J., Nield, J., Boonstra, A., Barber, J., Rogner, M. (1995). Supramolecular Structure of the Photosystem II from Green Plants and Cyanobacteria. *PNAS*. 92. 175-179.

Boekema, E.J., van Roon, H., van Breemen, J.F. and Dekker, J.P., 1999. Supramolecular organization of photosystem II and its light-harvesting antenna in partially solubilized photosystem II membranes. *The FEBS Journal*, 266(2), pp.444-452.

Bonardi, V., Pesaresi, P., Becker, T., Schleiff, E., Wagner, R., Pfannschmidt, T., Jahns, P. and Leister, D., 2005. Photosystem II core phosphorylation and photosynthetic acclimation require two different protein kinases. *Nature*, 437(7062), pp.1179-1182.

Chow, W.S., Kim, E.H., Horton, P. and Anderson, J.M., 2005. Granal stacking of thylakoid membranes in higher plant chloroplasts: the physicochemical forces at work and the functional consequences that ensue. *Photochemical & Photobiological Sciences*, 4(12), pp.1081-1090.

Bottin, H. and Mathis, P., 1985. Interaction of plastocyanin with the photosystem I reaction center: a kinetic study by flash absorption spectroscopy. *Biochemistry*, 24(23), pp.6453-6460.

Chitnis, V.P. and Chitnis, P.R., 1993. PsaL subunit is required for the formation of photosystem I trimers in the cyanobacterium *Synechocystis* sp. PCC 6803. *FEBS letters*, 336(2), pp.330-334.

Christensen, H.E., Conrad, L.S. and Ulstrup, J., 1991. Isolation and purification of plastocyanin from spinach stored frozen using hydrophobic interaction and ion-exchange chromatography. *Photosynthesis research*, 28(2), pp.89-93.

Chuartzman, S.G., Nevo, R., Shimoni, E., Charuvi, D., Kiss, V., Ohad, I., Brumfeld, V. and Reich, Z., 2008. Thylakoid membrane remodeling during state transitions in *Arabidopsis*. *The Plant Cell*, 20(4), pp.1029-1039.

Clark, R.D., Hawkesford, M.J., Coughlan, S.J., Bennett, J. and Hind, G., 1984. Association of ferredoxin-NADP<sup>+</sup> oxidoreductase with the chloroplast cytochrome b<sub>f</sub> complex. *FEBS letters*, 174(1), pp.137-142.

Cox, R.P. and Andersson, B., 1981. Lateral and transverse organisation of cytochromes in the chloroplast thylakoid membrane. *Biochemical and biophysical research communications*, 103(4), pp.1336-1342.

Danielsson, R. and Albertsson, P.Å., 2009. Fragmentation and separation analysis of the photosynthetic membrane from spinach. *Biochimica et Biophysica Acta (BBA)-Bioenergetics*, 1787(1), pp.25-36.

Danielsson, R. and Albertsson, P.Å., 2013. Aqueous polymer two-phase systems and their use in fragmentation and separation of biological membranes for the purpose of mapping the membrane structure. *Preparative Biochemistry and Biotechnology*, 43(5), pp.512-525.

Daum, B., Nicastro, D., Austin, J., McIntosh, J., Kuhlbrandt, W. (2010). Arrangement of Photosystem II and ATP Synthase in Chloroplast Membranes of Spinach and Pea. *The Plant Cell*. 22. 1299-1312.

Demmig-Adams, B., 1990. Carotenoids and photoprotection in plants: a role for the xanthophyll zeaxanthin. *Biochimica et Biophysica Acta (BBA)-Bioenergetics*, 1020(1), pp.1-24.

Derjaguin, B., V., Muller, V., M., and Toporov, YU., P. (1975). Effect of contact deformations on the adhesion of particles. *Journal of colloid and interface science*. 53. (2). 314-326

Dorowski, A., Hofmann, A., Steegborn, C., Boicu, M. and Huber, R., 2001. Crystal structure of paprika ferredoxin-NADP<sup>+</sup> reductase Implications for the electron transfer pathway. *Journal of Biological Chemistry*, 276(12), pp.9253-9263.

Drake, B., Prater, C.B., Weisenhorn, A.L., Gould, S.A.C. and Albrecht, T.R., 1989. Imaging crystals, polymers, and processes in water with the atomic force microscope. *Science*, 243(4898), p.1586.

Drepper, F., Carlberg, I., Andersson, B. and Haehnel, W., 1993. Lateral diffusion of an integral membrane protein: Monte Carlo analysis of the migration of phosphorylated light-harvesting complex II in the thylakoid membrane. *Biochemistry*, 32(44), pp.11915-11922.

Dufrêne, Y.F., Martínez-Martín, D., Medalsy, I., Alsteens, D. and Müller, D.J., 2013. Multiparametric imaging of biological systems by force-distance curve-based AFM. *Nature methods*, 10(9), pp.847-854.

Duneau, J.P. and Sturgis, J.N., 2013. Lateral organization of biological membranes. *European Biophysics Journal*, 42(11-12), pp.843-850.

Emerson, R., Chalmers, R. and Cederstrand, C., 1957. Some factors influencing the long-wave limit of photosynthesis. *Proceedings of the National Academy of Sciences*, 43(1), pp.133-143.

Engel, B.D., Schaffer, M., Albert, S., Asano, S., Plitzko, J.M. and Baumeister, W., 2015. In situ structural analysis of Golgi intracisternal protein arrays. *Proceedings of the National Academy of Sciences*, 112(36), pp.11264-11269.

Fassioli, F., Dinshaw, R., Arpin, P.C. and Scholes, G.D., 2014. Photosynthetic light harvesting: excitons and coherence. *Journal of The Royal Society Interface*, 11(92), p.20130901.

Förster, T., 1948. Zwischenmolekulare energiewanderung und fluoreszenz. *Annalen der physik*, 437(1-2), pp.55-75.

Fotiadis, D., Müller, D.J., Tsiotis, G., Hasler, L., Tittmann, P., Mini, T., Jenö, P., Gross, H. and Engel, A., 1998. Surface analysis of the photosystem I complex by electron and atomic force microscopy. *Journal of molecular biology*, 283(1), pp.83-94.

Galka, P., Santabarbara, S., Khuong, T.T.H., Degand, H., Morsomme, P., Jennings, R.C., Boekema, E.J. and Caffarri, S., 2012. Functional analyses of the plant photosystem I–light-harvesting complex II supercomplex reveal that light-harvesting complex II loosely bound to photosystem II is a very efficient antenna for photosystem I in state II. *The Plant Cell*, 24(7), pp.2963-2978.

Gilmore, A.M. and Hazlett, T.L., 1995. Xanthophyll cycle-dependent quenching of photosystem II chlorophyll a fluorescence: formation of a quenching complex with a short fluorescence lifetime. *Proceedings of the National Academy of Sciences*, 92(6), pp.2273-2277.

Goodchild, D.J. and Park, R.B., 1971. Further evidence for stroma lamellae as a source of photosystem 1 fractions from spinach chloroplasts. *Biochimica et Biophysica Acta (BBA)-Bioenergetics*, 226(2), pp.393-399.

Gross, E.L. and Prasher, S.H., 1974. Correlation between monovalent cation-induced decreases in chlorophyll a fluorescence and chloroplast structural changes. *Archives of biochemistry and biophysics*, 164(2), pp.460-468.

Guedeney, G., Corneille, S., Cuiné, S. and Peltier, G., 1996. Evidence for an association of ndh B, ndh J gene products and ferredoxin-NADP-reductase as components of a chloroplastic NAD (P) H dehydrogenase complex. *FEBS letters*, 378(3), pp.277-280.

Guergova-Kuras, M., Boudreaux, B., Joliot, A., Joliot, P. and Redding, K., 2001. Evidence for two active branches for electron transfer in photosystem I. *Proceedings of the National Academy of Sciences*, 98(8), pp.4437-4442.

Haehnel, W., Pröpper, A. and Krause, H., 1980. Evidence for complexed plastocyanin as the immediate electron donor of P-700. *Biochimica et Biophysica Acta (BBA)-Bioenergetics*, 593(2), pp.384-399.

Wolfgang Haehnel, R. and Robenek, H., 1989. Lateral distribution and diffusion of plastocyanin in chloroplast thylakoids. *The Journal of cell biology*, 108, pp.1397-1405.

Hill, R., 1937. Oxygen evolved by isolated chloroplasts. *Nature*, 139(3525), pp.881-882.

Hill, R. and Bendall, F.A.Y., 1960. Function of the two cytochrome components in chloroplasts: a working hypothesis. *Nature*, 186(4719), pp.136-137

Hinshaw, J.E. and Miller, K.R., 1993. Mapping the lateral distribution of Photosystem II and the Cytochrome b6/f complex by direct immune labeling of the thylakoid membrane. *Journal of structural biology*, 111(1), pp.1-8.

Janik, E., Bednarska, J., Zubik, M., Puzio, M., Luchowski, R., Grudzinski, W., Mazur, R., Garstka, M., Maksymiec, W., Kulik, A. and Dietler, G., 2013. Molecular architecture of plant thylakoids under

physiological and light stress conditions: a study of lipid–light-harvesting complex II model membranes. *The Plant Cell*, 25(6), pp.2155-2170.

Johnson, M.P., Vasilev, C., Olsen, J.D. and Hunter, C.N., 2014. Nanodomains of cytochrome b6f and photosystem II complexes in spinach grana thylakoid membranes. *The Plant Cell*, 26(7), pp.3051-3061.

Johnson MP (2016) Photosynthesis. *Essays In Biochemistry*, 60(3), 255-273.

Joliot, P., Lavergne, J. and Béal, D., 1992. Plastoquinone compartmentation in chloroplasts. I. Evidence for domains with different rates of photo-reduction. *Biochimica et Biophysica Acta (BBA)-Bioenergetics*, 1101(1), pp.1-12.

Karapetyan, N.V., Holzwarth, A.R. and Rögner, M., 1999. The photosystem I trimer of cyanobacteria: molecular organization, excitation dynamics and physiological significance. *FEBS letters*, 460(3), pp.395-400.

Kieselbach, T., Hagman, Å., Andersson, B. and Schröder, W.P., 1998. The Thylakoid Lumen of Chloroplasts ISOLATION AND CHARACTERIZATION. *Journal of Biological Chemistry*, 273(12), pp.6710-6716.

Kirchhoff, H., Borinski, M., Lenhert, S., Chi, L. and Büchel, C., 2004. Transversal and lateral exciton energy transfer in grana thylakoids of spinach. *Biochemistry*, 43(45), pp.14508-14516.

Kirchhoff, H., Schöttler, M.A., Maurer, J. and Weis, E., 2004. Plastocyanin redox kinetics in spinach chloroplasts: evidence for disequilibrium in the high potential chain. *Biochimica et Biophysica Acta (BBA)-Bioenergetics*, 1659(1), pp.63-72.

Kirchhoff, H., Hall, C., Wood, M., Herbstová, M., Tsabari, O., Nevo, R., Charuvi, D., Shimoni, E. and Reich, Z., 2011. Dynamic control of protein diffusion within the granal thylakoid lumen. *Proceedings of the National Academy of Sciences*, 108(50), pp.20248-20253.

Kirchhoff, H., Lenhert, S., Büchel, C., Chi, L. and Nield, J., 2008. Probing the organization of photosystem II in photosynthetic membranes by atomic force microscopy. *Biochemistry*, 47(1), pp.431-440.

Kok, B., Forbush, B. and McGloin, M., 1970. Cooperation of charges in photosynthetic O<sub>2</sub> evolution—I. A linear four step mechanism. *Photochemistry and Photobiology*, 11(6), pp.457-475.

Koornneef, M. and Meinke, D., 2010. The development of Arabidopsis as a model plant. *The Plant Journal*, 61(6), pp.909-921.

Kouřil, R., van Oosterwijk, N., Yakushevskaya, A.E. and Boekema, E.J., 2005. Photosystem I: a search for green plant trimers. *Photochemical & Photobiological Sciences*, 4(12), pp.1091-1094.

Kouřil, R., Oostergetel, G.T. and Boekema, E.J., 2011. Fine structure of granal thylakoid membrane organization using cryo electron tomography. *Biochimica et Biophysica Acta (BBA)-Bioenergetics*, 1807(3), pp.368-374.

Kouřil, R., Wientjes, E., Bultema, J.B., Croce, R. and Boekema, E.J., 2013. High-light vs. low-light: effect of light acclimation on photosystem II composition and organization in Arabidopsis thaliana. *Biochimica et Biophysica Acta (BBA)-Bioenergetics*, 1827(3), pp.411-419

Kovalenko, I.B., Khrushchev, S.S., Fedorov, V.A., Riznichenko, G.Y. and Rubin, A.B., 2016, May. The role of electrostatic interactions in the process of diffusional encounter and docking of electron transport proteins. In *Doklady Biochemistry and Biophysics* (Vol. 468, No. 1, pp. 183-186). Pleiades Publishing.

Kumar, S., Cartron, M.L., Mullin, N., Qian, P., Leggett, G.J., Hunter, C.N. and Hobbs, J.K., 2016. Direct Imaging of Protein Organization in an Intact Bacterial Organelle Using High-Resolution Atomic Force Microscopy. *ACS Nano*.

Lal, R. and John, S.A., 1994. Biological applications of atomic force microscopy. *American Journal of Physiology-Cell Physiology*, 266(1), pp.C1-C21.

Lavergne, J., Bouchaud, J.P. and Joliot, P., 1992. Plastoquinone compartmentation in chloroplasts. II. Theoretical aspects. *Biochimica et Biophysica Acta (BBA)-Bioenergetics*, 1101(1), pp.13-22.

le Maire, M., Champeil, P. and Møller, J.V., 2000. Interaction of membrane proteins and lipids with solubilizing detergents. *Biochimica et Biophysica Acta (BBA)-Biomembranes*, 1508(1), pp.86-111.

Lee, C.K., Pao, C.W. and Smit, B., 2015. PSII–LHCII supercomplex organizations in photosynthetic membrane by coarse-grained simulation. *The Journal of Physical Chemistry B*, 119(10), pp.3999-4008.

Li, X.P., Gilmore, A.M., Caffarri, S., Bassi, R., Golan, T., Kramer, D. and Niyogi, K.K., 2004. Regulation of photosynthetic light harvesting involves intrathylakoid lumen pH sensing by the PsbS protein. *Journal of Biological Chemistry*, 279(22), pp.22866-22874.

Liu, Z., Yan, H., Wang, K., Kuang, T., Zhang, J., Gui, L., An, X. and Chang, W., 2004. Crystal structure of spinach major light-harvesting complex at 2.72 Å resolution. *Nature*, 428(6980), pp.287-292.

Loll, B., Kern, J., Saenger, W., Zouni, A. and Biesiadka, J., 2005. Towards complete cofactor arrangement in the 3.0 Å resolution structure of photosystem II. *Nature*, 438(7070), pp.1040-1044.

Lunde, C., Jensen, P.E., Haldrup, A., Knoetzel, J. and Scheller, H.V., 2000. The PSI-H subunit of photosystem I is essential for state transitions in plant photosynthesis. *Nature*, 408(6812), pp.613-615.

Martin, W., Stoebe, B., Goremykin, V., Hansmann, S., Hasegawa, M. and Kowallik, K.V., 1998. Gene transfer to the nucleus and the evolution of chloroplasts. *Nature*, 393(6681), pp.162-165.

Mazor, Y., Borovikova, A. and Nelson, N., 2015. The structure of plant photosystem I super-complex at 2.8 Å resolution. *Elife*, 4, p.e07433.

McEvoy, J.P. and Brudvig, G.W., 2006. Water-splitting chemistry of photosystem II. *Chemical reviews*, 106(11), pp.4455-4483.

Metropolis, N., Rosenbluth, A.W., Rosenbluth, M.N., Teller, A.H. and Teller, E., 1953. Equation of state calculations by fast computing machines. *The journal of chemical physics*, 21(6), pp.1087-1092.

Michel, J.M. and Michel-Wolwertz, M.R. 1967. Fractionation of the photosynthetic apparatus from broken spinach chloroplasts by sucrose density gradient centrifugation. *Carnegie Inst. Wash. Year B.* 67: 508-514.

Miller, K.R. and Staehelin, L.A., 1976. Analysis of the thylakoid outer surface. Coupling factor is limited to unstacked membrane regions. *The Journal of Cell Biology*, 68(1), pp.30-47.

Minagawa, J., 2011. State transitions—the molecular remodeling of photosynthetic supercomplexes that controls energy flow in the chloroplast. *Biochimica et Biophysica Acta (BBA)-Bioenergetics*, 1807(8), pp.897-905.

Mitchell, R., Spillmann, A. and Haehnel, W., 1990. Plastoquinol diffusion in linear photosynthetic electron transport. *Biophysical journal*, 58(4), pp.1011-1024.

Müller, D.J., Schabert, F.A., Büldt, G. and Engel, A., 1995. Imaging purple membranes in aqueous solutions at sub-nanometer resolution by atomic force microscopy. *Biophysical journal*, 68(5), pp.1681-1686.

Müller, D.J., Amrein, M. and Engel, A., 1997. Adsorption of biological molecules to a solid support for scanning probe microscopy. *Journal of structural biology*, 119(2), pp.172-188.

Müller, D.J., Fotiadis, D., Scheuring, S., Müller, S.A. and Engel, A., 1999. Electrostatically balanced subnanometer imaging of biological specimens by atomic force microscope. *Biophysical journal*, 76(2), pp.1101-1111.

Mullet, J.E. and Arntzen, C.J., 1980. Simulation of grana stacking in a model membrane system. Mediation by a purified light-harvesting pigment-protein complex from chloroplasts. *Biochimica et Biophysica Acta (BBA)-Bioenergetics*, 589(1), pp.100-117.

Mullineaux, C.W., 2005. Function and evolution of grana. *Trends in plant science*, 10(11), pp.521-525.

Mulo, P., 2011. Chloroplast-targeted ferredoxin-NADP<sup>+</sup> oxidoreductase (FNR): Structure, function and location. *Biochimica et Biophysica Acta (BBA)-Bioenergetics*, 1807(8), pp.927-934.

Murata, N. and Brown, J., 1970. Photochemical activities of spinach chloroplast particles fractionated after French press treatment. *Plant physiology*, 45(3), p.360.

Murphy (1982)

Murphy, D. J. 1982. The importance of non-planar bilayer lipid regions in photosynthetic membranes and their stabilization by galactolipids. – *FEBS Lett.* 150: 19–26.

Neff, D., Tripathi, S., Middendorf, K., Stahlberg, H., Butt, H.J., Bamberg, E. and Dencher, N.A., 1997. Chloroplast F<sub>0</sub>F<sub>1</sub>ATP synthase imaged by atomic force microscopy. *Journal of structural biology*, 119(2), pp.139-148.

Nelson, N. and Ben-Shem, A., 2004. The complex architecture of oxygenic photosynthesis. *Nature Reviews Molecular Cell Biology*, 5(12), pp.971-982.

Barkema, G.T. and Newman, M.E.J., 2001. *Monte Carlo methods in statistical physics*. Oxford University Press.

Nicholls, D.G. and Ferguson, S.J., 2013. *Bioenergetics*. Vol. 4.

Novoderezhkin, V., Marin, A. and van Grondelle, R., 2011. Intra- and inter-monomeric transfers in the light harvesting LHClI complex: the Redfield–Förster picture. *Physical Chemistry Chemical Physics*, 13(38), pp.17093-17103.

Oh-oka, H., Takahashi, Y., Wada, K., Matsubara, H., Ohyama, K. and Ozeki, H., 1987. The 8 kDa polypeptide in photosystem I is a probable candidate of an iron-sulfur center protein coded by the chloroplast gene *frxA*. *FEBS letters*, 218(1), pp.52-54.

Olsen, J.D., Tucker, J.D., Timney, J.A., Qian, P., Vassilev, C. and Hunter, C.N., 2008. The organization of LH2 complexes in membranes from *Rhodospirillum rubrum*. *Journal of Biological Chemistry*, 283(45), pp.30772-30779.

Onoa, B., Schneider, A., Brooks, M., Grob, P., Nogales, E., Geissler, P., Niyogi, K.K. and Bustamante, C.J., 2014. Atomic Force Microscopy and Particle Clustering Reveal Altered Photosystem II Organization in the Suppressor of Quenching 1 Mutant of Arabidopsis. *Biophysical Journal*, 106(2), p.800a.

Phuthong, W., Huang, Z., Wittkopp, T.M., Sznee, K., Heinnickel, M.L., Dekker, J.P., Frese, R.N., Prinz, F.B. and Grossman, A.R., 2015. The use of contact mode atomic force microscopy in aqueous medium for structural analysis of spinach photosynthetic complexes. *Plant physiology*, pp.pp-00706.

Picas, L., Rico, F. and Scheuring, S., 2012. Direct measurement of the mechanical properties of lipid phases in supported bilayers. *Biophysical journal*, 102(1), pp.L01-L03.

Pierre, Y., Breyton, C., Kramer, D. and Popot, J.L., 1995. Purification and characterization of the cytochrome b6 f complex from *Chlamydomonas reinhardtii*. *Journal of Biological Chemistry*, 270(49), pp.29342-29349.

Porra, R., Thompson, W. And Kriedmann , P. (1989). Determination of Accurate Extinction Coefficients and Simultaneous Equations for Assaying Chlorophylls a and b Extracted With Four Different Solvents: Verification of the Concentration of Chlorophyll Standards by Atomic Absorption Spectroscopy. *BBA*. 975. 384-394.

Pribil, M., Pesaresi, P., Hertle, A., Barbato, R. and Leister, D., 2010. Role of plastid protein phosphatase TAP38 in LHClI dephosphorylation and thylakoid electron flow. *PLoS Biol*, 8(1), p.e1000288.

Pribil, M., Labs M, Leister D (2014) Structure and dynamics of thylakoids in land plants. *J. Exp. Bot*, 65(8), pp.1955-1972.

Puthiyaveetil, S., Tsabari, O., Lowry, T., Lenhert, S., Lewis, R.R., Reich, Z. and Kirchhoff, H., 2014. Compartmentalization of the protein repair machinery in photosynthetic membranes. *Proceedings of the National Academy of Sciences*, 111(44), pp.15839-15844.

Quiles, M.J. and Cuello, J., 1998. Association of ferredoxin-NADP oxidoreductase with the chloroplastic pyridine nucleotide dehydrogenase complex in barley leaves. *Plant Physiology*, 117(1), pp.235-244.

Quinn, P.J. and Williams, W.P., 1983. The structural role of lipids in photosynthetic membranes. *Biochimica et Biophysica Acta (BBA)-Reviews on Biomembranes*, 737(2), pp.223-266.

Rees, D.M., Montgomery, M.G., Leslie, A.G. and Walker, J.E., 2012. Structural evidence of a new catalytic intermediate in the pathway of ATP hydrolysis by F1-ATPase from bovine heart mitochondria. *Proceedings of the National Academy of Sciences*, 109(28), pp.11139-11143.

Renger, G. and Renger, T., 2008. Photosystem II: the machinery of photosynthetic water splitting. *Photosynthesis research*, 98(1-3), pp.53-80.

Ruban, A. 2013. The Photosynthetic Membrane: Molecular Mechanisms and Biophysics of Light Harvesting. John Wiley & Sons.

Sanderson, D.G., Anderson, L.B. and Gross, E.L., 1986. Determination of the redox potential and diffusion coefficient of the protein plastocyanin using optically transparent filar electrodes. *Biochimica et Biophysica Acta (BBA)-Bioenergetics*, 852(2), pp.269-278.

Sane, P.V., Goodchild, D.J. and Park, R.B., 1970. Characterization of chloroplast photosystems 1 and 2 separated by a non-detergent method. *Biochimica et Biophysica Acta (BBA)-Bioenergetics*, 216(1), pp.162-178.

Saxton, M.J., 1994. Anomalous diffusion due to obstacles: a Monte Carlo study. *Biophysical journal*, 66(2), pp.394-401.

Schneider, A., and Geissler, P. (2013). Coexistence of Fluid and Crystalline Phases of Proteins in Photosynthetic Membranes. *Biophysical Journal*. 105. 1161 – 1170.

Scheuring, S. and Sturgis, J.N., 2005. Chromatic adaptation of photosynthetic membranes. *Science*, 309(5733), pp.484-487.

Seelert, H., Poetsch, A., Dencher, N.A., Engel, A., Stahlberg, H. and Müller, D.J., 2000. Structural biology: proton-powered turbine of a plant motor. *Nature*, 405(6785), pp.418-419.

Seelert, H., Dencher, N.A. and Müller, D.J., 2003. Fourteen protomers compose the oligomer III of the proton-rotor in spinach chloroplast ATP synthase. *Journal of molecular biology*, 333(2), pp.337-344.

Şener, M.K., Park, S., Lu, D., Damjanović, A., Ritz, T., Fromme, P. and Schulten, K., 2004. Excitation migration in trimeric cyanobacterial photosystem I. *The Journal of chemical physics*, 120(23), pp.11183-11195.

Senior, A.E., Nadanaciva, S. and Weber, J., 2002. The molecular mechanism of ATP synthesis by F<sub>1</sub>F<sub>0</sub>-ATP synthase. *Biochimica et Biophysica Acta (BBA)-Bioenergetics*, 1553(3), pp.188-211.

Simpson, D.J. and Andersson, B., 1986. Extrinsic polypeptides of the chloroplast oxygen evolving complex constitute the tetrameric ESs particles of higher plant thylakoids. *Carlsberg Research Communications*, 51(6), p.467.

Shahak, Y., Crowther, D. and Hind, G., 1981. The involvement of ferredoxin-NADP<sup>+</sup> reductase in cyclic electron transport in chloroplasts. *Biochimica et Biophysica Acta (BBA)-Bioenergetics*, 636(2), pp.234-243.

Shapiguzov, A., Ingelsson, B., Samol, I., Andres, C., Kessler, F., Rochaix, J.D., Vener, A.V. and Goldschmidt-Clermont, M., 2010. The PPH1 phosphatase is specifically involved in LHCII dephosphorylation and state transitions in Arabidopsis. *Proceedings of the National Academy of Sciences*, 107(10), pp.4782-4787.

Seddon, A.M., Curnow, P. and Booth, P.J., 2004. Membrane proteins, lipids and detergents: not just a soap opera. *Biochimica et Biophysica Acta (BBA)-Biomembranes*, 1666(1), pp.105-117.

Sommer, F., Drepper, F., Haehnel, W. and Hippler, M., 2004. The hydrophobic recognition site formed by residues PsaA-Trp651 and PsaB-Trp627 of photosystem I in *Chlamydomonas reinhardtii* confers distinct selectivity for binding of plastocyanin and cytochrome c6. *Journal of Biological Chemistry*, 279(19), pp.20009-20017.

Staehelin, L.A., 1976. Reversible particle movements associated with unstacking and restacking of chloroplast membranes in vitro. *J. Cell Biol*, 71(136), p.15.

Standfuss, J., van Scheltinga, A.C.T., Lamborghini, M. and Kühlbrandt, W., 2005. Mechanisms of photoprotection and nonphotochemical quenching in pea light-harvesting complex at 2.5 Å resolution. *The EMBO journal*, 24(5), pp.919-928.

Stiehl, H.H. and Witt, H., 1969. Quantitative treatment of the function of plastoquinone in photosynthesis. *Zeitschrift für Naturforschung B*, 24(12), pp.1588-1598.

Stroebel, D., Choquet, Y., Popot, J.L. and Picot, D., 2003. An atypical haem in the cytochrome b6f complex. *Nature*, 426(6965), pp.413-418.

Sznee, K., Dekker, J.P., Dame, R.T., van Roon, H., Wuite, G.J. and Frese, R.N., 2011. Jumping mode atomic force microscopy on grana membranes from spinach. *Journal of Biological Chemistry*, 286(45), pp.39164-39171.

Tikhonov, A.N. and Vershubskii, A.V., 2014. Computer modeling of electron and proton transport in chloroplasts. *BioSystems*, 121, pp.1-21.

Tremmel, I.G., Kirchhoff, H., Weis, E. and Farquhar, G.D., 2003. Dependence of plastoquinol diffusion on the shape, size, and density of integral thylakoid proteins. *Biochimica et Biophysica Acta (BBA)-Bioenergetics*, 1607(2), pp.97-109.

Van Amerongen, H., Van Grondelle, R. and Valkunas, L., 2000. *Photosynthetic excitons*. World Scientific.

Van Roon, H., Van Breemen, J.F., De Weerd, F.L., Dekker, J.P. and Boekema, E.J., 2000. Solubilization of green plant thylakoid membranes with n-dodecyl- $\alpha$ , D-maltoside. Implications for the structural organization of the Photosystem II, Photosystem I, ATP synthase and cytochrome b6 f complexes. *Photosynthesis research*, 64(2), pp.155-166.

Vinyard, D.J. and Brudvig, G.W., 2017. Progress Toward a Molecular Mechanism of Water Oxidation in Photosystem II. *Annual Review of Physical Chemistry*, 68(1).

Voet, D., Voet, J., 2011. *Biochemistry* (4<sup>th</sup> edition). John Wiley & Sons.

Wada, H. and Murata, N., 2007. The essential role of phosphatidylglycerol in photosynthesis. *Photosynthesis research*, 92(2), pp.205-215.

Walczyk, W., Schön, P.M. and Schönherr, H., 2013. The effect of PeakForce tapping mode AFM imaging on the apparent shape of surface nanobubbles. *Journal of physics: Condensed matter*, 25(18), p.184005.

Watanabe, M., Kubota, H., Wada, H., Narikawa, R. and Ikeuchi, M., 2011. Novel supercomplex organization of photosystem I in *Anabaena* and *Cyanophora paradoxa*. *Plant and cell physiology*, 52(1), pp.162-168.

Webber, A.N., Platt-Aloia, K.A., Heath, R.L. and Thomson, W.W., 1988. The marginal regions of thylakoid membranes: a partial characterization by polyoxyethylene sorbitan monolaurate (Tween 20) solubilization of spinach thylakoids. *Physiologia Plantarum*, 72(2), pp.288-297.

Wehrmeyer, W., 1964. Über Membranbildungsprozesse im Chloroplasten. *Planta*, 63(1), pp.13-30.

Wettstein, D.V., 1961. Nuclear and cytoplasmic factors in development of chloroplast structure and function. *Canadian Journal of Botany*, 39(6), pp.1537-1545.

Wollenberger, L., Stefansson, H., Yu, S.G. and Albertsson, P.Å., 1994. Isolation and characterization of vesicles originating from the chloroplast grana margins. *Biochimica et Biophysica Acta (BBA)-Bioenergetics*, 1184(1), pp.93-102.

Wollenberger, L., Weibull, C. and Albertsson, P.Å., 1995. Further characterization of the chloroplast grana margins: the non-detergent preparation of granal Photosystem I cannot reduce ferredoxin in the absence of NADP<sup>+</sup> reduction. *Biochimica et Biophysica Acta (BBA)-Bioenergetics*, 1230(1-2), pp.10-22.

Wraight, C.A. and Crofts, A.R., 1970. Energy-dependent quenching of chlorophyll a fluorescence in isolated chloroplasts. *European Journal of Biochemistry*, 17(2), pp.319-327.

Yadav, K.S., Semchonok, D.A., Nosek, L., Kouřil, R., Fucile, G., Boekema, E.J. and Eichacker, L.A., 2017. Supercomplexes of plant photosystem I with cytochrome b6f, light-harvesting complex II and NDH. *Biochimica et Biophysica Acta (BBA)-Bioenergetics*, 1858(1), pp.12-20.

Yamori, W. and Shikanai, T., 2016. Physiological functions of cyclic electron transport around photosystem I in sustaining photosynthesis and plant growth. *Annual review of plant biology*, 67, pp.81-106.

Zhang, H., Whitelegge, J.P. and Cramer, W.A., 2001. Ferredoxin: NADP<sup>+</sup> oxidoreductase is a subunit of the chloroplast cytochrome b6fComplex. *Journal of Biological Chemistry*, 276(41), pp.38159-38165.

Zhao, J., Warren, P.V., Li, N., Bryant, D.A. and Golbeck, J.H., 1990. Reconstitution of electron transport in photosystem I with PsaC and PsaD proteins expressed in *Escherichia coli*. *FEBS letters*, 276(1-2), pp.175-180.

Zhou, A., Rohou, A., Schep, D.G., Bason, J.V., Montgomery, M.G., Walker, J.E., Grigorieff, N. and Rubinstein, J.L., 2015. Structure and conformational states of the bovine mitochondrial ATP synthase by cryo-EM. *Elife*, 4, p.e10180.

## Appendix 1. Source code for the identification of PSI in AFM images.

```
1. #!/usr/bin/python
2.
3. #wwood 01/04/16
4.
5. # a program for PSI identification in AFM images
6. # use ascii files as input
7.
8.
9. import sys, math
10.
11. def reflect(boundary, x):
12.     if x > boundary:
13.         return boundary-x//boundary
14.     else:
15.         return x
16.
17.
18. def initial_formatting(filename):
19.     """1. opens the file.
20.         2. identifies X,Y, step size, data
21.         3. allocates to single variable and returns"""
22.     #1. open the file
23.     raw_file = open(filename).readlines()
24.
25.     for n in range(len(raw_file)):
26.         if raw_file[n].strip() == "Height(nm)":
27.             START = n+1
28.
29.     # make data floats
30.     height_data = raw_file[START:]
31.     for i in range(len(height_data)):
32.         temp = float(height_data[i])
33.         height_data[i] = temp
34.
35.     global zero # this is made global to use later
36.     zero = min(height_data)
37.     for i in range(len(height_data)):
38.         height_data[i] -= zero
39.
40.     return height_data
41.
42. def Make_xyz(scan_size,spl,Nlines,heights):
43.     dx = scan_size/spl
44.     if spl*Nlines != len(heights):
45.         print "Error: data size not correct"
46.         sys.close()
47.
48.     coords = []
49.     for y in range(Nlines):
```

```

50.     LINE = []
51.     for x in range(spl):
52.         LINE.append(heights[x+y*spl])
53.     coords.append(LINE)
54.     return coords
55.
56. def difference(HEIGHT, AREA, X, Y):
57.     D = 0
58.     for i in AREA:
59.         D+= (HEIGHT[i[0]][i[1]]-(HEIGHT[X][Y] - 3.2*math.exp(-(X-i[0])**2+(Y-
        i[1])**2)/22.3))**2
60.
61.     return float(D)/len(AREA)
62.
63. def filter_by_height(z, difference):
64.     MIN = 8.0
65.     MAX = 13.0
66.     if z < MIN or z > MAX:
67.         return difference*(10-z)**2
68.     else:
69.         return difference
70.
71. def correlation_map(scan_size,spl,Nlines,HEIGHT):
72.     dx = scan_size/spl
73.     R = int(10.0/dx)+1
74.     Cmap = []
75.     for line in range(Nlines):
76.
77.         for samp in range(spl):
78.
79.             AREA = []
80.             for r1 in range(2*R):
81.                 for r2 in range(2*R):
82.                     AREA.append([reflect(Nlines-1, abs(line-R+r1)), reflect(spl-1,abs(samp-R+r2))])
83.                     d = filter_by_height(HEIGHT[line][samp], difference(HEIGHT,AREA, line, samp))
84.
85.                 Cmap.append([line,samp,d])
86.     return Cmap
87.
88. def location_map(scan_size,spl,Nlines, Cmap):
89.
90.     # conversion Cmap [[x,y,z],...] to [[z(x1,y1),...][z(x1,y2),...]]
91.     Cmap_blank = []
92.     for x in range(Nlines):
93.         L = []
94.         for y in range(spl):
95.             L.append(0)
96.         Cmap_blank.append(L)
97.     for z in Cmap:
98.         Cmap_blank[z[0]][z[1]] = z[2]
99.     Cmap = Cmap_blank

```

```

100.
101.     dx = scan_size/spl
102.     threshold = ((int(10.0/dx)+1)**2)/2
103.     used_pix = []
104.     clusters = []
105.     for line in range(Nlines):
106.         for samp in range(spl):
107.             if [line, samp,Cmap[line][samp]] not in used_pix: # make sure the cluster is not
detected twice
108.                 if Cmap[line][samp] <= threshold:
109.                     used_pix.append([line, samp,Cmap[line][samp]])
110.                     local_cluster = [[line, samp,Cmap[line][samp]])
111.                     end_of_cluster = False
112.                     while end_of_cluster == False:
113.                         end_of_cluster = True
114.                         for x in local_cluster:
115.                             temp = []
116.
117.                             # the following need to be made so that they are within the indices
118.                             try:
119.                                 if Cmap[x[0]-1][x[1]-1] <= threshold and [x[0]-1,x[1]-1,Cmap[x[0]-1][x[1]-
1]] not in used_pix:#(-1,-1)
120.                                     end_of_cluster = False
121.                                     temp.append([x[0]-1,x[1]-1,Cmap[x[0]-1][x[1]-1]))
122.                                     used_pix.append([x[0]-1,x[1]-1,Cmap[x[0]-1][x[1]-1]))
123.                                 except IndexError:
124.                                     pass
125.
126.                                 try:
127.                                     if Cmap[x[0]-1][x[1]] <= threshold and [x[0]-1,x[1],Cmap[x[0]-
1][x[1]]] not in used_pix:#(-1,0)
128.                                         end_of_cluster = False
129.                                         temp.append([x[0]-1,x[1],Cmap[x[0]-1][x[1]]])
130.                                         used_pix.append([x[0]-1,x[1],Cmap[x[0]-1][x[1]]])
131.                                     except IndexError:
132.                                         pass
133.
134.                                     try:
135.                                         if Cmap[x[0]-1][x[1]+1] <= threshold and [x[0]-1,x[1]+1,Cmap[x[0]-
1][x[1]+1]] not in used_pix: #(-1,1)
136.                                             end_of_cluster = False
137.                                             temp.append([x[0]-1,x[1]+1,Cmap[x[0]-1][x[1]+1]))
138.                                             used_pix.append([x[0]-1,x[1]+1,Cmap[x[0]-1][x[1]+1]))
139.                                         except IndexError:
140.                                             pass
141.
142.                                         try:
143.                                             if Cmap[x[0]+1][x[1]-1] <= threshold and [x[0]+1,x[1]-1,Cmap[x[0]+1][x[1]-
1]] not in used_pix:#(1,-1)
144.                                                 end_of_cluster = False
145.

```

```

146.         temp.append([x[0]+1,x[1]-1,Cmap[x[0]+1][x[1]-1]])
147.         used_pix.append([x[0]+1,x[1]-1,Cmap[x[0]+1][x[1]-1]])
148.     except IndexError:
149.         pass
150.
151.     try:
152.         if Cmap[x[0]+1][x[1]] <= threshold and [x[0]+1,x[1],Cmap[x[0]+1][x[1]]] not i
n used_pix: #(1,0)
153.         end_of_cluster = False
154.         temp.append([x[0]+1,x[1],Cmap[x[0]+1][x[1]]])
155.         used_pix.append([x[0]+1,x[1],Cmap[x[0]+1][x[1]]])
156.     except IndexError:
157.         pass
158.
159.     try:
160.         if Cmap[x[0]+1][x[1]+1] <= threshold and [x[0]+1,x[1]+1,Cmap[x[0]+1][x[1]+
1]] not in used_pix: #(1,1)
161.         end_of_cluster = False
162.         temp.append([x[0]+1,x[1]+1,Cmap[x[0]+1][x[1]+1]])
163.         used_pix.append([x[0]+1,x[1]+1,Cmap[x[0]+1][x[1]+1]])
164.     except IndexError:
165.         pass
166.
167.
168.     try:
169.         if Cmap[x[0]][x[1]-1] <= threshold and [x[0],x[1]-1,Cmap[x[0]][x[1]-
1]] not in used_pix: #(0,-1)
170.         end_of_cluster = False
171.         temp.append([x[0],x[1]-1,Cmap[x[0]][x[1]-1]])
172.         used_pix.append([x[0],x[1]-1,Cmap[x[0]][x[1]-1]])
173.     except IndexError:
174.         pass
175.
176.     try:
177.         if Cmap[x[0]][x[1]+1] <= threshold and [x[0],x[1]+1,Cmap[x[0]][x[1]+1]] not i
n used_pix: #(0,1)
178.         end_of_cluster = False
179.         temp.append([x[0],x[1]+1,Cmap[x[0]][x[1]+1]])
180.         used_pix.append([x[0],x[1]+1,Cmap[x[0]][x[1]+1]])
181.     except IndexError:
182.         pass
183.
184.     for t in temp:
185.         local_cluster.append(t)
186.         clusters.append(local_cluster)
187.
188.
189.
190.     # secondly to clusters into points
191.     #print len(clusters)
192.     location_map = []

```

```

193.         for c in clusters:
194.             if len(c) == 1:
195.                 location_map.append([c[0][0],c[0][1]])
196.             else:
197.                 X = 0
198.                 Y = 0
199.                 for xy in c:
200.                     X += xy[0]
201.                     Y += xy[1]
202.                 location_map.append([float(X)/len(c), float(Y)/len(c)])
203.         return location_map
204.
205.
206.     #main
207.     filename = sys.argv[1]
208.     scan_size= float(sys.argv[2])
209.     spl = int(sys.argv[3])
210.     Nlines= int(sys.argv[4])
211.     HEIGHT = initial_formatting(filename)
212.
213.     coords = Make_xyz(scan_size,spl,Nlines,HEIGHT)
214.     """
215.     for i in range(Nlines):
216.         for j in range(spl):
217.             print i, j, coords[i][j]
218.     """
219.
220.     C = correlation_map(scan_size,spl,Nlines,coords)
221.     #L = location_map(scan_size,spl,Nlines, C)
222.     #print len(L)
223.
224.     dx = scan_size/spl
225.     #threshold = ((int(5.0/dx)+1)**2) # 0.5 nm difference per pixel
226.
227.     for i in C:
228.         if i[2] > 100:
229.
230.             #print i[1]*dx,i[0]*dx, 100
231.             pass
232.         else:
233.             print i[1]*dx,i[0]*dx, i[2]

```

## Appendix 2. Source code for estimating the diffusive distance of PC.

```
1. import math
2. import random
3. import numpy as np
4. import matplotlib.pyplot as plt
5.
6. def generate_path(S):
7.     R = 250-6.7
8.     t = S/R
9.     e1 = 6.7
10.    e2 = 5.0
11.    PSI = [0.0000000,0.0212766,0.1453901,0.3226951,0.5035461,0.6631206,0.773049
12.    7,0.8546099,0.9078014,0.9432624,0.9539007,0.9716312,0.9751773,0.9893617,0.989
13.    3617,0.9929078,0.9964539,0.9964539,0.9964539,0.9964539,0.9964539,0.9964539,0.
14.    9964539,1.0000000]
15.    p = random.random()
16.    x = 10
17.    for i in range(len(PSI)-1):
18.        if p >= PSI[i+1]:
19.            x +=1
20.        else:
21.            break
22.    r = math.sqrt(random.random()*(R**2))
23.    Tg = random.random()*math.pi
24.    if Tg <= t/2:
25.        P = R-r
26.    elif Tg > t/2:
27.        P = math.sqrt((r**2)+(R**2)-2*r*R*math.cos(Tg-t/2))
28.    return P + x + e1 - e2
29.
30. #main
31.
32. data_file = open("Jslit3_10to1000 20_09_16",'w')
33. for Sw in range(10,1500,10):
34.     data = ""
35.     for n in range(1000):
36.         data += str(generate_path(Sw))+ " "
37.     data_file.writelines(data+"\n")
```

### Appendix 3. Source code for Brownian dynamics simulations of PC.

```
1. import random,math
2. import numpy as np
3. import time
4.
5.
6. T0 = time.time()
7.
8. ## wwood 25/10/16
9. # simulating the diffusion of plastocyanin
10. # uses brownian motion and monte carlo for a single particle
11. ##### The -350 centering has been removed
12.
13.
14. ## Model constants ( in nm )
15. PSII_radius = 6.7
16. PSI_radius = 5
17. grana_radius = 250
18. stroma_radius = 350
19. boundary = 700 #total width
20.
21. # Diffusion constants
22. # constants
23. dx = 1
24. dt = 1 #/(0.9*10**8)
25. D = 0.9
26. RateConst=D*dt/(dx**2) # must be less than one half
27.
28.
29.
30. def dist(P1,P2):
31.     return np.sqrt((P1[0]-P2[0])**2 + (P1[1]-P2[1])**2)
32.
33. # download PSII/PSII/b6f particles from previous MCMC
34. # change to integer (nm grid at a later stage)
35.
36. PSII_COORDINATES = open('grana_particles_04_11_16_experiment_',r').readlines
    (# this is double layer overlapped)
37. PSII_POPULATION = []
38. for i in PSII_COORDINATES:
39.     i.strip("\n")
40.     F = i.split(" ")
41.     PSII_POPULATION.append([int(float(F[0])),int(float(F[1]))]) ## - 350 is needed t
    o normalise
42.
43.
44. # x2 PSI coordinates representing 2 layers
45. PSI_COORDINATES = open('stroma_particles_22_07_16_experiment_1',r').readline
    s()
```

```

46. PSI_POPULATION = []
47. for i in PSI_COORDINATES:
48.     i.strip("\n")
49.     F = i.split(" ")
50.     PSI_POPULATION.append([int(float(F[0])),int(float(F[1]))])
51. PSI_COORDINATES = open('stroma_particles_22_07_16_experiment_2','r').readline
    s()
52. for i in PSI_COORDINATES:
53.     i.strip("\n")
54.     F = i.split(" ")
55.     PSI_POPULATION.append([int(float(F[0])),int(float(F[1]))])
56. ## create boundaries no. 2 commented out for now
57.
58.
59. # outer boundary
60. BOUNDARIES2 = [(int(stroma_radius*np.cos(T*(2*np.pi/1000.0))-
    np.sin(T*(2*np.pi/1000.0))),int(stroma_radius*np.sin(T*(2*np.pi/1000.0))+np.cos(T*
    (2*np.pi/1000.0)))) for T in range(1000)]
61.
62.
63.
64. # create b6f population
65. """
66. Nb6f = int(len(PSII_POPULATION)/3.0) # this is where the fraction of particles that
    are b6f is set
67. B6F_POPULATION = []
68. while len(B6F_POPULATION) <= Nb6f:
69.     NEW = random.choice(PSII_POPULATION)
70.     NEW2 = [int(NEW[0]),int(NEW[1])]
71.     if NEW2 not in B6F_POPULATION:
72.         B6F_POPULATION.append(NEW)
73.         PSII_POPULATION.pop(PSII_POPULATION.index(NEW))
74. """
75.
76. def step(P):
77.     S = random.choice([[-1,0],[0,-1],[1,0],[0,1]])
78.
79.     for psii in PSII_POPULATION:
80.         if dist([P[0]+S[0],P[1]+S[1]],psii)<PSII_radius:
81.             return P
82.
83.     if (P[0]-350+S[0],P[1]-350+S[1]) in BOUNDARIES:
84.         return P
85.     else:
86.         return [P[0]+S[0],P[1]+S[1]]
87.
88.
89.
90. #main
91. DATA = { }

```

```

92.
93. for B in [98]:
94.     print "Current B:"+str(B)+" Current time" +str(time.time()-T0)
95.     Swidth = 1571-B
96.     BOUNDARIES1 = [(int(grana_radius*np.cos(T*(2*np.pi/1500.0))-
        np.sin(T*(2*np.pi/1500.0))),int(grana_radius*np.sin(T*(2*np.pi/1500.0))+np.cos(T*(
        2*np.pi/1500.0)))) for T in range(Swidth)]
97.     BOUNDARIES = set(BOUNDARIES1[:]) | set(BOUNDARIES2[:])
98.     T = []
99.     datafile=open("results_16_11_16_slit_"+str(Swidth)+"graph2", 'w')
100.
101.
102.         for i in range(500):
103.
104.             P = random.choice(PSII_POPULATION)
105.             PSII_POPULATION.pop(PSII_POPULATION.index(P)) # remove the c
urrent particle from the population
106.             B6F = P
107.             psi_collision = False
108.             t = 0
109.
110.             while psi_collision == False and t <= 10**8: # the 10**8 is meant to sign
ify trapped particles
111.                 P = step(P)
112.                 t += dt
113.                 #X.append(P[0])
114.                 #Y.append(P[1])
115.                 for psi in PSI_POPULATION:
116.                     if dist(P,psi)<PSI_radius:
117.                         psi_collision = True
118.                 T.append(t)
119.                 datafile.write(str(B6F[0])+" "+str(B6F[1])+" "+str(t)+"\n")
120.                 PSII_POPULATION.append(B6F)
121.                 DATA[B] = T
122.
123.     print time.time()-T0

```